



**HAL**  
open science

# Cortical based mathematical models of geometric optical illusions

Benedetta Franceschiello

► **To cite this version:**

Benedetta Franceschiello. Cortical based mathematical models of geometric optical illusions. *Neurons and Cognition [q-bio.NC]*. Université Pierre et Marie Curie - Paris VI; Università degli studi (Bologne, Italie). Dipartimento di matematica, 2017. English. NNT : 2017PA066131 . tel-01633515

**HAL Id: tel-01633515**

**<https://theses.hal.science/tel-01633515>**

Submitted on 13 Nov 2017

**HAL** is a multi-disciplinary open access archive for the deposit and dissemination of scientific research documents, whether they are published or not. The documents may come from teaching and research institutions in France or abroad, or from public or private research centers.

L'archive ouverte pluridisciplinaire **HAL**, est destinée au dépôt et à la diffusion de documents scientifiques de niveau recherche, publiés ou non, émanant des établissements d'enseignement et de recherche français ou étrangers, des laboratoires publics ou privés.



UNIVERSITÉ PIERRE ET MARIE CURIE  
UNIVERSITY OF BOLOGNA

DOCTORAL SCHOOL BRAIN-COGNITION-BEHAVIOUR  
DOCTORAL SCHOOL IN MATHEMATICS

PREPARED AT CENTRE D'ANALYSE ET MATHÉMATIQUES SOCIALES CAMS  
(CNRS - EHESS) AND AT DEPARTMENT OF MATHEMATICS OF UNIVERSITY OF  
BOLOGNA,

# Cortical based mathematical models of geometric optical illusions

*Benedetta Franceschiello*

A Dissertation in fulfilments of the requirements for the degree of  
Ph. Doctor in Cognitive Neuroscience and Mathematics

Directed by Alessandro Sarti and Giovanna Citti

Defended publicly the 28th of September 2017 in front of a jury composed of

Advisors	Alessandro Sarti	CAMS (CNRS-EHESS), Paris, France
	Giovanna Citti	DM, Bologna, Italy
Reviewers	Bart ter Haar Romeny	TU/e, Eindhoven, The Netherlands
	Federica Dragoni	DM, Cardiff University, UK
Examiners	Jean Lorenceau	UPMC, LSP, ENS, Paris, France
	Agnès Desolneux	CMLA, ENS Cachan, France
	Fiorella Sgallari	CIRAM/DM, Univ. di Bologna, Italy





UNIVERSITÉ PIERRE ET MARIE CURIE  
UNIVERSITÉ DE BOLOGNE

ÉCOLE DOCTORALE CERVEAU, COGNITION ET COMPORTEMENT  
ÉCOLE DOCTORALE DES MATHÉMATIQUES

PRÉPARÉ AU CAMS (CNRS - EHESS) ET AU DÉPARTEMENT DES  
MATHÉMATIQUES DE L'UNIV. DE BOLOGNE

# Modèles mathématiques corticaux pour illusions d'optiques géométriques

*Benedetta Franceschiello*

Thèse de doctorat pour obtenir le grade de Docteur en Neurosciences  
Cognitives et Mathématiques

Dirigée par Alessandro Sarti et Giovanna Citti.

Présentée et soutenue publiquement le 28 Septembre 2017 devant  
un jury composé de :

Directeurs	Alessandro Sarti	CAMS (CNRS - EHESS), Paris, France
	Giovanna Citti	DM, Università di Bologna, Italy
Rapporteurs	Bart ter Haar Romeny	TU/e, Eindhoven, The Netherlands
	Federica Dragoni	DM, Cardiff University, UK
Examineurs	Jean Lorenceau	UPMC, LSP, ENS Paris, France
	Agnès Desolneux	CMLA, ENS Cachan, France
	Fiorella Sgallari	CIRAM/DM, Univ. di Bologna, Italy



**Keywords:** Mathematical Modeling - Geometrical Optical Illusions - Neurogeometry - Cortical based model - Visual Cortex - Perception - Subriemannian Geometry - Geodesics - Gabor filters - Image Processing - Inpainting - Enhancement - Hering - Poggendorff - Delboeuf - Ebbinghaus - Zollner.



## Acknowledgements

This project has received funding from the European Union's Seventh Framework Programme, Marie Curie Actions- Initial Training Network, under Grant Agreement No. 607643, "Metric Analysis For Emergent Technologies (MAnET)".

I always believed acknowledgements needed to be made in an every-day situation, picking up one of the usual day life put in front of us. I'm actually in a library, working hard on my thesis and taking a small break. Now that my days in Paris are almost over, an heart rending feeling overwhelms me and it is as simple as beautiful.

My first words of gratitude go to my advisors, Alessandro Sarti and Giovanna Citti. It is hard to go through the deep thankful feeling I have for them, for dedicating me so much time and sharing their expertise, always pushing me to my best and to learn. I would like to thank them for being available during evenings, week-ends and mostly important, thanks for the research topics you assigned me at the very beginning. Modeling and having the chance to learn from you how to do it has been one of the greatest experience of my life. In the last year I also had the chance to work with Giampaolo Cristadoro, who introduced me in the beautiful world of information theory applied to signals. I would like to thank him for his patience, for being always available to discuss and work together. I learned a lot from the time spent together and I am really grateful for this. This work would have not been possible without the help of my co-authors Gonzalo Sanguinetti, Alexey Mashtakov, Filippo Bonora. I would like to thank also all the professors who took time to discuss with me during conferences and meetings: Bart Romeny, Paolo Bartolomeo, Federica Dragoni and Mauro Ursino.

Many thanks to the jury members, for the time and attention they devoted to my work.

Thanks to my office colleagues in Paris and in Bologna. Spending time knowing each other and growing up in such a cultural rich environment has been wonderful. Noemi, Davide, Chiara, Gianmarco (the crew), Camilla, Alessio, Elena, Martin, Annalisa, Alessio, Matteo, Giulio (and Clio), Eugenio, Marco, Gianluca, Giacomo, Marta (per gli after post 19 pm), Michele (i libri!), Monica (il caffè), Romain, François, Alessandro, Andrea, Luca, Laurent.

I would like to thank three special people for me. Lorenzo, the way you allow me to be your friend is one of the most pure joy for which I'll be always grateful. Serena, Erika, you have

always been there, working with me, chatting, helping me out when I could not do it anymore. We are family, and I hope this will last also after this experience together. Emre, you've been a very special friend for me. I always have the feeling that you'd always understand, no matter what strange philosophical or private matter I was submitting you. Marta, you have been not only a colleague, but a real present and important friend. You just have been there, all the time, day by day and I will always remember the sustain and support we gave each other, in this strange period in which we grew up together. Vittorio, thank you for your time, not only the one spent during examinations or talking about mathematics, but most importantly the one we spent outside the department. Fabian, Valentina, thanks for your honesty (as scientists), your hospitality and generosity (as persons). You are a very great source of inspiration to me.

During these years I met so many great people which help me out being the person that I now am, not only from the scientific point of view but mostly important from the human one. I would like to thank the ones who contributed actively to reopen and made me discover a part of myself I was trying to hide, but now is here and keeps me alive and present day by day. Thanks Dani, Carla, Roberta and thank to my aunts, zia Dani and zia Titti, zio Matteo, zia Giusy and all my huge southern family, my cousins: Chiara, Vladimiro (alla seconda con W), Carmelo, Medea, Piero, Robi, Riccardo, Eleonora, Giovanni, Bea, Andrea and my aunts Tecla, Titina and Grazia. You always made me feel protect, and covered, no matter what would have happened. The sense of serenity those thoughts made me arise are the ones who help me think peacefully.

Tutto questo non sarebbe stato possibile se non avessi avuto al mio fianco gli amici di una vita, quelli che è impossibile mollare, nonostante i chilometri, la lontananza e l'essere costretti a sentirsi poco. Però ci siete, sempre, e ci siete sempre stati, e avete contribuito ai miei passi, ogni giorno. Rendete speciale ogni mio viaggio, ogni mio rientro, ogni messaggio che riusciamo a scrivervi. Grazie Alice e Micha (I'll always be with you), Bea (il medico che avrei voluto essere), Maggy (thanks for coming back), Marta (per esserci sempre), Chiara e Ali (perchè ogni volta che vi rivedo mi sembra che il tempo non sia mai passato), Tasso (per la nostra amicizia e per darmi l'opportunità di coltivare i nostri comuni interessi), Filli (sei e sarai sempre una delle persone più intelligenti che io conosca, dannatamente, oserei dire), Laura (la tua amicizia così pura e gratuita è una benedizione, ogni giorno), Veronica (riesci ad essere presente e penso che in fondo, mi hai sempre capita dall'inizio. Grazie anche alla tua metà), Martina (ti stimo e ti voglio molto bene). E come non

ringraziare gli amici sparsi per il mondo e per l'Italia, Giovanni e Ele, Linda e Michele, Greta, Michelino, Luca, Tambu, Ana, Simon, Danilo, Fede, a quelli persi e a quelli ritrovati. Ognuno di voi sa quanto conta, e quanto conterà per me, in termini di presenza, condivisione e ricordi. Grazie.

Allo stesso tempo, un grazie profondo agli amici Parigini, quelli che hanno reso speciali questi anni grazie alla loro compagnia. Grazie di esserci stati, Fra e Chiara (sapete perchè, ogni volta è come tornare a casa), Fra e Migui (per le suonate e le serate), Luca (cuor di Romagna) e Pietro (la qualità)!

In questi ultimi anni ho capito profondamente il significato di famiglia, e di cosa voglia dire avere delle responsabilità e farsene carico. Insieme, abbiamo fatto molto, e assieme a voi ho potuto ridefinire quali sono, in ultimo le mie priorità. Voi siete una di queste, Antonio, Martina, Mamma, Marisa, Raquel, Maria. Jan, tu sei un fratello, e di questo ti devo ringraziare. La presenza e l'affetto che ricevo ogni giorno da voi fratelli, è qualcosa che cambia drasticamente una persona. Voi mi avete cambiata, in meglio, e reso la persona buona e aperta che chiedevo di essere. Mamma, il giorno in cui abbiamo bevuto la prima birra insieme mi dicesti: "Io e te avremmo potuto essere amiche". Vista la mia età, posso dire che aver avuto una madre come te mi stimolerà sempre a fare meglio, con onestà. I sentimenti di amore incondizionato privi di qualunque attaccamento politico o religioso che sei stata in grado di trasmettere a noi figli sono un dono prezioso. Grazie. Quanto a te Nick, hai e avrai sempre tutto il mio supporto. Un grazie profondo anche a Margherita e Gianni, grazie per avermi fatto sempre sentire parte della famiglia, per me lo siete, e molto. Lo stesso ringraziamento lo devo a Simona e Rudy, e mi sento molto fortunata ad essere cresciuta con voi a fianco.

G., grazie per la vita condivisa insieme, per quella che è stata e quella che sarà. Averti al mio fianco mi rende una persona migliore, spiritualmente e nella vita di tutti i giorni. Nessuno era mai riuscito a farsi largo in me, così tanto. Tu, che mi hai resa indipendente e forte, grande e adulta, pur restando sempre al mio fianco. Che tu ci sia e la possibilità di crescere insieme e viverci, è uno dei più bei regali che la vita potesse farmi. Il nostro tempo è sacro, e lo sarà sempre.

*A Giulia, Antonio and Martina,  
Antonella, mia madre  
e Maria-Luisa, mia nonna*





# Contents

<b>1 Introduction</b>	<b>15</b>
<b>2 Phenomenology of perception and neurophysiology of V1 and V2</b>	<b>29</b>
2.1 <i>Phenomenology of perception</i> . . . . .	31
2.2 <i>The visual cortex</i> . . . . .	34
2.3 <i>V1 and its functional architecture</i> . . . . .	37
2.4 <i>V2, the prestriate cortex</i> . . . . .	41
<b>3 Differentiable manifold, Lie groups and Sub-Riemannian geometry</b>	<b>45</b>
3.1 <i>Differentiable manifold theory</i> . . . . .	46
3.2 <i>Lie groups and their properties</i> . . . . .	52
3.3 <i>Riemannian and Sub-Riemannian manifolds</i> . . . . .	53
<b>4 Neurogeometry of V1/V2</b>	<b>61</b>
4.1 <i>Neurogeometry of the primary visual cortices</i> . . . . .	62
4.2 <i>Functional architectures of V1/V2 and their connectivity</i> . . . . .	66
4.3 <i>The lifting of a curve</i> . . . . .	68
4.4 <i>Carnot Caratheodory distances</i> . . . . .	71
<b>5 Sub-Riemannian mean curvature flow for image processing</b>	<b>73</b>

5.1	<i>Notation and lifting of an image in <math>SE(2)</math></i>	74
5.2	<i>Sub-Riemannian mean curvature flow for image processing</i>	76
5.3	<i>Existence of vanishing viscosity solutions</i>	80
5.4	<i>Numerical scheme</i>	91
5.5	<i>Results</i>	94
5.6	<i>Discussion</i>	99
<b>6</b>	<b>Geometrical optical illusions</b>	<b>101</b>
6.1	<i>Role of Geometrical optical illusions (GOIs)</i>	104
6.2	<i>Mathematical models proposed in literature</i>	104
6.3	<i>A neuro-mathematical model for GOIs</i>	106
6.4	<i>Results</i>	112
6.5	<i>Discussion</i>	117
<b>7</b>	<b>Geodesics as perceptual curves in GOIs</b>	<b>121</b>
7.1	<i>Sub-Riemannian Geodesics as perceptual curves in GOIs</i>	123
7.2	<i>Geodesics, distance and Eikonal equation</i>	124
7.3	<i>Sub-riemannian fast marching</i>	125
7.4	<i>Poggendorff illusion</i>	128
7.5	<i>Round Poggendorff</i>	141
7.6	<i>Discussion</i>	142
<b>8</b>	<b>Scale/size Geometrical Optical Illusions</b>	<b>145</b>
8.1	<i>Scale and size of an object</i>	147
8.2	<i>The model</i>	147
8.3	<i>Implementation and Results</i>	150
<b>9</b>	<b>Conclusion and Perspectives</b>	<b>161</b>
9.1	<i>Contributions</i>	161
9.2	<i>Research Perspectives</i>	161

# Bibliography



# 1 Introduction

## English version

THE AIM of this thesis is to present neuromathematical models for visual perception and to deal with such phenomena in which there is a visible gap between what is represented and what we are able to perceive. Such breaches are particularly interesting because they allow to understand the difficult and fascinating mechanisms of seeing, enabling scientists to fill the gap (or at least trying) wheter it is possible. This is the reason why illusory phenomena have always been at the center of many studies, from the psychological, quantitative and qualitative point of view [57, 185, 130]. In the field of *phenomenology of perception*, i.e. the branch studying how percept arises to our consciousness (Husserl, Merleau-Ponty, [118]), the integration of contours in vision has been largely studied by the Gestalt theory since the beginning of the twentieth century [184, 105, 106, 100]. The Gestalt psychology established basic “grouping laws” which are crucial in constructing a phenomenological representation of the physical world: points having one or several characteristics in common, are grouped together to form a new and larger visual object, a gestalt. This approach jointed with quantitative measured parameters provided computational models of Gestalt (for example [48]). One of the phenomenon which drew the interest most is *amodal completion*, deeply analyzed by Kanizsa [100]: it consists in perceiving a completion of a partially occluded object, as the one presented in figure 1.2. The observer perceives a black circle occluded by a gray square. The circle is perceived without the modality of vision, since we only guess its presence, in contrast with *modal completion* present for example in the Kanizsa triangle of figure 1.1, where we perceive the triangle with the modality of vision, even though its boundaries are not present in the stimulus. Boundaries reconstructed by our visual system with both modalities are called *illusory contours*. How we are able to perform completion is an important question, who lead research in vision and image

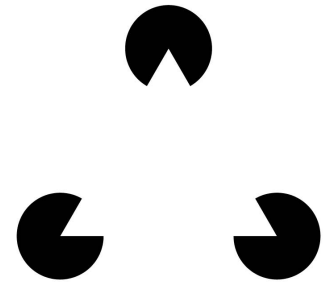


Figure 1.1: The Kanizsa triangle. A white triangle occluding three black disks is phenomenologically perceived. There is an apparent contour separating the triangle from the figure, indeed the interior looks whiter than the background. There is also a stratification of figures, the triangle emerges and seems to be above the disks. This type of phenomenon is classified by Kanizsa as *modal completion*.

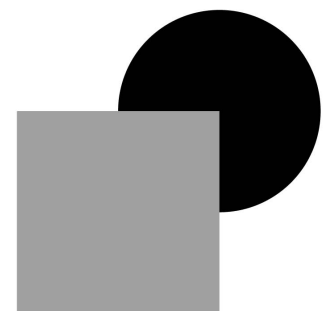


Figure 1.2: An example of *amodal completion*. The figure is perceived as a black circle occluded by a gray square. The circle is present in the visual field, but the completion is performed without an illusory contour.

processing. The prototype of models for curve completion and illusory contours can be found in [125, 132] (Mumford) and has been generalized to level sets of a surface in [115]. On the other hand, partial occlusion occurs also when we look at damaged images such as the ones presented in figure 1.3. Such processing, known as inpainting, has been introduced by Bertalmio et al. in [9]. In neurophysiology, most of the neural processing



Figure 1.3: Left: macula cieca, an example of corrupted surface. Center: an occluded image (from U. Boscain et al. ([14])). Right: a well known example of damaged image, from Bertalmio et al [9].

for boundary coding is performed by the primary visual cortex (V1/V2), [95]. This evidence emerges from an impressive amount of experiments based mostly on measuring the neural activity by means of dye-electrode recording and cortical imaging [93, 94]. The word *neurogeometry* has been introduced by Jean Petitot [139] in 1990s and refers to geometrical models of the functional architecture of primary visual areas. The first geometric models of the functionality of the visual cortex date back to the papers of Hoffmann [86], Koenderink and van Doorn [104], and August and Zucker [3]. Petitot and Tondut in [139] proposed a model of single boundaries completion through constraint minimization, obtaining a neural counterpart of the models of Mumford. In this setting Citti and Sarti introduced a cortical based model [28], which justifies the presented illusory phenomena at a neural level and provides a neurogeometrical model for the primary visual cortex.

Another class of very interesting phenomena are Geometrical optical illusions (GOIs), known in literature since the end of the XIX century [83, 187, 190]. GOIs arise when there is a mismatch of geometrical properties between an item in object space and its associated percept [185]. Let us consider an example such as the one presented in figure 1.4 top left: the Hering illusion. In this image the presence of a radial background bends the two vertical lines, which are actually parallel instead. Psychological and mathematical models for explaining such phenomena have been presented and summarized for example in [85, 58, 57, 130] as well as quantitative studies to measure the magnitude of the illusion. Both topics will be addressed to in chapter 6 and 7 and an overview of the huge amount of literature for these phenomena will be provided. The fundamen-

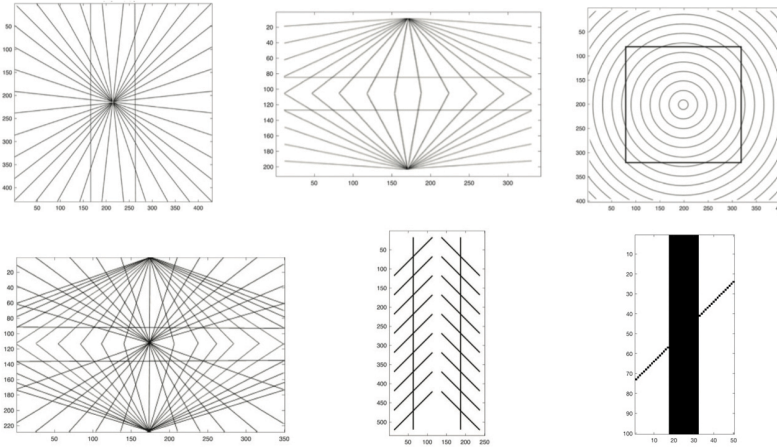
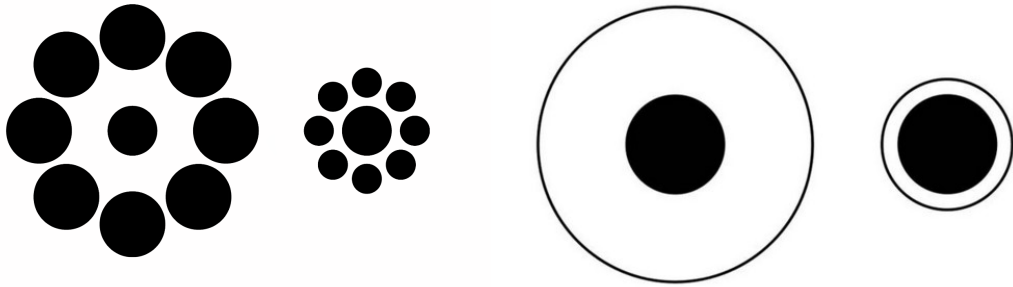


Figure 1.4: Top, from left to right. Hering illusion: two straight vertical lines in front of a radial background appear as if they were bowed outwards. Wundt-Illusion: an opposite bending effect with respect to the Hering illusion. Ehm [58] Square: the context of concentric circles bends inwards the edges of the square. Bottom, from left to right. Wundt-Hering illusions merged together: the bending effect is inhibited by the presence of conflicting inducers. Zollner illusion: a pattern of oblique inducers surrounding parallel lines creates the illusion they are unparallel. Poggendorff illusion: the presence of a central surface induces a misalignment of the crossing transversals.

tal idea developed in this thesis is that these phenomena arise due to a polarization of the connectivity of the primary visual cortex, which will be responsible for the misperception. Starting from the neuromathematical model proposed by Citti and Sarti in [28] in which the connectivity building contours in the primary visual cortex is modeled through a sub- Riemannian metric, we will extend it claiming that in such phenomena the cortical response to the stimulus modulates the connectivity of the cortex, becoming a coefficient for the sub- Riemannian metric. Many GOIs will be processed through the presented method, also complex illusions, such as the ones involving the size. Size is an estimation of the actual width of an object, and the context in which a target is immersed can affect its size perception. If we look at images as the ones presented in figure 1.5, left, the central target is perceived as shrinking or enlarging depending on the size of the surrounding circles, which form an annulus around the central circle (target). The challenge of this last approach is to introduce a plausible mathematical model which would justify the phenomenon. A comparison which judgemental studies will be provided, in the attempt to uniform a theory which has been divided and compared to a “babel tower” [130] since when those phenomena have been studied. We believe that the only way to uniform it is to provide a cortical based mathematical model, which will provide an explanation for those phenomena correct from the quantitatively and qualitatively point of view.



The first three chapters of this thesis introduce and define concepts that will be at the basis of the original contributions we will present. The other chapters can be read independently of each other, except for chapter 8 which is linked to chapter 6. Original contributions and their relative published material are referenced at the beginning of each chapter.

In chapter 2 neurophysiological and phenomenological preliminaries are provided. First we will perform an overview of illusory phenomena, starting from Gestalt theory and finishing with Geometrical optical illusions. The second part of the chapter contains the neurophysiology of the primary visual cortices V1/V2. The visual process is explained starting from its early stage, from when the light impacts the retina and its signal is further processed by the cortex. The functional architecture of the primary visual cortices will be described, particularly focusing on the hypercolumnar structure (Hubel and Wiesel [93, 94]): for each point of the retina a whole set of cortical cells will respond, each one sensitive to a specific instance of a certain feature. In case of simple cells, we will have a whole set of cells, each one sensitive to a specific orientation. The maximum over this set will be the tangent direction of the visual stimulus. A cortical mechanism of non maxima suppression is able to select the maxima orientation. This mechanisms can be extended to other features, such as the scale (i.e. distance from a boundary). We will conclude the chapter introducing the connectivity mechanisms responsible for the formation of contours and surfaces.

In chapter 3 all mathematical instruments necessary for understanding the cortical based models we will introduce later on are presented. We will provide an introduction to differential geometry, explaining the concept of fiber bundle, which will model the hypercolumnar structure of the cortex. Then we will focus on Lie Groups and their properties, ending the chapter with notion of sub- Riemannian geometry. The anisotropic structure arising from these elements will account for the connectivity arising in the cortex.

Figure 1.5: Left couple: Ebbinghaus (or Titchner) illusion: two circles of identical size are placed near to each other, and one is surrounded by large circles while the other is surrounded by small circles. In the left part of the stimulus, inducers are larger in size than the central circle, inducing a decreasing size-perception of the latter. In the same way when inducers are smaller in size than the target size, the size-perception of the latter increases. Right couple: Delbouef illusion: the presence of an annulus around the target (black circle) induces a misperception of the size of the latter. If the annulus is big, the target tends to shrink or not displace at all (left). As long as we decrease its width, the target is perceived as expanding.

In chapter 4 we will present the neurogeometric model introduced by Citti and Sarti in [28]. Their ideas are at the basis of all concepts developed later on in this thesis. We will see how neurophysiology of V1 and the geometrical notions introduced before merge together, providing a differential structure which naturally endow the cortex and allows to model the connectivity. In this setting perceptual phenomena arise as curves and surfaces of differential operator of  $\mathbb{R}^2 \times S^1$  in the sub-Riemannian metric introduced as model for the anisotropic connectivity of the cortex.

In chapter 5 we will develop the sub-Riemannian operator of mean curvature flow which allows to model the perceptual arising of surfaces. In particular, the phenomenon of amodal completion will be explained and we will see how this approach is at the basis of a performant image processing algorithm, allowing to recover damaged parts of an image (inpainting, [9]). Furthermore, the problem of existence of vanishing viscosity solutions (in the sense of Crandall, Ishii and Lions [37]) will be faced from a theoretical point of view. The main idea of the proof will be to look for solutions of the approximating operator for which the classical results hold. Then we will pass to the limit in order to recover the sub-Riemannian solution of the mean curvature flow equation. The latter will have the property of being a surface of minima area and will model the perceptual completion of missing parts of an image. If we let the equation evolving on the whole image, we can perform enhancement, i.e. a technique allowing to put in evidence contours and make them brighter [53, 54]. These results are published in [30].

In chapter 6 we will look for a mathematical model able to explain Geometrical optical illusions, i.e. those situations in which there is a mismatch of geometrical properties between the item in the object space and its associated percept ([185]). The main idea is to consider a polarization of the sub-Riemannian metric introduced before which is now modelled by the response of simple cells to the initial stimulus. In this approach is the output of simple cells which modulates the connectivity responsible for the deformation of the initial stimulus, see for example the set of images in figure 1.4. Projecting the polarized metric from  $\mathbb{R}^2 \times S^1$  to  $\mathbb{R}^2$  we obtain a new metric from which we can derive a direct expression for the displacement, using infinitesimal strain theory tools. We will end with displacement vector fields that once applied to the initial stimulus will allow to represent what we actual perceive when we look at such images. These results are published in [69, 68].

In chapter 7 the previous approach is extended, but the challenge is to understand if the deformation curves derived as ex-

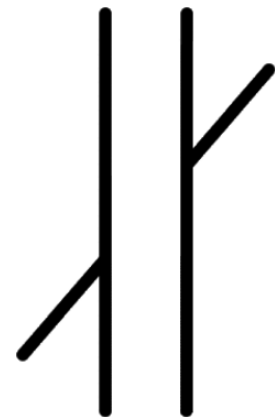


Figure 1.6: Poggendorff illusion: the presence of a central surface induces a misalignement of the crossing transversals.

plained in chapter 6 can arise as minima of the polarized metric modulated by the output of simple cells. This allows to explain such phenomena in which the amodal completion of a surface intervenes, generating misalignment of transversals, see for example the well known Poggendorff illusion 1.6. Once the output of receptive profiles of V1 is determined and the polarized metric arise as model for the connectivity, geodesics are computed through sub- Riemannian Fast- Marching, a method which extends the one introduced by Sethian [156], developed by Sanguinetti et al. in [152] starting from a Riemannian adaptation due to Mirebeau, see [120]. It consists in computing the approximating solution of the Eikonal equation, from which a distance map in the sub- Riemannian metric from a certain given boundary condition is calculated. In this setting, geodesics are back- tracked (gradient descent) on this map and minimize the length of their paths. The perceptual curves arising in GOIs will be these geodesics. These results will be contained in the papers [67, 66].

In chapter 8 we extend the previous models to the analysis of scale/size illusions, such as the ones presented in figure 1.5. The mechanism is similar to the one applied in section 6, but with a different feature: first the distance (scale) of a point from the nearest boundary is detected, then the size is evaluated from it. Here we will evaluate the interaction between the individuated perceptual units (circles, figure 1.5) introducing an isotropic functional connectivity related to the feature of scale, starting from the model proposed in [154]. The perceived size of the central target in the Ebbinghaus and Delbouef illusion will be then derived and these results will be compared with judgemental studies [116] which evaluate how the perceived size changes in relation with the numbers of inducers and their sizes. The result will be contained in [65].

Finally chapter 9 summarizes the original contributions of this thesis and possible extensions

## French version

L'OBJECTIF de cette thèse est de présenter des modèles neuro-mathématiques pour la perception visuelle et de s'intéresser aux phénomènes dans lesquels on identifie une brèche visible entre ce qui est représenté et ce qui est perçu. Ces brèches constituent un intérêt particulier parce qu'elles permettent de comprendre le difficile et fascinant mécanisme de la vision et les scientifiques peuvent donc essayer de remplir ce "gap", à condition que cela soit réalisable. Cela explique en grande partie la raison pour laquelle les phénomènes illusoires ont toujours été au centre de nombreuses études, d'un point de vue psychologique, quantitatif et qualitatif [57, 185, 130]. Dans la branche de la phénoménologie de la perception, c'est-à-dire des études analysant la manière dont le percept apparaît à notre conscience (Husserl, Merleau-Ponty, [118]), l'intégration des contours en vision a été énormément étudié par les théoriciens de la Gestalts, et ce à partir du début du 20ème siècle [184, 105, 106, 100]. La psychologie de la Gestalt a établi des règles basiques de "grouping" qui sont cruciales pour construire une représentation phénoménologique du monde physique: les points qui ont une ou plusieurs caractéristiques en commun sont groupés (grouping) ensemble pour former un nouveau et plus large objet, une "gestalt". Cette approche, jointe avec les paramètres mesurés quantitativement, a permis de construire des modèles computationnels pour la Gestalt (voir exemple [48]). Un phénomène des plus intéressants est la *complétion amodale*, largement analysée par Kanizsa [100]: ce phénomène consiste à percevoir la complétion d'un objet partiellement occlus, comme celui représenté dans l'image 1.8. L'observateur perçoit un cercle noir occlus par un carré gris. Le cercle est perçu sans la modalité de la vision, car nous devinons seulement sa présence. Ce phénomène contraste avec celui de la complétion modale, présente par exemple dans le triangle de Kanizsa, image 1.7, dans laquelle nous percevons le triangle avec la modalité de la vision, même si les contours ne sont pas présents dans le stimulus. Les contours reconstruits par notre système visuel avec les deux modalités sont appelés des *contours illusoires*. Comment sommes-nous capables de réaliser la complétion est une question absolument centrale, qui a guidé la recherche dans la branche de la vision et du traitement des images. Le prototype des modèles pour la complétion de courbes et contours illusoires - que nous pouvons retrouver dans [125, 132] (Mumford) - a été généralisé aux courbes de niveau d'une surface en [115]. Ce processus, connu sous le nom d' "inpaint-

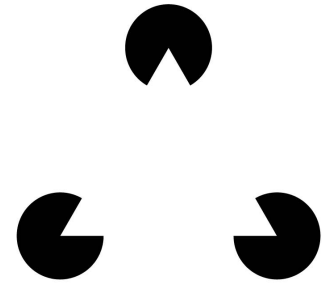


Figure 1.7: Le triangle de Kanizsa. On perçoit un triangle blanc obstrué par trois cercles noirs. Un contour illusoire sépare le triangle du reste de l'image, et la partie intérieure du triangle apparaît plus blanche que celle au dehors. On observe aussi une stratification des figures: le triangle émerge et semble être au-dessus des cercles. Ce type de phénomène est classifié par Kanizsa sous le nom de *complétion modale*.

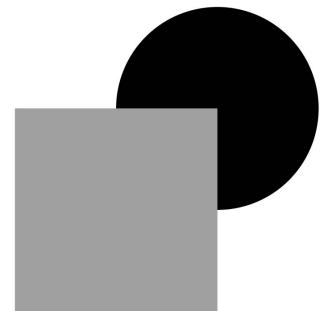


Figure 1.8: Un exemple de *complétion amodale*. L'image est perçue comme un cercle noir occlus par un carré gris. Le cercle est présent dans le champ visuel, mais la complétion est effectuée sans un contour illusoire.

ing”, a été introduit par Bertalmio et al. dans [9]. En neuro-



Figure 1.9: Gauche: macula cieca, un exemple de surface corrompue. Centre: une image occluse (dans U. Boscain et al. ([14])). Droite: un exemple connu d’image endommagée, dans Bertalmio et al [9].

physiologie, la plupart du traitement du signal neural pour le coding des contours est réalisé par les cortex visuels primaires (V1/V2) [95]. Cette évidence émerge de nombreuses expériences de mesures de l’activité neurale par enregistrement avec électrodes et instruments d’imagerie cérébrale [93, 94]. Le mot neuro-géométrie a été introduit par Jean Petitot [139] en 1990 et se réfère aux modèles géométriques pour l’architecture fonctionnelle des régions visuelles primaires. Les premiers modèles géométriques pour la fonctionnalité du cortex visuel sont attribués aux travaux de Hoffmann [86], Koenderink et van Doorn [104], et August et Zucker [3].

Petitot et Tondut dans [139] ont proposé un modèle pour la complétion de contours avec des contraintes de minimisation, équivalent neurale du modèle proposé par Mumford. Dans cet environnement, Citti et Sarti introduisent un modèle basé sur l’architecture fonctionnelle du cortex visuel [28], qui justifie les illusions à un niveau neurale et envisage un modèle neuro-géométrique pour V1.

Une autre classe des phénomènes particulièrement intéressantes est celle des illusions d’optique géométrique (GOIs), connues en littérature à partir de la fin du XIX-ème siècle [83, 187, 190]. GOIs apparaît en présence d’une différence entre ce qui est présent dans l’espace (objet) et la perception associée [185]. On se référera par exemple à l’image de la figure 1.10, en haute à gauche: il s’agit de l’illusion de Hering. Dans cette image, la présence du fond radial courbe les lignes verticales, qui sont tout-à-fait parallèles.

Des modèles mathématiques et psychologiques pour expliquer ces phénomènes ont été introduits et résumés dans [85, 58, 57, 130], ainsi que des études quantitatives pour mesurer la magnitude de l’illusion. Nous traiterons les deux sujets dans les chapitres 6 et 7, et un résumé d’une grande partie de la littérature sur ces phénomènes sera fournie. L’idée fondamentale développée dans cette thèse est que ces phénomènes se produisent suite à une polarisation de la connectivité des cortex visuels primaires, responsables de l’illusion. A partir du mod-

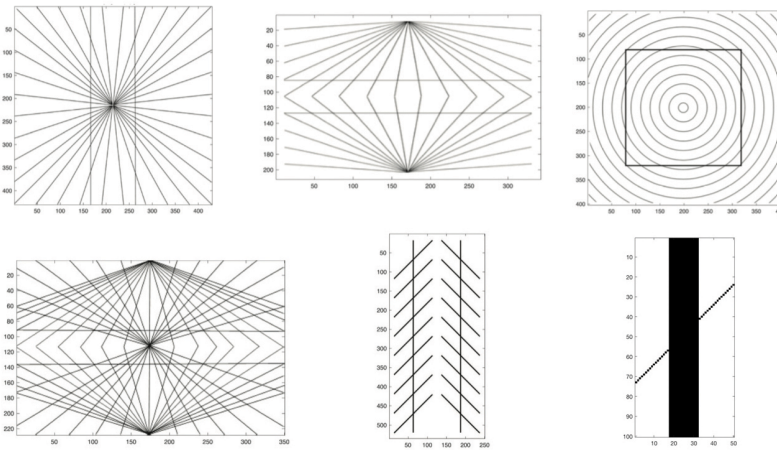
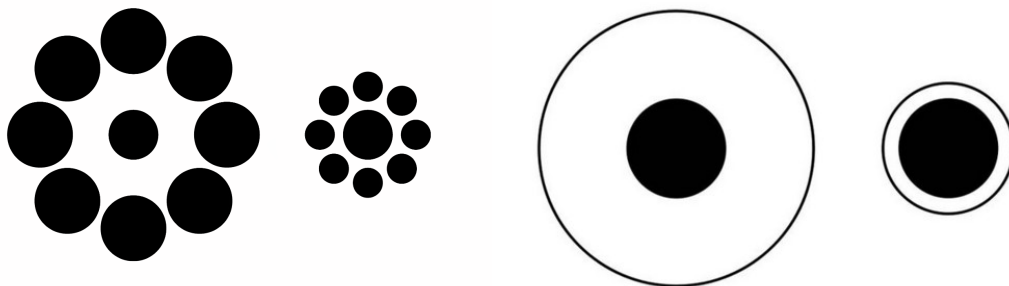


Figure 1.10: En haut, de gauche à droite. Illusion de Hering: deux lignes parallèles sont posées sur un fond constitué des lignes radiales, en apparaissant courbées vers l'extérieur. Illusion de Wundt: un effet de courbure opposé à celui présenté dans l'illusion de Hering. Carré de Ehm [58]: le contexte de cercles concentriques courbe vers l'intérieur les bords du carré. En bas, de gauche à droite. Les illusions de Wundt et Hering fusionnées: l'effet de courbure est annulé par la présence des inducteurs en conflit. Illusion de Zollner: des inducteurs obliques environnant deux lignes parallèles donnent lieu à un effet de non-parallélisme. Illusion de Poggendorff: la présence d'une surface coupant une ligne cause un effet de désalignement.

èle neuro-mathématiques proposé par Citti et Sarti en [28], où la connectivité qui construit les contours en V1 est modélisée avec une métrique sub-Riemannienne, on étend cela en disant que pour les GOIs la réponse corticale du stimulus initial module la connectivité du cortex, en devenant un coefficient pour la métrique. Beaucoup de GOIs seront traitées avec la méthode présentée ici, ainsi que des illusions plus complexes, comme celles qui concernent l'échelle. L'échelle est une estimation de la largeur réelle d'un objet et le contexte dans lequel l'objet dont on cherche à évaluer la largeur est immergé peut affecter cette évaluation. Si nous regardons les images représentées dans la figure 1.11, le cercle central est perçu rétréci ou agrandi par rapport à l'échelle des cercles qui entourent le cercle central (cible). Le challenge de cette approche est d'introduire un modèle mathématique plausible décrivant le phénomène présenté. Nous fournirons une comparaison avec des études "judgemental", en cherchant à unifier une théorie qui a été comparée à "la tour de Babel" [130] depuis que ces phénomènes ont été découverts. Nous croyons que la seule façon de réaliser cela est de fournir un modèle mathématique basé sur l'architecture fonctionnelle, capable d'expliquer les illusions du point de vue quantitatif et qualitatif.

Les trois premiers chapitres de cette thèse introduisent et définissent des concepts qui seront à la base des contributions originales que nous présentons. Les autres chapitres peuvent être lus de manière indépendante, sauf le chapitre 8 qui est lié au chapitre 6. Les contributions originales et les matériaux publiés qui les contiennent sont cités au début de chaque chapitre.

Dans le chapitre 2 nous présentons les prérequis neuro-physiologiques et phénoménologiques. D'abord, on fera une présentation des phénomènes illusoire, à partir de la théorie de la Gestalt et en finissant avec les illusions d'optique géométrique.



La deuxième partie du chapitre décrira la neurophysiologie des cortex visuels primaires V1/V2. Nous expliquerons le processus visuel à partir de ses étapes initiales, quand la lumière touche la rétine et le signal est traité par le cortex. L'architecture fonctionnelle des cortex visuels primaires sera décrite, en se concentrant sur la structure hypercolumnnaire (Hubel et Wiesel [93, 94]): pour chaque point sur la rétine une collection entière de cellules corticales répond, et chacune de ces cellules est sensible à une certaine valeur de la caractéristique (couleur, orientation, échelle) que le cortex est en train de traiter. Dans le cas des cellules simples de V1, nous aurons un ensemble entier de cellules, chacune sensible à une orientation spécifique. Le maximum sur cet ensemble sera la direction tangente du stimulus visuel passant par le point considéré. Le mécanisme cortical de suppression non-maximal est capable de sélectionner l'orientation maximale. Ce mécanisme peut être étendu aux autres caractéristiques de l'image, comme l'échelle (distance entre un point et les contours le plus proches). Nous concluons le chapitre en introduisant le mécanisme de connectivité responsable de la réalisation des contours et surfaces dans le cortex.

Nous verrons dans le chapitre 3 les instruments mathématiques nécessaires pour comprendre les modèles corticaux qu'on introduira dans les chapitres suivants. Nous donnerons une introduction à la géométrie différentielle, en expliquant le concept de fibration, qui modélisera la structure hypercolumnnaire du cortex. Ensuite les groupes de Lie et leurs propriétés seront traités et on terminera le chapitre avec des notions de géométrie sub-Riemannienne. La structure anisotrope que nous obtenons des éléments traités nous aidera à expliquer la connectivité que l'on retrouve dans V1/V2.

Dans le chapitre 4 on présentera le modèle neurogéométrique introduit par Citti et Sarti en [28]. Leurs idées sont à la base de toutes les contributions développés dans cette thèse.

Nous verrons comment la neurophysiologie de V1 et les notions de géométrie dont on a parlé dans les chapitres précédents fusionnent en donnant une structure différentielle qui

Figure 1.11: Couple à gauche: illusion de Ebbinghaus (ou Titchner): deux cercles centraux qui ont la même échelle sont entourés, l'un des cercles plus larges (gauche), l'autre de cercles plus petits (droite). Les grands inducteurs modifient la perception du cercle central (cible), qui apparaît plus petit que sa largeur réelle (son échelle). L'effet opposé se produit quand les inducteurs sont petits. Couple à droite: illusion de Delbouef. La présence d'un anneau autour du cercle central crée une mauvaise perception de son échelle. Si l'anneau est grand, la cible ressemble plus petit. Si la largeur de l'anneau diminue, la cible est perçue comme s'il était plus grande en échelle.

modélise naturellement le cortex et sa connectivité. Dans cet environnement, les phénomènes perceptifs émergent comme courbes et surfaces des opérateurs différentiels de  $\mathbb{R}^2 \times S^1$  dans la métrique sub- Riemannienne introduite comme modèle pour la connectivité anisotrope du cortex.

Dans le chapitre 5, nous développons l'opérateur de flux de courbure moyenne qui permet de modéliser l'émergence perceptuelle des surfaces. En particulier nous expliquerons la complétion amodale et nous verrons comment cette approche est à la base des algorithmes de traitement des images, en nous permettant de reconstruire des parties corrompues d'une figure (inpainting, [9]). En plus, le problème d'existence des solutions de type vanishing viscosity (dans le sens de Crandall, Ishii et Lions [37]) sera traité d'un point de vue théorique. L'idée principale de l'épreuve est de chercher des solutions, approximations de l'opérateur initial, pour lesquelles les résultats classiques sont valides. Ensuite nous ferons la limite pour retrouver la solution sub- Riemannienne à l'équation du flux de courbure moyenne. Cette solution aura la propriété d'être une surface avec aire minimale et modélisera la complétion perceptuelle des parties manquantes d'une image. Si nous laissons évoluer l'équation sur la figure entière on peut effectuer l'enhancement, c'est à dire une technique qui permet de mettre en évidence les contours [53, 54]. Ces résultats sont publiés en [30].

Dans le chapitre 6, nous cherchons un modèle mathématique capable d'expliquer les illusions d'optique géométrique, qui apparaissent en présence d'une différence entre ce qui est présent dans l'espace (objet) et la perception associée ([185]). L'idée fondamentale est de considérer une polarisation de la métrique sub- Riemannienne introduite auparavant, modulée maintenant par les réponses des cellules simples de V1 au stimulus initial. En suivant cette idée, la réponse des cellules modulant la connectivité est responsable de la déformation du stimulus initial (par exemple, regarder l'ensemble d'images de figure 1.10). En faisant une projection de la métrique polarisée de l'espace  $\mathbb{R}^2 \times S^1$  à l'espace  $\mathbb{R}^2$ , on obtient une nouvelle métrique, à partir de laquelle nous dérivons une expression directe pour le déplacement. Les instruments utilisés viennent de la théorie infinitésimale des déformations. Cela nous permettra de calculer les champs vectoriels du déplacement qui, une fois appliqués à l'image initiale, représenteront le percept, c'est-à-dire ce que nous percevons en présence des stimuli illusoire. Ces résultats sont publiés en [69, 68].

Dans le chapitre 7, l'approche précédente est étendue, mais le challenge est de comprendre si les courbes de déformation obtenues en suivant l'explication du chapitre 6 peuvent être

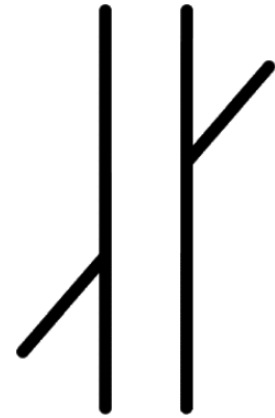


Figure 1.12: Illusion de Poggen-dorff: la présence d'une surface coupant une ligne cause un effet de désalignement.

aussi calculées comme minima de la métrique polarisée par la réponse des cellules simples. Cela permettra d'expliquer les phénomènes dans lesquels la complétion amodale des surfaces joue un rôle, en créant le désalignement d'une ligne (par exemple illusion de Poggendorff, 1.12). Une fois que les réponses des profils récepteurs de V1 et V2 sont déterminées, et que la métrique polarisée émerge comme modèle pour la connectivité neurale, les géodésiques sont calculées avec le Fast-Marching sub-Riemannienne, une méthode qui élargit celle qui fut introduite par Sethian [156], développée par Sanguinetti et al. en [152] à partir d'une adaptation Riemannienne due à Mirebeau, voir [120]. La méthode consiste à calculer la solution approchée de l'équation Eikonal, avec laquelle on peut déduire une fonction distance entre les points de l'ensemble et la condition à la frontière, en métrique sub-Riemannienne.

Dans cet environnement, les géodésiques sont trouvées par descente du gradient sur la fonction distance et elles minimisent la longueur de leurs trajets. Les courbes perceptives que nous voyons dans le GOIs seront ces géodésiques. Les résultats sont contenues dans les articles [67, 66].

Dans le chapitre 8, nous poursuivons avec le modèle précédent en cherchant une extension aux illusions d'échelle, comme celles que nous pouvons observer dans l'image 1.11. Le mécanisme décrit est similaire à celui appliqué dans le chapitre 6 mais avec une caractéristique (feature) différente analysée: d'abord, la distance (échelle) entre un point et le contour le plus proche est calculée. Ensuite, la taille de l'objet est évaluée. Ici, nous considérons l'interaction entre les unités perceptives détectées dans l'image (les cercles, figure 1.11) et nous introduirons une connectivité fonctionnelle isotrope liée à l'échelle à partir du modèle proposé en [154]. La taille de la cible centrale perçue dans les illusions de Ebbinghaus et Delbouef sera calculée et ces résultats seront comparés avec des études "judgemental" [116], qui évaluent comment la taille perçue change en relation avec le numéro des inducteurs et leurs tailles. La contribution originale sera contenue dans [65].

Le chapitre final 9 résume toutes les contributions originales de la thèse et leurs possibles extensions.





## 2 Phenomenology of perception and neurophysiology of V1 and V2

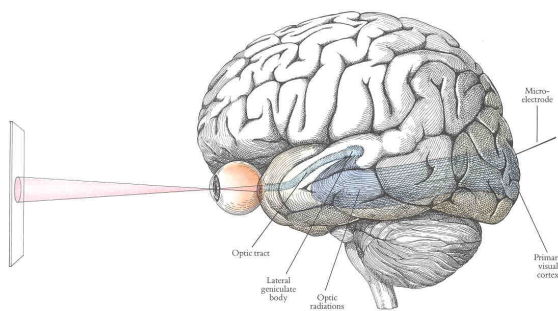


Figure 2.1: A representation of the visual path, from Hubel [95].

OUR AIM IN THIS CHAPTER is to give the psychological and neurophysiological basis for understanding the visual processes responsible for the phenomenon of amodal completion of surfaces and for the illusory contours formation in Geometrical optical illusions. Many concepts were introduced by the exponents of Gestalt movement in psychology and we will understand the role this approach had in carrying out researches in perception. In fact, the interest on illusions relies on the fact that they could provide an insight about how the visual process is actually carried out while a subject undergoes a visual stimulus. The first class of stimuli refers to the psychological principles organizing visual contents while we look at a stimulus. The second class contains deformation of the space, introducing a pure mismatch between what is represented in the *real world* and what is perceived. On the other hand the enlightened mechanisms in psychology need to be contextualized through an overview of the neuro-physiology of brain parts involved, i.e. the functional architecture of the primary visual cortices (V1/V2, Brodmann area 17/18 respectively). The basic idea is that neural interaction strongly depends on the organization and connectivity of neurons in the cortex and it actively participates in generating such phenomena. We will restrict our attention to the structures relevant to the model presented

in the later chapters: receptive fields and receptive profiles of simple cells in V1/V2, the hypercolumnar structure of V1, the cortical connectivity. In the following table you can find the organization of the contents for this chapter.

## 2.1 Phenomenology of perception

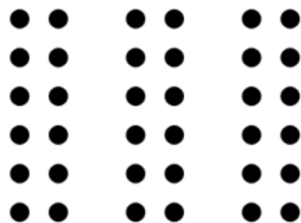
### 2.1.1 Gestalt psychology

One of the big question about vision is how the act of sight happens and which elements participate to realize it. Visual perception is not a simple acquisition of the real stimulus, but is the result of a series of complex processes which mediate between the physical stimuli and the phenomenological organization of such stimuli. According to Gaetano Kanizsa, one of the main exponents of the Gestalt psychology,

“Perception consists of an active construction by means of which sensory data are selected, analyzed and integrated with properties not directly noticeable but only hypothesized, deduced, or anticipated, according to available information and intellectual capacities.”

The movement of Gestalt was started by Wertheimer, Köhler and Koffka, with the basic idea that the visual phenomena need to be considered as global events, not reducible to the set of its parts. There exist local and global laws which justify the “act of sight ” (the appearance of the perceptual units which compose an image). Then complex phenomena can be understood considering the *idea of structure* more than a single element, i.e. the parts of a visual stimulus are grouped together to form the whole, and the whole is what we actual see first. These characteristics allowing the formation of the percept are defined as laws that describe the influence of global context in the perception of local features. Elements tend to be perceptually grouped and made salient in case of *proximity, similarity, closure, good continuation and alignment*. Let us go through these local rules (Kanizsa, [100]):

- *Proximity*: elements constitute a single perceptual unit if they are close to each other and apart from the rest of the elements which belong to the image, see Figure 2.3.



- *Similarity*: elements constitute a single perceptual unit if they are similar in color, shape, texture or orientation, see Figure 2.4.



Figure 2.2: Gaetano Kanizsa, one of the father of the Gestalt psychology, author of *Grammatica del vedere* (Organization in Vision, [100]).

Figure 2.3: An example of proximity, [100]. In this example three groups of elements are perceived.

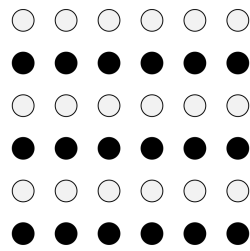


Figure 2.4: An example of similarity, Kanizsa, [100]. in this example we identify six groups, divided by law of proximity and similarity. Black dots which form a line are separated from the other black dots and form a perceptual unit.

- *Closure*: our perception tends to close contours, because perception is stronger in case of closed contours and to facilitate a pop up of the figure, see Figure 2.5.

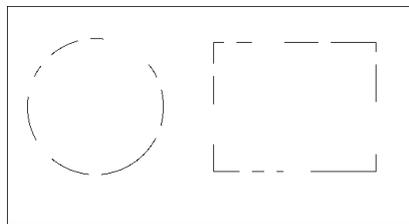


Figure 2.5: An example of closure: we clearly perceive a pop-up of a rectangle and a circle, even if the contours are interrupted.

- *Good continuation and alignment*: elements aligned (or with comparable alignment) tend to form a continuous curve. In figure 2.6 we perceive a unique curve of black dots even if the black bar interrupts them.



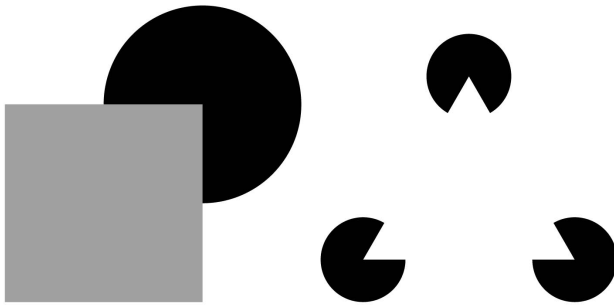
Figure 2.6: An example of good continuation, adapted from Kanizsa, [100]

More than one grouping law at a time, as we saw in the previous example, can contribute to the perception of a complex object. In this sense the local laws contribute to the formation of the percept. Another observation coming out from the previous experiments is that the perceptual reality is formed in each time by a discrete number of objects, which do not necessarily depend on the existence of correspondent physical objects.

### 2.1.2 Perceptual completion

Phenomena in which there is a phenomenological presence of boundaries without a physical stimulus (such as in the famous

Kanizsa-Triangle, figure 2.7 right) describe the mechanisms of modal and amodal completion, which are examples of grouping according to *good continuation and alignment*. *Perceptual completion* refers to the ability of the perceptual process to clearly individuate and identify the presence of objects even if they are occluded (figure 2.7 left, amodal completion) or the boundaries are not present in the image (figure 2.7 right). Illusory contours, as the ones presented in figure 2.7 right, constitute an example of modal completion. They generate a percept of a contrast border in image regions that are physically homogeneous [172]. Kanizsa studied in depth these examples, which are important because they underline the fact that the visual stimuli and their phenomenological organization in general do not coincide and for this reason such phenomena help to understand the behaviour of the visual cortex during the act of sight.



A point underlined by these studies is that in both cases of completion the occluding and the occluded objects are perceived at the same time in the scene and therefore there are points in the input stimulus corresponding to more than one figure at the perceptual level. This suggests that the phenomenological space has a higher dimension than that of the physical space, as in this example of a two dimensional image.

### 2.1.3 Geometrical optical illusions

Perception and the corresponding meaning of the act of perception are a deep research theme and constitute a huge field of investigation, in which many disciplines converge into. For our purposes it will be enough to take into account the difference between the physical source of the stimulus and its perception. In psychology the distal stimulus is defined as *the light reflected off a physical object in the external world*: when we look at an image (distal stimulus) we cannot actually experience the image physically with vision, we can only experience it in our mind as proximal stimulus, i.e. *the internal sensory response* [105, 77]. Geometrical optical illusions arise when the

Figure 2.7: (Left) An example of *amodal completion*. The figure is perceived as a black circle occluded by a gray square. The circle is present in the visual field, but the completion is performed without an illusory contour. (Right) The Kanizsa triangle. A white triangle occluding three black disks is phenomenologically perceived. There is an apparent contour separating the triangle from the figure, indeed the interior looks whiter than the background. There is also a stratification of figures, the triangle emerges and seems to be above the disks. This type of phenomenon is classified by Kanizsa as *modal completion*.

distal stimulus and its percept differ in a *perceivable way*. Simple images where the illusion is particularly strong can help to study vision mechanisms which usually take place, so that they appear to be fundamental in understanding the act of visual perception. As explained by Westheimer in [185], we can conveniently divide illusions into those in which spatial deformations are a consequence of the exigencies of the processing in the domain of brightness and the true geometrical-optical illusions, which are misperceptions of geometrical properties of contours in simple figures. Some of the most famous geometric illusions of this last type are shown in figure 2.8. Since the aim

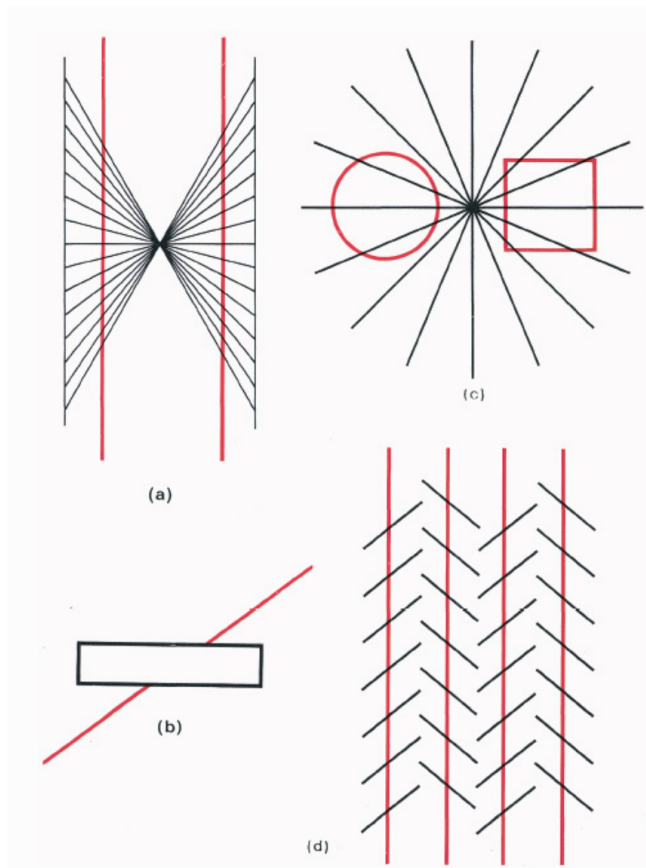


Figure 2.8: From [80]. Top (left), Hering illusion: the presence of a crossing background induce a deformation of the red lines, which are parallel. Top (right) Ehrenstein illusion: a circle and a square are represented over a radial background, which induces a deformation of the geometrical shapes. Bottom (left) Poggendorff illusion: the presence of a central surface creates a perceived misalignment of two segments belonging to the same transversal. Bottom (right) Zollner illusion: the oblique inducers generate a phenomenon of divergence of the four parallel lines.

of this thesis is to present a neuro-mathematical model which rely on the structure and phenomenology of the primary visual cortex (V1/V2) for both presented phenomena (perceptual completion and geometric optical illusions), we need to go through to its physiological structure and organization.

## 2.2 The visual cortex

In order to describe from a mathematical point of view the previous phenomena in which we are interested in, we first need to focus on the functional architecture of the primary visual cor-

tex (Brodmann area 17) and in its basic structures. Receptive fields and receptive profiles of simple cells will be fundamental for boundary coding, one of the first process we will treat, as basis for all other complex functions of the cortex. The three most important structures implemented in the neural circuitry, the layered, the retinotopic and the hypercolumnar structure will be described from the neurophysiological and functional point of view with a qualitatively characterization. Then the pinwheel structure, the topological implementation of the hypercolumnar structure will be introduced. In particular we will focus on simple cells of the primary visual cortex, the first ones which process the visual signal, and on the connectivity pattern between them. For further references about these part see Hubel in [95], Hubel and Wiesel [93, 94] and Petitot [138].

### 2.2.1 The cerebral cortex and the visual pathway

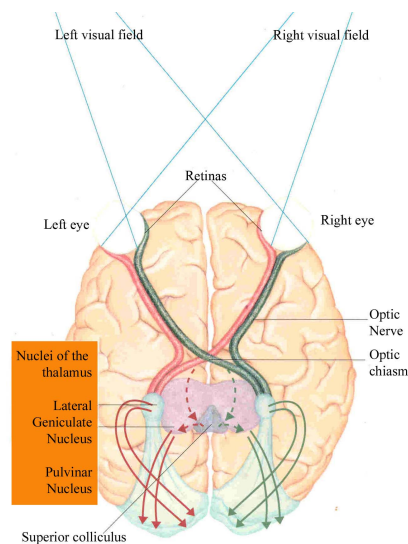


Figure 2.9: The visual path of the brain.

The cerebral cortex is the outermost layer of neural tissue in the two cerebral hemispheres. It plays a central role in sensory and cognitive processing since most of the neurons responsible for these processes are located here. It is commonly divided in three parts: sensory, motor, and association. We are interested in the first of these, which is the part of the cortex that receives sensory inputs. In particular the visual cortex is the area that serves the sense of vision and receives the optical information from the visual path (see figure (2.9)). Light enters the eyes and arrives to the retina, which is composed of thin layers of brain tissue where the neural processing of visual stimuli begins. One of those layer, the nearer one to the optic nerve, is formed mainly of photoreceptors: they have the role of measuring the signal and pixelize it. It is composed by rods and

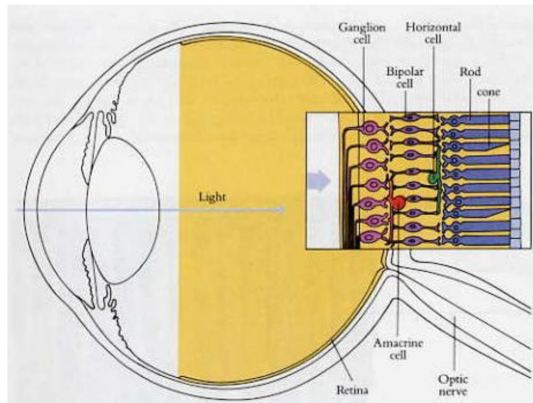


Figure 2.10: An enlarged portion of the retina, at the right, shows the relative positions of the three main retinal layers. Image from Hubel, see [95].

cones. The other two layers consist of ganglion cells and bipolar cells: these layers are connected together through horizontal and amacrine cells. Figure 2.10 shows the organization of cells in the retina layers. The mechanisms connecting these layers are direct and indirect: photoreceptors are responsible for the transduction of the optical signal in action potential. *The receptive field* of a ganglion cell is the region of retina over which a light stimulation can produce a firing. In section 2.2.2 we will go through the concept of receptive field and receptive profile, and their role in decoding the visual signal. As figure 2.10 explains, the layers send the final output of the retina (in the form of action potentials) away from the eyes using their long axons. These axons form the optic nerve, which transmits the visual signals to the lateral geniculate nucleus (LGN) of the thalamus, a structure in the middle of the brain which connects the sensory organs to their main sensory processing cortical areas. From the LGN the signal goes to various destinations: the most important is the visual cortex, situated in the back of the head, where the larger part of the visual processing is performed. The primary visual cortex (V1) is the area to which most of the retinal output first arrives and is the most widely studied visual area, associated to the other layer responsible for what it is called *early stage visual process*.

### 2.2.2 Simple cells of V1/V2: Receptive fields and receptive profiles

As the axons of the ganglion cells project a detailed spatial representation of the retina to the LGN, the LGN projects a similar representation to the primary visual cortex. As we saw each cell in V1 is characterized by its receptive field, the portion of the retinal plane which responds to visual stimulation: the action of light alters the firing of the neuron starting from the ganglion layer of the retina. Classically a receptive field is sub-

divided into *ON* and *OFF* areas. The area is considered *ON* if the cell spikes in positive way responding to a signal (excitatory response to a light stimulus) and *OFF* if it spikes negatively responding to a signal (inhibitory response to a light signal). Hence it is possible to define the receptive profile of a

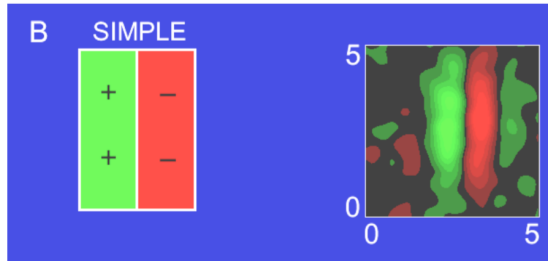


Figure 2.11: In this representation, a receptive profile of a simple neuron (simple cell) of V1. On the right, from De Angelis et al. [44], the recording of level set lines, on the left, the scheme of the structure of the receptive profile with its + (ON) part and its - (OFF) part.

neuron as a function  $\psi(x, y)$  measuring the response of the cell,  $\psi : D \rightarrow \mathbb{R}$  where  $D$  is the receptive field and  $(x, y)$  are retinal coordinates. In this way what is measured is the response of the neuron relatively to a signal at point  $(x, y)$  of the retina. This function models the neural output of the cell in response to a punctual stimulus in the 2 dimensional point  $(x, y)$ . The temporal precision with whom the stimulus is treated is around the millisecond order. Accurate electrophysiological method allowed De Angelis et al. [44], see figure 2.11 to map receptive fields and their correspondent receptive profiles. The characterization given by Hubel and Wiesel in ([93, 94]) classifies the cells in V1 according to their responses. Cells which have separate *ON/OFF* zones are called *simple cells*, all the others *complex cells*. Simple cells have directional receptive profiles, while complex cells are not sensitive to orientation, [138].

## 2.3 V1 and its functional architecture

To understand the processing of the image operated by these cells, it is necessary to consider the functional structures of the primary visual cortex: the layered, the retinotopic and the hypercolumnar structure. We refer to the functional architecture as the spatial organization and the connectivity between neurons inside a cortical area. In V1 we can identify three structures we mentioned before: the layered structure, the retinotopic structure, the hypercolumnar structure.

### 2.3.1 The layered structure

*The layered structure* indicates that the primary visual cortex is formed of 6 horizontal layers, as shown in figure 2.12. This feature made V1 to be the first area of the cortex to be distin-

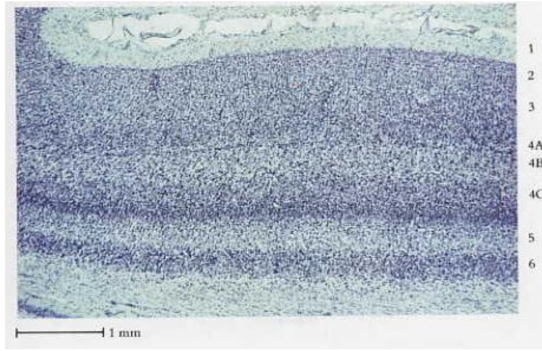


Figure 2.12: A cross section of the striate cortex taken at higher magnification shows cells arranged in layers. Layers 2 and 3 are indistinguishable; layer 4A is very thin. The thick, light layer at the bottom is white matter. Image from Hubel, [95].

guished from the rest. We also refer to it as *striate cortex*, due to this property. Figure 2.13 schematizes the neural projection of each layer of V1 to other cortical regions. For example Layers 2 and 3 and layer 4B project mainly to other regions, while the deep layers project down to subcortical structures. Layer 6 projects mainly back to the lateral geniculate body. All layers except 1, 4A and 4C send fibers out of the cortex. Let us notice that Ramon y Cajal was the first, at the beginning of 1900, to realize how short connections within the cortex are: the richest connections run up and down.

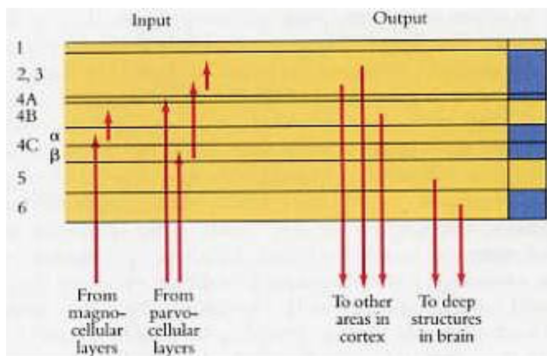


Figure 2.13: The main connections made by axons from the lateral geniculate body to the striate cortex and from the striate cortex to other brain regions. Image from Hubel, [95].

### 2.3.2 The retinotopic structure

The *retinotopic structure* is the topographical organization of the cells in the cortex. The simple cells are arranged in the cortex in such a way that what is near in the visual field is near in the cortex. Precisely we can define a map from the retina to the layers of the primary visual cortex, which introduces a simple deformation of the stimulus, quantitative modeled as a complex logarithmic map.

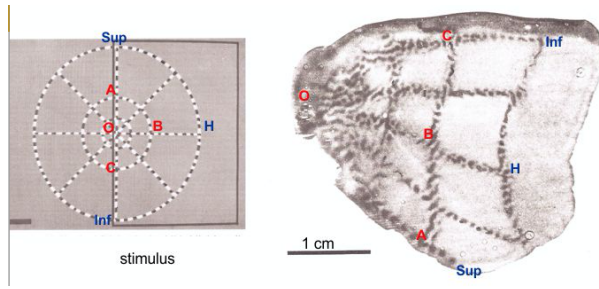
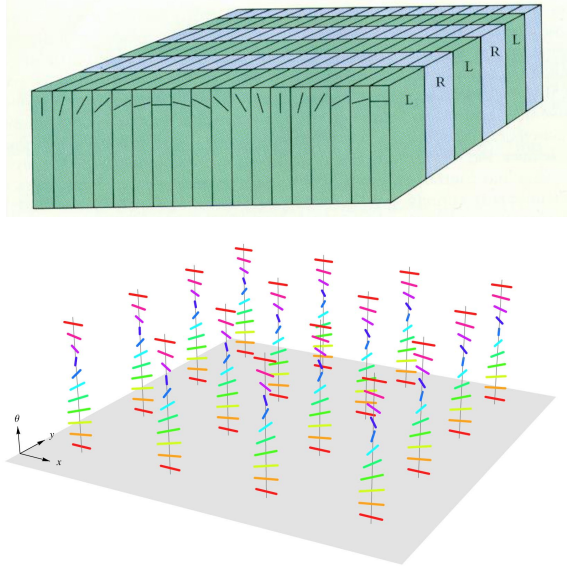


Figure 2.14: In this experiment by Roger Tootell [165], the target-shaped stimulus with radial lines was centered on an anesthetized macaque monkey's right visual field for 45 minutes after injection with radioactive 2-deoxyglucose. One eye was held closed. The right picture shows the labeling in the striate cortex of the left hemisphere. This autoradiograph shows a section parallel to the surface. The roughly vertical lines of label represent the (semi)circular stimulus lines; the horizontal lines of label represent the radial lines in the right visual field.

### 2.3.3 The hypercolumnar structure

The *hypercolumnar structure* refers to the organization of cortical cells in columns corresponding to parameters such as orientation, ocular dominance, color, etc. For the simple cells, sensitive to orientation, columnar structure means that to every retinal position is associated a set of cells (hypercolumn) sensitive to all the possible orientations. At a certain scale and resolution, for each point of the retina  $(x, y)$  there exists a whole set of neurons in V1, each one maximally responding to a specific local orientation  $\theta$  of the stimulus at the point  $(x, y)$ . Since ideally the position on the retina takes values in the plane  $\mathbb{R}^2$  and the orientation preference in the circle  $S^1$ , the visual cortex can be locally modelled as the product space  $\mathbb{R}^2 \times S^1$ . Each point  $(x, y, \theta)$  of this 3D space, represents a column of cells in the cortex associated to a retinal position  $(x, y)$ , all of which are tuned to the orientation given by the angle  $\theta$ .

Figure 2.15 shows a schematic representation of the visual cortex. The hypercolumns are drawn vertically. The different colors represent different orientations. The coordinates  $(x, y, \theta)$  of this 3D space isomorphic to  $\mathbb{R}^2 \times S^1$  are the parameters of the receptive fields (RPs):  $(x, y)$  is the retinotopic position and  $\theta$  the angle of tuning. The fundamental consideration here is that V1 is modelled as a 3D space of positions and orientations, while the cortex is in fact a 2D layer. In fact, the 3D representation provided in figure 2.15 schematizes what in reality is a 2D layer: it has been shown by Hubel and Wiesel in [93, 94] that tangential penetration in the superficial layers of the cortex reveals that the RPs of cells close to each other strongly overlap while the orientation preference varies smoothly generating the orientation hypercolumnar structure. The structure of the cortex allows us to code 3D information in a 2D structure: this dimensional collapse has been illustrated visually by the pinwheel structure, a fascinating configuration observed by William Bosking et al. using optical imaging techniques in which the cells' orientation preference is color-coded and every hypercolumn is represented by a pinwheel. These are the



structures presented in the two small pictures in the right hand side of figure 2.16. A fixed point  $(x, y)$  is surrounded by all orientations  $\theta$  represented in different colors. The same structure is repeated over the whole 2D cortical surface in an almost periodic way. For references see [16]), for its representation see figure 2.16. To an overview of experiments which lead to the discovery of this structure and its neurophysiological basis see Sanguinetti in [149].

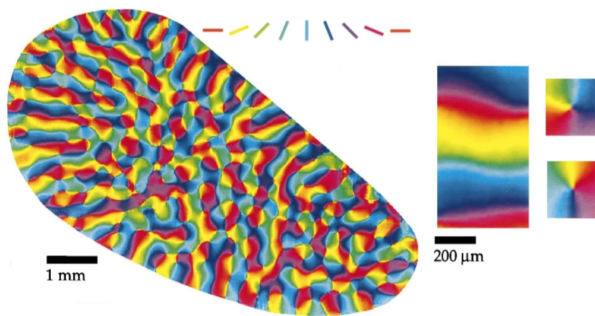


Figure 2.15: Top: classical cube representation (in [93, 94]) of the hypercolumnar structure, for the orientation parameter, where L and R represent the ocular dominance columns (Petitot [138]). The orientation hypercolumns are arranged tangentially to the cortical sheet. Bottom: Over each retinotopic point  $(x_1, x_2)$  there is a set of cells coding for the set of orientations  $\{\theta \in S^1\}$  and generating the 3D space  $\mathbb{R}^2 \times S^1$ . Each bar represent a possible orientation. The color coded map is the same used in figure 2.16. Image from [149].

Figure 2.16: Image from Bosking et al. [16]. The pinwheel structure observed by the authors in [16]. Cells' orientation preferences are color-coded as before, and every hypercolumn results to be squeezed on the 2D layer. Portions of the orientation preference map shown on the left are enlarged to demonstrate that the orientation preference maps contained both linear zones and pinwheel arrangements.

### 2.3.4 The cortical connectivity of V1

#### The short range connectivity

To conclude our review of the functional architecture of V1 we discuss now the connectivity between neurons inside the structure we have seen. In the hypercolumnar structure we can identify two types of communication between neurons which play a central role in the model we want to present: *The intracortical circuitry* is able to select within the hypercolumns the cell which gives the maximal response to a visual stimulus and to

suppress all the others. The mechanism able to produce this selection is called non-maximal suppression or feature selection.

### The long range connectivity

The *horizontal or cortical connectivity* of the primary visual cortex ensures connectivity between hypercolumns. Neurophysiological experiments, for example as the ones conducted in [16] and [78] revealed the existence of connections parallel to the cortical surface (along the structure of pinwheels) that run several millimeters (6 to 8 mm in the visual cortex). These horizontal (or long range) connections connect cells with the same orientation belonging to different hypercolumns, with non overlapping receptive fields, as shown by the injected marker in figure 2.17, from [16]. The injected chemical tracer into a small area of the visual cortex of a tree shrew was propagated through the lateral connections and the resulting image was combined with the orientation maps obtained with optical imaging. In the immediate vicinity of each neuron, the connections are relatively isotropic, but over larger distances they follow the orientation preferences.

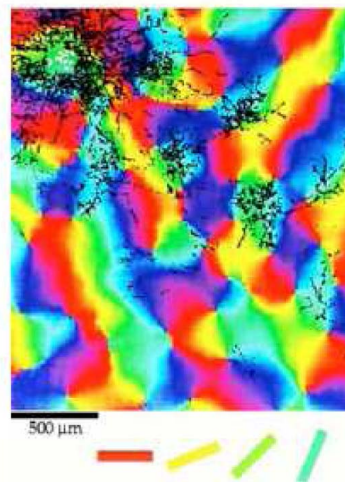


Figure 2.17: Image from Bosking et al. [16]. A marker (biocytin) is injected in the cortex, at a specific point, and it diffuses mainly in regions with the same orientation as the point of injection (see the black path). Same color refers to same orientation preference along the 2D orientation preference map.

## 2.4 V2, the prestriate cortex

Visual area V2 (Brodmann area 18), or secondary visual cortex, also called prestriate cortex [75], is the second major area in the visual cortex, and the first region within the visual association area. It receives strong feedforward connections from V1 (direct and via the pulvinar) and sends strong connections to upper layers of the visual cortex. Not only the feedforward but also feedback connections to V1 are strong. In terms of

anatomy, V2 is split into four quadrants, a dorsal and ventral representation in the left and the right hemispheres.

Together, these four regions provide a complete map of the visual world. V2 has many properties in common with V1: cells are tuned to simple properties such as orientation, spatial frequency, and colour. The responses of many V2 neurons are also modulated by more complex properties, such as the orientation of illusory contours [168, 2], binocular disparity [169], and whether the stimulus is part of the figure or the ground [140, 19]. Recent research has shown that V2 cells are tuned for moderately complex patterns, and may be driven by multiple orientations at different subregions within a single receptive field.

#### 2.4.1 Receptive fields of V2

As we will recall later, from the neurophysiological point of view the orientation selectivity, the spatial and temporal frequency of cells in V2 differs little from the one in V1 ([110, 111]). Receptive fields in V2 are larger from those in V1 ([101, 110]). Some of them show more elongated ON-OFF zone in their RFs. Many studies, which relies on neuro-physiological and imaging data, show the evidence that neurons in at least two visual areas, V1 and V2, carry signals related to illusory contours, and that signals in V2 are more robust than in V1 ([168, 127], reviews [57, 126]). The cells with elongated RFs observed by Liu et al. in [111] may be responsible for such behaviour. Finally, as observed by Tootell et al. in [165], also V2 shows orientation column organization: columns are spaced further apart than those in V1, by a factor of about 1.6, but the columns are not correspondingly wider.

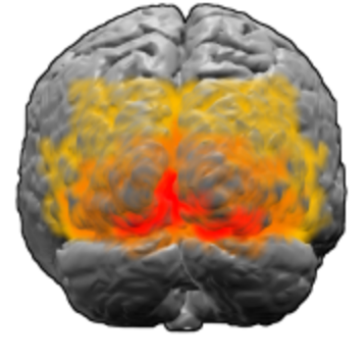


Figure 2.18: View of the brain from behind. Red is Brodmann area 17 (primary visual cortex); orange is area 18 (secondary visual cortex, V2); yellow indicates area 19. The brain's surface is extracted from structural MRI data, from Wellcome Dept. Imaging Neuroscience, UCL, UK.





### 3 *Differentiable manifold, Lie groups and Sub-Riemannian geometry*

IN THIS CHAPTER we will introduce the mathematical instruments that will allow us to model the cortical space introduced in the previous section. We are mainly interested in the structure of the cortex, which we know is responsible for its functionality: the hypercolumnar structure of the primary visual cortex will be modelled as the principal fiber bundle of the Lie group  $SE(2)$ , endowed with a sub-Riemannian structure. This is crucial for explaining the orientation selection performed by cells in V1. Instruments of Lie groups and differential geometry for the description of the visual cortex have been introduced by Hoffmann in [86], August and Zucker in [3], Petitot and Tondut in [139] and Duits and Franken in [53, 54]. Before focusing on their models, we first need to review the definition and basic properties of differentiable manifold and Lie group theory, which are fundamental for explaining the symmetry and the organization of simple cells in the cortex, and the construction and the properties of a sub-Riemannian manifold which explain the connectivity we will introduce.

### 3.1 Differentiable manifold theory

In order to introduce Lie groups and Sub- Riemannian structures we need to first recall fundamental notions of differentiable manifold theory. All definitions and theorems can be found in [166].

#### 3.1.1 Topological manifolds, charts and smooth manifolds

**Definition 3.1.1.** A topological space  $M$  is *locally Euclidean of dimension  $n$*  if every point  $p \in M$  has a neighborhood  $U$  such that there is a homeomorphism  $\phi$  from  $U$  onto an open subset of  $\mathbb{R}^n$ . We call the pair  $(U, \phi)$  a *chart*,  $U$  a *coordinate neighborhood* and  $\phi$  a *coordinate map*. We say that a chart  $(U, \phi)$  is *centered* at  $p \in U$  if  $\phi(p) = 0$ .

**Definition 3.1.2.** A *topological manifold* is said to be of *dimension  $n$*  if it is locally Euclidean of dimension  $n$ .

Suppose  $(U, \phi)$  and  $(V, \psi)$  are two charts of a topological manifold. Since  $U \cap V$  is open in  $U$  and  $\phi : U \rightarrow \mathbb{R}^n$  is a homeomorphism onto an open subset of  $\mathbb{R}^n$ , the image  $\phi(U \cap V)$  will also be an open subset of  $\mathbb{R}^n$ . Similarly,  $\psi(U \cap V)$  is an open subset of  $\mathbb{R}^n$ .

**Definition 3.1.3.** The two charts  $(U, \phi)$  and  $(V, \psi)$  of a topological manifold are  $C^\infty$ -compatible if the two maps:

$$\phi \circ \psi^{-1} : \psi(U \cap V) \rightarrow \phi(U \cap V) \quad \psi \circ \phi^{-1} : \phi(U \cap V) \rightarrow \psi(U \cap V)$$

are  $C^\infty$ . These two maps are called the *transition functions* between the charts. If  $U \cap V$  is empty, then the two charts are automatically  $C^\infty$ -compatible. To simplify the notation, we sometimes write  $U_{\alpha\beta}$  for  $U_\alpha \cap V_\beta$ .

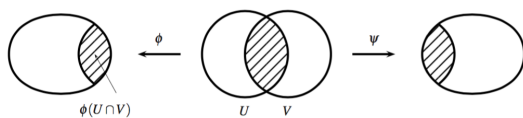


Figure 3.1: From Tu, [166]. The transition function  $\psi \circ \phi^{-1}$  is defined on  $\phi(U \cap V)$

**Definition 3.1.4.** A  $C^\infty$  *atlas* or simply an *atlas* on a locally Euclidean space  $M$  is a collection  $\mathfrak{U} = \{(U_\alpha), \phi_\alpha\}$  of pairwise  $C^\infty$ -compatible charts that cover  $M$ , i.e.  $M = \bigcup_\alpha U_\alpha$ .

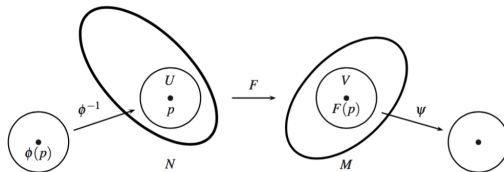
An atlas  $\mathfrak{U}$  on a locally Euclidean space is said to be *maximal* if it is not contained in a larger atlas; in other words, if  $\mathfrak{M}$  is any other atlas containing  $\mathfrak{U}$ , then  $\mathfrak{U} = \mathfrak{M}$ .

**Definition 3.1.5.** A *smooth or  $C^\infty$  manifold* is a topological manifold  $M$  together with a  $C^\infty$  maximal atlas. The maximal

atlas is also called a *differentiable structure on  $M$*  and  $M$  is called differentiable ( $C^\infty$  differentiable) manifold. A manifold is said to have dimension  $n$  if all of its connected components have dimension  $n$ . A 1-dimensional manifold is also called a *curve*, a 2-dimensional manifold a *surface*, and a  $n$ -dimensional manifold is an  $n$ -manifold.

### 3.1.2 Tangent spaces, differential of a map, vector fields and integral curves

**Definition 3.1.6.** Let  $N$  and  $M$  be smooth manifolds of dimension  $n$  and  $m$  respectively. A map  $F : N \rightarrow M$  is  $C^\infty$  at a point  $p$  in  $N$  if there are charts  $(V, \psi)$  about  $F(p)$  in  $M$  and  $(U, \phi)$  about  $p$  in  $N$  such that the composition  $\psi \circ F \circ \phi^{-1}$ , a map from the open subset  $\phi(F^{-1}(V) \cap U)$  of  $\mathbb{R}^n$  to  $\mathbb{R}^m$ , is  $C^\infty$  at  $\phi(p)$ . If  $F$  is  $C^\infty$  at every point of  $N$ ,  $F$  is said to be smooth.



Let consider  $p \in M$ , then  $C_p^\infty(M)$  is the set of all function  $f : M \rightarrow \mathbb{R}$  which are  $C^\infty$  at  $p$ . A basic principle in manifold theory is the linearization principle, according to which a manifold can be approximated near a point by its tangent space at that point. For any point  $p$  in an open set  $U$  in  $\mathbb{R}^n$  there are two equivalent ways to define a tangent vector at  $p$ :

- as a vector, see figure 3.2 (see first margin note).
- as a point-derivation of  $C_p^\infty$ , the algebra of germs (see second margin note) of  $C^\infty$  functions at  $p$ .

Both definitions generalize to a manifold. In the first approach, one defines a tangent vector at  $p$  in a manifold  $M$  by first choosing a chart  $(U, \phi)$  at  $p$  and then denoting a tangent vector at  $p$  to be an “arrow” at  $\phi(p)$  in  $\phi(U)$ . This approach, while more visual, is complicated to work with, since a different chart  $(V, \psi)$  at  $p$  would give rise to a different set of tangent vectors at  $p$  and one would have to decide how to identify the arrows at  $\phi(p)$  in  $U$  with the arrows at  $\psi(p)$  in  $\psi(V)$ . This happens because the first definition depends on the immersion of the manifold  $M$  in  $\mathbb{R}^n$ . The cleanest and most intrinsic definition of a tangent vector at  $p$  in  $M$  is as a point-derivation, and this is the approach we adopt.

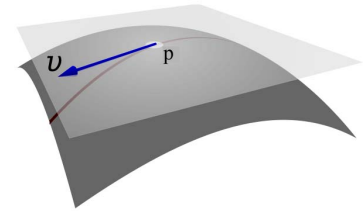


Figure 3.2: A tangent vector as an arrow.

Figure 3.3: From Tu [166]. Checking that a map  $F : N \rightarrow M$  is  $C^\infty$  at  $p$ .

Intuitively the tangent plane to a surface at  $p$  in  $\mathbb{R}^n$  is the plane that just “touches” the surface at  $p$ . A vector at  $p$  is tangent to a surface if it lies in the tangent plane at  $p$ .

We define a *germ* of a  $C^\infty$  function at  $p$  in  $\mathbb{R}^n$  to be an equivalence class of smooth functions defined in a neighborhood at  $p$  in  $\mathbb{R}^n$ , the two functions being equivalent if they agree on some, possibly smaller, neighborhood of  $p$ . The set of germs of smooth real-valued functions at  $p$  in  $\mathbb{R}^n$  is denoted by  $C_p^\infty(\mathbb{R}^n)$ , an unitary commutative ring. This concept generalizes to a manifold  $M$  using the local coordinates given by the atlas, for each point  $p$  in  $M$

**Definition 3.1.7.** Generalizing a derivation at a point  $p$  in  $\mathbb{R}^n$ , we define a *derivation at a point* in a manifold  $M$ , or a point-derivation of  $C_p^\infty$  to be a linear map  $D_p : C_p^\infty(M) \rightarrow \mathbb{R}$  such that

$$D_p(fs) = (D_p f)s(p) + f(p)D_p s.$$

**Definition 3.1.8.** A *tangent vector* at a point  $p$  in a manifold  $M$  is a derivation at  $p$ .

**Definition 3.1.9.** The tangent vectors at  $p$  form a vector space  $T_p(M)$ , called the tangent space of  $M$  at  $p$ . We also write  $T_p M$ .

**Definition 3.1.10.** A *vector field* on an open subset  $U$  of  $M$  is a function that assigns to each point  $p$  in  $U$  a tangent vector  $X_p \in T_p(M)$ . Since we can assign a basis  $\{\partial/\partial x_i|_p\}$  to  $T_p(M)$ <sup>1</sup>, where the elements of the basis are the  $n$  directional derivatives which come from the local coordinates of  $U$  in  $\mathbb{R}^n$ , the vector  $X_p$  is a linear combination:

$$X_p = \sum a_i(p) \frac{\partial}{\partial x_i} \Big|_p \quad p \in U, \quad a^i(p) \in \mathbb{R}$$

where  $a_i$  are smooth functions on  $U$ . The set of vector fields on a manifold  $M$  is denoted by  $\mathfrak{X}(M)$ .

**Remark 3.1.11.** An equivalent definition is that a *vector field*  $X$  is a derivation on  $C^\infty(M)$ , i.e.  $D : C^\infty(M) \rightarrow C^\infty(M)$   $\mathbb{R}$ -linear which satisfies the Leibniz rule, see [166] for the proof.

We will now define the concept of a smooth map between two manifolds in order to introduce the *differential* of a map:

**Definition 3.1.12.** Let  $F : N \rightarrow M$  be a  $C^\infty$  map between two manifolds. At each point  $p \in N$ , the map  $F$  induces a linear map of tangent spaces called its *differential at  $p$* :

$$(dF)_p : T_p(N) \rightarrow T_{F(p)}(M)$$

If  $X_p \in T_p N$ , then  $(dF)_p(X)$  is the tangent vector in  $T_{F(p)} M$  defined by:

$$(dF)_p(X)(f) = X_p(f \circ F) \in \mathbb{R} \quad \text{for } f \in C_{F(p)}^\infty(M).$$

Here  $f$  is a germ at  $F(p)$ , represented by a  $C^\infty$  function in a neighborhood of  $F(p)$ . Since the previous definition is independent of the representative of the germ, in practice we can be relaxed about the distinction between a germ and a representative function for the germ.

**Remark 3.1.13.** If  $f : M \rightarrow \mathbb{R}$  is a  $C^\infty$ -function, the differential of  $f$ :

$$df := \mathfrak{X}(M) \rightarrow C^\infty(M)$$

<sup>1</sup>This result is proved in a theorem which states that, once we fix a local frame  $(x_1, \dots, x_n)$ ,  $\{\frac{\partial}{\partial x_i}|_p\}_{i=1, \dots, n}$  form a basis for  $T_p(M)$  (see [166])

is globally defined as the map which acts as follows on each vector field  $X \in \mathfrak{X}(M)$ :

$$df(X) := X(f)$$

It is clear that this definition descends directly from the general one.

**Remark 3.1.14.** If instead of  $N$  and  $M$  we consider a map  $F$  between  $\mathbb{R}^n$  and  $\mathbb{R}^m$  we discover with some computations that the matrix associated to the linear map

$$(dF)_p : T_p(\mathbb{R}^n) \rightarrow T_{F(p)}(\mathbb{R}^m)$$

is precisely the Jacobian matrix of  $F$  at  $p$ . Thus, the differential of a map between manifolds generalizes the derivative of a map between Euclidean spaces.

**Definition 3.1.15.** A smooth curve in a manifold  $M$  is by definition a smooth map  $\gamma : (a, b) \rightarrow M$  from some open interval  $(a, b)$  into  $M$ . Usually we assume  $0 \in (a, b)$  and we say that  $\gamma$  is a curve starting at  $p$  if  $\gamma(0) = p$ . The tangent vector (or velocity vector)  $\gamma'(x)$  to the curve  $\gamma$  in  $x \in (a, b)$  is defined to be:

$$\gamma'(x) = (d\gamma)_x \left( \frac{d}{dt} \right) \in T_{\gamma(x)}M$$

**Definition 3.1.16.** We call  $\gamma$  an integral curve of the vector field  $X$  on  $M$  if  $\gamma'(x) = X_{\gamma(x)}$ ,  $\forall x \in (a, b)$ , i.e. a smooth parametrized<sup>2</sup> curve  $\gamma$  whose tangent vector at any point coincides with the value of  $X$  at the same point. In local coordinates  $(x_1, \dots, x_n)$  this means:

$$\begin{aligned} \gamma : (a, b) &\rightarrow \phi_u(U) \in \mathbb{R}^n \\ t &\mapsto (\gamma_1(t), \dots, \gamma_n(t)) \end{aligned}$$

If we make some calculations we observe:

$$\left( D_Y \frac{d}{dt} \right) (f(x_1, \dots, x_n)) = \frac{d}{dt} f(\gamma_1(t), \dots, \gamma_n(t)) = \sum_{i=1}^n \frac{\partial f}{\partial x_i} \gamma'_i(t)$$

Hence

$$\gamma'(t) = \sum_{i=1}^n \gamma'_i(t) \frac{\partial}{\partial x_i}$$

With respect to the basis  $\left\{ \frac{\partial}{\partial x_1}, \dots, \frac{\partial}{\partial x_n} \right\}$  we have

$$\gamma'(t) = (\gamma'_1(t), \dots, \gamma'_n(t)).$$

Following the previous definition  $\gamma'(x) = X_{\gamma(x)}$  this means  $\sum \gamma'_i(t) \frac{\partial}{\partial x_i} = \sum a_i(\gamma_1(t), \dots, \gamma_n(t)) \frac{\partial}{\partial x_i}$ , where  $a_i$  are the coefficients of  $X$  in the coordinates  $(x_1, \dots, x_n)$ . Since  $\left\{ \frac{\partial}{\partial x_i} \right\}$  forms a basis,  $\gamma$  is an integral curve iff  $\gamma'_i(t) = a_i(\gamma_1(t), \dots, \gamma_n(t))$  for all  $i$ , i.e.  $\gamma_1, \dots, \gamma_n$  is a solution of the previous system of autonomous ODEs of the first order.

<sup>2</sup> A parametrization is the process of deciding and defining the parameters necessary for a complete or relevant specification (characterization) of a geometric object.

### 3.1.3 Fiber bundles and tangent spaces

The collection of tangent spaces in a manifold is called tangent bundle. It is a locally trivial family of tangent vector spaces parametrized by points of the manifold. It *locally* looks like a certain product space, but *globally* may have a different topological structure. More generally it is possible to define *fiber bundles*, or *vector bundles*, with analogous properties: they locally look like a cartesian product of a base set and a fiber (which reduces to a vector space in case of vector bundles) but can have a rich global structure.

**Definition 3.1.17.** A *fiber bundle* is a structure  $(E, B, \pi, F)$  where  $E, B$  and  $F$  are topological spaces and  $\pi : E \rightarrow B$  is a continuous surjection satisfying the local triviality condition outlined below. The space  $B$  is called the *base space* of the bundle,  $E$  the *total space*, and  $F$  the *fiber*. The map  $\pi$  is called the *projection map*. We require that  $\forall x \in E$  there is an open neighborhood  $U \subset B$  of  $\pi(x)$  (which will be called *trivializing neighborhood*) such that  $\pi^{-1}(U)$  is homeomorphic to the product space  $U \times F$ , in such a way that  $\pi$  agrees with the projection onto the first factor. Thus the following diagram should commute:

$$\begin{array}{ccc} \pi^{-1}(U) & \xrightarrow{\phi} & U \times F \\ \pi \downarrow & \swarrow \text{proj}_1 & \\ U & & \end{array}$$

where  $\text{proj}_1 : U \times F \rightarrow U$  is the natural projection and  $\phi : \pi^{-1}(U) \rightarrow U \times F$  is a homeomorphism. The set of all  $\{(U_i, \phi_i)\}$  is called *system of local trivializations* of the bundle. Thus for any  $p$  in  $B$ , the preimage  $\pi^{-1}(\{p\})$  is homeomorphic to  $F \times \{p\}$  (since  $\text{proj}_1^{-1}(\{p\})$  clearly is  $F$ ) and is called the *fiber over  $p$* . Every fiber bundle  $\pi : E \rightarrow B$  is an *open map*, since projections of products are open maps.

**Example 3.1.18.** The Moebius strip is the simplest example of a non-trivial bundle  $E$ . The base  $B$  is the circle  $S^1$  and the fiber  $F$  is a line segment. Given  $x \in B$ ,  $U$  is a small arc (neighborhood of  $x$  on the circle) and  $\pi^{-1}(U)$  is homeomorphic to the square  $U \times F$ . Globally this is not true.

A special class of fiber bundles, called *vector bundles*, are those whose fibers are *vector spaces* and the composition of local trivializations is linear over the fiber  $F$ .

**Definition 3.1.19.** Let  $M$  be a smooth manifold and  $T_pM$  is the tangent space at  $p$  defined in 3.1.9. The *tangent bundle* of

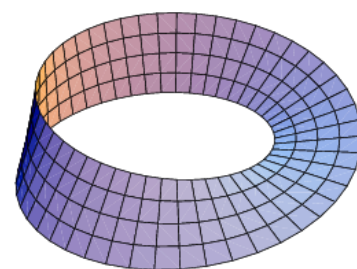


Figure 3.4: The Moebius strip, an example of non-trivial bundle.

$M$  is the disjoint union of all tangent spaces of  $M$ :

$$TM = \bigsqcup_{p \in M} T_p M$$

In this definition the union is disjoint because for distinct points  $p$  and  $q$  in  $M$ , the tangent spaces  $T_p M$  and  $T_q M$  are already disjoint.  $TM$  has the structure of a differentiable manifold and the bundle structure is given by the natural map  $\pi : TM \rightarrow M$  where  $\forall p \in M$ ,  $\pi^{-1}(p)$  is the tangent space of the manifold  $M$  at the point  $p$  and this map does not depend on the choice of atlas or local coordinates for  $M$ . As a matter of notation, sometimes a tangent vector  $v \in T_p M$  can be identified by the pair  $(p, v)$ , to make explicit the point  $p \in M$  at which  $v$  is a tangent vector.

Another special class of fiber bundles, called *principal bundles*, are those bundles on whose fibers there is a free and transitive action (see margin note) by a group  $G$  is given. The bundle is often specified along with the group by referring to it as a principal  $G$ -bundle. As we will see we are interested in this definition because *principal fiber bundles* are used in our model to describe the visual cortex.

**Definition 3.1.20.** A topological group is a group  $G$  together with a topology on  $G$  such that the group's binary operation and the group's inverse function are continuous functions with respect to the topology.

**Definition 3.1.21.** If  $G$  is a group and  $X$  is a set, then a (*right*) *group action* of  $G$  on  $X$  is a function

$$\begin{aligned} X \times G &\rightarrow X \\ (x, p) &\mapsto x \cdot p \end{aligned}$$

that satisfies the following two axioms:

- *Compatibility*  $x \cdot (ph) = (x \cdot p) \cdot h$ , for all  $p, h \in G$ ,  $x \in X$
- *Identity*  $x \cdot e = x$  for all  $x \in X$

An action is *free* if, given  $p, h \in G$ , the existence of an  $x \in X$  with  $x \cdot p = x \cdot h$  implies  $p = h$ . Equivalently: if  $p$  is a group element and there exists an  $x \in X$  with  $x \cdot p = x$  (that is, if  $p$  has at least one fixed point), then  $p$  is the identity. An action is *transitive* if  $X$  is non-empty and if for any  $x, y \in X$  there exists a  $p$  in  $G$  such that  $x \cdot p = y$ .

**Definition 3.1.22.** A *principal fiber  $G$ -bundle*, where  $G$  denotes any topological group, is a *fiber bundle*  $\pi : P \rightarrow X$  together with a continuous right action  $P \times G \rightarrow P$  such that

$G$  preserves the fibers of  $P$  and acts freely and transitively on them. This implies that the fiber of the bundle is homeomorphic to the group  $G$  itself.

**Definition 3.1.23.** Let  $\pi : E \rightarrow M$  be a vector bundle on  $M$ . We call a section of the vector bundle a map  $\phi : M \rightarrow E$  such that  $\pi \circ \phi = Id_M$

**Remark 3.1.24.** A vector field  $X$  (defined in 3.1.10) on manifold  $M$  is a section of the tangent bundle  $\pi : TM \rightarrow M$  and the vector field is smooth if it is smooth as a map from  $M$  to  $TM$ .

All these instruments allow us to define other concepts such as an affine connection, the parallel transport, covariant derivatives and geodesic without requiring the concept of metric. For reader convenience, since we will deal with a sub-Riemannian metric and its Riemannian approximation, we are going to define these concepts directly in the enriched framework provided by considering a Riemannian manifold.

## 3.2 Lie groups and their properties

In this section we will provide some basic definitions of the Lie group theory. Definitions and theorems can be found in [167].

### 3.2.1 Definition

**Definition 3.2.1.** A *Lie Group* is a group which also carries the structure of a differentiable manifold in such a way that both the group operation

$$\cdot : G \times G \rightarrow G, \quad (p, h) \mapsto p \cdot h \text{ for } p, h \in G$$

and the inversion

$$i : G \rightarrow G, i(p) = p^{-1}, p \in G$$

are smooth maps.

Examples of Lie Groups are:

- The Euclidean space  $\mathbb{R}^n$ , with the usual sum as group law.
- The set of real/complex square matrices  $n \times n$ , with the determinant different from 0. In this set we consider the standard product of matrices, and the existence of an inverse is ensured by the condition on the determinant. Note that this group is not commutative.
- The circle  $S^1 \subset \mathbb{C}$  of angles mod  $2\pi$ , with the standard sum of angles.
- The group of rotations and translations on the plane  $SE(2)$  which will be described in detail in this thesis.

### 3.2.2 Properties

**Definition 3.2.2.** For two vector fields (i.e. two derivations)  $X$  and  $Y$  in  $\mathfrak{X}(M)$ , their *Lie bracket* (or *commutator*) is defined by their action on functions  $f : M \rightarrow \mathbb{R}$ :

$$[X, Y](f) = X(Y(f)) - Y(X(f))$$

Note that the Lie bracket is a measurement of the non-commutativity of the operators; it is defined as the difference of applying them in reverse order. In particular  $[X, Y]$  is identically 0 if  $X$  and  $Y$  commute.

**Definition 3.2.3.** Let  $G$  be a Lie group. For any element  $p \in G$ , we define the *left-multiplication* (or *left-translation*)  $L_p : G \rightarrow G$  by:

$$L_p(h) = p \cdot h \quad \text{for all } p \in G$$

where  $\cdot$  denotes the group operation in  $G$ .

**Definition 3.2.4.** A vector field  $X$  on  $G$  is called *left-invariant* if:

$$X(f \circ L_p) = (Xf) \circ L_p \quad \text{for all } p \in G$$

**Definition 3.2.5.** The *Lie Algebra* of a Lie group  $G$  is the vector space of all left-invariant vector fields on  $G$ :

$$\text{Lie}(G) := \{X \in \mathfrak{X}(M) : X \text{ is left invariant, i.e.}$$

$$X(f \circ L_p) = (Xf) \circ L_p\}$$

for all  $p \in G$  and  $f$  smooth on  $M$ .

**Remark 3.2.6.** A result (see [175]) states that the Lie algebra associated to a Lie group can be identified as the tangent space at the identity of the group  $e$ , i.e.

$$\text{Lie}(G) \cong T_e G$$

## 3.3 Riemannian and Sub-Riemannian manifolds

So far we have dealt with differentiable objects. Now we will introduce some concepts, the affine connection (and the ones that follow: Christoffel symbols, parallel transport and geodesics) that could have been introduced without mentioning any metric in our space, as the reader will notice directly from the definition. A *metric* (or *inner product*) is an instrument which allows to measure the length of any vector of the tangent space. In order to simplify the concepts and their usage, we work directly in Riemannian manifolds, i.e. manifolds equipped with a Riemannian metric. However, for reader convenience we will

clearly state whether in the definitions there will be dependence on the metric. For further references see [84], [186, 121], [99].

**Definition 3.3.1.** Let  $V$  be a vector space. An *inner product (or metric)* on  $V$  is a bilinear form, symmetric and positive defined, i.e.

$\langle \cdot, \cdot \rangle : V \times V \rightarrow \mathbb{R}$  such that:

$$(i) \langle u_1 + u_2, v \rangle = \langle u_1, v \rangle + \langle u_2, v \rangle \quad \forall u_1, u_2, v \in V;$$

$$(ii) \langle \lambda u, v \rangle = \lambda \langle u, v \rangle \quad \forall u, v \in V, \forall \lambda \in \mathbb{R};$$

$$(iii) \langle u, v \rangle = \langle v, u \rangle \quad \forall u, v \in V.$$

$$(iv) \langle u, u \rangle \geq 0 \quad \forall u \in V, \text{ with } \langle u, u \rangle = 0 \Leftrightarrow u = 0.$$

### 3.3.1 Riemannian manifolds

**Definition 3.3.2.** Let  $M$  be a  $C^\infty$  manifold of dimension  $m$ . A *Riemannian metric*  $g$  on  $M$  is given by a scalar product on each tangent space  $T_p M$  which depends smoothly on the base point  $p \in M$  (i.e. for each couple of vector fields  $X, Y$ , the map  $p \rightarrow g_p(X_p, Y_p)$  is differentiable). A *Riemannian manifold* is a differentiable manifold, equipped with a Riemannian metric.

The easiest example of Riemannian manifold is  $\mathbb{R}^n$  equipped with the Euclidean metric.

**Definition 3.3.3.** Let  $M$  be a  $C^\infty$  manifold of dimension  $m$ . An *affine connection* on  $M$  is a differential operator, sending smooth vector fields  $X$  and  $Y$  to a smooth vector field  $\nabla_X Y$  which satisfies the following conditions:

- $\nabla_X Y$  is  $C^\infty(M)$  - linear in  $X$ :

$$\nabla_{fX_1 + sX_2} Y = f \nabla_{X_1} Y + s \nabla_{X_2} Y$$

- $\nabla_X Y$  is linear over  $\mathbb{R}$  in  $Y$ :

$$\nabla_X (aY_1 + bY_2) = a \nabla_X Y_1 + b \nabla_X Y_2$$

- Product rule:

$$\nabla_X (fY) = f \nabla_X Y + (Xf)Y$$

where  $f, s \in C^\infty(M)$ ,  $a, b \in \mathbb{R}$ .  $\nabla_X Y$  is called the covariant derivative of the vector field  $Y$  along the tangent vector  $X$ .

The compatibility condition mean that  $\nabla g \equiv 0$ . From an intuitive point of view this ensures that Leibniz condition holds along the fiber bundle  $TM$ . Furthermore the metric is constant along parallel transport, which means that parallel transport is an isometry.

In general there are an infinite number of affine connections for a given metric tensor. However, in this specific case, we are interested in a connection compatible with the Riemannian metric of the space (i.e. a metric connection). The unique affine

connection compatible with the Riemannian metric is the Levi-Civita connection (and it satisfies the Koszul identity). *Christoffel symbols*  $\Gamma_{ij}^k$  are the local coefficients of a connection. They can be defined for any affine connection:

$$\nabla_{\frac{\partial}{\partial x_i}} \frac{\partial}{\partial x_j} = \Gamma_{ij}^k \frac{\partial}{\partial x_k}$$

with  $i, j, k \in \{1, \dots, n\}$ . However, in case of the Levi-Civita connection in a Riemannian manifold, Christoffel symbols have an expression which depend directly on the Riemannian metric. Given a local frame for  $TM$ ,  $\{\frac{\partial}{\partial x_i}\}_{i=1, \dots, n}$ , then the Christoffel symbols  $\Gamma_{ij}^k$  will have the following expression:

$$\Gamma_{ij}^k = \frac{1}{2} g^{lk} \left( \frac{\partial}{\partial x_i} g_{jl} + \frac{\partial}{\partial x_j} g_{il} + \frac{\partial}{\partial x_l} g_{ij} \right) \quad (3.1)$$

where we apply Einstein summation convention<sup>3</sup> and  $(g^{ij}) = (g_{ij})^{-1}$ , (i.e.  $g^{il} g_{lj} = \delta_{ij}$ ). Let now  $[a, b]$  be a closed interval in  $\mathbb{R}$ ,  $\gamma : [a, b] \rightarrow M$  a smooth curve. The length of  $\gamma$  is defined as:

$$L(\gamma) := \int_a^b \|\gamma'(t)\| dt \quad (3.2)$$

where given a tangent vector  $v \in T_p M$  the norm is  $\|v\| = \sqrt{\langle v, v \rangle}$ . The energy of  $\gamma$  is defined as

$$E(\gamma) := \frac{1}{2} \int_a^b \|\gamma'(t)\|^2 dt \quad (3.3)$$

**Lemma 3.3.4.** The Euler-Lagrange equations for the energy  $E$  are

$$\ddot{x}^i(t) + \Gamma_{jk}^i(x(t)) \dot{x}^j(t) \dot{x}^k(t) = 0 \quad (3.4)$$

where  $\Gamma_{jk}^i$  have the previous definition.

**Definition 3.3.5.** Geodesics are critical points of the energy functional  $E$ .

In particular minima of the energy functional  $E$  are critical points, hence geodesics. In addition it can be proved that minima of the functional  $E$  also minimize the length functional  $L$  defined in 3.2. These geodesics will be called minimizing geodesics:

**Definition 3.3.6.** Minimizing geodesics are minima of the length functional  $L$ .

**Definition 3.3.7.** A smooth curve  $\gamma : [a, b] \rightarrow M$  which satisfies equation (3.4) is called a *geodesic*.

This means that geodesics are critical points of the energy functional  $E$ .

The result that states the Levi-Civita connection is the unique connection compatible with the metric is fundamental in Riemannian geometry, because it ensures all conditions presented in the previous footnote are satisfied.

<sup>3</sup> It means that all contravariance indexes which have a covariant counterpart have to be summed. For example:

$$y = c_i x^i = \sum_{i=1}^3 c_i x^i$$

where in this case  $i \in \{1, 2, 3\}$ . In our general example  $i, j, l \in \{1, \dots, n\}$ .

### 3.3.2 Sub-Riemannian manifolds

We will now establish a notation to introduce the concept of the sub-Riemannian metric, a tool which allows us to describe the connections between the hypercolumns in our model. Let us start from the definition of *distribution*, which is still an object which does not depend on the metric.

**Definition 3.3.8.** Let  $M$  be a  $C^\infty$  manifold of dimension  $m$ , and let  $n \leq m$ . Suppose that for each  $p \in M$ , we assign an  $n$ -dimensional subspace  $\Delta_p \subset T_p(M)$  of the tangent space in such a way that for a neighborhood  $N_p \subset M$  of  $p$  there exist  $n$  linearly independent smooth vector fields  $X_1, \dots, X_n \in \mathfrak{X}(M)$  such that for any point  $q \in N_p$  we have  $X_1(q), \dots, X_n(q)$  span  $\Delta_q$ . We let  $\Delta$  refer to the collection of all the  $\Delta_p$  for all  $p \in M$  and we will call  $\Delta$  a *distribution* of dimension  $n$  on  $M$ . The set of smooth vector fields  $\{X_1, \dots, X_n\}$  is called a *local basis* of  $\Delta$ .

**Definition 3.3.9.** A *sub-Riemannian manifold* is the datum of a smooth manifold  $M$ , a smooth constant rank distribution  $HM \subset TM$  and a smooth inner product  $\langle \cdot, \cdot \rangle$  on  $HM$ . The bundle  $HM$  is known as the horizontal bundle.

**Definition 3.3.10.** A sub-Riemannian manifold with a *complement*, henceforth a *sRC manifold*, is a sub-Riemannian manifold together with a smooth bundle  $VM$  such that  $HM \oplus VM = TM$ . The bundle  $VM$  is known as the vertical bundle. The two sRC-manifolds  $M, N$ , are sRC-isometric if there exists a diffeomorphism  $\pi : M \rightarrow N$  such that  $(d\pi)HM = HN$ ,  $(d\pi)VM = VN$  and  $\langle (d\pi)X, (d\pi)Y \rangle_N = \langle X, Y \rangle_M$  for all horizontal vectors  $X, Y$ .

**Remark 3.3.11.** The definition of a sub-Riemannian manifold is more general than the one of Riemannian manifold. This last one can be seen as a sub-Riemannian manifold in which the smooth rank distribution has the same dimension as the manifold, i.e.  $HM = TM$  (this implies that the vertical bundle is null). Equivalently a sub-Riemannian manifold can be seen as a Riemannian manifold in which the metric is degenerate, i.e. a sub-Riemannian metric can be seen as the *limit* of a Riemannian metric.

**Remark 3.3.12.** If we consider a Riemannian manifold  $(M, g_p)$  and  $f \in C^1(M)$  a function, for each  $p \in M$  we define the *gradient of  $f$  in  $p$*  as the vector field  $\nabla f$  satisfying:

$$d_p f(v) = g_p(\nabla f, v) \quad \forall v \in T_p M$$

The Riemannian gradient has the same useful properties as the gradient of the Euclidean calculus, such as it *vanishes* in the

The Euclidean gradient is defined as the vector of the partial derivatives of a function  $f$  with respect to the set of coordinates.

extremal point for  $f$ . We can also write the formula for the gradient in local coordinates:

$$\nabla f(x) = \sum_{i=1}^n \left( \sum_{j=1}^n g^{ij}(x) \frac{\partial f}{\partial x_j} \right) \frac{\partial}{\partial x_i} \quad (3.5)$$

where  $g^{ij}$  are the local expressions of the inverse of the matrix of the metric.

**Definition 3.3.13.** A sub-Riemannian manifold with a complement  $(M, HM, VM, \langle \cdot, \cdot \rangle)$  is  $r$ -graded if there are  $r$  smooth constant rank bundles  $V^{(j)}$ , with  $0 < j \leq r$ , such that:

$$VM = V^{(1)} \oplus \dots \oplus V^{(r)}$$

and we have:

$$HM \oplus V^{(j)} \oplus [HM, V^{(j)}] \subseteq HM \oplus V^{(j)} \oplus V^{(j+1)}$$

for each  $0 \leq j \leq r$ . Here we have adopted the convention that  $V^{(0)} = HM$  and  $V^{(k)} = 0$  for  $k > r$ .

**Definition 3.3.14.** The grading is  $j$ -regular if

$$HM \oplus V^{(j)} \oplus [HM, V^{(j)}] = HM \oplus V^{(j)} \oplus V^{(j+1)}$$

and *equiregular* if it is  $j$ -regular for all  $0 \leq j \leq r$ .

Let us now define a metric extension:

**Definition 3.3.15.** A metric extension for an  $r$ -graded sub-Riemannian manifold is a Riemannian metric which coincides with  $\langle \cdot, \cdot \rangle$  on  $HM$  that makes the split

$$TM = HM \bigoplus_{1 \leq j \leq r} V^{(j)}$$

orthogonal.

For convenience of notation, we shall denote a section  $V^{(k)}$  by  $X^{(k)}$  and set:

$$\hat{V}^{(j)} = \bigoplus_{k \neq j} V^{(k)}$$

**Definition 3.3.16.** From the previous observations we can define the horizontal gradient for a sub-Riemannian manifold as

$$\nabla_0 = (X_1, \dots, X_m)$$

where  $\{X_1, \dots, X_m\}$  span the horizontal bundle. In the same way if a metric extension (which is a Riemannian metric) has been chosen we can denote the gradient as

$$\nabla = (X_1, \dots, X_m, X_{m+1}, \dots, X_n)$$

where  $\{X_{m+1}, \dots, X_n\}$  span the vertical bundle.

**Remark 3.3.17.** If a metric extension has been chosen then  $\hat{V}^{(j)} = (V^{(j)})^\perp$  is the orthogonal complement of  $V^{(j)}$ .

**Remark 3.3.18.** Every sRC-manifold that admits an  $r$ -grading also admits  $k$ -gradings for all  $1 \leq k < r$  by setting:

$$\tilde{V}^{(j)} = V^{(j)} \quad 0 \leq j < k, \quad \tilde{V}^{(k)} = \bigoplus_{j \geq k} V^{(j)}$$

**Definition 3.3.19.** The unique 1-grading on each sRC-manifold,  $V^{(1)} = VM$  is known as the *basic grading*.

**Example 3.3.20.** A Carnot group (of step  $r$ ) is a Lie group, whose Lie algebra  $\mathfrak{g}$  is stratified in the sense that:

$$\mathfrak{g} = \mathfrak{g} \oplus \mathfrak{g}_1 \oplus \dots \oplus \mathfrak{g}_{r-1}$$

and

$$[\mathfrak{g}_i, \mathfrak{g}_j] = \mathfrak{g}_{i+j} \quad j = 1 \dots r, \quad \mathfrak{g}_r = 0$$

together with a left-invariant metric  $\langle \cdot, \cdot \rangle$  on  $HM$ . The vertical bundle  $VM$  consists of the left translates of  $\mathfrak{g}_1 \oplus \dots \oplus \mathfrak{g}_{r-1}$ .





## 4 Neurogeometry of V1/V2

IN THIS CHAPTER, starting from the functional architecture of the primary visual cortices V1/V2 introduced in chapter 2, a neuro-mathematical model involving tools presented in chapter 3 will account for the organization of cells in the cortex and their connectivity. In particular the modelization of receptive fields and profiles of simple cells will be recalled, as well as how orientation detection could be modelled through the introduced instruments. Oriented filters have been used as models for receptive fields of simple cells since the 80's and lots of possible interpretations have been presented. However in this work we will focus on Gabor filters, which result to be a biologically based model for receptive profiles of V1/V2. The roto-translations invariance intrinsic in the organization of the simple cells in the cortex suggests that a good model for the hypercolumnar structure of V1/V2 is given by the fiber bundle of the roto-translation group  $SE(2) = \mathbb{R}^2 \times S^1$ . For each point of the retina  $(x_1, x_2)$  a whole fiber of orientations  $\{\theta \in S^1\}$  is associated and a tangent direction is selected, through the short range connectivity (intra-cortical circuitry). The action of the group  $SE(2)$  over the basis of the tangent bundle  $\{\frac{\partial}{\partial x_1}, \frac{\partial}{\partial x_2}, \frac{\partial}{\partial \theta}\}$  allows to recover the vector fields  $X_1, X_2, X_3$ , left invariant with respect to the group law and generators of the fiber bundle. The metric living in the tangent space spanned by those vector field will be sub-Riemannian, to model the strongly anisotropy in the  $X_3$  direction of the cortical connection.

The first geometric models of the functionality of the visual cortex date back to the papers of Hoffmann [86], Koenderink and van Doorn [104] and August and Zucker [3]. Petitot and Tondut [139] proposed a model of single boundaries completion through constraint minimization in a contact structure, obtaining a neural counterpart of the models of Mumford [125]. The latter will be analyzed and discussed in chapter 7. Here we focus on the model proposed by Sarti and Citti in [28], and we will analyze its applications and extensions in the next chapters.

## 4.1 Neurogeometry of the primary visual cortices

The visual process is the result of several retinic and cortical mechanisms which act on the visual signal. In chapter 2 the whole mechanism has been analyzed in dept. Let us recall that the receptive field (RF) of a cortical neuron is the portion of the retina which the neuron reacts to, and the receptive profile (RP)  $\psi(\xi)$  is the function that models the activation of a cortical neuron when a stimulus is applied to a point  $\xi = (\xi_1, \xi_2)$  of the retinal plane. The latter is identified with the  $\mathbb{R}^2$ -plane, while  $\xi$  denotes its local coordinates.

### 4.1.1 The set of simple cells receptive profiles

Simple cells of visual cortices V1 and V2 are sensitive to position and orientation of the contrast gradient of an image. Their properties have been experimentally described by De Angelis in [44], see figure 4.1, who performed sophisticated electrophysiological measurements. From the neurophysiological point of

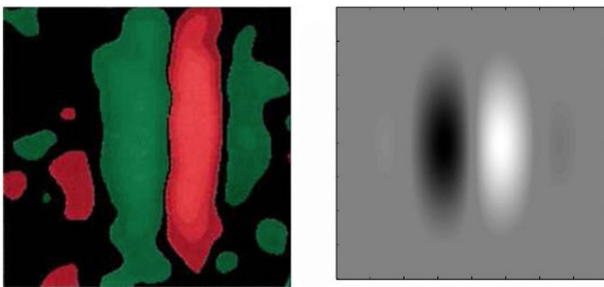


Figure 4.1: In vivo registered odd receptive field (left, from (De Angelis et al., 1995) [44]) and a schematic representation of it as a Gabor filter (right), see equation (4.1).

view the orientation selectivity, the spatial and temporal frequency of cells in V2 differs little from the one in V1 ([110]). Receptive fields in V2 are larger from those in V1 ([101], [110]). Considering a basic geometric model, the set of simple cells RPs can be obtained via translations of vector  $(x_1, x_2)$  and rotation of angle  $\theta$  from a unique mother profile  $\psi_0(\xi)$ . These symmetries between cells in the primary visual cortices suggest the *Rototranslation group* could play a role to model the hypercolumnar structure of V1/V2 and its physiological properties. In literature it is also known as the *2D Euclidean motion group*  $SE(2)$ , and it is the 3D group of rigid motions in the plane (or equivalently the group of elements invariant to rotations and translations).

### 4.1.2 Orientation detection

Receptive fields have been modelled as oriented filters in the middle of 80's and since then extraction of orientation in im-

A classification of different visual neurons starting from their receptive profiles has been possible through those recordings as well as make a list of their properties: size, preferred orientation of corresponding RF, position. For example it is known that receptive profile of LGN neurons (and those of retinal ganglion cell) can be modelled as Laplacian of Gaussian. Receptive fields of simple cells of V1 and V2 have an ON zone elongated, as shown in figure 4.1.

age analysis has been subject of several works. The first models have been presented by Daugman (1985) [39], Jones and Palmer (1987) [98]: they showed that Gabor filters were a good approximation for receptive profiles of simple cells in the primary visual cortices V1 and V2.

Gabor filters are the natural filters of this space: in [109] Lee showed that they allow a complete representation of an image, and they minimize the uncertainty principle ([39]). Almost in the same years Young in [188] (1987) and Koenderink in [103] (1990) introduced Gaussian derivatives (DoG) to model receptive profiles of simple cells of V1. These filters can be considered special cases of steerable filters, which have been studied in full generality in [73] (1991) and [137] (1995). They are a very efficient tool for extracting multiple orientations and performing computations since all filters are expressed as a linear combination of basis filters. We also refer to [145] (2008) and [138] (2008) for further explanations and details. More recently a new class of multi-orientation filters have been introduced by Duits et al. in [56] (2007): cake-wavelets. These wavelets are particularly useful since they induce an invertible map (called orientation scores) between the image domain and the features space of positions and orientations. In this space complex structures such as crossings, T-junctions are disentangled. A comparison between cake-wavelets and Gabor filters efficiency has been presented in [5]. Other lifting approaches are orientation lifts and orientation channel representations, see Felsberg in [61]. Another technique based on orientation detection is inpainting, which consists in restoring damaged portions of an image. The word was coined by Bertalmio et al. in [9] and the idea was to perform diffusion along the orientation of level-lines of the image. Masnou and Morel proposed in [115] a method in accord with Kanizsa's theory of amodal completion. We will see in chapter 5 how the model presented in this chapter applies to image restoration.

Our scope is to model the functionality of the visual cortex. Hence we choose Gabor filters which are a good model of receptive profiles and they provide a good estimation of the spiking responses. In our contribution we will consider odd and even part of Gabor filters, since we will need to be able to measure  $\theta$  correctly for both contours and lines. A good expression for the mother Gabor filter is:

$$\psi_0(\xi) = \psi_0(\xi_1, \xi_2) = \frac{1}{2\pi\sigma^2} e^{-\frac{(\xi_1^2 + \alpha^2 \xi_2^2)}{2\sigma^2}} e^{\frac{2i\bar{b}\xi_2}{\sigma}}, \quad (4.1)$$

where  $\bar{b} > 0$  is the ratio between  $\sigma$  and the spatial wavelength of the cosine factor,  $\alpha > 0$  is the spatial aspect ratio of the Gaus-

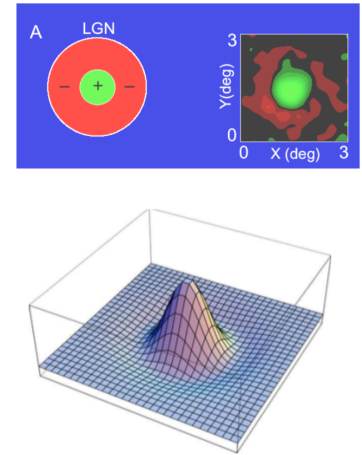


Figure 4.2: Top: receptive profile of a LGN neuron, on the left is presented a scheme of the receptive profile with its + (ON) and - (OFF) domains and on the right a recording of its levels lines, from De Angelis [44]. Bottom: a scheme of the Laplacian of Gaussian model for a LGN receptive profile, see [138].

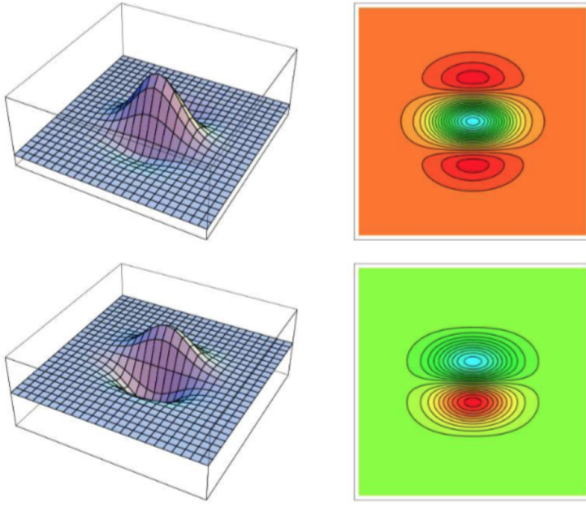


Figure 4.3: Even and odd part of the mother profile  $\psi_0(\xi)$ , see (4.1), [138], chapter 10, joint work with G. Citti and A. Sarti.

sian envelope. Translations and rotations can be expressed as:

$$A_{(x_1, x_2, \theta)}(\xi) = \begin{pmatrix} x_1 \\ x_2 \end{pmatrix} + R_\theta \begin{pmatrix} \xi_1 \\ \xi_2 \end{pmatrix}. \quad (4.2)$$

where  $R_\theta$ :

$$R_\theta = \begin{pmatrix} \cos\theta & -\sin\theta \\ \sin\theta & \cos\theta \end{pmatrix}$$

and represents a rotation of angle  $\theta$ . Hence a general RP can be expressed as:

$$\psi_{(x_1, x_2, \theta)}(\xi_1, \xi_2) = \psi_0(A_{(x_1, x_2, \theta)}^{-1}(\xi_1, \xi_2)).$$

### 4.1.3 The group law

A way of visualizing this space obtained through rotations and translations of a mother receptive profile  $\psi_0$  is illustrated in figure 4.4: the half-white/half-black circles represent the oriented receptive profiles of odd simple cells, where the angle indicated by the diameter of each circle is the angle of tuning. Every possible receptive profile is obtained from the origin by translating it through the vector  $(x_1, x_2)$  and rotating it over itself by an angle  $\theta$ . It results clear that the set of all parameters  $\{p = (x_1, x_2, \theta), (x_1, x_2) \in \mathbb{R}^2 \text{ and } \theta \in S^1\}$ , forms a group with the operation induced by the composition  $A_{p_1} \circ A_{p_2}$ . This turns out to be:

$$\begin{aligned} p_1 \circ p_2 &= (x_1, x_2, \theta_1) +_R (y_1, y_2, \theta_2) \\ &= \left( \left( \begin{pmatrix} x_1 \\ x_2 \end{pmatrix} + R_{\theta_1} \begin{pmatrix} y_1 \\ y_2 \end{pmatrix} \right)^T, \theta_1 + \theta_2 \right) \end{aligned}$$

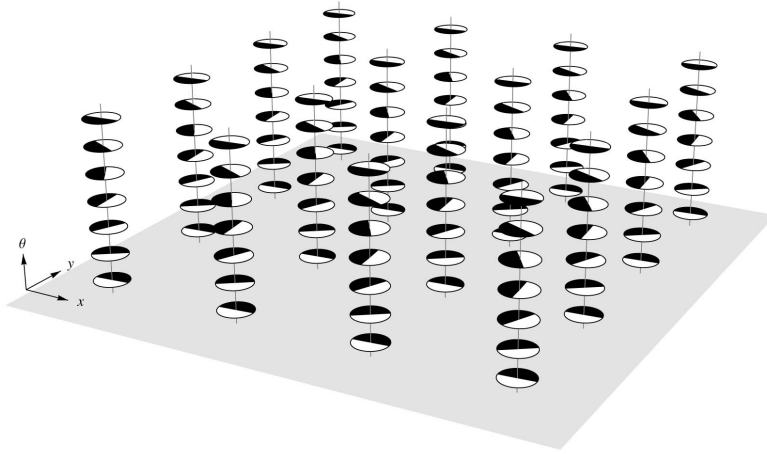


Figure 4.4: The visual cortex modelled as the group invariant under translations and rotations, [149].

Being induced by the composition law, one can easily check that  $+_R$  verifies the group operation axioms, where the inverse of a point  $p = (x_1, x_2, \theta)$  is induced by the rototranslation

$$A_{x_1, x_2, \theta}^{-1} = R_{\theta}^{-1} \circ T_{x_1, x_2}^{-1}$$

and the identity element is given by the trivial point  $e = (0, 0, 0)$ . The group generated by the operation  $+_R$  in the space  $\mathbb{R}^2 \times S^1$  is called Rototranslation group or equivalently  $SE(2)$ . The structured space of receptive profiles with the symmetries described above accounts for the rototranslation invariance of the V1/V2 in the representation of a retinal image; the signals will be identical no matter what their position or orientation in the phenomenological space. In the figure 4.5 a set of RPs generated with equation (4.2) is shown.

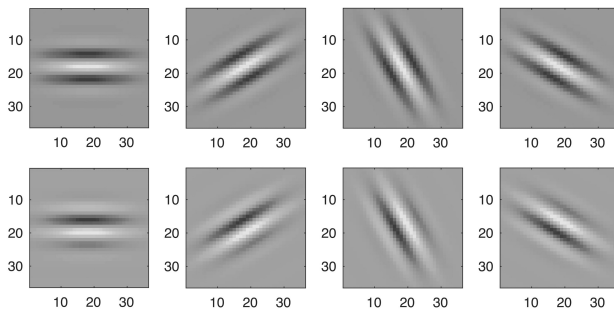


Figure 4.5: In each image: (top) even part of Gabor filters (real part), (bottom) odd one (imaginary part). Corresponding orientation from left to right:  $\theta = 0$ ,  $\theta = \pi/6$ ,  $\theta = 2\pi/3$ ,  $\theta = 5\pi/6$ , with  $\sigma = 4.48$  pixels

#### 4.1.4 Output of receptive profiles

The retinal plane is identified with the  $\mathbb{R}^2$ -plane, whose local coordinates will be denoted with  $(\xi_1, \xi_2)$ . When a visual stimulus  $I$  of intensity  $I : M \subset \mathbb{R}^2 \rightarrow \mathbb{R}^+$ , activates the retinal layer of photoreceptors, the neurons whose RFs intersect  $M$

spike and their spike frequencies  $O(x_1, x_2, \theta)$  can be modeled (taking into account just linear contributions) as the integral of the signal  $I$  with the set of Gabor filters. Indeed we assume the treated visual stimulus  $I$  to be integrable, i.e.  $I \in L^1(\mathbb{R}^2)$ . The expression for this output is:

$$O(x_1, x_2, \theta) = \int_M I(\xi_1, \xi_2) \psi_{(x_1, x_2, \theta)}(\xi_1, \xi_2) d\xi_1 d\xi_2. \quad (4.3)$$

In the right hand side of the equation the integral of the signal with the real and imaginary part of the Gabor filter is expressed. The two families of cells have different shapes, hence they detect different features. In particular odd cells will be responsible for boundary detection, see figure 4.6.

## 4.2 Functional architectures of V1/V2 and their connectivity

The roto-translation group accounts for the organization of cells in the primary visual cortices, but in order to model long range connectivity between receptive profiles a differential structure is needed. For this reason  $SE(2)$  will be considered equipped with its differential structure of Lie group (principal fiber bundle), with a sub-Riemannian metric. The base space of the fibration is the retina and there will be a map associating to each retinotopic position  $(\xi_1, \xi_2) \in \mathbb{R}^2$  a fiber, which is a copy of the whole possible set of orientations (the hypercolumn).

### 4.2.1 Hypercolumnar structure

The term *functional architecture* refers to the organisation of cells in the primary visual cortex in structures. As presented in chapter 2, the hypercolumnar structure, discovered by the neuro - physiologists Hubel and Wiesel in the 60s ([94]), organizes the cells of V1/V2 in columns (called hypercolumns) covering a small part of the visual field  $M \subset \mathbb{R}^2$  and corresponding to parameters such as orientation, scale, direction of movement, color, for a fixed retinal position  $(\xi_1, \xi_2)$ . In our framework over each retinal point we will consider a whole hypercolumn of cells, each one sensitive to a specific instance of orientation. Hence for each cortical position  $(x_1, x_2)$ , corresponding to the retinal position  $(\xi_1, \xi_2) \in M \subset \mathbb{R}^2$ , we associate a whole set of filters

$$RP_{(x_1, x_2)} = \{\psi_{(x_1, x_2, \theta)} : \theta \in S^1\}. \quad (4.4)$$

This expression associates to each point of the proximal stimulus in  $\mathbb{R}^2$  all possible feature orientations into the space of

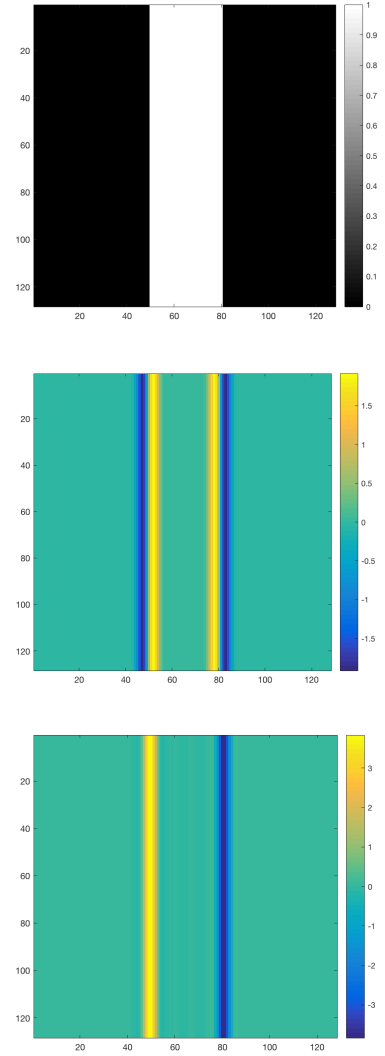


Figure 4.6: From top to bottom: initial stimulus. A surface is considered for convolution with the bank of odd and even receptive profiles. Center: result of the convolution of the initial surface with even Gabor filters (Real part). Contours are detected. Bottom: result of the convolution of the initial surface with odd Gabor filters (Imaginary part). Since the initial image is a surface, polarity plays a role, it means that contours with the same orientation but opposite contrast are referred to opposite angles, see Favali et al. [60].

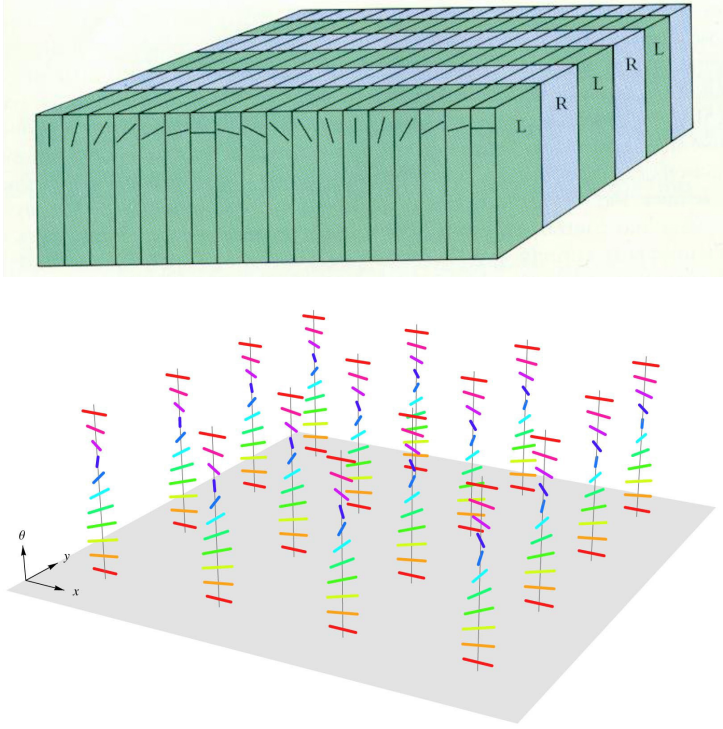


Figure 4.7: Top: representation of hypercolumnar structure, for the orientation parameter, where L and R represent the ocular dominance columns (Petitot [138]). Bottom: for each position of the retina  $(x_1, x_2)$  we have the set of all possible orientations, [149].

features  $S^1$ , and defines a fiber over each point

$$\{\theta \in S^1\}.$$

In this way the hypercolumnar structure is described in terms of differential geometry, but we need to explain how the orientation selectivity is performed by the cortical areas in the space of feature  $S^1$  ([28]).

#### 4.2.2 Cortical connectivity

Physiologically the orientation selectivity is the action of short range connections between simple cells belonging to the same hypercolumn to select the most probable response from the energy of receptive profiles. Horizontal connections are long ranged and connect cells of approximately *the same orientation*. Since the connectivity between cells is defined on the tangent bundle, we define now the generator of this space. The change of variable defined through  $A$  in (4.2) acts on the basis for the tangent bundle  $(\frac{\partial}{\partial x_1}, \frac{\partial}{\partial x_2})$  giving as frame in polar coordinates:

$$X_1 = \cos \theta \frac{\partial}{\partial x_1} + \sin \theta \frac{\partial}{\partial x_2}, \quad X_3 = -\sin \theta \frac{\partial}{\partial x_1} + \cos \theta \frac{\partial}{\partial x_2} \quad (4.5)$$

As presented in [28], the whole space of features  $(x_1, x_2, \theta)$  is described in terms of a 3-dimensional fiber bundle, whose generators are  $X_1, X_3$  for the base and

$$X_2 = \frac{\partial}{\partial \theta}, \quad (4.6)$$

for the fiber. These vector fields generate the tangent bundle of  $\mathbb{R}^2 \times S^1$ . Since horizontal connectivity is very anisotropic, the three generators are weighted by a strongly anisotropic metric. We introduce now the sub-Riemannian metric with whom Citti and Sarti in [28] proposed to endow the  $\mathbb{R}^2 \times S^1$  group to model the long range connectivity of the primary visual cortex V1. Starting from the vector fields  $X_1$ ,  $X_2$  and  $X_3$  they first defined the horizontal tangent bundle  $HM$ , as the distribution generated by  $X_1, X_2$  (see definition 3.3.9). Then they proved that cortical curves in V1 are always integral curves of vector fields in  $HM$ , which clarify the role of the geometry. As a consequence the connectivity pattern is described by integral curves of vector fields of the horizontal tangent space  $HM$ .

### 4.3 The lifting of a curve

Properties of the curves lifted in the cortical space can be obtained analyzing the lifting process operated by simple cells. If we consider a real stimulus, represented as an image  $I : M \rightarrow \mathbb{R}$ , we know that cells over each point  $(\xi_1, \xi_2) \in M$  can code the *orientation* of the level lines of  $I$ . Mathematically a level set is defined as follows:

$$\Gamma_c(I) = \{(\xi_1, \xi_2) \mid I(\xi_1, \xi_2) = c\}$$

i.e. it is a set where the function takes on a given constant value  $c$  of  $I$ . If  $I$  is sufficiently regular, the gradient vector to  $I$ , denoted by  $\nabla I$ , is orthogonal to the level lines of  $I$ . At points where the gradient does not vanish, we can perform a normalization and associate an orientation to the latter. Formally:

$$\frac{\nabla I}{|\nabla I|} = (-\sin \bar{\theta}, \cos \bar{\theta}).$$

This procedure defines at every considered point an orientation

$$\bar{\theta} : M \rightarrow S^1$$

such that  $(-\sin \bar{\theta}, \cos \bar{\theta})$  is orthogonal to the level lines of  $I$ . This means that  $(\cos \bar{\theta}(\xi), \sin \bar{\theta}(\xi))$  is tangent to the level lines of  $I$  at the point  $(\xi_1, \xi_2)$ . This orientation selectivity is performed by the short-range action of the connectivity which selects at the point  $\xi$  the simple cell with the maximum response within the whole hypercolumn and suppresses all the others. This mechanism is called *lifting*. The whole 2D level line can also be identified with a 2D *retinical* curve

$$\gamma_{2D} = (\xi_1(t), \xi_2(t)),$$

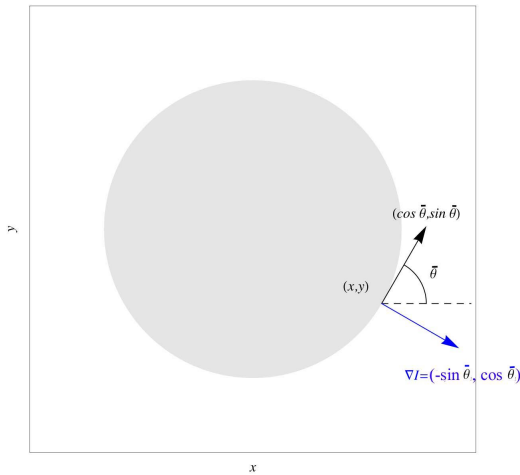


Figure 4.8: A contour in a 2D image can be modelled as a curve whose tangent is the vector  $(\cos \bar{\theta}, \sin \bar{\theta})$  and its normal direction is  $\nabla I / |\nabla I| = (-\sin \bar{\theta}, \cos \bar{\theta})$  as indicated in the figure, [149].

which is *lifted* to a new curve  $\gamma(t)$  in the 3D *cortical* space:

$$(\xi_1(t), \xi_2(t)) \rightarrow (x_1(t), x_2(t), \bar{\theta}(t)), \quad (4.7)$$

where indeed  $x_1 = \xi_1$ ,  $x_2 = \xi_2$ . We call an *admissible curve* a curve in  $\mathbb{R}^2 \times S^1$  if it is the lifting of a contour (identified by a planar curve). In figure 4.9 we can see an illustration of the lift-

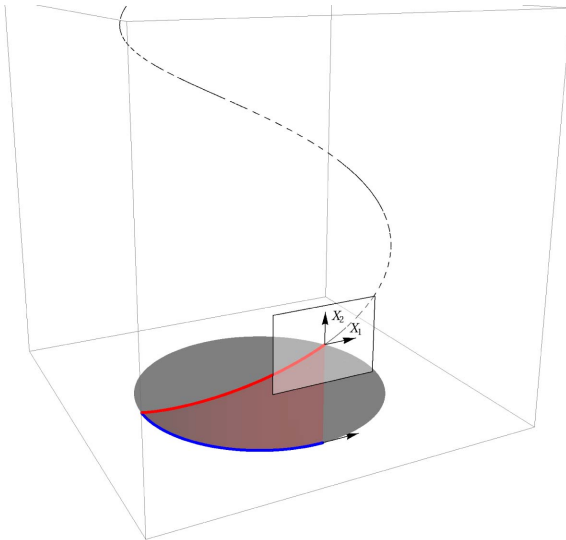


Figure 4.9: A contour represented by the curve  $\gamma_{2D}(t)$  is lifted into the rototranslation group obtaining the red curve  $\gamma(t)$ . The tangent space of the rototranslation group is spanned by the vectors  $X_1$  and  $X_2$ . Courtesy of Sanguinetti, [149].

ing process. By the parametrization we have chosen before for the curve  $\gamma_{2D}$  (the blue curve in figure 4.9) we can immediately express the value of  $\bar{\theta}$ :

$$\bar{\theta} = -\arctan\left(\frac{x'_2}{x'_1}\right).$$

The lifting  $\gamma$  (red curve in figure 4.9) of the curve  $\gamma_{2D}$  previously seen in ((4.7)) can be expressed by  $(x_1, x_2, \bar{\theta})$  where

$$\gamma' = (x'_1, x'_2, \bar{\theta}') = (\cos \theta, \sin \theta, \bar{\theta}') = X_1 + \bar{\theta}' X_2$$

$\gamma'(t)$  has a non-vanishing component in the direction  $X_1$  and a second component  $\bar{\theta}'$  in the direction of  $X_2$ . Admissible curves are integral curves of the two vector fields in a 3D (cortical) space, and cannot have components in the orthogonal direction given by the gradient  $\nabla I/|\nabla I| = X_3$ . This property clarifies the geometry of the cortical space starting from a biological and neurophysiological evidence and allows to perform a first choice of a metric.

#### 4.3.1 The metric of the cortical space

Since the only lifted curves in the cortical space are integral curves of the vector fields  $X_1$  and  $X_2$ , Citti and Sarti [28] defined a sub-Riemannian metric on the space, imposing that the horizontal tangent space is spanned by  $X_1$  and  $X_2$ . Imposing that they are orthonormal, we obtain a metric  $\mathcal{H}$  on  $HM$ , with inverse  $\mathcal{H}^{-1}$ , which expressed in the frame  $X_1, X_2$  are simply the identity:

$$\mathcal{H} = \begin{pmatrix} 1 & 0 \\ 0 & 1 \end{pmatrix}, \quad \mathcal{H}^{-1} = \begin{pmatrix} 1 & 0 \\ 0 & 1 \end{pmatrix} \quad (4.8)$$

If we consider  $a = a_1X_1 + a_2X_2 \in HM$ , its horizontal norm is:

$$\|a\| = \sqrt{(a_1)^2 + (a_2)^2}. \quad (4.9)$$

The inverse metric  $\mathcal{H}^{-1}$  can be formally extended to the whole space, to a new degenerate metric  $\mathcal{G}^{-1}$  requiring that  $X_3$  is orthogonal to the other directions and that  $\mathcal{G}^{-1}$  vanishes along  $X_3$ . This extended metric can be expressed in the standard frame  $\partial_{x_1}, \partial_{x_2}, \partial_\theta$ , as the metric:

$$g^{ij}(x_1, x_2, \theta) = \begin{pmatrix} \cos^2 \theta & \sin \theta \cos \theta & 0 \\ \sin \theta \cos \theta & \sin^2 \theta & 0 \\ 0 & 0 & 1 \end{pmatrix}, \quad (4.10)$$

with  $i, j = 1, 2, 3$ . Let us underline that  $X_1, X_2$  and  $X_3$  are *left invariant* with respect to the group law of rotations and translations, so that they are the generators of the associated *Lie algebra*. The first classical properties of the distance in these spaces have been established by Nagel, Stein and Wainger (see [128]), and Gromov (see [82]). The Hörmander condition is satisfied, see [87]:

**Definition 4.3.1.** We say that the Hörmander condition is satisfied if  $X_1, X_2$  and their commutators of any order span the Euclidean tangent space at every given point.

#### 4.4 Carnot Caratheodory distances

In the sub- Riemannian setting, the length of such curves is defined as follows:

$$l(\gamma) := \int_0^T \sqrt{\mathcal{H}_{\gamma(t)}(\dot{\gamma}(t), \dot{\gamma}(t))} dt \quad (4.11)$$

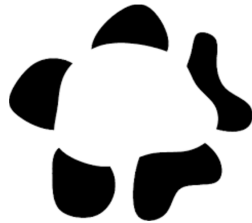
If the Hörmander condition holds, if we arbitrarily fix two points  $\eta_0$  and  $\eta_1$ , there is always an horizontal curve connecting them. Hence it is possible to define a sub- Riemannian distance between the two given points, as follows: see [128]:

$$d(\eta_0, \eta_1) = \inf_{\substack{\gamma \in \text{Lip}([0, T], SE(2)), \\ \dot{\gamma} \in \Delta|_{\gamma}, \gamma(0) = \eta_0, \gamma(T) = \eta_1}} l(\gamma). \quad (4.12)$$



## 5 Sub-Riemannian mean curvature flow for image processing

IN THIS CHAPTER, we start from the model of perceptual completion introduced by Citti and Sarti in [28] expressed via a diffusion driven motion by curvature. The main contribution



of the chapter is the proof of existence of vanishing viscosity solutions for the mean curvature flow in the rototranslation group  $SE(2)$ . Then we apply the algorithm to real images to perform inpainting, which means to recover missing or damaged parts of an initial stimulus [9]. Our second contribution

Figure 5.1: An example of amodal completion. The internal surface arises even if the contours are not actually present in the image, due to the presence of black inducers. We will see in this chapter how this perceptual phenomenon is model through mean curvature flow.



Figure 5.2: Left: macula cieca, an example of corrupted surface. Center: an occluded image (from U. Boscain et al. ([14])). Right: a well known example of damaged image, from Bertalmio et al [9].

is to extend the algorithm to perform boundary enhancement, which means make the structures of images more visible, while reducing the noise [131, 33, 176, 177]. Other enhancement algorithms in an analogous geometric setting has been developed by Duits and Franken, see figure 5.3, and comparison of our results with the ones detected via the previous algorithms are performed. This chapter uses material from the following publication by the author [30].

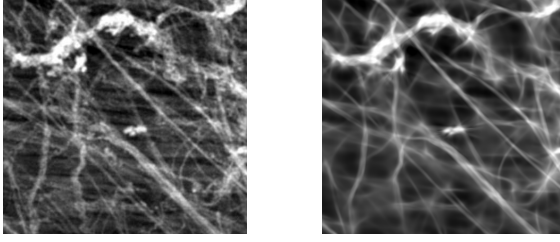


Figure 5.3: Left: the original image, from Duits and Franken ([54, Fig. 7]); right: the enhanced image using CED-OS, see [54].

## 5.1 Notation and lifting of an image in $SE(2)$

### 5.1.1 Subriemannian differential calculus

Scope of this section is to introduce differential calculus in the sub-Riemannian structure defined in section 4. Precisely, we will denote  $X_1$  and  $X_2$  the vector fields defined in (4.5) and (4.6) and we will say that a function  $u : \mathbb{R}^2 \times S^1 \rightarrow \mathbb{R}$  is of class  $C^1$  in the sub-Riemannian sense (we will denote it as  $u \in C_{SR}^1$ ) if there exists  $X_1u$  and  $X_2u$  and they are continuous. In this case we will call horizontal gradient of  $u$ ,  $\nabla u$ , applying definition 3.3.16:

$$\nabla u = (X_1u)X_1 + (X_2u)X_2.$$

Thanks to definition 4.9, the norm of the horizontal gradient is:

$$\|\nabla u\| = \sqrt{(X_1u)^2 + (X_2u)^2}. \quad (5.1)$$

Let us recall here that the horizontal gradient is the projection of the standard gradient of  $u$  on the horizontal plane  $HM$ .

### 5.1.2 Lifting of an image to a regular surface

In section 4.3 we introduced the lifting of a curve in the 3D cortical space. We will now describe the lifting of the whole image at a time. Since each level line of an initial image  $I$  is lifted to a curve in the 3D cortical space, the whole image is lifted to a graph, see figure 5.4 (center):

$$(\xi_1, \xi_2) \rightarrow (x_1(\xi_1, \xi_2), x_2(\xi_1, \xi_2), \bar{\theta}(\xi_1, \xi_2)).$$

Using the fact that  $x_1(\xi_1, \xi_2) = \xi_1$  and  $x_2(\xi_1, \xi_2) = \xi_2$ , we can interpret this surface as the zero level set of the function  $u$ :

$$u(x_1, x_2, \theta) = \theta - \bar{\theta}(x_1, x_2),$$

and it can be identified as a regular surface in the sub-Riemannian structure. The notion of regular surface  $S$  was first introduced by Franchi, Serapioni and Serracassano in [70]:

$$S = \{(x_1, x_2, \theta) : u(x_1, x_2, \theta) = 0 \text{ and } \nabla u(x_1, x_2, \theta) \neq 0\}. \quad (5.2)$$

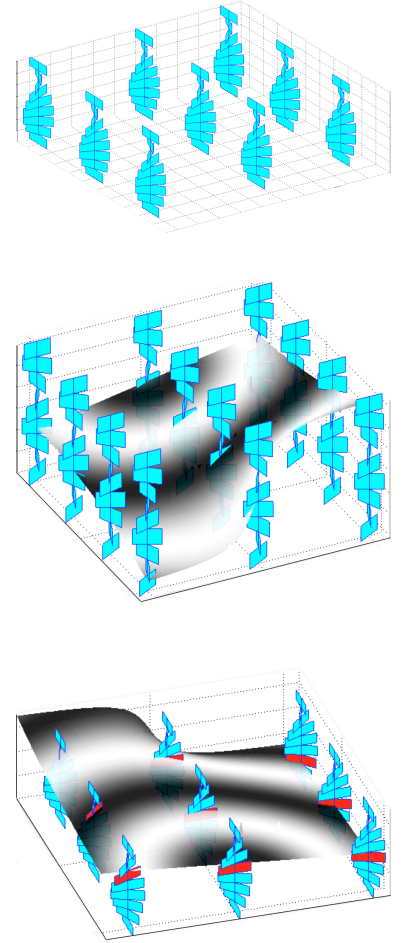


Figure 5.4: Top: the horizontal tangent planes  $HM$  of  $SE(2)$ , span of the vector fields  $X_1$  and  $X_2$ , adapted from [153]. Center: lifting of an image to a regular surface, inside the contact structure. Bottom: lifted surface: in red we marked the contact planes of  $HM$  tangent to the level lines of the surface.

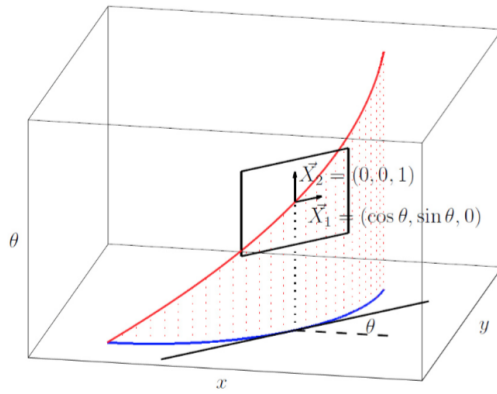


Figure 5.5: Recalling section 4.3: a contour represented by the curve  $\gamma_{2D}(t)$  is lifted into the rototranslation group obtaining the red curve  $\gamma(t)$ . The tangent space of the rototranslation group is spanned by the vectors  $X_1$  and  $X_2$ . From Sanguinetti, [151].

The horizontal normal of  $S$  is defined as

$$v = \frac{\nabla u}{|\nabla u|}.$$

Note that in a smooth surface there can be points where the Riemannian gradient is not 0, but its projection on the  $HM$  plane vanishes:

$$\nabla u = 0.$$

Points which have this property are called *characteristics* and the normal is not defined at them. However these points are not present in lifted surfaces. At every point of the surface there is a unique unitary tangent vector, which is horizontal:

$$T = \frac{(X_2 u, -X_1 u)}{|\nabla u|}. \quad (5.3)$$

The integral curves of this vector field define a foliation of the surface in horizontal curves (also called Legendrian foliation - see [136], [27], [23] and [74] for the properties of these curves).

### 5.1.3 Diffusion and concentration algorithm

We have seen in subsection 5.1.2 how to lift an image  $I$  to a surface  $S$ . After that we also lift the level lines of the image  $I$  to the function  $v$  defined on the surface as

$$v(x_1(\xi_1, \xi_2), x_2(\xi_1, \xi_2), \bar{\theta}(\xi_1, \xi_2)) = I(\xi_1, \xi_2)$$

defined on the surface. The surface  $S$  and the function  $v$  defined on  $S$  will be processed through differential operators defined on  $SE(2)$ , which model the propagation of information in the cortex. More precisely two mechanisms operate on the lifted surface  $S$ :

- (a) a sub-Riemannian diffusion along the vector fields  $X_1$  and  $X_2$  which model the propagation of information through the

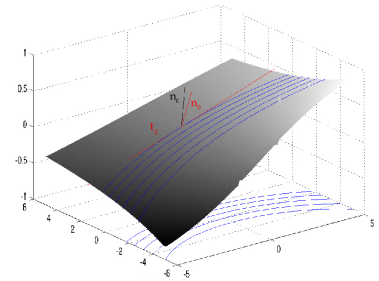


Figure 5.6: A lifted surface, foliated in Goedesics in the sense of [136, 27, 23, 74]. Tangent vector in the bundle  $TSE(2)$  is denoted as  $t_\epsilon$ , normal vector is  $n_\epsilon$ . The projection of  $n_\epsilon$  on the contact plane generated by  $X_1$  and  $X_2$  is  $n_0$ .

cortical lateral connectivity. This operator can be expressed as

$$\partial_t - X_{11} - X_{22}$$

where  $X_{11}$  and  $X_{22}$  are the second derivative in the direction  $X_1$  and  $X_2$  respectively. The operator is formally degenerated, in the sense that its second fundamental form has 0 determinant at every point. It has been deeply studied starting from the classical works of Hörmander in [88], Rothschild and Stein in [146] and Jerison [97] and it is known that it is hypoelliptic. After that a large literature has been produced on these type of operators, and we refer to [22] for a recent presentation of the state of the art.

- (b) a concentration on the surface of maxima to model the non-maximal suppression mechanism and the orientation tuning.

In the Euclidean setting Merrimann, Bence and Osher proved in [119] the convergence of a similar two step algorithm to the motion by curvature. In Citti and Sarti [28] the authors studied the motion when (a) and (b) are applied iteratively and proved that at each step the surface performs an increment in the normal direction with speed equal to the sub-Riemannian mean curvature.

## 5.2 Sub-Riemannian mean curvature flow for image processing

### 5.2.1 Mean curvature flow

The notion of curvature of a  $C^2$  surface at non characteristic points is already well understood, see ([38, 84, 26, 142, 22]). It can be defined either as first variation of the area functional, either as limit of the mean curvature of the Riemannian approximation (see section 5.3) or as horizontal divergence of the horizontal normal:

$$K = \operatorname{div}(v) = \operatorname{div}\left(\frac{\nabla u}{|\nabla u|}\right).$$

where the horizontal divergence of a horizontal vector field  $w = w_1 X_1 + w_2 X_2$  is defined as follows:

$$\operatorname{div}(w) = X_1(w_1) + X_2(w_2).$$

If each point of the surface evolves in the direction of the normal vector with speed equal to the mean curvature, we say that the surface is evolving by mean curvature. From the previously expression of the curvature we formally get the follow-

Curvature is in general related to the choice of the connection of the space. However since we deal with surfaces immersed (canonical) in  $SE(2)$ , the definition we are going to introduce depends on the metric induced by the ambient metric of  $SE(2)$ . Then we can provide the definition of curvature with metric objects (the divergence). Intuitively it measures how much a manifold, locally and once defined the metric, differs from being flat.

ing equation for the flow, which we can call horizontal (or sub-Riemannian) mean curvature flow:

$$\begin{cases} u_t = \sum_{i,j=1}^2 \left( \delta_{ij} - \frac{X_i u X_j u}{|\nabla u|^2} \right) X_i X_j u & \text{in } \Omega \subset \mathbb{R}^2 \times S^1 \\ u(\cdot, 0) = u_0 \end{cases} \quad (5.4)$$

where  $\delta_{ij}$  is the Kronecker function. An existence result for this equation was not known, and we will provide in the next section an existence theorem. In order to simplify notations we will denote:

$$A_{ij}^0(\nabla u) = \delta_{ij} - \frac{X_i u X_j u}{|\nabla u|^2}, \quad i, j = 1, 2. \quad (5.5)$$

### 5.2.2 Laplace-Beltrami flow

Citti and Sarti also conjectured that as a result of the previous mechanisms the function  $v$ , which contains the gray-levels values, evolves through the flow described by the Laplace Beltrami operator  $\Delta_{LB}$ :

$$\begin{cases} v_t = \Delta_{LB} v \\ v(\cdot, 0) = v_0. \end{cases} \quad (5.6)$$

This operator expresses a diffusion of the variable  $v$  on the surface level set of the variable  $u$ . The definition of Laplace Beltrami operator is recalled in the margin note. Let us note that the described equations become degenerate and the solutions are regular only along the directions of the foliation defined in (5.3).

The Laplace Beltrami is a second order operator on the horizontal tangent space to the surface (i.e the subset of the horizontal bundle which is tangent to the manifold). In the present setting we consider the surface

$$S = \{(x_1, x_2, \theta) : u(x_1, x_2, \theta) = 0\},$$

which has a unique tangent vector field (see 5.3):

$$T = \frac{X_2 u X_1 - X_1 u X_2}{|\nabla u|}.$$

If  $v : S \rightarrow R$  we will call Laplace Beltrami operator the second derivative in the direction of the vector  $T$ :

$$\Delta_{LB} v = T^2 v.$$

### 5.2.3 Enhancement and Inpainting in Sub-Riemannian geometry

#### 5.2.4 Inpainting of missing parts of the image

In the previous sections and chapters we described the main instruments necessary for describing the completion model of [28]. Let us recall here the proposed algorithm. As usual while restoring damaged portions of an image we assume that the corrupted set  $\omega$  is known a priori.

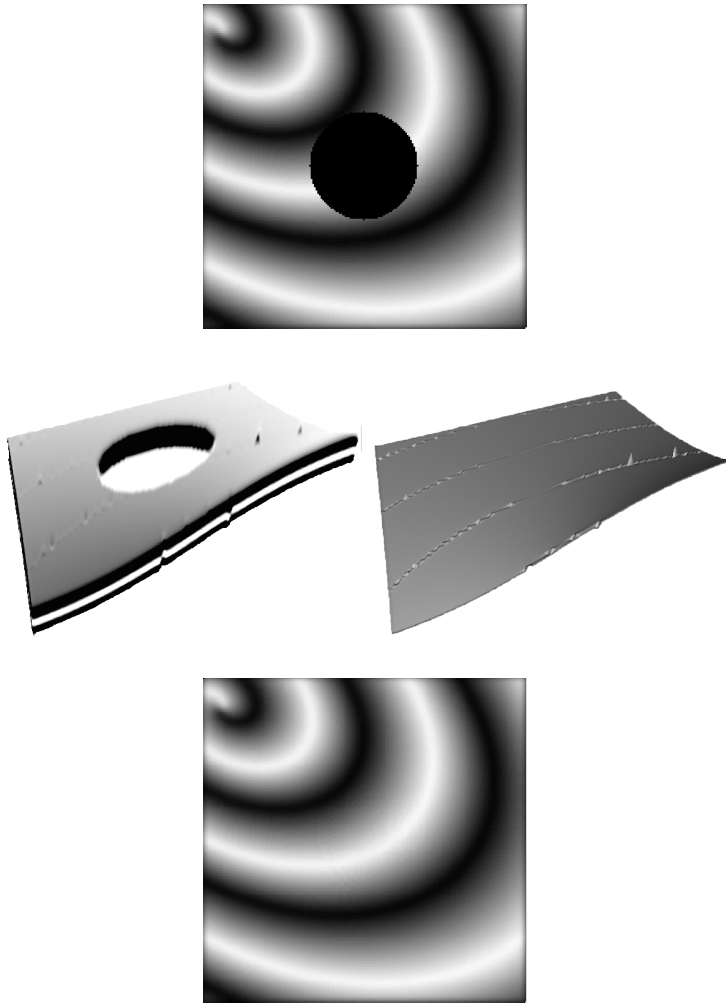


Figure 5.7: Top: the initial stimulus considered. It presents a damaged portion, the black hole in the center of the image. Center, left: the image is lifted to the  $SE(2)$  cortical space. Center, right: the lifted image is diffused and concentrated through the mechanism in 5.1.3, item (a), (b). This models the information propagation through the cortical lateral connectivity. This leads to the motion by mean curvature of the surface  $S$ . Bottom: the completed image is reprojected and the color is completed through the Laplace Beltrami operator, 5.2.2.

- 1 An image  $I$  is lifted to a surface  $S = \{(x_1, x_2, \bar{\theta}(x_1, x_2))\}$  in the Lie group  $SE(2)$  of rotations and translations, and the gray levels of  $I$  to a function  $v$  defined on  $S$ . In the lifting the corrupted part of the image becomes  $\Omega = \omega \times S^1$ , where no surface is defined.
- 2 The surface  $S$  and  $v$  are processed via the algorithm of diffusion and concentration in the corrupted region  $\Omega$ , where we impose Dirichlet boundary conditions. This leads to the

motion by mean curvature of the surface  $S$  and to a Laplace Beltrami flow for  $v$ .

- 3 The final result is obtained by re-projecting onto the plane of the image the values of the intensity  $v$ .

The algorithm has been implemented in [150] via a diffusion and concentration method, while it has been implemented via the curvature equation in [28]. The process is shown and described in figure 5.7.

### 5.2.5 Enhancement of boundaries

One of the scope of [30] was to extend the previous completion algorithm to solve the problem of contours enhancement. The aim of this technique is to provide a regularization in the direction of the boundaries, making them clearer and brighter and eliminating noise. We refer to the paper of Duits and Franken [54],[71] for some results of image enhancement in this space. Precisely they lift the image  $I$  in the 3D features space, using an invertible map defined through Fourier analysis. The lifted version of the image  $I$  is processed in the 3D space and then re-projected on the 2D plane to recover an enhanced version of the image  $I$ . In particular they also provide results of enhancement in presence of bifurcation or crossing. In our contribution [30], we face the same problem adapting the algorithm recalled in the previous section.

- 1 First we lift the level lines of an image  $I$  to a surface  $S = \{(x_1, x_2, \bar{\theta}(x_1, x_2))\}$  and we lift the gray levels of  $I$  to a function  $v$  always defined on  $S$ .
- 2 Then we process the surface  $S$  via a mean curvature flow and  $v$  via a Laplace-Beltrami flow. In order to perform enhancement we propose here to let equations (5.4) and (5.6) evolve in the full domain  $\mathbb{R}^2 \times S^1$ . Let us remark that lifting the image in the 3D group allows to solve the problem of crossing elongated structures. Indeed if two lines cross in the 2D space and have different orientations, they are lifted to the 3D space to two different planes, allowing completion and enhancement. The directional diffusion will give place to a regularization only in the direction of contours.
- 3 Finally we project into the plane of the image the values of the gray intensity  $v$ .

### 5.3 Existence of vanishing viscosity solutions

In this section we provide the main result of this chapter which is the proof of existence of solutions for the mean curvature flow in  $SE(2)$ . We explicitly note that we do not need to develop new results for the Laplace-Beltrami operator, which is linear. As we can immediately observe the PDE becomes degenerate in the singularities of the horizontal gradient of the solution  $u(\cdot, t)$ . The notions of viscosity and vanishing viscosity solutions have been introduced in order to overcome this problem. The method of generalized (viscosity) solutions independently developed by Chen, by Giga and Goto [25], by Evans and Spruck [59], by Crandall, Ishii and Lions [37] is now applied to large classes of degenerate equations [96]. Recently it has been extended also in Carnot groups, see [174] [21], and in the Heisenberg group, [63]. Finally let us recall that Dirr, Dragoni and Von Renesse in [50] have recently studied a probabilistic approach to the mean curvature flow in the general setting of Hörmander vector fields. Here we follow the presentation of Evans and Spruck [59], who used the notion of vanishing viscosity to establish existence of solution. Since the curvature equation is degenerate, the idea is to approximate the given equation with an uniformly elliptic one, establish results for the approximating problem and prove that in the limit this leads an existence result for the given equation. In the last section we introduce other notions of viscosity solutions and we clarify the relation between the different definitions of solutions we have introduced.

#### 5.3.1 The notion of vanishing viscosity solution

A vanishing viscosity solution is the limit of the solutions of approximating regular problems. Let us first explicitly note that the coefficients  $A_{ij}^0$  are degenerate: when the gradient vanishes, they are not defined. Hence we will apply the regularization procedure proposed by Evans and Spruck in [59] to face singularities, which consists in replacing the coefficients with the following ones:

$$A_{ij}^\tau(p) = \left( \delta_{ij} - \frac{p_i p_j}{|p|^2 + \tau} \right).$$

This approximation has a clear geometric interpretation, already provided by Evans and Spruck. In equation (5.4) each level set of  $u$  evolves by mean curvature. What we obtain adding a new parameter is the evolution of the graph of  $u$

$$\Gamma_t^\tau = \{(\xi, \xi_{n+1}) \in \mathbb{R}^{n+1} | \xi_{n+1} = u(\xi, t)\}$$

and the introduction in the space of a metric depending on  $\tau$ . In this approximation equation (5.4) reads as:

$$\begin{cases} u_t = \sum_{i,j=1}^2 A_{ij}^\tau (\nabla_0 u) X_i^0 X_j^0 u & \text{in } \Omega \subset \mathbb{R}^2 \times S^1 \\ u(\cdot, 0) = u_0. \end{cases} \quad (5.7)$$

We will now introduce a Riemannian approximation of the mean curvature flow in the graph approximation we made before. We extend  $\mathcal{G}$  ( $= \mathcal{G}_0$  to underline the passage to the limit) to a metric  $\mathcal{G}_\epsilon$  defined on the whole tangent space of  $SE(2)$  which makes the vectors  $X_1^0, X_2^0, \epsilon X_3$  orthonormal. Let us note that  $\mathcal{G}_\epsilon$  is the Riemannian completion of the horizontal metric. We will always denote

$$X_1^\epsilon = X_1^0, \quad X_2^\epsilon = X_2^0, \quad X_3^\epsilon = \epsilon X_3. \quad (5.8)$$

This notation justifies the choice of calling  $X_i^0$  the sub-Riemannian vector fields: we want to underline they can be obtained for  $\epsilon = 0$ . Recalling section 4.3.1,  $\mathcal{G}_\epsilon$  is the Riemannian approximation of  $\mathcal{G}$ . Let us recall that the Riemannian gradient associated to the metric  $\mathcal{G}_\epsilon$ , in the sense of definition 3.3.16, will be represented as:

$$\nabla_\epsilon u = X_1^\epsilon u X_1^\epsilon + X_2^\epsilon u X_2^\epsilon + X_3^\epsilon u X_3^\epsilon$$

and, using the fact that  $X_i^\epsilon$  are orthonormal, we get:

$$|\nabla_\epsilon u| = \sqrt{(X_1^\epsilon u)^2 + (X_2^\epsilon u)^2 + (X_3^\epsilon u)^2}. \quad (5.9)$$

In the Riemannian setting equation (5.7) reads as:

$$\begin{cases} u_t = \sum_{i,j=1}^3 A_{ij}^{\epsilon,\tau} (\nabla_\epsilon u) X_i^\epsilon X_j^\epsilon u & \text{in } \Omega \subset \mathbb{R}^2 \times S^1 \\ u(\cdot, 0) = u_0 \end{cases} \quad (5.10)$$

where

$$A_{ij}^{\epsilon,\tau} (\nabla_\epsilon u) = \left( \delta_{i,j} - \frac{X_i^\epsilon u X_j^\epsilon u}{|\nabla_\epsilon u|^2 + \tau} \right).$$

In order to prove the existence of a solution we apply another regularization, always introduced by Evans and Spruck. It consists in adding a Laplacian, ensuring that the matrix of the coefficients has strictly positive smallest eigenvalue. Then the approximated coefficients will be:

$$A_{ij}^{\epsilon,\tau,\sigma} (p) = A_{ij}^{\epsilon,\tau} (p) + \sigma \delta_{ij}$$

and the associated equation becomes:

$$\begin{cases} u_t = \sum_{i,j=1}^3 A_{ij}^{\epsilon,\tau,\sigma} (\nabla_\epsilon u) X_i^\epsilon X_j^\epsilon u & \text{in } \Omega \subset \mathbb{R}^2 \times S^1 \\ u(\cdot, 0) = u_0. \end{cases} \quad (5.11)$$

This condition makes the coefficients satisfy the coercivity condition and allows to apply the standard theory of uniformly parabolic equations. We are now in condition to give the definition of vanishing viscosity solution:

**Definition 5.3.1.** A function  $u$  is a vanishing viscosity solution of (5.4) if it is limit in the space of locally Lipschitz continuous functions of a sequence of solutions  $u^{\epsilon_k, \tau_k, \sigma_k}$  of equation (5.11).

### 5.3.2 Solution of the approximating equations

The aim of this sub-section is to study the approximating equation (5.11). Since it is uniformly parabolic we will recognize that standard PDE results provide existence of the solution. We are here interested in establishing estimates independent of all parameters for the solution and its gradient.

**Theorem 5.3.2.** Assume that  $u_0 \in C^\infty(\mathbb{R}^2 \times S^1)$  and that it is constant on the exterior of a cylinder, i.e. there exists  $M_0 > 0$  such that:

$$u_0 \text{ is constant on } \mathbb{R}^2 \times S^1 \cap \{(x_1, x_2, \theta) \text{ such that } x_1^2 + x_2^2 \geq M_0^2\}. \quad (5.12)$$

Then there exists a unique solution  $u^{\epsilon, \tau, \sigma} \in C^{2, \alpha}(\mathbb{R}^2 \times S^1 \times [0, \infty))$  of the initial value problem (5.11). Moreover, for all  $t > 0$  one has:

$$\|u^{\epsilon, \tau, \sigma}(\cdot, t)\|_{\mathcal{L}^\infty(\mathbb{R}^2 \times S^1)} \leq \|u_0\|_{\mathcal{L}^\infty(\mathbb{R}^2 \times S^1)} \quad (5.13)$$

$$\begin{aligned} \|\partial_{x_1} u^{\epsilon, \tau, \sigma}(\cdot, t)\|_{\mathcal{L}^\infty(\mathbb{R}^2 \times S^1)} + \|\partial_{x_2} u^{\epsilon, \tau, \sigma}(\cdot, t)\|_{\mathcal{L}^\infty(\mathbb{R}^2 \times S^1)} &\leq \quad (5.14) \\ &\leq \|\partial_{x_1} u_0^{\epsilon, \tau, \sigma}\|_{\mathcal{L}^\infty(\mathbb{R}^2 \times S^1)} + \|\partial_{x_2} u_0^{\epsilon, \tau, \sigma}\|_{\mathcal{L}^\infty(\mathbb{R}^2 \times S^1)} \end{aligned}$$

$$|\partial_\theta u^{\epsilon, \tau, \sigma}(x, \theta, t)| \leq (1 + 2M_0 + 2|x|) \|\nabla_E u_0\|_{\mathcal{L}^\infty(\mathbb{R}^2 \times S^1)} \quad (5.15)$$

for every  $x \in \mathbb{R}^2$ , and  $\nabla_E(\cdot)$  denotes the Euclidean gradient.

This result generalizes to  $SE(2)$  the previous results of [59] and [21]. The first step of the proof of Theorem 5.3.2 is the existence of the function  $u$  and its  $L^\infty$  bound:

**Theorem 5.3.3.** Under the assumption of Theorem 5.3.2 on the initial datum, the initial value problem (5.11) has an unique solution  $u^{\epsilon, \tau, \sigma} \in C^{2, \alpha}(\mathbb{R}^2 \times S^1 \times [0, \infty))$  such that

$$\|u^{\epsilon, \tau, \sigma}(\cdot, t)\|_{\mathcal{L}^\infty(\mathbb{R}^2 \times S^1)} \leq \|u_0\|_{\mathcal{L}^\infty(\mathbb{R}^2 \times S^1)} \quad (5.16)$$

*Proof.* For  $\sigma > 0$ , consider the problem associated to equation (5.11) on a cylinder  $B(0, r) \times [0, T]$ , with initial data

$$u_r^{\epsilon, \tau, \sigma}(\cdot, 0) = u_0, \quad (5.17)$$

and constant value on the lateral boundary of the cylinder. Note that coefficients  $A_{ij}^{\epsilon, \tau, \sigma}$  satisfy the uniform parabolic condition:

$$\sigma |p|^2 \leq A_{ij}^{\epsilon, \tau, \sigma}(\tilde{p}) p_i p_j \quad (5.18)$$

for each  $\tilde{p}, p \in \mathbb{R}^3$ . Hence the theory of parabolic equations on bounded cylinders ensures that for every fixed value of the parameters there exists a unique smooth solution  $u_r^{\epsilon, \tau, \sigma}$  (see for example Ladyzenskaja, Solonnikov, Ural'tseva [133]). By the maximum principle we have

$$\|u_r^{\epsilon, \tau, \sigma}(\cdot, t)\|_{\mathcal{L}^\infty(\mathbb{R}^2 \times S^1)} \leq \|u_0\|_{\mathcal{L}^\infty(\mathbb{R}^2 \times S^1)}. \quad (5.19)$$

Letting  $r$  tend to  $\infty$ , we obtain a solution  $u^{\epsilon, \tau, \sigma}$  defined on the whole  $\mathbb{R}^n \times [0, T]$  such that

$$\|u^{\epsilon, \tau, \sigma}\|_\infty \leq \|u_0\|_{\mathcal{L}^\infty(\mathbb{R}^2 \times S^1)}.$$

□

The second step of the proof is the estimate of the gradient. In order to obtain this estimate we differentiate equation (5.11), obtaining the equation satisfied by the gradient, and we apply the maximum principle. The main difficulty to face is the fact that the vector fields  $X_i^\epsilon$  do not commute, hence it is not easy to find a nice equation satisfied by the gradient. We will take the derivatives along the direction of a family of vector fields

$$\begin{aligned} Y_1 &= \partial_{x_1} \\ Y_2 &= \partial_\theta - x_2 \partial_{x_1} + x_1 \partial_{x_2} \\ Y_3 &= \partial_{x_2}. \end{aligned}$$

which are right invariant with respect to the group law. These vector fields are widely used: Mumford in [125] used them for a different purpose. In particular it is well known that these vector fields commute with the left invariant ones  $X_i^\epsilon$ .

Let us start directly verifying that the vector fields  $(X_i^\epsilon)$  and  $(Y_i)$  commute.

**Lemma 5.3.4.** The vector fields  $\{X_i^\epsilon\}_{i=1,2,3}$  defined in (5.8) commute with  $\{Y_i\}_{i=1,2,3}$ , just defined.

*Proof.* We calculate their Lie bracket:

$$\begin{aligned} [X_1^0, Y_1] &= (\cos \theta \partial_{x_1} + \sin \theta \partial_{x_2}) \partial_{x_1} - \partial_{x_1} (\cos \theta \partial_{x_1} + \sin \theta \partial_{x_2}) \\ &= \cos \theta \partial_{x_1 x_1} + \sin \theta \partial_{x_2 x_1} - \cos \theta \partial_{x_1 x_1} - \sin \theta \partial_{x_1 x_2} \\ &= 0. \end{aligned}$$

Since the coefficients of  $Y_2$  do not depend on  $\theta$  it is clear that

$$[X_2^0, Y_2] = 0.$$

Finally

$$\begin{aligned} [X_3, Y_3] &= (\sin \theta \partial_{x_1} - \cos \theta \partial_{x_2}) \partial_{x_2} - \partial_{x_2} (\sin \theta \partial_{x_1} - \cos \theta \partial_{x_2}) \\ &= \sin \theta \partial_{x_1 x_2} - \cos \theta \partial_{x_2 x_2} - \sin \theta \partial_{x_1 x_2} + \cos \theta \partial_{x_2 x_2} \\ &= 0 \end{aligned}$$

The other combinations can be analogously computed.  $\square$

We can now obtain the estimate of the gradient:

**Theorem 5.3.5.** Under the assumption of Theorem 5.3.2 and 5.3.3, the solution of the initial value problem (5.11) satisfies

$$\begin{aligned} \|\partial_{x_1} u^{\varepsilon, \tau, \sigma}(\cdot, t)\|_{\mathcal{L}^\infty(\mathbb{R}^2 \times S^1)} + \|\partial_{x_2} u^{\varepsilon, \tau, \sigma}(\cdot, t)\|_{\mathcal{L}^\infty(\mathbb{R}^2 \times S^1)} &\leq \quad (5.20) \\ &\leq \|\partial_{x_1} u_0^{\varepsilon, \tau, \sigma}\|_{\mathcal{L}^\infty(\mathbb{R}^2 \times S^1)} + \|\partial_{x_2} u_0^{\varepsilon, \tau, \sigma}\|_{\mathcal{L}^\infty(\mathbb{R}^2 \times S^1)} \end{aligned}$$

$$|\partial_\theta u^{\varepsilon, \tau, \sigma}(x, \theta, t)| \leq (1 + 2M_0 + 2|x|) \|\nabla_E u_0\|_{\mathcal{L}^\infty(\mathbb{R}^2 \times S^1)} \quad (5.21)$$

for every  $x \in \mathbb{R}^2$  and  $M_0$  has been defined in 5.3.2.

*Proof.* From Theorem 5.3.3 we know that there exists a unique smooth solution  $u^{\varepsilon, \tau, \sigma}$  of equation (5.11) and we only have to estimate its gradient. To this end, we can differentiate equation (5.11) along the directions  $\{Y_i\}_{i=1,2,3}$ , and using Lemma 5.3.4, we obtain the following equation for  $w_i = Y_i u^{\varepsilon, \tau, \sigma}$ , for all  $i = 1, 2, 3$ , and for  $\omega_4 = Y_2 u^{\varepsilon, \tau, \sigma} - (y_2 \partial_{x_1} - y_1 \partial_{x_2}) u^{\varepsilon, \tau, \sigma}$  (for every fixed value  $(y_1, y_2)$ ):

$$\begin{aligned} \frac{\partial}{\partial t} w_i &= \sum_{i,j,k=1}^3 \left( A_{i,j}^{\varepsilon, \tau, \sigma} (\nabla_\varepsilon u^{\varepsilon, \tau, \sigma}) X_i^\varepsilon X_j^\varepsilon w_i \right. \\ &\quad \left. + (\partial_{\xi_k} A_{i,j}^{\varepsilon, \tau, \sigma}) (\nabla_\varepsilon u^{\varepsilon, \tau, \sigma}) X_i^\varepsilon X_j^\varepsilon u^{\varepsilon, \tau, \sigma} X_k^\varepsilon w_i \right). \end{aligned} \quad (5.22)$$

The parabolic maximum principle ([133]) applied to the previous equation yields:

$$\|Y_i u^{\varepsilon, \tau, \sigma}(\cdot, t)\|_{\mathcal{L}^\infty(\mathbb{R}^2 \times S^1)} \leq \|Y_i u_0\|_{\mathcal{L}^\infty(\mathbb{R}^2 \times S^1)} \quad (5.23)$$

This implies (5.14). Now we have to establish the estimate of the derivative  $\partial_\theta$ . For every fixed value of  $y = (y_1, y_2)$  we have,

using in the last inequality the fact that  $|x_1| \leq M_0$ ,  $|x_2| \leq M_0$ :

$$\begin{aligned}
|\partial_\theta u^{\epsilon, \tau, \sigma}(y_1, y_2, \theta)| &= |(Y_2 u^{\epsilon, \tau, \sigma} - (y_2 \partial_{x_1} - y_1 \partial_{x_2}) u^{\epsilon, \tau, \sigma})(y_1, y_2, \theta)| \leq \\
&\leq |Y_2 u^{\epsilon, \tau, \sigma}(y_1, y_2, \theta)| + |y_2| |\partial_{x_1} u^{\epsilon, \tau, \sigma}(y_1, y_2, \theta)| + \\
&\quad + |y_1| |\partial_{x_2} u^{\epsilon, \tau, \sigma}(y_1, y_2, \theta)| \leq \\
&\leq \max_{(x_1, x_2, \theta)} |Y_2 u_0(x_1, x_2, \theta)| + |y_2| \max_{(x_1, x_2, \theta)} |\partial_{x_1} u_0(x_1, x_2, \theta)| + \\
&\quad + |y_1| \max_{(x_1, x_2, \theta)} |\partial_{x_2} u_0(x_1, x_2, \theta)| \\
&\leq \max_{(x_1, x_2, \theta)} |\partial_\theta u_0(x_1, x_2, \theta)| + \max_{(x_1, x_2, \theta)} |x_2| |\partial_{x_1} u_0(x_1, x_2, \theta)| \\
&\quad + \max_{(x_1, x_2, \theta)} |x_1| |\partial_{x_2} u_0(x_1, x_2, \theta)| + |y_2| \max_{(x_1, x_2, \theta)} |\partial_{x_1} u_0(x_1, x_2, \theta)| \\
&\quad + |y_1| \max_{(x_1, x_2, \theta)} |\partial_{x_2} u_0(x_1, x_2, \theta)| \leq \\
&\leq (1 + 2M_0 + 2|y|) \|\nabla_E u_0\|_{\mathcal{L}^\infty(\mathbb{R}^2 \times S^1)}
\end{aligned}$$

Then  $|\partial_\theta u^{\epsilon, \tau, \sigma}|$  is locally Lipschitz, and it grows with  $y$   $\square$

Let us conclude this section remarking that the proof of Theorem 5.3.2 is a direct consequence of the two Theorems 5.3.3 and 5.3.5.

### 5.3.3 Existence for the sub-Riemannian mean curvature equation

In order to extend to our setting Evans and Spruck's argument in the proof of [59], as well as the proof of [21], we need to let the three approximating parameters  $\sigma \rightarrow 0$ ,  $\tau \rightarrow 0$  and  $\epsilon \rightarrow 0$  go to 0. Since the estimates we have established are uniform in all parameters, we immediately have the existence of a vanishing viscosity solution:

**Theorem 5.3.6.** Assume that  $u_0 \in C(\mathbb{R}^2 \times S^1)$  is Lipschitz continuous and satisfies (5.12). Then there exists a vanishing viscosity solution  $u \in C_{loc}^{1,0}$  of (5.4), which satisfies the following properties:

$$\|u(\cdot, t)\|_{\mathcal{L}^\infty(\mathbb{R}^2 \times S^1)} \leq \|u_0\|_{\mathcal{L}^\infty(\mathbb{R}^2 \times S^1)} \quad (5.24)$$

$$\|\partial_{x_1} u^{\epsilon, \tau, \sigma}(\cdot, t)\|_{\mathcal{L}^\infty(\mathbb{R}^2 \times S^1)} + \|\partial_{x_2} u^{\epsilon, \tau, \sigma}(\cdot, t)\|_{\mathcal{L}^\infty(\mathbb{R}^2 \times S^1)} \leq \quad (5.25)$$

$$\leq \|\partial_{x_1} u_0^{\epsilon, \tau, \sigma}\|_{\mathcal{L}^\infty(\mathbb{R}^2 \times S^1)} + \|\partial_{x_2} u_0^{\epsilon, \tau, \sigma}\|_{\mathcal{L}^\infty(\mathbb{R}^2 \times S^1)}$$

$$|\partial_\theta u^{\epsilon, \tau, \sigma}(x, \theta, t)| \leq (1 + 2M_0 + 2|x|) \|\nabla_E u_0\|_{\mathcal{L}^\infty(\mathbb{R}^2 \times S^1)} \quad (5.26)$$

*Proof.* Since  $u_0$  is constant at infinity, we immediately deduce from Weierstrass theorem that the Euclidean gradient  $\nabla_E u_0$  is bounded. Employing estimates (5.13), (5.14), (5.15) and Ascoli Arzelà Theorem on each compact subset we can extract two sequences  $\{\sigma_k\}, \{\epsilon_k\}, \{\tau_k\} \rightarrow 0$  of positive numbers such that  $\frac{\epsilon_k}{\tau_k} \rightarrow 0$  and such that the corresponding solutions  $\{u^k = u^{\epsilon_k, \tau_k, \sigma_k}\}_{k \in \mathbb{N}}$  are convergent in the space of locally Lipschitz functions. Then by definition the limit is a continuous vanishing viscosity solution.  $\square$

Here we prove that solutions are uniformly Lipschitz continuous. Even in the Euclidean setting this is the best regularity results for solutions of equations expressed as level sets, due to the degeneracy of the equation. Only in the special case of motion by curvature of graphs, higher regularity can be obtained. (see for example Capogna, Citti, Manfredini [24]).

### 5.3.4 Other notions of viscosity solution

#### Viscosity solutions in the sense of Jet spaces

The cortical model previously discussed associates to each planar curve  $\gamma_{2D}$  its orientation. This procedure can be considered as a lifting of the initial image  $I(x_1, x_2)$  to a new function  $u$  defined in the space  $\mathbb{R}^2 \times S^1$  of positions and orientations. We refer to Petitot and Tondut, who first described the analogous cortical process as a lifting in a jet space [139]. Another lifting process can be obtained if we associate to each function  $u : \mathbb{R}^2 \times S^1 \rightarrow \mathbb{R}$  its derivatives. In this way a function  $u$  is lifted into a Jet-space which contains the formal analogous of its sub-Riemannian gradient  $\nabla_0 u$  and the formal analogous of the elements of its horizontal Hessian matrix  $X_i^0 X_j^0$  (please refer to the Appendix for the definition of the horizontal Hessian). The definition of viscosity solution in Jet-spaces has been introduced in [37], and is now widely used in the sub-Riemannian setting (see for example [11]). It is based on the Taylor expansion, expressed in terms of these differential objects. The analogous of the increment in the direction of the gradient  $p$  is expressed through the notion of exponential map (see the appendix for its precise definition), then the increment from a point  $\xi$  in the direction  $\sum_{i=1}^2 \eta_i X_i^0$  is expressed as

$$u\left(\exp\left(\sum_{i=1}^2 \eta_i X_i^0\right)(\xi), t + s\right) - u(\xi, t).$$

At non regular points, such as kinks, there is not either a unique vector  $p$  which identifies the horizontal gradient and a unique matrix  $r_{ij}$  which identifies the horizontal Hessian. Hence we

need to give a more general notion. If  $p_i, i = 1, 2$  denotes an horizontal vector,  $(r_{ij})$  a  $2 \times 2$  matrix and  $q$  a real number, the triplet  $(p, r, q)$  is an element of the superjet  $\mathcal{J}^+$  for  $u$  if it satisfies the following formal analogous of the Taylor development:

$$\begin{aligned} & u\left(\exp\left(\sum_{i=1}^2 \eta_i X_i^0\right)(\xi), t + s\right) - u(\xi, t) \\ & \leq \sum_{i=1}^2 p_i \eta_i + \frac{1}{2} \sum_{i,j=1}^2 r_{ij} \eta_i \eta_j + qs + o(|\eta|^2 + s^2). \end{aligned} \quad (5.27)$$

Let us note that if the super jet exists it can be used in place of the derivatives; furthermore a function  $u$  is a Jet-space viscosity solution if the differential equation in which the derivatives are replaced with the elements of the superjet is satisfied. More precisely:

**Definition 5.3.7.** A function  $u \in C(\mathbb{R}^2 \times S^1 \times [0, \infty)) \cap \mathcal{L}^\infty(\mathbb{R}^2 \times S^1 \times [0, \infty))$  is a jet space-viscosity subsolution of equation (5.4) if for every  $(p, r, q)$  in the super-Jet we have:

$$q \leq \begin{cases} \sum_{i,j=1}^2 A_{ij}^0(p) r_{ij} & \text{if } |p| \neq 0 \\ \sum_{i,j=1}^2 A_{ij}^0(\tilde{p}) r_{ij} & \text{for some } |\tilde{p}| \leq 1, \text{ if } |p| = 0. \end{cases} \quad (5.28)$$

An analogous definition is provided for a viscosity supersolution. Then a viscosity solution is a function which is both a subsolution and a supersolution.

### Viscosity solutions via test functions

The definition of viscosity solution in Jet-space of a second order equation can be identified as the approximation of the solution  $u$  via a second order polynomial, whose coefficients are exactly the elements  $(p, r, q)$  of the Jet space. The definition of viscosity solution via test functions is similar, but it estimates the given solution using smooth functions instead of polynomials alone. This definition imposes the behavior of the function  $u$  at points where  $u - \phi$  attains a maximum. At such points  $u$  and  $\phi$  will have the same first derivatives, so that  $\nabla_0 \phi$  results to be an exact evaluation of the approximation of  $\nabla_0 u$ . Looking at second derivatives, it follows that for every  $i$  we have:

$$X_i^0 X_i^0 (u - \phi) \leq 0,$$

so that the curvature of  $\phi$  is an upper bound for the curvature of  $u$ . Due to this observations we can give the following definition:

**Definition 5.3.8.** A function  $u \in C(\mathbb{R}^2 \times S^1 \times [0, \infty))$  is a viscosity subsolution of (5.4) in  $\mathbb{R}^2 \times S^1 \times [0, \infty)$  if for any  $(\xi, t)$  in  $\mathbb{R}^2 \times S^1 \times [0, \infty)$  and any function  $\phi \in C(\mathbb{R}^2 \times S^1 \times [0, \infty))$  such that  $u - \phi$  has a local maximum at  $(\xi, t)$  it satisfies:

$$\partial_t \phi \leq \begin{cases} \sum_{i,j=1}^2 A_{ij}^0(\nabla_0 \phi) X_i^0 X_j^0 \phi & \text{if } |\nabla_0 \phi| \neq 0 \\ \sum_{i,j=1}^2 A_{ij}^0(\tilde{p}) X_i^0 X_j^0 \phi, & \text{for some } \tilde{p} \in \mathbb{R}^2, |\tilde{p}| \neq 1, \text{ if } |\nabla_0 \phi| = 0 \end{cases} \quad (5.29)$$

A function  $u \in C(\mathbb{R}^2 \times S^1 \times [0, \infty))$  is a viscosity supersolution of (5.4) if:

$$\partial_t \phi \geq \begin{cases} \sum_{i,j=1}^2 A_{ij}^0(\nabla_0 \phi) X_i^0 X_j^0 \phi & \text{if } |\nabla_0 \phi| \neq 0 \\ \sum_{i,j=1}^2 A_{ij}^0(\tilde{p}) X_i^0 X_j^0 \phi, & \text{for some } \tilde{p} \in \mathbb{R}^2, |\tilde{p}| \neq 1, \text{ if } |\nabla_0 \phi| = 0 \end{cases} \quad (5.30)$$

**Definition 5.3.9.** A viscosity solution of (5.4) is a function  $u$  which is both a viscosity subsolution and a viscosity supersolution.

#### Relation between the different notions of solutions

**Theorem 5.3.10.** The two definitions of jet spaces viscosity solution and viscosity solution are equivalent.

*Proof.* We will recall here that a subelliptic equation in  $SE(2)$  group can be locally reduced to an equation in the Heisenberg group, via a simple change of variables, so that we will be able to apply the the analogous result proved in the Heisenberg setting in [11]. Indeed, calling  $b = -x_1 \sin \theta + x_2 \cos \theta$ , we can consider the vector fields  $Z_1, Z_2$  and  $Z_3$  introduced in [29]:

$$Z_1 = X_1, \quad Z_2 = X_2 - b X_1, \quad Z_3 = [Z_1, Z_2] = X_3;$$

It is easy to see that all the other commutators vanishes, so that the Lie algebra generated by  $\{Z_i\}$  is an Heisenberg algebra. If we call

$$B = \begin{pmatrix} 1 & 0 \\ b & 1 \end{pmatrix} \quad \nabla_{Heis} = (Z_1, Z_2), \quad (5.31)$$

where  $\nabla_{Heis}$  denotes the horizontal gradient in the Heisenberg group. Then we have

$$X_i = B_{ih} Z_h$$

We can express equation (5.4) in terms of these vector fields:

$$\begin{aligned}
u_t &= \sum_{i,j,h,k=1}^2 A_{ij}^0(B \nabla_{Heis} u) B_{ih} Z_h (B_{ik} Z_k) u = \quad (5.32) \\
&= \sum_{i,j,h,k=1}^2 A_{ij}^0(B \nabla_{Heis} u) B_{ih} B_{ik} Z_h Z_k u \\
&+ \sum_{i,j,h,k=1}^2 A_{ij}^0(B \nabla_{Heis} u) B_{ih} Z_h B_{ik} Z_k u =
\end{aligned}$$

Now we call

$$\begin{aligned}
C_{hk} &= \sum_{i,j=1}^2 A_{ij}^0(B \nabla_{Heis} u) B_{ih} B_{ik} \\
c_k &= \sum_{i,j,h=1}^2 A_{ij}^0(B \nabla_{Heis} u) B_{ih} Z_h B_{ik}
\end{aligned}$$

As a result equation (5.4) becomes:

$$u_t = \sum_{h,k=1}^2 C_{hk} Z_h Z_k u + \sum_{k=1}^2 c_k Z_k u.$$

The matrix  $C_{hk}$  is positive defined by construction, so that we can apply to this equation the analogous result proved in the Heisenberg setting in [11], which ensures that the two definitions of jet spaces viscosity solution and viscosity solution are equivalent.  $\square$

We will now prove that a vanishing viscosity solution is indeed a viscosity solution:

**Theorem 5.3.11.** Assume that  $u_0 \in C(\mathbb{R}^2 \times S^1)$  is continuous and satisfies (5.12). Then the vanishing viscosity solution detected in Theorem 5.3.6 is a viscosity solution  $u \in C^{1,0}$  of (5.4).

*Proof.* In order to prove that  $u$  is a viscosity solution we consider a function  $\phi \in C^\infty(\mathbb{R}^2 \times S^1 \times [0, \infty))$  and we suppose that  $u - \phi$  has a strict local maximum at a point  $(\xi_0, t_0) \in \mathbb{R}^2 \times S^1 \times [0, \infty)$ . Since  $u$  is a Lipschitz continuous vanishing viscosity solution, it can be uniformly approximated by solutions  $(u^k)$  of the approximating Riemannian problem (see also Theorem 5.3.11). As  $u^k \rightarrow u$  uniformly near  $(\xi_0, t_0)$ ,  $u^k - \phi$  has a local maximum at a point  $(\xi_k, t_k)$ , with

$$(\xi_k, t_k) \rightarrow (\xi_0, t_0) \quad \text{as } k \rightarrow \infty \quad (5.33)$$

Since  $u^k$  and  $\phi$  are smooth, we have

$$\nabla_E u^k = \nabla_E \phi, \quad \partial_t u^k = \partial_t \phi \quad \text{and} \quad D_E^2(u^k - \phi) \leq 0 \quad \text{at } (\xi_k, t_k)$$

where  $D_E^2$  is the Euclidean Hessian. Thus

$$\partial_t \phi - \left( \delta_{ij} - \frac{X_i^{\epsilon_k} \phi X_j^{\epsilon_k} \phi}{|\nabla_{\epsilon_k} \phi|^2 + \tau_k^2} \right) X_i^{\epsilon_k} X_j^{\epsilon_k} \phi \leq 0 \text{ at } (\xi_k, t_k) \quad (5.34)$$

This inequality can be equivalently expressed in terms of the coefficients  $A_{i,j}^{\epsilon_k, \tau_k}$  as follows. At the point  $(\xi_k, t_k)$

$$\begin{aligned} \partial_t \phi &- A_{i,j}^{\epsilon_k, \tau_k} (\nabla_{\epsilon_k} \phi) X_i^{\epsilon_k} X_j^{\epsilon_k} \phi & (5.35) \\ &\leq \partial_t u^k - A_{i,j}^{\epsilon_k, \tau_k} (\nabla_{\epsilon_k} u^k) X_i^{\epsilon_k} X_j^{\epsilon_k} (u^k + \phi - u^k) \leq 0 & (5.36) \end{aligned}$$

If  $\nabla_0 \phi(\xi_0, t_0) \neq 0$ , also  $\nabla_0 \phi(\xi_k, t_k) \neq 0$  for sufficiently large  $k$ . Then letting  $k \rightarrow \infty$  we obtain from (5.36):

$$\partial_t \phi \leq \sum_{i,j=1}^2 \left( \delta_{ij} - \frac{X_i^0 \phi X_j^0 \phi}{|\nabla_0 \phi|^2} \right) X_i^0 X_j^0 \phi \text{ at } (\xi_0, t_0) \quad (5.37)$$

which implies that  $u$  is a viscosity subsolution.

If  $\nabla_0 \phi(\xi_0, t_0) = 0$  then we set

$$\eta^k = \frac{\nabla_{\epsilon_k} \phi(\xi_k, t_k)}{\sqrt{|\nabla_{\epsilon_k} \phi(\xi_k, t_k)|^2 + \tau_k^2}}$$

There exists  $\eta \in \mathbb{R}^3$  such that  $\eta^k \rightarrow \eta$ . Note that

$$\begin{aligned} |(\eta^k)_3| &= \frac{\epsilon_k |X_3 \phi(\xi_k, t_k)|}{\sqrt{|\nabla_{\epsilon_k} \phi(\xi_k, t_k)|^2 + \tau_k^2}} \\ &\leq \frac{(\epsilon_k / \tau_k) |X_3 \phi(\xi_k, t_k)|}{\sqrt{(\epsilon_k / \tau_k)^2 \sum_{i=1}^2 (X_i^0 \phi(\xi_k, t_k))^2 + 1}} \end{aligned}$$

Since the expression vanishes as  $k \rightarrow \infty$  we have  $\eta_3 = 0$ . The PDE (5.36) now reads as:

$$\partial_t \phi(\xi_k, t_k) - \sum_{i,j=1}^3 (\delta_{ij} - \eta_i^k \eta_j^k) X_i^{\epsilon_k} X_j^{\epsilon_k} \phi(\xi_k, t_k) \leq 0$$

so as  $k \rightarrow \infty$  we obtain

$$\partial_t \phi(\xi_0, t_0) \leq \sum_{i,j=1}^2 (\delta_{ij} - \eta_i \eta_j) X_i^0 X_j^0 \phi(\xi_0, t_0) \quad (5.38)$$

concluding the proof for the case in which  $u - \phi$  has a local strict maximum at point  $(\xi_0, t_0)$ . If  $u - \phi$  has a local maximum, but not necessarily a strict local maximum at  $(\xi_0, t_0)$ , we can repeat the argument above replacing  $\phi(x_1, t)$  with

$$\tilde{\phi}(\xi, t) = \phi(\xi, t) + |\xi - \xi_0|^4 + (t - t_0)^4$$

again to obtain (5.37), (5.38). Consequently  $u$  is a weak subsolution. That  $u$  is a weak supersolution follows analogously.  $\square$

From the above result we can only say that there is a subsequence of  $u^{\epsilon, \tau, \sigma}$  which is convergent to the vanishing viscosity solution  $u$ . In order to prove the uniqueness of the vanishing viscosity solution, we would need the sub-Riemannian analogous of estimate established by Deckelnick and Dziuk in [46]:

**Proposition 5.3.12.** There exists a constant  $C > 0$  independent of  $\sigma, \tau$  and  $\epsilon$  such that:

$$\|u^{\epsilon, \tau, \sigma} - u\|_{\infty} \leq C\tau^{\alpha} \quad (5.39)$$

Letting  $\epsilon$  and  $\sigma$  go to 0 we also get:

$$\|u^{\tau} - u\|_{\infty} \leq C\tau^{\alpha} \quad (5.40)$$

where  $u^{\tau}$  is a solution of (5.7).

#### 5.4 Numerical scheme

In this part we provide the numerical approximation we used to implement the sub-Riemannian motion by curvature which performs inpainting and enhancement. Since our scheme is directly inspired by the classical one of Osher and Sethian (see [135]), we will explain how to adapt the discretization to the sub-Riemannian setting. The mean curvature flow (5.7) can be explicitly written as:

$$\begin{aligned} u_t = & \\ = & \frac{(X_2^0(u))^2 \cdot X_{11}^0(u) + (X_1^0(u))^2 \cdot X_{22}^0(u) - X_1^0(u)X_2^0(u) \cdot 2X_{12}^0(u)}{(X_1^0(u))^2 + (X_2^0(u))^2 + \tau} \\ & + \frac{X_1^0(u)X_2^0(u) \cdot [X_1^0, X_2^0](u)}{(X_1^0(u))^2 + (X_2^0(u))^2 + \tau} \end{aligned} \quad (5.41)$$

This equation presents two distinct terms: the first part of the flow presents second order derivatives and corresponds to the curvature term, the second one has only first order derivatives and correspond to the metric connection.

The solution  $u(x_1, x_2, \theta, t)$  is discretized on a regular grid with points  $x_{1,i} = i\Delta x_1, x_{2,j} = j\Delta x_2, \theta_k = k\Delta\theta$ , with time discretization  $t_s = s\Delta t$ . We will denote  $D^{+x_1}U(i, j, k, s), D^{-x_1}U(i, j, k, s), D^{0x_1}U(i, j, k, s)$  the forward, backward and central difference of a discrete function  $U$  at point  $(i, j, k, s)$  with respect to  $x_1$ , and use analogous notations for the other variables  $x_2$  and  $\theta$ . In terms of these derivatives we will define the analogous differences in the direction of the vector fields  $X_1^0$  and  $X_2^0$ . Precisely if we have discretized the direction  $\theta$  with  $K$  points, we will denote  $\theta_k = k\pi/K$  for  $k = 1, \dots, K$ , and we will call

$$D^{+X_1}U(i, j, k, s) = \cos \theta_k D^{+x_1}U(i, j, k, s) + \sin \theta_k D^{+x_2}U(i, j, k, s)$$

and analogously define backward and central difference  $D^{-X_1}$ ,  $D^{0X_1}$  for the vector  $X_1^0$  and for the vector  $X_2^0$ . Let us adapt the scheme proposed by Osher and Sethian in [135] to our case:

- (i) the first order term  $X_1^0(u)X_2^0(u) \cdot [X_1^0, X_2^0](u)$  is discretized using the upwind scheme for  $[X_1^0, X_2^0] = X_3$ . Taking into account the upwind scheme for the vector field  $X_3$ , the first order term is given by:

$$\begin{aligned} W^1(U) = & -\frac{\max(-\sin \theta_k D^{0X_1} U D^{0X_2} U, 0) D^{-x_1} U}{|D^{0X_1} U|^2 + |D^{0X_2} U|^2 + \tau} \quad (5.42) \\ & + \frac{\min(-\sin \theta_k D^{0X_1} U D^{0X_2} U, 0) D^{+x_1} U}{|D^{0X_1} U|^2 + |D^{0X_2} U|^2 + \tau} \\ & - \frac{\max(\cos \theta_k D^{0X_1} U D^{0X_2} U, 0) D^{-x_2} U}{|D^{0X_1} U|^2 + |D^{0X_2} U|^2 + \tau} \\ & + \frac{\min(\cos \theta_k D^{0X_1} U D^{0X_2} U, 0) D^{+x_2} U}{|D^{0X_1} U|^2 + |D^{0X_2} U|^2 + \tau}. \end{aligned}$$

- (ii) second order derivatives are implemented as usual as

$$D^{-X_1} D^{+X_1}, \quad D^{-X_2} D^{+X_2}, \quad D^{0X_1} D^{0X_2},$$

which lead to second order central finite difference. We will implement as central differences the first derivatives coefficients of  $D^{-X_1} D^{+X_1}$ ,  $D^{-X_2} D^{+X_2}$ . The first derivative with respect to  $X_1^0$ , coefficient of the second mixed derivative, will be upwinded as before. Generalizing an idea of [189], the denominator will be a mean of central derivatives:

$$\begin{aligned} |D_{int} U|^2(i, j, k, s) + \tau = & \frac{1}{3} \sum_{k_1 \in \{k-1, k, k+1\}} |D^{0X_1} U|^2(i, j, k_1, s) \\ & + \frac{1}{5} \sum_{i_1 \in I} |D^{0X_2} U|^2(i_1, j_1, k, s) + \tau, \end{aligned}$$

where  $I$  is the family of indices

$$I = \{(i-1, j), (i, j), (i+1, j), (i, j-1), (i, j+1)\}.$$

The second order discretized operator will be denoted

$$W^2(U)(i, j, k, s).$$

The difference equation associated to the continuous equation (5.41) will be expressed as:

$$\begin{aligned} U(i, j, k, s+1) = & U(i, j, k, s) + \Delta t (W^2 U)(i, j, k, s) \\ & + \Delta t (W^1 U)(i, j, k, s) \end{aligned}$$

with initial condition  $U(., 0) = U_0$ . We recall that convergence of difference schemes for the mean curvature flow inspired by

the scheme of Osher and Sethian has been object of a large number of papers in the Euclidean setting. The stability of one of them was proved in [189]. Another monotone scheme was proposed by Crandall and Lions (see [35]) and its convergence was proved by Deckelnick in [45] and Deckelnick & Dziuk in [46]. The ideas at the basis of the stability proof of [189] can be extended to the present version of the Osher and Sethian scheme, leading to the following result:

**Theorem 5.4.1.** The difference scheme presented above is stable in the sense that if  $\Delta t \leq \frac{h^2}{10}$ , then

$$\|U\|_\infty \leq \|U_0\|_\infty$$

*Proof.* If  $U$  is a solution of the discrete equation, also  $V = U - \|U_0\|_\infty$  is a solution of the same equation:

$$\begin{aligned} V(i, j, k, s + 1) &= V(i, j, k, s) + \Delta t(W^2V)(i, j, k, s) \\ &\quad + \Delta t(W^1V)(i, j, k, s). \end{aligned}$$

Hence  $V(0) \leq 0$ , and we have to prove  $V \leq 0$ , for all time. In order to study the term  $W^1(V)$  we have to discuss the sign of  $a_1 = -\sin \theta_k D^{0X_1} V D^{0X_2} V$  and  $a_2 = \cos \theta_k D^{0X_1} V D^{0X_2} V$ : we will assume that they are both positive since the proof is similar in all the other cases: In this case

$$\begin{aligned} (W^1V)(i, j, k, s) &= -\frac{a_1(V(i, j, k, s) - V(i-1, j, k, s))}{|D^{0X_1}V|^2 + |D^{0X_2}V|^2 + \tau} \\ &\quad + \frac{a_2(V(i, j, k, s) - V(i, j-1, k, s))}{|D^{0X_1}V|^2 + |D^{0X_2}V|^2 + \tau} \\ &\leq -\frac{(\cos(\theta_k) - \sin(\theta_k))D^{0X_1}V(i, j, k, s)D^{0X_2}V(i, j, k, s)}{(|D^{0X_1}V|^2 + |D^{0X_2}V|^2 + \tau)h^2}V(i, j, k, s) \\ &\leq -\frac{V(i, j, k, s)}{2h^2} \end{aligned}$$

Analogously, having upwinded the coefficient of  $(W^2V)(i, j, k, s)$ , we get a similar behavior. The mixed derivatives term can be estimated as:

$$-\frac{2 \cos \theta_k D^{0X_1}(D^{0X_2})VD^{0X_2}V}{|D_{int}V|^2 + \tau}V(i, j, k, s) \leq -\frac{10V(i, j, k, s)}{h^2}.$$

In conclusion

$$V(i, j, k, s + 1) \leq V(i, j, k, s)\left(1 - \frac{10\Delta t}{h^2}\right) \leq 0.$$

The assertion then follows by induction.  $\square$

Now we recall that the equation is uniformly parabolic in the sub-elliptic sense. Arguing as in [46] the estimates of 4th order

derivatives can be reduced to the estimates of graphs over the considered group. Hence estimates can be obtained by a recent result of Capogna, Citti and Manfredini (see [24]). Since for  $\tau$  fixed the equation is uniformly parabolic in the sub-elliptic sense, these estimates allow to prove that:

**Theorem 5.4.2.** If  $u^\tau$  is the solution of (5.7) with initial condition  $u_0$  and  $U$  is the solution of the discrete scheme considered here and  $\alpha$  is fixed, there exist a constant  $C = C(\tau, h, \alpha)$  such that if  $\Delta t \leq C(\tau, h)$ , then

$$|u^\tau(i\Delta x_1, j\Delta x_2, k\Delta\theta, s\Delta t) - U(i, j, k, s)| \leq \tau^\alpha,$$

As a consequence, applying the uniqueness Theorem 5.3.12, we deduce the following convergence result for the solution of the mean curvature equation (5.4) with initial condition  $u_0$

$$|u(i\Delta x_1, j\Delta x_2, k\Delta\theta, s\Delta t) - U(i, j, k, s)| \leq \tau^\alpha$$

as  $\Delta t \leq C(\tau, h)$ .

## 5.5 Results

In this section we present and discuss our results. We first compare the results obtained with the original algorithm [28] with some results recently appeared in the literature. Results of our new model for enhancement are proposed and compared with previous results of Duits and Franken [54]. Finally we show examples of inpainting and enhancement of images.

### 5.5.1 Inpainting results

In all the upcoming numerical experiments we have discretized the angular coordinate  $\theta$  in 32 different orientations (see Section 5.4). The evolution time (or equivalently the number of iterations of the discrete versions) for both the mean curvature flow (5.4) and the Laplace-Beltrami flow (5.6) have been set long enough so that a steady solution is ensured. Our algorithm performs particularly well for completing gray level images which have non vanishing gradient at every point. We start with a couple of images already contained in [150]: an artificial one (see figures 5.8), and a natural one (see figure 5.8, bottom). In both images a very big black hole is present, and the algorithm correctly reconstructs the missed part of the image.

Recently Boscaïn et al. in [14] tried to replace this non linear equation by a diffusion followed by a ‘heuristic complement’. In figure 5.9 left we consider an image from [14] partially occluded by a grid: first we show the results of completion per-

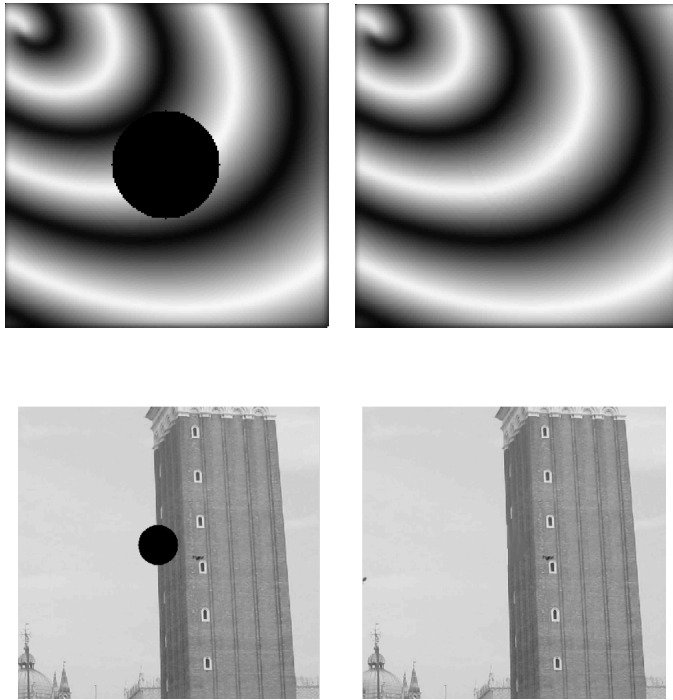


Figure 5.8: Top: An example of completion performed by the algorithm. In this artificial image the image gradient is lifted in the  $\mathbb{R}^2 \times S^1$  space and the black hole is completed by mean curvature flow. Since the level lines of the image are approximately circular, the algorithm performs very well. Bottom: completion result on a real image through sub-Riemannian mean curvature flow in  $\mathbb{R}^2 \times S^1$ , as described in [30].

formed in [14] (second image from left), then the results obtained through the heat equation in the 2D space (third image from left) and finally the ones obtained with Citti and Sarti model (right). A detail is shown in figure 5.10. Since the considered image is a painting, extremely smooth, with low contrast, the 2D heat equation is able to perform a simple version of completion (see for example [10]). The curvature model reconstructs correctly the missed contours and level lines, and presents a strong completion capability, absent in the other two methods. In figure 5.11 (and in the detail taken from it in fig-

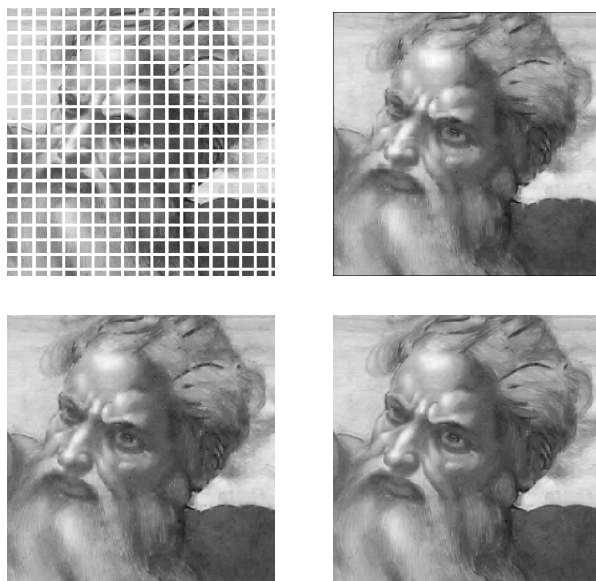


Figure 5.9: Left: an occluded image (from U. Boscain et al. ([14])). Second image from left: the image processed in ([14]). Third image from left: the same image processed through the heat equation. Right: the image inpainted using Citti and Sarti algorithm.

ure 5.12) we consider an other example taken from the same paper. In this image the grid of points which are missed is larger, and the previous effect is even more evident. In a more

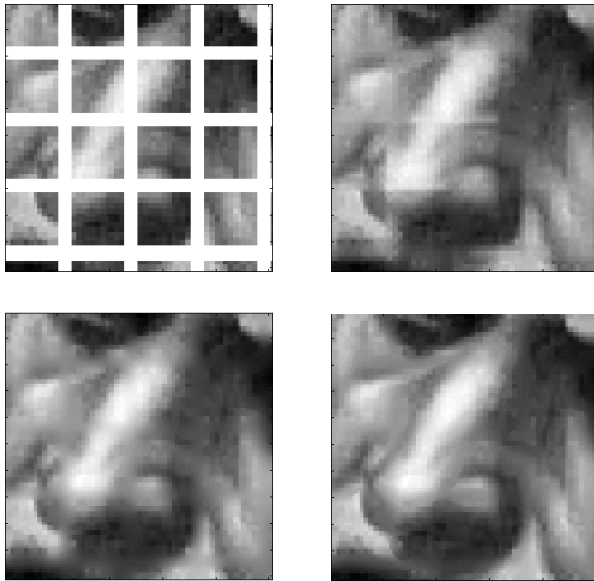


Figure 5.10: A detail of previous image: Left: the original image ([14]); Second image from left: the image processed in ([14]); Third image from left: the image processed through the heat equation; Right: image inpainted using the proposed algorithm.

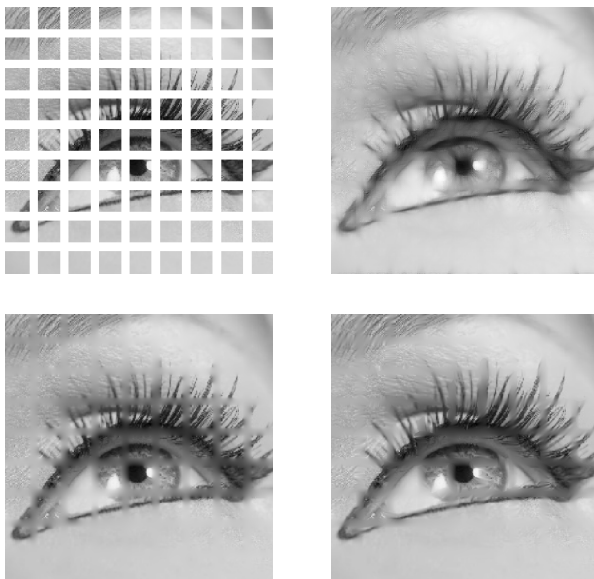


Figure 5.11: From left to right: the original image ([14]); the image processed in ([14]); the image processed through the heat equation; the image inpainted using the proposed algorithm.

recent paper Prandi et al. (see [15]) introduced a linear diffusion with coefficients depending on the gradient of the initial image, which they call ‘heuristic’. In figure 5.13 we compare the results obtained with this model, with the heat equation on the image plane and with the strongly geometric model of Citti and Sarti. Then we test our implementation on piecewise constant images. Since the gradient is 0 in large part of the image, the lifted gradient is not defined in the largest part of the image. On the other side, since the lifting mimics the behavior of the simple cells of the V1 cortical layer, the Citti and Sarti algo-

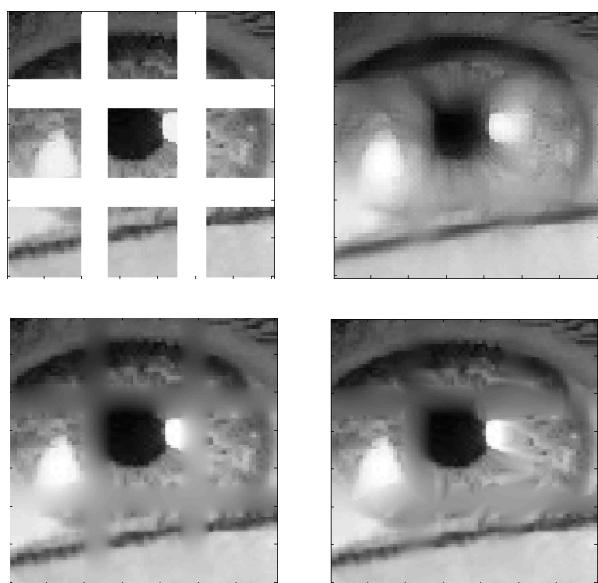


Figure 5.12: A detail of previous image. Left: the original image ([14]); second image from left: the image processed in ([14]); third image from left: the image processed through the heat equation; right: image inpainted using the original algorithm of Citti and Sarti.

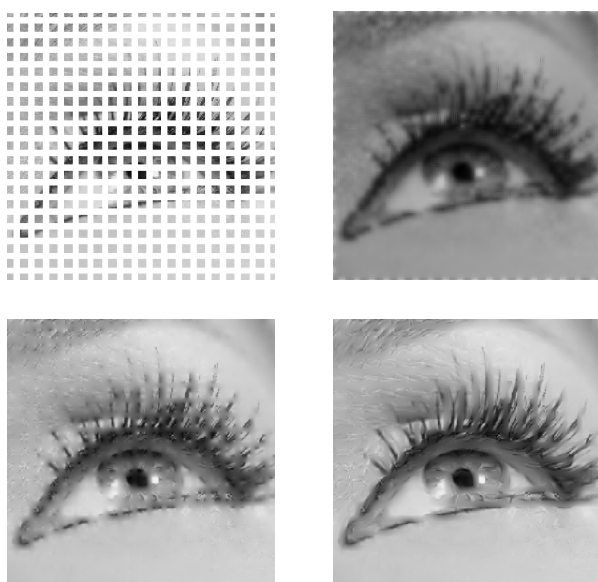


Figure 5.13: On the left the occluded image. From left to right: results from [15], with 2D heat equation and our model.

rithm is always applied on a smoothed version of the image. We have applied it on a classical toy problem proposed for example in [9] by Bertalmio, Sapiro, Caselles and Ballester. Results are shown in figure 5.14. In figure 5.15 we test our method on



Figure 5.14: Inpainting a constant coefficient image with the Sarti and Citti algorithm.

an image taken from the survey [10]. The present reconstruction is correct in the part of the image characterized by strong boundaries, but the results of [10] obtained with the model of Masnou and Morel (see [115]) seems to be better. The main point is the boundary detection, which is very accurate in the model of Masnou and Morel, while here the boundaries are detected with a gradient, after smoothing the image.



Figure 5.15: Left the occluded image. Center: image from [10] processed with the model of [115]. Right: image processed with our model.

### 5.5.2 Enhancement results

We will show in this section results of the application of the enhancement method we have introduced in Section 5.2.5. Let us recall that enhancement consists in an image filtering that underlines directional coherent structures. With respect to the completion problem there is no part of the image to be disclosed and all the parts of the initial data are evolved. In Figure 5.16 it is shown a microscopy image of bone tissue to be filtered to reconstruct the crossing fibers (from Duits and Franken([54]). The second image from left shows the enhancement computed by using CED-OS, see [54, 71], while the third image shows the result obtained using the proposed method. Finally, we show in figure 12 (zoomed in figure 13) an example combining the techniques of completion and enhancement. We see in this case that enhancement homogenizes the original non occluded part with the reconstructed one. Here we

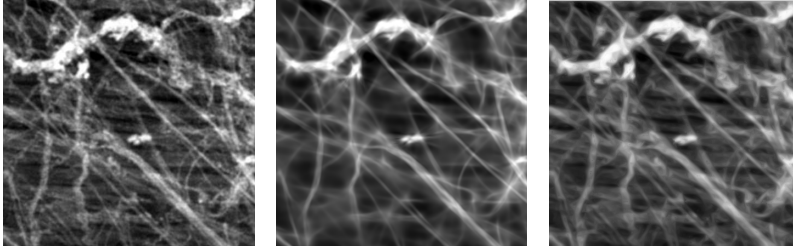


Figure 5.16: From left to right: the original image, from Duits and Franken ([54, Fig. 7]); the enhanced image using CED-OS, see [54]; the enhanced image obtained using the proposed method.



Figure 5.17: Left: the original image ([14]). Center: image inpainted using the proposed algorithm. Right: image inpainted and enhanced with this algorithm.

propose a detail of the previous image in order to underline the effects of the discussed techniques.

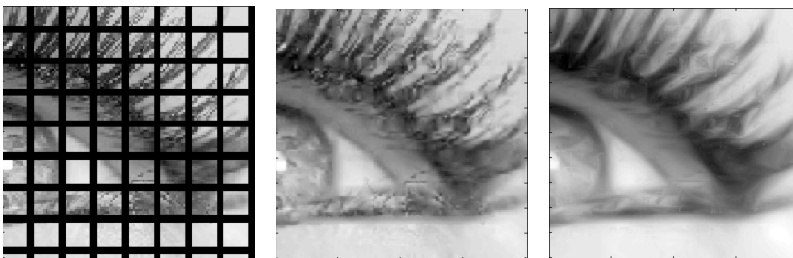


Figure 5.18: From left to right: a detail of the original image ([14]); a detail of the image inpainted using the proposed algorithm; same detail of the image inpainted and enhanced with this algorithm.

## 5.6 Discussion

In this chapter we have proved existence of viscosity solutions of the mean curvature flow PDE in  $SE(2) = \mathbb{R}^2 \times S^1$  equipped with a sub-Riemannian metric. The flow has been implemented with a suitable adaptation of the Osher and Sethian technique [135] and a sketch of the proof of convergence of the numerical scheme is provided. Results of completion and enhancement are obtained on artificial and natural images both. We also provide comparisons with other existing algorithms. The algorithm leads to results comparable with the classical ones of Bertalmio et al. in [9], of Masnou and Morel in [115], but performs much better than the results shown by Boscain et al. in [14], or by Prandi et al. [15]. The method can be applied in presence of crossing edges and to perform enhancement: our results have been compared with the previous of Duits et al. [55].



## 6 Geometrical optical illusions

IN THIS CHAPTER we introduce a neuro-mathematical model for Geometrical Optical illusions, based on the cortical based model introduced in chapter 4. Geometrical-optical illusions (GOIs) have been discovered in the XIX century by German psychologists (Oppel 1854 [134], Hering, 1878, [83]) and have been defined as situations in which there is an awareness of a mismatch of geometrical properties between an item in object space and its associated percept [185]. The distinguishing feature of these illusions is that they relate to misjudgements of geometrical properties of contours and they show up equally for dark configurations on a bright background and viceversa. An historical survey of the discovery of geometrical-optical illusions is included in Appendix I of [185]. The reason why we should be interested generally in illusory phenomena has been well explained by Eagleman in [57]:

“The historical study of systematic misperceptions, combined with a recent explosion of techniques to measure and stimulate neural activity, has provided a rich source for guiding neurobiological frameworks and experiments.”

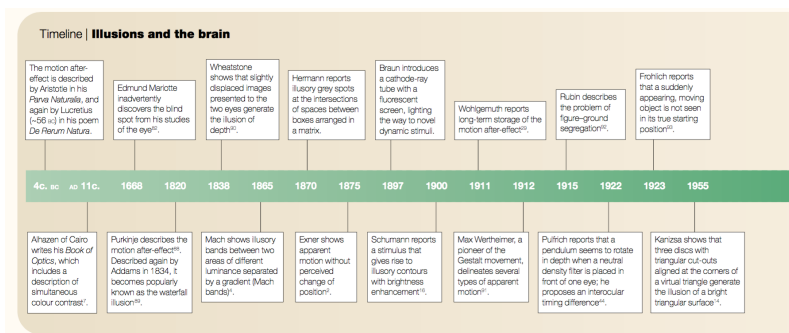


Figure 6.1: In [57] Eagleman provided an historical summary in which he pointed how the link between Illusory phenomena and the relevance they had in guiding researches in neuroscience. In this image we present the first part. See next pages for the following, figure 6.1.

Our intention here is not to make a classification of these phenomena, which is already widely present in literature (Coren e Girgus, 1978, [32]; Robinson, 1998, [144]; Wade, 1982, [171]). The aim of this chapter is to propose a mathematical model for

GOIs based on the functional architecture of low level visual cortex (V1/V2). This neuro-mathematical model will allow us to interpret at a neural level the origin of GOIs and to reproduce the arised percept for this class of phenomena. The main idea is to adopt the model of the functional geometry of V1 provided in [28] and presented in chapter 4, and to consider that the image stimulus will modulate the connectivity. When projected onto the visual space, the modulated connectivity gives rise to a Riemannian metric which is at the origin of the visual space deformation. The displacement vector field at every point of the stimulus is mathematically computed by solving a Poisson problem and the perceived image is finally reproduced. The considered phenomena consist, as shown in figure 6.3, in straight lines over different backgrounds (radial lines, concentric circles, etc). The interaction between target and context either induces an effect of curvature of the straight lines (fig. 6.3, (a), (b), (c) ), eliminates the bending effect (fig. 6.3, (d)), or induces an effect of unparallelism (fig. 6.3, (e)). This chapter is or-

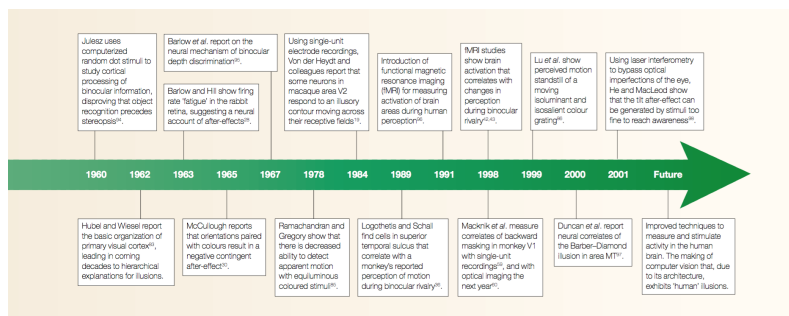
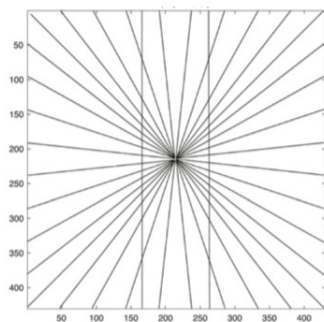
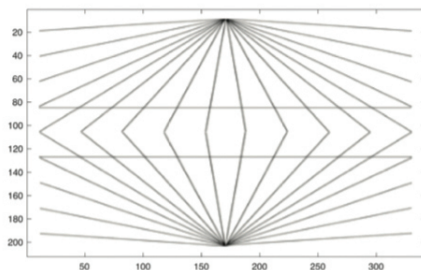


Figure 6.2: Second part of the timeline, from figure 6.1: in [57] Eagleman provided an historical summary in which he pointed how the link between Illusory phenomena and the relevance they had in guiding researches in neuroscience.

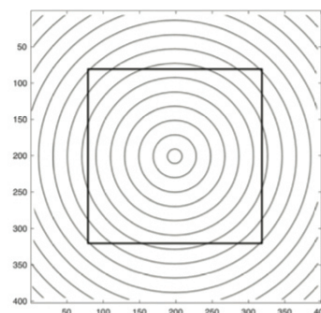
ganised as follows: in section 2.1.3 geometrical optical illusions are presented from the neurophysiological and phenomenological point of view. In section 6.2 previous mathematical models for GOIs are presented. The state of the art for what concerns mathematical modeling will be reviewed. In 6.3.1 starting from the cortical based model introduced in chapter 4 a neuro-mathematical model for GOIs will be proposed, taking into account the modulation of the functional architecture induced by the stimulus. Finally in 6.4 the numerical implementation of the mathematical model will be explained and applied to a number of examples. Results are finally discussed as well as conclusions and perspectives of this work. The contributions developed in this chapter are published in the following papers by the author et al. [69, 68].



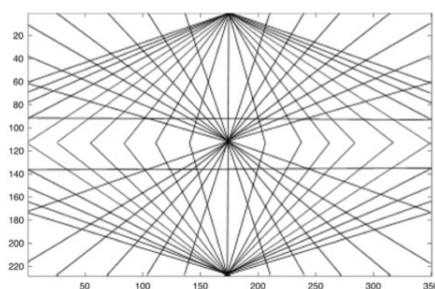
(a) Hering illusion



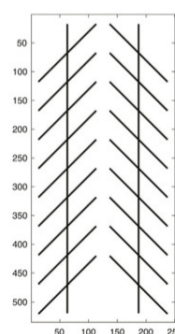
(b) Wundt Illusion



(c) Square in Ehrenstein context



(d) Wundt-Hering illusion



(e) Zollner illusion

Figure 6.3: (a) Hering illusion: the two vertical lines are straight and parallel, but since they are presented in front of a radial background the lines appear as if they were bowed outwards. (b) Wundt-Illusion: the two horizontal lines are both straight, but they look as if they were bowed inwards. (c) Square shape over Ehrenstein context: the context of concentric circles bends the edges of the square toward the center of the image. (d) Wundt-Hering illusions merged together: the horizontal lines are straight and parallel and the presence of inducers which bow them outwards and inwards at the same time inhibits the bending effect. (e) Zollner illusion: a pattern of oblique inducers surrounding parallel lines creates the illusion they are unparallel.

## 6.1 Role of Geometrical optical illusions (GOIs)

The importance of this study, particularly focused on GOIs, lies in the possibility, through the analysis of these phenomena combined with physiological recordings, to help to guide neuroscientific research (Eagleman, [57]) in understanding the role of lateral inhibition, feedback mechanisms between different layers of the visual process and to lead new experiments and hypothesis on receptive fields of V1 and V2. Many studies, which relies on neuro-physiological and imaging data, show the evidence that neurons in at least two visual areas, V1 and V2, carry signals related to illusory contours, and that signals in V2 are more robust than in V1 ([168, 127], reviews [57, 126]), see figure 6.4 from [126]. A more recent study on the tilt illusion, see

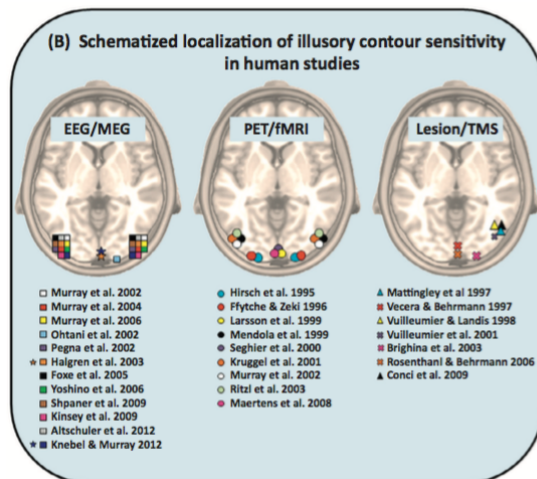


figure 6.5, in which the perceived orientation of a grating differs from its physical orientation when surrounded by a tilted context, measured the activated connectivity in and between areas of early visual cortices ([161]). These findings suggest that for GOIs these areas may be involved as well. Neurophysiology can help to provide a physical basis to phenomenological experience of GOIs opening to the possibility of mathematically modeling them and to integrate subjective and objective experiences.

## 6.2 Mathematical models proposed in literature

The pioneering work of Hoffman [85] dealt with illusions of angle (i.e. the ones involving the phenomenon of acute-angle expansion, which is the tendency to perceive under certain conditions acute angles as larger) modeling the generated perceived curves as orbits of a Lie group acting on the plane. The proposed model allows to classify the perceptual invariance of the

Figure 6.4: Quoting from Murray and Herrmann [126]: (B) Schematic localization of Illusory contours (IC) sensitivity in human studies. The colored symbols indicate the approximate locations of IC sensitivity for human studies using electroencephalography (EEG)/magnetoencephalography (MEG) source estimations (left), positron emission tomography (PET) and functional magnetic resonance imaging (fMRI) (middle), and lesion studies or transcranial magnetic stimulation (TMS) (right). The stars in the left panel indicate secondary and subsequent effects.

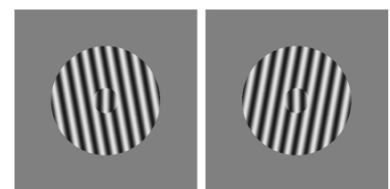


Figure 6.5: The tilt illusion: the perceived orientation of a test line or grating is altered by the presence of surrounding lines or grating with a different orientation (spatial context).

considered phenomena in terms of Lie Derivatives, and to predict the slope. Another model mathematically equivalent to the one proposed by Hoffman has been proposed by Smith, [160], who stated that the apparent curve of geometrical optical illusions of angle can be modeled by a first-order differential equation depending on a single parameter. By computing this value an apparent curve can be corrected and plotted in a way that make the illusion being not perceived anymore (see for example fig. 8 of [160]). This permits to introduce a *quantitative* analysis of the perceived distortion. Ehm and Wackerman in [58], started from the assumption that GOIs depend on the context of the image which plays an active role in altering components of the figure. On this basis they provided a variational approach computing the deformed lines as minima of a functional depending on length of the curve and the deflection from orthogonality along the curve. This last request is in accordance to the phenomenological property of regression to right angle. One of the problems pointed out by the authors is that the approach doesn't take into account the underlying neurophysiological mechanisms. This model will be discussed later on, in chapter 7. An entire branch for modeling neural activity, the Bayesian framework, had its basis in Helmholtz's theory [170]: *our percepts are our best guess as to what is in the world, given both sensory data and prior experience*. The described idea of unconscious inference is at the basis of the Bayesian statistical decision theory, a principled method for determining optimal performance in a given perceptual task ([76]). These methods consists in attributing a probability to each possible true state of the environment given the stimulus on the retina and then to establish the way prior experience influences the final guess, the built proximal stimulus (see [102] for examples of Bayesian models in perception). An application of this theory to motion illusions has been provided by Weiss et al in [183], and a review in [76]. Fermüller and Malm in [62] attributed the perception of geometric optical illusions to the statistics of visual computations. Noise (uncertainty of measurements) is the reason why systematic errors occur in the estimation of the features (intensity of the image points, of positions of points and orientations of edge elements) and illusions arise as results of errors due to quantization. Walker ([173]) tried to combine neural theory of receptive field excitation together with mathematical tools to provide an equation able to determine the disparity between the apparent line of an illusion and its corresponding actual line, in order to reproduce the perceptual errors that occur in GOIs (the ones involving straight lines). In our model we aim to combine psycho-physical evidence and neurophysiological

findings, in order to provide a neuro-mathematical model able to interpret and simulate GOIs.

**Scope of the chapter** The contribution of this chapter is to introduce a mathematical model which takes into account the cortical activation of simple cells in V1 and V2. The modulated connectivity in the cortex is projected onto the visual space and gives rise to a Riemannian metric, at the basis of the visual deformation. Our intention is to interpret the new metric in the infinitesimal strain theory framework to compute the displacement vector field solving a Poisson problem which arises from the proposed model. The proximal stimulus is finally recovered.

### 6.3 A neuro-mathematical model for GOIs

#### 6.3.1 From the classical neuromathematical model for V1-V2

In chapter 4 we saw the expression for the sub-Riemannian metric  $(g_{ij})_{i,j=1,2,3}$  which models the connectivity patterns in the primary visual cortex, as proposed by Citti and Sarti in [28]. The functional architectures built in  $\mathbb{R}^2 \times S^1$  correspond to the neural connectivity measured by Angelucci et al. in [1] and Bosking et al. in [16]. A qualitative and quantitative comparison between the kernels and the connectivity patterns has been done by Favali et al. in [60]. In this contribution a local formulation of the kernel presented in [60] will be used: in [60] the connectivity is modelled with the sub-Riemannian heat kernel with minima defined by the distributional lift [28],  $(x_1, x_2, \bar{\theta})$  where  $\bar{\theta}$  is the lifted orientation.

Here we consider just the restriction of the heat kernel to the point  $(x_1, x_2)$  by varying the orientation  $\theta$ . It corresponds to  $\exp\left(\frac{-\sin(\theta-\bar{\theta})^2}{2\sigma}\right)$ , expressing the local polarization of the horizontal connectivity, well estimated by the energy in (6.1). In figure 6.6 the local polarization of the hypercolumn is shown: for each  $(x_1, x_2, \theta)$  the corresponding value of  $\exp\left(\frac{-\sin(\theta-\bar{\theta})^2}{2\sigma}\right)$  weights the sub-Riemannian metric  $(g_{ij})_{i,j=1,2,3}$ . We will see in section 6.3.2 how the Riemannian metric is introduced. Let us remark that it has been shown by Sanguinetti et al. in [151] that the geometry of functional architecture formally introduced in chapter 4 is naturally encoded in the statistics of natural images. Hence these geometrical structures are compatible with Bayesian learning methods.

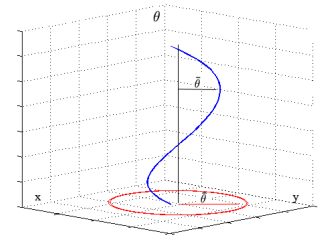


Figure 6.6: Representation of the orientation response  $\exp\left(\frac{-\sin(\theta-\bar{\theta})^2}{2\sigma}\right)$  over each fiber, with maximum activity registered in  $\bar{\theta}$ .

### 6.3.2 Output of Simple Cells and connectivity metric

We will now define a connectivity metric tensor on the image plane  $\mathbb{R}^2$  starting from the connectivity metric  $(g_{ij})_{i,j=1,2,3}$  and the output of simple cells. Let us first recall other interesting techniques for extracting local features of images: first the more recent, tensor voting, by Medioni [117], [124], which propagates contour saliency information from input points to their neighbors through tensor fields, providing with a completion technique. An extension of Medioni's work has been provided in [72], where tensor voting is implemented based on steerable filters theory. The already well-known structure tensor, present in literature and directly inspired by the structure of the image, has been introduced in its linear formulation by Förstner and Gülch in [64] (1987) and by Bigün et al. in [12] (1987). It encodes local gradient features of a processed image and the application of a Gaussian convolution averages the information within a neighborhood, allowing to perform orientation estimation, optic flow computation, corner detection, etc. Steps forward to overcome limitations due to the linear approach have been proposed by Weickert [176] (1998) and Brox et al. in [17] (2006). Weickert replaced Gaussian smoothing with non-linear diffusion techniques, which adapt tensor to the original data respecting discontinuities. He also pointed out that new filter models would allow to accomplish tasks in image processing which involve semi-local or global information. Here we build a modified structure tensor: it would give very similar results to the one in [176] in case of using only odd Gabor filters ([28]). Our images are composed by lines, they are not cartoon images, hence we need a technique able to correctly measure  $\theta$  for contours and lines: this is the reason why we combine odd and even Gabor filters. Another point is that in our tensor, we do not normalize over the gradient as in [176]. Finally we propose a tensor biologically based, since it encodes the action of Gabor filters and the cortical connectivity. We consider simple cells at fixed value of  $\sigma$  depending on position and orientation. For each point  $(x_1, x_2, \theta) \in \mathbb{R}^2 \times S^1$ , we restrict the connectivity tensor  $(g^{ij}(x_1, x_2, \theta))_{i,j=1,2,3}$  to the  $\mathbb{R}^2$  plane generated by  $\{\partial_{x_1}, \partial_{x_2}\}$ , subset of the tangent space to  $\mathbb{R}^2 \times S^1$  at the point  $(x_1, x_2, \theta)$ , and obtain the tensor

$$\begin{pmatrix} \cos^2 \theta & \sin \theta \cos \theta \\ \sin \theta \cos \theta & \sin^2 \theta \end{pmatrix}.$$

The metric  $(g^{ij})_{i,j=1,2,3}$  is invariant for rotation and translation, then we can fix a point without loss of generality. For every value of  $\theta$  this tensor has only one non zero eigenvalue. The

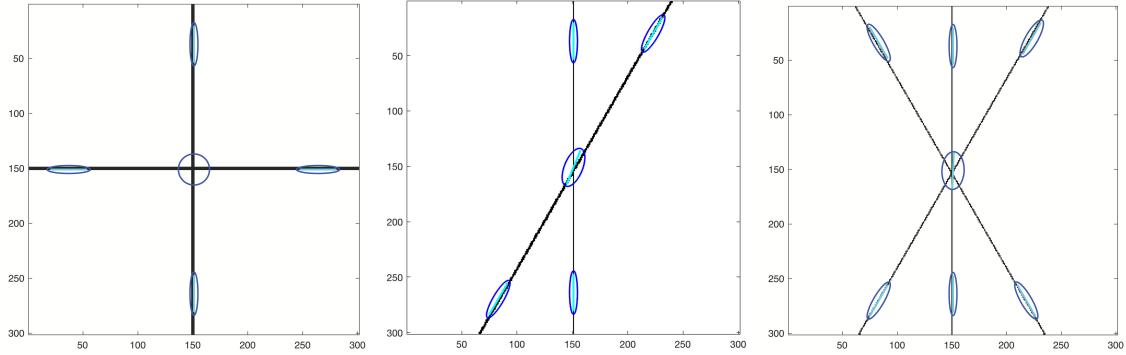


Figure 6.7: Representation of  $\mathbf{p}^{-1}$  (blue). Principal and second eigenvectors correspond to first and second semi-axes of the ellipses. Lengths of the semi-axes is given by the magnitude of the corresponding eigenvalues. Principal eigenvectors of ellipses are oriented along the maximum activity registered at  $\bar{\theta}$  over each point  $(x_1, x_2)$ , marked in cyan vector. Along part of the stimulus strongly oriented, ellipses are elongated. At the crossing point the orientation of the tensor, resulting by the vectorial sum of the orientations of the orthogonal lines, will be ball, with no preferred orientation. The tensor at the crossing point of two non-orthogonal lines is no more rounded, and will have a preferred orientation (vectorial sum of the orientations of the two crossing lines). The previous observation is amplified if we consider three crossing lines

corresponding eigenvector has orientation  $\theta$ . We will assign to the norm of the output the usual meaning of energy

$$E(x_1, x_2, \theta) = \|O(x_1, x_2, \theta)\|, \quad (6.1)$$

where  $\|\cdot\|$  denotes the complex modulus of the output  $O$  defined in (4.3), which is evaluated at the fixed value of  $\sigma$ . We will discuss in section 6.3.4 the choice of  $\sigma$  for our experiments. Each point of the hypercolumn is weighted by the energy of simple cells normalized over the whole set of hypercolumn responses:

$$\frac{E(x_1, x_2, \theta)}{\int_0^\pi E(x_1, x_2, \theta) d\theta}. \quad (6.2)$$

The normalization of the output expresses the probability that a specific cell sensitive to  $\theta$  within the hypercolumn over  $(x_1, x_2)$  is selected. The mechanism of intracortical selection attributing a probability to each possible orientation given the initial stimulus is connected to the long-range activity: simple cells belonging to different hypercolumns in a neighbourhood of a point  $(x_1, x_2)$  sensitive to the same orientation will have a high probability. The connectivity tensor restricted to the  $\mathbb{R}^2$  plane and modulated by the output of simple cells will become:

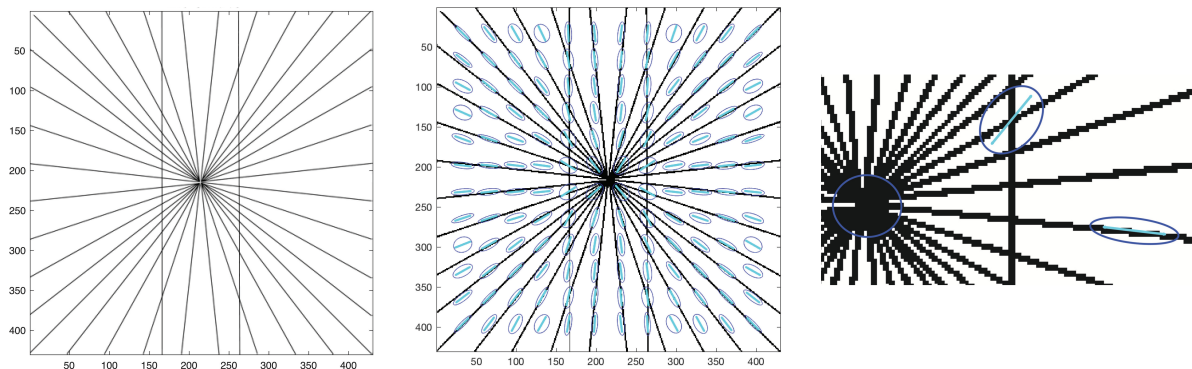
$$\frac{E(x_1, x_2, \theta)}{\int_0^\pi E(x_1, x_2, \theta) d\theta} \begin{pmatrix} \cos^2 \theta & \sin \theta \cos \theta \\ \sin \theta \cos \theta & \sin^2 \theta \end{pmatrix}. \quad (6.3)$$

This last expression corresponds to a connectivity polarized by the normalized energy of simple cells shown in (6.2) at points  $(x, y, \theta)$ . From the mathematical point of view it is the pull-back onto the  $\mathbb{R}^2$  of  $g^{ij}$ , weighted by the energy. The overall cometric (inverse of the metric tensor) arising from the action within the hypercolumn over each retinal point  $(x_1, x_2)$  is obtained summing up along  $\theta$  the previous modulated metric in

(6.3) and will have the following expression:

$$\mathbf{p}^{-1}(x_1, x_2) = \gamma^{-1} \frac{\int_0^\pi E(x_1, x_2, \theta) \begin{pmatrix} \cos^2 \theta & \sin \theta \cos \theta \\ \sin \theta \cos \theta & \sin^2 \theta \end{pmatrix} d\theta}{\int_0^\pi E(x_1, x_2, \theta) d\theta}, \quad (6.4)$$

where  $\gamma^{-1}$  is a normalization constant obtained as the  $L^\infty$  norm of the inverse of the determinant of the metric which appears in (6.4). This tensor will have principal eigenvector along the ori-



entation  $\bar{\theta}$ , corresponding to the maximum energy within the hypercolumn. A visualization of  $\mathbf{p}^{-1}$  is given in figure 6.7 and 6.8. Hence this process describes the selection at every point  $(x_1, x_2)$  of the most likely orientation of propagation of the connectivity, expressed by the values attained by the energy.

### 6.3.3 From metric tensor field to image distortion

In the previous section we described the response of the cortex in the presence of a visual stimulus.

- (1) The distal stimulus is projected onto the cortex by means of activity of simple cells.
- (2) The joint action of the short and long range connectivity induces a Riemannian tensor  $\mathbf{p}^{-1}$  on the  $\mathbb{R}^2$  retinal plane.

Even though it is not completely clear in which cortical area the perceived image is reconstructed, from a phenomenological point of view it is evident that our visual system reconstructs the perceived image. Hence a third mechanism takes place, able to construct the perceived stimulus from the cortical activation. With this mechanism the image distortion which induces the metric tensor  $\mathbf{p}$  (inverse of  $\mathbf{p}^{-1}$ ) is estimated. Here we propose to apply infinitesimal strain theory and to identify its inverse  $\mathbf{p}$  with the strain tensor to compute the deformation. Once the

Figure 6.8: Proximal stimulus (Hering illusion). Representation of  $\mathbf{p}^{-1}$  (blue). Principal and second eigenvectors correspond to first and second semi-axes of the ellipses. Lengths of the semi-axes is given by the magnitude of the corresponding eigenvalues. Principal eigenvectors of ellipses are oriented along the maximum activity registered at  $\bar{\theta}$  over each point  $(x_1, x_2)$ , marked in cyan vector. Here we show a detail of the tensor field representation: we notice that along parts of the stimulus strongly oriented, ellipses are elongated. As far as we move toward crossing points, ellipses lost their elongated form and become less or more rounded, in dependence with the orientation response of lines at crossing points

displacement vector field is applied to the distal stimulus, we obtain a distorted image which models the proximal one. In this way we justify the mechanism at the basis of geometrical optical illusions. The mechanism of reconstruction of the image at a neuro-physiological level is still an open problem. Although the cortex with its complete set of Gabor filters would be able to reconstruct the image (Lee et al. [109]), it is not clear if the cortex accomplishes this task and we did not take into account this process. We considered just the capability of the cortex to generate a Riemannian metric which is able to deform the image, without considering its reconstruction. We simply apply the deformation vector field to the original image. In this approach we consider the medium to be subjected only to small displacements, i.e. the geometry of the medium and its constitutive properties at each point of the space are assumed to be unchanged by deformation.

#### Strain tensor - displacement vector field

The mathematical question is how to reconstruct the displacement starting from the strain tensor  $\mathbf{p}$ . We think at the deformation induced by a geometrical optical illusion as an isometry between the  $\mathbb{R}^2$  plane equipped with the metric  $\mathbf{p}$  and the  $\mathbb{R}^2$  plane with the Euclidean metric  $\mathbf{Id}$ :

$$\Phi : (\mathbb{R}^2, \mathbf{p}) \rightarrow (\mathbb{R}^2, \mathbf{Id}).$$

From the mathematical point of view this means that we look for the change of variable which induces the new metric (see Jost [99]), i.e.

$$\left( \frac{\partial \Phi^k}{\partial x_i} \right) Id_{kl} \left( \frac{\partial \Phi^l}{\partial x_j} \right) = p_{ij}(x), \quad (6.5)$$

where  $x = (x_1, x_2) \in \mathbb{R}^2$ ,  $p_{ij}$  and  $Id_{kl}$  indicate the components of tensor  $\mathbf{p}$  and the identity  $\mathbf{Id}$  respectively and we use Einstein summation convention. Using this expression, we obtain:

$$\mathbf{p}(x) = (\nabla \Phi)^T (\nabla \Phi). \quad (6.6)$$

Let us notice  $\mathbf{p}^{-1}$  corresponds to  $\Phi^{-1}$ , the map representing the process which builds the modulated connectivity we discussed before. In strain theory  $\mathbf{p}$  satisfying (6.6) is called *right Cauchy-Green tensor* associated to the deformation  $\Phi$ , which from the physical point of view is a map  $\Phi : \bar{\Omega} \rightarrow \mathbb{R}^2$  associating the points of the closure of a bounded open set  $\Omega \subset \mathbb{R}^2$  (initial configuration of a body) to  $\Phi(\Omega) \subset \mathbb{R}^2$  (deformed configuration). For references see [112], [113]. It is possible to introduce the

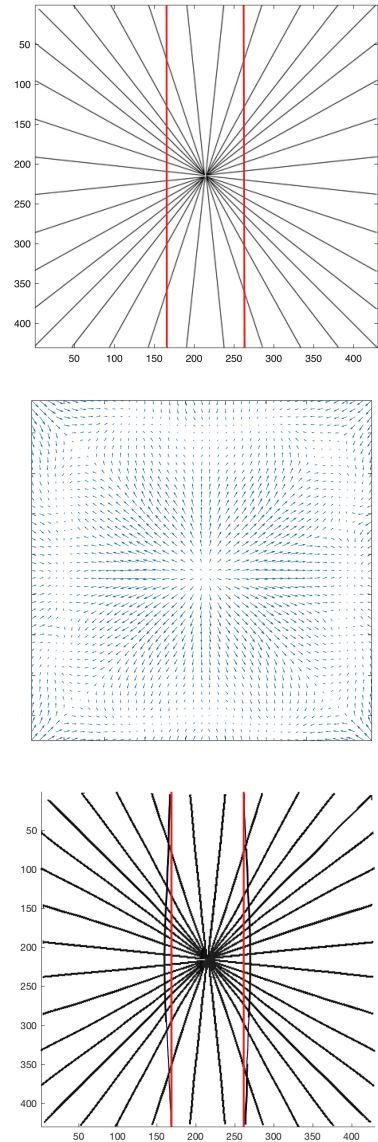


Figure 6.9: Here we superimpose two red lines to the original distal stimulus (Hering illusion) to remark that vertical lines present in the stimulus are straight. Representation of the displacement field  $\{\bar{u}(x_1, x_2)\}_{(x_1, x_2) \in \mathbb{R}^2}$ . Perceived deformation.

displacement as a map  $\bar{u}(x_1, x_2) = \Phi(x_1, x_2) - (x_1, x_2)$ , where  $(x_1, x_2) \in \mathbb{R}^2$ . It follows

$$\nabla \bar{u} = \nabla \Phi - \mathbf{Id}.$$

We can now express the right Cauchy-Green tensor in terms of displacement:

$$\begin{aligned} \mathbf{p} = p_{ij}(x) &= (\nabla \Phi)^T (\nabla \Phi) = (\nabla \bar{u} + \mathbf{Id})^T (\nabla \bar{u} + \mathbf{Id}) \\ &= (\nabla \bar{u})^T (\nabla \bar{u}) + (\nabla \bar{u}) + (\nabla \bar{u})^T + \mathbf{Id}. \end{aligned}$$

The concept of strain is used to evaluate how much a given displacement differs locally from a rigid body displacement. For *infinitesimal deformations* of a continuum body, in which the displacement gradient is small ( $\|\nabla \bar{u}\| \ll 1$ ), it is possible to perform a geometric linearization of strain tensor introduced before, in which the non-linear second order terms are neglected. The *linearized right Cauchy-Green tensor* has the following form:

$$G(\bar{u}) \approx (\nabla \bar{u}) + (\nabla \bar{u})^T, \quad (6.7)$$

which is used in the study of linearized elasticity, i.e. the study of such situations in which the displacements of the material particles of a body are assumed to be small (infinitesimal strain theory.)

Here we give the expression in components of  $\epsilon(\bar{u}) = \frac{1}{2}G(\bar{u})$  (the so called Green-Lagrangian strain tensor):

$$\epsilon_{ij}(\bar{u}) = \begin{pmatrix} \frac{\partial u_1}{\partial x_1} & \frac{1}{2} \left( \frac{\partial u_1}{\partial x_2} + \frac{\partial u_2}{\partial x_1} \right) \\ \frac{1}{2} \left( \frac{\partial u_2}{\partial x_1} + \frac{\partial u_1}{\partial x_2} \right) & \frac{\partial u_2}{\partial x_2} \end{pmatrix}, \quad (6.8)$$

where  $\bar{u} = (u_1, u_2)$ . Expressing  $\epsilon_{ij}$  in terms of the metric  $(p_{ij})_{i,j}$  with whom the initial configuration of the considered body was equipped we obtain:

$$\epsilon_{ij}(\bar{u}) \approx \frac{1}{2}((p_{ij})_{ij} - \mathbf{Id}), \quad (6.9)$$

and in its matrix form:

$$\begin{pmatrix} p_{11} & p_{12} \\ p_{21} & p_{22} \end{pmatrix} - \begin{pmatrix} 1 & 0 \\ 0 & 1 \end{pmatrix} = \begin{pmatrix} \frac{\partial u_1}{\partial x_1} & \frac{1}{2} \left( \frac{\partial u_1}{\partial x_2} + \frac{\partial u_2}{\partial x_1} \right) \\ \frac{1}{2} \left( \frac{\partial u_2}{\partial x_1} + \frac{\partial u_1}{\partial x_2} \right) & \frac{\partial u_2}{\partial x_2} \end{pmatrix}. \quad (6.10)$$

### Poisson problems - displacement

Starting from (6.10) we obtain a system of equations with this form:

$$\begin{cases} p_{11} - 1 = & \frac{\partial u_1}{\partial x_1} \\ p_{22} - 1 = & \frac{\partial u_2}{\partial x_2} \\ p_{12} = p_{21} = & \frac{1}{2} \left( \frac{\partial}{\partial x_2} u_1 + \frac{\partial}{\partial x_1} u_2 \right) \end{cases} \quad (6.11)$$

Differentiating, substituting and imposing Neumann boundary conditions to system (6.11) we end up with the following differential system:

$$\left\{ \begin{array}{ll} \Delta u_1 = \frac{\partial}{\partial x_1} p_{11} + 2 \frac{\partial}{\partial x_2} p_{12} - \frac{\partial}{\partial x_1} p_{22} & \text{in } M \\ \Delta u_2 = \frac{\partial}{\partial x_2} p_{22} + 2 \frac{\partial}{\partial x_1} p_{12} - \frac{\partial}{\partial x_2} p_{11} & \\ & \frac{\partial}{\partial \vec{n}} u_1 = 0 \\ & \frac{\partial}{\partial \vec{n}} u_2 = 0 \end{array} \right. \quad \text{in } \partial M \quad (6.12)$$

where  $M$  is an open subset of  $\mathbb{R}^2$  and  $\partial M$  is Lipschitz continuous, with normal defined almost everywhere. Solutions for equation (6.12) are well defined up to an additive constant, which is recovered imposing  $u(0, 0) = v(0, 0) = 0$  for symmetry reasons, where  $(0, 0)$  is the center of our initial domain  $M$ . Let us explicitly note that tensor  $\mathbf{p}$  is obtained after convolution of Gabor filters, so that it is differentiable, allowing to write the system. Hence we solve (6.12), recovering the displacement field  $\bar{u}(x_1, x_2)$ .

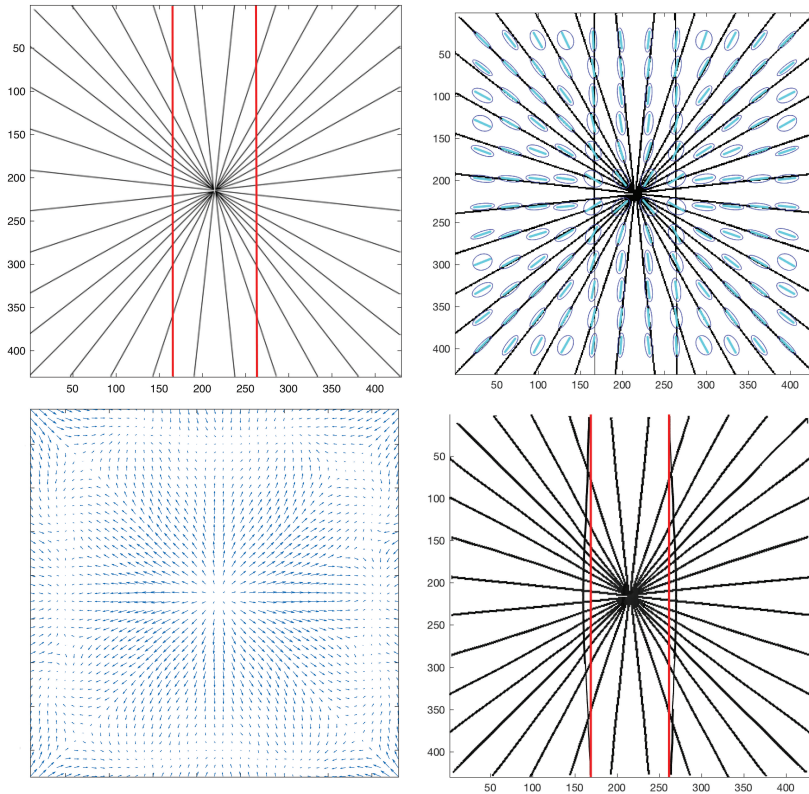
### 6.3.4 Numerical Implementation

The inverse of tensor expressed in formula (6.4) is computed discretizing  $\theta$  as a vector of 32 values equally spaced in the interval  $[0, \pi]$ . The scale parameter  $\sigma$  varies in dependence of the image resolution and is set in concordance with the stimulus processed. It is taken quite large in all examples in such a way to obtain a smooth tensor field covering all points of the image. This is in accordance with the hypothesis previously introduced that mechanisms in V2, where the receptive field of simple cells is larger than in V1, play a role in such phenomena. The constant  $\gamma$  has been chosen for all the examples as  $\gamma = 2 \cdot 10^{-2}$ . The differential problem in (6.12) is approximated with a central finite difference scheme and it is solved with a classical PDE linear solver. We now start discussing all results obtained through the presented algorithm.

## 6.4 Results

### 6.4.1 Hering illusion

The Hering illusion, introduced by Hering, a German physiologist, in 1861 [83] is presented in figure 6.10. In this illusion two vertical straight lines are presented in front of radial background, so that the lines appear as if they were bowed outwards. In order to help the reader, in figure 6.10 (top left) we superpose to the initial illusion two red vertical lines, which indeed coincide with the ones present in the stimulus. As described in the



previous sections, we first convolve the distal stimulus with the entire bank of Gabor filters: we take 32 orientations selected in  $[0, \pi)$ ,  $\sigma = 6.72$  pixels. Following the process, we compute  $\mathbf{p}^{-1}$  using equation (6.4), we solve equation (6.12) obtaining the perceived displacement  $\bar{\mathbf{u}} : \mathbb{R}^2 \rightarrow \mathbb{R}^2$ . Once it is applied to the initial stimulus, the proximal stimulus is recovered. The result of computation is shown in figure 6.10 (bottom right). The distorted image folds the parallel lines (in black) against the straight lines (in red) of the original stimulus (given in figure 6.3, a).

#### 6.4.2 Wundt Illusion

A variant of the Hering illusion, introduced by Wundt in the 19th century, [187] is presented in figure 6.12. In this illusion two straight horizontal lines look as if they were bowed inwards, due to the distortion induced by the crooked lines on the background. For the convolution of the distal stimulus with Gabor filters we select 32 orientations in  $[0, \pi)$ ,  $\sigma = 11.2$  pixels. Then we apply the previous model, and obtain the result presented in figure 6.12. Computed vector fields are concentrated in the central part of the image and point toward the center. They indicate the direction of the displacement, which bends the parallel lines inwards. In figure 6.12 (center right) the proximal stim-

Figure 6.10: We superimpose two red vertical lines to the Hering illusion, represented in figure 6.3, in order to remark that vertical lines present in the stimulus are straight. Representation of  $\mathbf{p}^{-1}$ , projection onto the retinal plane of the polarized connectivity in 6.3. The first eigenvalue is tangent to the level lines of the distal stimulus. In blue the tensor field, in cyan the eigenvector related to the first eigenvalue. Computed displacement field  $\bar{\mathbf{u}} : \mathbb{R}^2 \rightarrow \mathbb{R}^2$ . Displacement applied to the image. In black we represent the proximal stimulus as displaced points of the distal stimulus:  $(x_1, x_2) + \bar{\mathbf{u}}(x_1, x_2)$ . In red we give two straight lines as reference, in order to better clarify the curvature of the target lines.

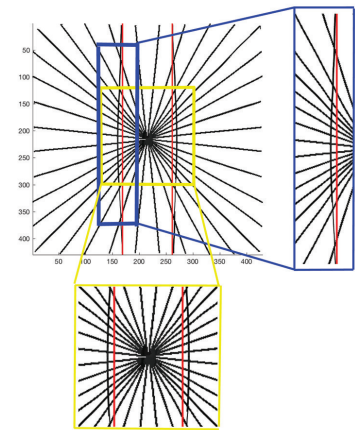


Figure 6.11: Details of the perceived distortion in the computed proximal stimulus in the Hering illusion.

ulus is computed through the expression:  $(x_1, x_2) + \bar{u}(x_1, x_2)$ . In black we indicate displaced dots of the initial image: the straight lines of the distal stimulus are bent by the described mechanism (black). In red we put the straight lines of the original distal stimulus. This provide a comparison between the lines pre/post processing. In figure 6.12 (bottom) details of the distances between the bent curves and the original straight lines are shown.

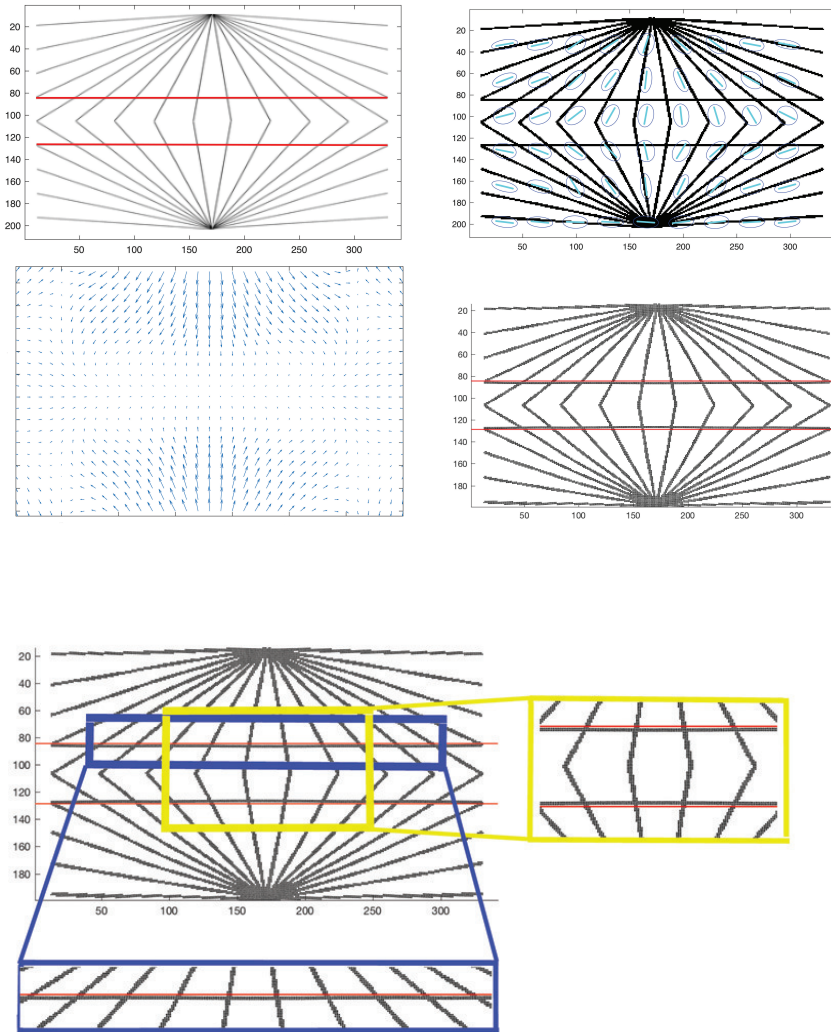


Figure 6.12: Here we superimpose two red lines to the Wundt illusion, presented in figure 6.3, b, in order to clarify that the horizontal lines present in the image are indeed straight. Representation of  $\mathbf{p}^{-1}$ , projection onto the retinal plane of the polarized connectivity in 6.3. The first eigenvalue is tangent to the level lines of the distal stimulus. In blue the tensor field, in cyan the eigenvector related to the first eigenvalue. Computed displacement field  $\bar{u}$ . Displacement applied to the image. In black we represent the proximal stimulus as displaced points of the distal stimulus:  $(x_1, x_2) + \bar{u}(x_1, x_2)$ . In red we give two straight lines as reference, in order to put in evidence the curvature of the target lines. Finally, details of the perceived distortion in the computed proximal stimulus in the Wundt illusion are presented.

### 6.4.3 Square shape over Ehrenstein context

This illusion, introduced by Ehm and Wackermann in [58], consists in presenting a square over a background of concentric circles, figure 6.3, c. This context, the same we find in Ehrenstein illusion, bends the edges of the square (red lines in figure 6.13, top left) toward the center of the image. Here we take the same number of orientations, 32, selected in  $[0, \pi)$  and  $\sigma = 13.44$  pixels. The resulting distortion is shown in figure 6.13, bottom

right.

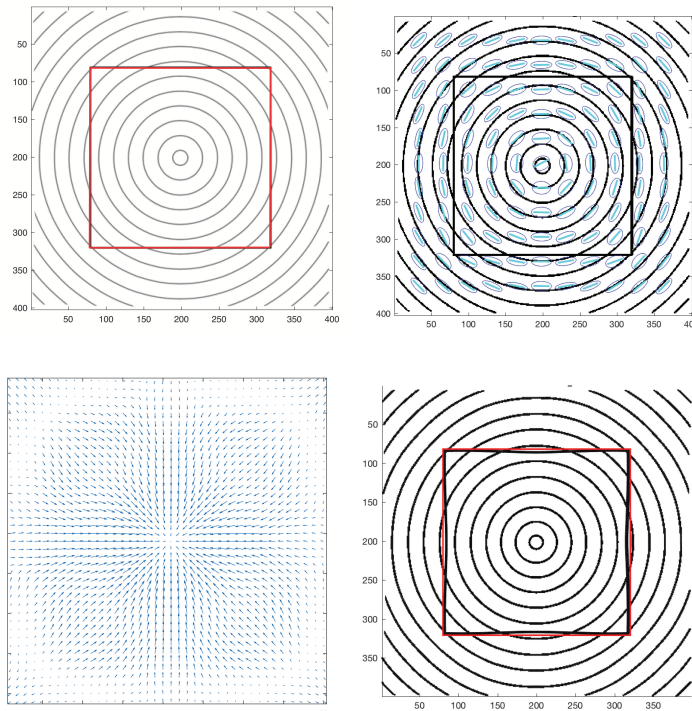


Figure 6.13: Here we superimpose red edges to the original illusion shown in 6.3, (c). Representation of  $\mathbf{p}^{-1}$ , projection onto the retinal plane of the polarized connectivity in 6.3. The first eigenvalue is tangent to the level lines of the distal stimulus. In blue the tensor field, in cyan the eigenvector related to the first eigenvalue. Computed displacement field  $\bar{u}$ . Displacement applied to the image. In black we represent the proximal stimulus as displaced points of the distal stimulus:  $(x_1, x_2) + \bar{u}(x_1, x_2)$ . In red we give a square as reference, in order to put in evidence the curvature of the target lines.

#### 6.4.4 Modified Hering illusion

Here we present three modified Hering illusions (see figure 6.14): in the first one straight lines are positioned further from the center than in the classical Hering illusion. In the second one straight lines are positioned nearer the center than in the reference Hering illusion. For coherence with the Hering example, orientations selected are 32 in  $[0, \pi)$  and  $\sigma = 6.72$  pixels. All other parameters are fixed during these three experiments. In the proposed modified Hering illusions, see figure 6.14 the vertical lines are straight and parallel as in the Hering, but since they are located further/nearer the center of the image the perceived bending results to be less/more intense. In accordance with the displacement vector fields shown in figure 6.10, bottom left, as far as we outstrip/approach the center the magnitude of the computed displacement decreases/increases. In figure 6.14, bottom right, two straight lines are put over an incoherent background, composed by random oriented segments. As we can see from figure 6.15, bottom right, any displacement is perceived nor computed by the present algorithm.

#### 6.4.5 Wundt-Hering illusion

The Wundt-Hering illusion (figure 6.3, (d)) combines the effect of the background of the Hering and Wundt illusions. In this

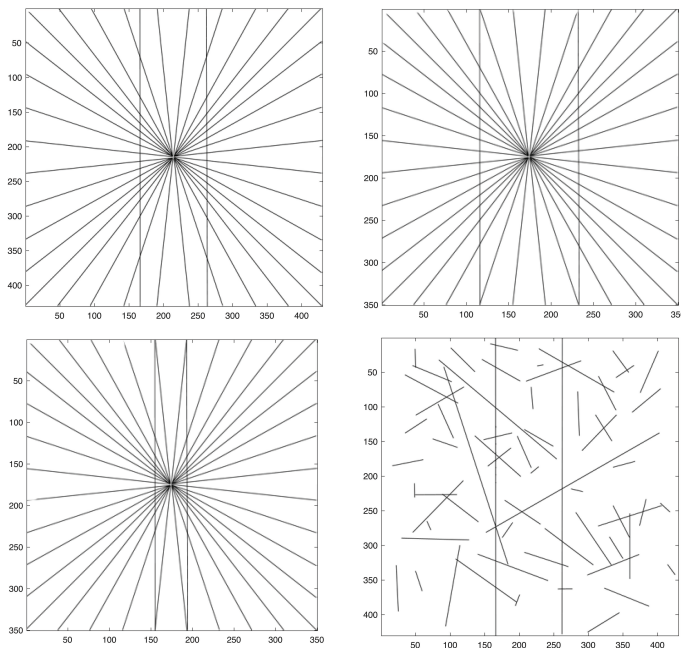


Figure 6.14: Top left: Hering illusion, distal stimulus. Top right: modified Hering illusion: in this example straight lines are further from the center with respect to the classical example of Hering illusion. Bottom left: modified Hering illusion: in this example straight lines are placed nearer the center with respect to the classical example of the Hering illusion. Bottom right: modified Hering illusion with an incoherent background, composed by random-oriented segments.

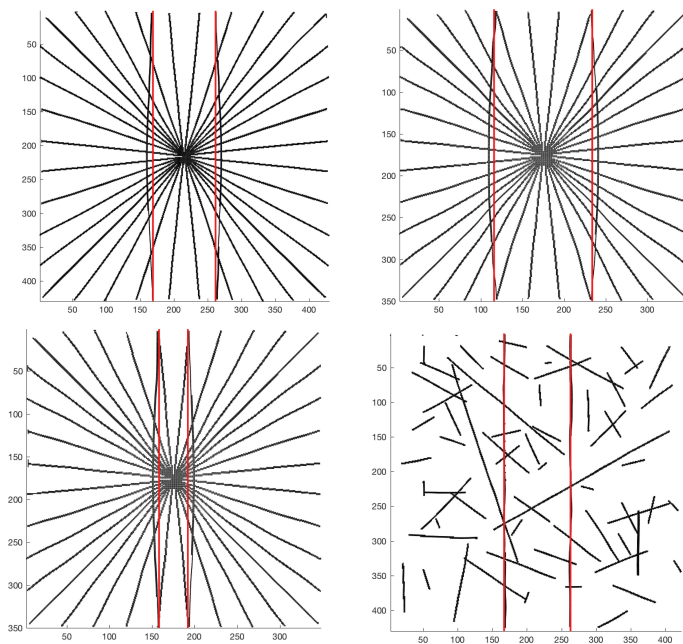


Figure 6.15: Displacement applied to the Hering illusion. Displacement applied to the first modified Hering illusion, in which the distance from the center is increased. Displacement applied to second modified Hering illusion, in which the distance from the center is decreased. Displacement applied to the third modified Hering illusion, with an incoherent background of random-oriented segments. In this last example no deformation is perceived. In black we represent the proximal stimulus as displaced points of the distal stimulus:  $(x_1, x_2) + \bar{u}(x_1, x_2)$ . In red we give two straight lines as reference, in order to put in evidence how much target lines are bent, or not bent.

illusion two straight horizontal lines are presented in front of inducers which bow them outwards and inwards at the same time, inhibiting the bending effect. As a consequence the horizontal lines are indeed perceived as straight. As previously explained for the modified Hering illusion, also this phenomenon can be interpreted in terms of lateral interaction between cells belonging to the same neighborhood. Here we take 32 orientations selected in the interval  $[0, \pi)$ ,  $\sigma = 6.72$  pixels.

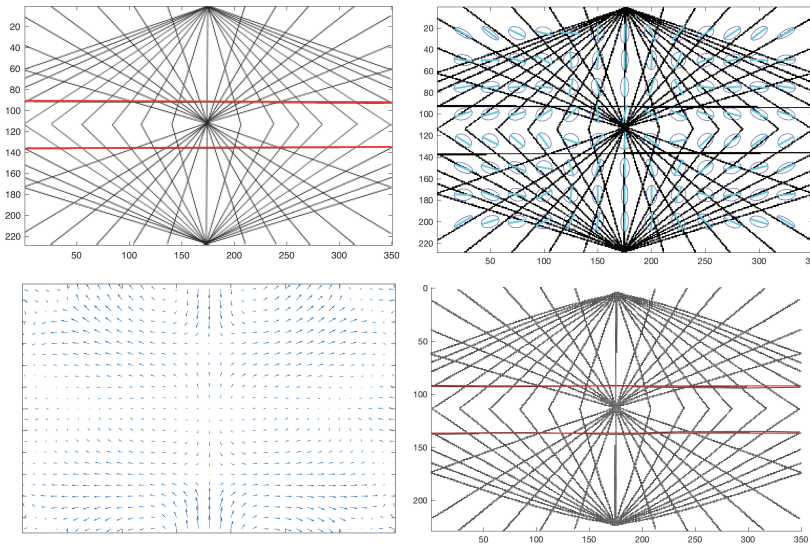


Figure 6.16: Here we superimpose two red horizontal lines to the original Wundt-Hering illusion, figure 6.3, (d). Representation of  $\mathbf{p}^{-1}$ , projection onto the retinal plane of the polarized connectivity in 6.3. The first eigenvalue is tangent to the level lines of the distal stimulus. In blue the tensor field, in cyan the eigenvector related to the first eigenvalue. Computed displacement field  $\bar{u}$ . Displacement applied to the image. In black we represent the proximal stimulus as displaced points of the distal stimulus:  $(x_1, x_2) + \bar{u}(x_1, x_2)$ . In red we give two straight lines as reference, in order to put in evidence the curvature of the target lines.

#### 6.4.6 Zöllner illusion

The Zöllner illusion (figure 6.3, (e)) consists in a pattern of oblique segments surrounding parallel lines, which creates the effect of unparallelism, [190]. As in the previous experiments, in figure 6.3, (e), we superimpose two red lines to identify the straight lines. Here we take 32 orientations selected in the interval  $[0, \pi)$ ,  $\sigma = 10.08$  pixels.

#### 6.4.7 Ehrenstein illusion

In the Ehrenstein illusion, see figure 6.18 top left, the top and bottom edges of the square appear to be unparallel due to the presence of the crossing lines in the background.

### 6.5 Discussion

In this chapter we presented a neuro-mathematical model based on the functional architecture of the visual cortex to explain

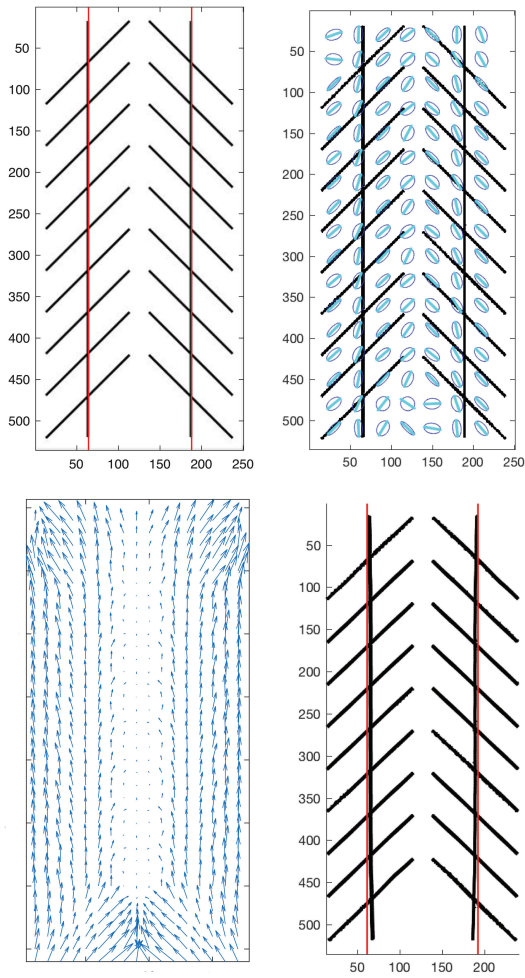


Figure 6.17: Here we superimpose two red horizontal lines to the original Zollner Illusion. Representation of  $\mathbf{p}^{-1}$ , projection onto the retinal plane of the polarized connectivity in 6.3. The first eigenvalue is tangent to the level lines of the distal stimulus. In blue the tensor field, in cyan the eigenvector related to the first eigenvalue. Computed displacement field  $\bar{u}$ . Displacement applied to the image. In black we represent the proximal stimulus as displaced points of the distal stimulus:  $(x_1, x_2) + \bar{u}(x_1, x_2)$ . In red we give two straight lines as reference, in order to put in evidence the unparallelism of the target lines.

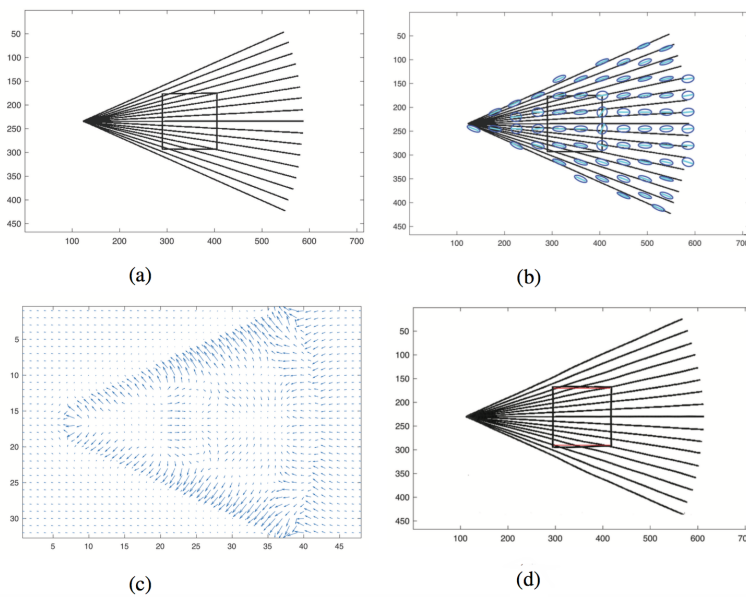


Figure 6.18: Ehrenstein illusion, same process as before. Top Left the original stimulus; top left the tensorial representation, bottom left the computed displacement vector fields; bottom right: the displacement applied to the initial image, which bends the square edges.

and simulate perceptual distortion due to geometrical-optical illusions and to embed geometrical context. In our model perceptual distortion is due to the Riemannian metric induced on the image plane by the connectivity activated by the image stimulus. Its inverse is interpreted as a strain tensor and we computed the deformation in terms of displacement field which arises as solution of (6.12). This technique has been applied to a number of test cases and results are qualitatively in good agreement with human perception. In the future this work could be extended to functional architectures involving the feature of scale, starting from models provided by Sarti, Citti and Petitot in [154], [155]. This will allow to provide a model for scale illusions, such as the Delbouf, see [31]. Indeed, another direction for future works will be to provide a quantitative analysis for the described phenomena, such as the one proposed by Smith [160] and to direct compare the developed theory with observations of GOIs through neuro-imaging techniques.



## 7 Geodesics as perceptual curves in GOIs

THE AIM of this chapter is to model geometrical optical illusions as geodesics of the polarized metric in  $SE(2)$  introduced in the previous chapter (6). In this framework, starting from the model proposed in [28] which looks for illusory contours as length minimizers of the distance between two points (geodesic, [121]) in the sub- Riemannian (SR) metric  $g^{ij}$ , see (4.10) in chapter 4, we extend the model to this framework, in which we state illusory contours in GOIs arise as geodesics of the polarized metric. From the numerical point of view a very fast and accurate method for computing geodesics in the Euclidean metric has been introduced by Sethian in [156, 157, 158], and it is called Fast- Marching (FM). Fast - marching consists in looking for approximate solutions for the Eikonal problem:

$$\begin{cases} \|\nabla_E W(x_1, x_2, x_3)\|_E = \frac{1}{f(x_1, x_2, x_3)} \text{ for } \eta \neq e, \\ W(e) = 0. \end{cases} \quad (7.1)$$

where  $e$  is the boundary initial value and  $\nabla_E$  denotes the Euclidean gradient;  $(x_1, x_2, x_3) \in \mathbb{R}^3$  (we refer to section 5.3 for a review definition and properties of solutions in the viscosity sense, first introduced by [37, 35]). Physically the solution  $W(\eta)$  is the shortest time needed to travel from  $e$  to  $\eta$  inside the domain of the equation, with  $f(x)$  being the speed at  $\eta$ . When  $f = 1$ ,  $W$  is the distance from the boundary  $e$ . In the latter case, once the distance map  $W$  has been computed, geodesics are recovered as integral curves of its gradient starting from the final point  $\eta$  on  $W$ , and ending at point  $e$ . Indeed they will be minimal length path from  $e$  to  $\eta$ . In this way they can be interpreted as the fastest paths connecting the two points. The Eikonal equation has been studied from the analytical point of view in different setting by many authors. Viscosity solution for this type of PDEs have been provided in the 80s by Crandall and Lions, see [34] and for uniqueness see [4] (recent version). The theoretical counterpart for viscosity solu-

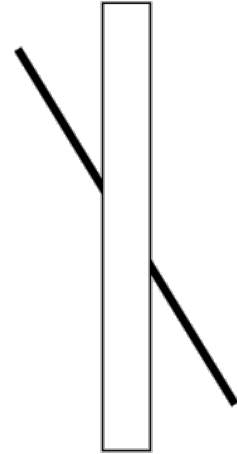


Figure 7.1: In this image we show the Poggendorff illusion, in which a surface makes the two collinear transversals appear misaligned. The perceptual curve projects in at some point over the right boundary of the surface.

tion of the Eikonal equation in the sub-Riemmanian case can be found in [20, 51, 52]. The Fast marching method for computing approximate solutions has been extended in other setting by Mirebeau,[120], and in [6] was developed in the  $SE(2)$  equipped with a SR metric.

In this chapter we look for perceptual curves as sub-Riemannian geodesics of  $SE(2)$  and we will compute them through the FM method. Especially we will apply our hypothesis over Poggendorff illusion, see figure 7, in which a surface makes the two collinear transversals appear misaligned. The perceptual curve projects in at some point over the right boundary of the surface, and our aim is to compute it, stating it will be a length minimizer for the polarized metric in the  $SE(2)$  space. The contributions relative to modeling illusory curves as Geodesics in  $\mathbb{R}^2 \times S^1$  will be contained in [66, 67].

## 7.1 Sub-Riemannian Geodesics as perceptual curves in GOIs

In the previous chapter we have presented a neuro-geometrical model for GOIs in which the deformation induced by the stimulus is recovered through infinitesimal strain theory instruments.

Let us consider now the contribution given in [28] by Citti and Sarti, in which the natural connectivity metric with whom the cortical space  $SE(2)$  is endowed is sub-Riemannian. In the presented metric, in formula (4.10), completion curves (subjective boundaries) arise as geodesics of the  $\mathbb{R}^2 \times S^1$  space. Furthermore, they are lifting in the 3D space of the classic elastica curves. Elastica curves, i.e. curves minimizing the functional

$$\int_{\gamma} (1 + k^2) ds$$

were introduced in [132] as classical reconstruction for subjective boundaries, which can be either linear or curvilinear. In the previous formula, the integral is computed along the missing boundary  $\gamma$  and  $k$  denotes its curvature. The equivalence between the minimization problem proposed by Nitzberg, Mumford and Shiota in [132] and the one proposed by Citti and Sarti in [28] has been shown in [28]. In this way the problem of looking for minima has been reduced to a problem of geodesics in the natural metric of the space  $\mathbb{R}^2 \times S^1$ . The idea is then to extend this approach for modeling Geometrical Optical Illusions. In the same way as subjective boundaries, the deformation curves of the proximal stimulus of Geometrical Optical illusions arise as geodesics of a metric strongly polarized by the output of simple cells of V1/V2. So the basic idea is to provide a natural environment for this type of phenomena and to model them through geodesics of this space. We assume that the output of the simple cells induce a reinforcement of the connectivity which become stronger at the activated cells. This idea is modelled through a polarized metric of the sub-Riemannian space, obtained multiplying the natural metric  $\mathcal{H}^{-1}$  of the space, defined in (4.8) with a suitable function  $R = R(x_1, x_2, \theta)$  which only depends on the output  $O$  of the cells, defined in formula 4.3). In the frame  $X_1, X_2$  the metric and its inverse become (for definitions see section 4.3.1)

$$\mathcal{H} = \frac{1}{R} \begin{pmatrix} 1 & 0 \\ 0 & 1 \end{pmatrix}, \quad \mathcal{H}^{-1} = R \begin{pmatrix} 1 & 0 \\ 0 & 1 \end{pmatrix} \quad (7.2)$$

We postulate that perceptual curves for the GOIs such as the one presented in figure 7 are length minimizers of the polarized metric in (7.2). Until now psychologists have been looking

For reader convenience we recall here both formulas introduced in Chapter 4 the mother Gabor filter has the following expression:

$$\psi_0(\xi) = \frac{1}{2\pi\sigma^2} e^{-\frac{(\xi_1^2 + \alpha^2 \xi_2^2)}{2\sigma^2}} e^{\frac{2i\bar{b}\xi_2}{\sigma}},$$

where  $\bar{b} = 0.56$  is the ratio between  $\sigma$  and the spatial wavelength of the cosine factor. The output of the convolution between the image and the entire bank of Gabor filters is

$$O(x_1, x_2, \theta) = \int_M I(\xi_1, \xi_2) \psi_{(x_1, x_2, \theta)}(\xi_1, \xi_2) d\xi_1 d\xi_2.$$

Later on we will consider  $R(x_1, x_2, \theta)$ , the odd filter part contribution to the previous output.

for the paths of perceptual curves through quantitative perceptual experiments, [181, 107]. Here we will provide spatial coordinates for such curves, looking for them through a neural-based mathematical model.

The original contribution of this chapter will be to provide a neural based mathematical model able to recover perceptual curves in GOIs, and to compare them with previous psychophysical estimations of those curves.

## 7.2 Geodesics, distance and Eikonal equation

In Definitions 3.3.5 and 3.3.6 we provided the definition of Riemannian geodesics and minimizing geodesics. The same definitions could be given in the sub-Riemannian setting, but for our application we are mainly interested in minimizing geodesics [121]:

**Definition 7.2.1.** Given two points  $\eta_0, \eta_1$  and a curve  $\gamma$  on which the minimum in 4.11 is attained, we call such curve a geodesic.

Sub-Riemannian geodesics and their application to image analysis were also studied in [7, 84, 114]. For explicit formulas of SR-geodesics in  $SE(2)$  in the particular case of uniform external cost  $R = 1$ , see [148]. By the definition 4.12, the length of the minimizing geodesics between two points  $\eta_0$  and  $\eta_1$  is the Carnot Carathéodory distance between them (section 4.4). It is known that this distance is a solution of the sub-Riemannian eikonal equation, see [20].

In the metric defined in (7.2) the equation has the following expression:

$$\begin{cases} \|\nabla_{\mathcal{H}} W(\eta)\|_{\mathcal{H}} = 1 \text{ for } \eta \neq e, \\ W(e) = 0, \end{cases} \quad (7.3)$$

where  $\mathcal{H}$  is the metric defined in (4.8). The Eikonal equation belongs to the class of Hamilton- Jacobi equations. Let us recall that viscosity solutions for this kind of problems in the Euclidean setting have been provided by Crandall and Lions [34, 36]. For uniqueness see [4] (recent version). We refer to section 5.3 for a summary of the contributions to the notion of viscosity solution. Monti improved the previous result showing that the equation holds almost everywhere. Because of the uniqueness of the solution, necessarily the solution  $W$  will be the distance from a point [123]. See also Dragoni, [51, 52]. For the solution in the case of the Heisenberg group, see [122]. In this theoretical framework the solution of (7.3) will be the sub-Riemannian distance in the metric  $\mathcal{H}$ , opportunely weighted

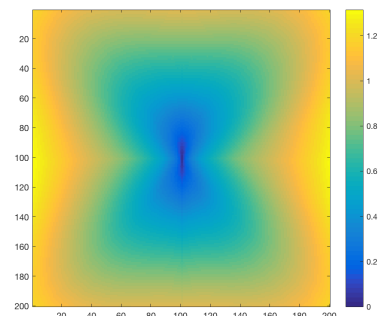


Figure 7.2: Minimum along  $\theta$  of the distance map  $W$ , numerical solution of equation 7.3, from initial boundary condition  $e = (0, 0, 0)$  and  $R = 1$ , i.e. Sub-riemannian distance as shown in formula (4.10).

by  $R$ , from the point  $e$ . In figure 7.2 the minimum along  $\theta$  of the sub-Riemannian distance map computed through the SR-FM is presented. Colors indicate the distance from the boundary value  $e$ .

### 7.2.1 Riemannian approximation of sub-Riemannian distance

Let us recall that the subriemannian distance  $d$  can be approximated via a family of suitable Riemannian distances. For  $0 < \epsilon \ll 1$  we define the metric

$$\mathcal{G}_\epsilon = \text{diag}\left(\frac{1}{R}, \frac{1}{R}, \frac{1}{\epsilon^2 R}\right),$$

with respect to the frame  $X_1, X_2, X_3$ , and we call  $d_\epsilon$  the associated Riemannian distance.  $\mathcal{G}_\epsilon$  is the Riemannian approximation of the metric  $\mathcal{G}$ , which extends to the whole space the metric  $\mathcal{H}$ . See sections 4.3.1 and 5.3.1, here the reference frame is modified up to a constant with respect to sec 5.3.1. Its inverse is expressed as

$$\mathcal{G}_\epsilon^{-1} = \text{diag}(R, R, \epsilon^2 R),$$

so that  $\mathcal{G}_\epsilon^{-1}$  formally tends to  $\mathcal{G}^{-1}$ .

Accordingly for every  $\epsilon > 0$  the Riemannian distance  $d_\epsilon(\eta, e)$  satisfies the Riemannian Eikonal equation:

$$\begin{cases} \|\nabla_{\mathcal{G}_\epsilon} W_\epsilon(\eta)\|_{\mathcal{G}_\epsilon} = 1 \text{ for } \eta \neq e, \\ W_\epsilon(e) = 0, \end{cases} \quad (7.4)$$

It is important to note that the equality in the limit is not only formal. Indeed it has been proved by Gromov in [82] that  $d$  is approximated by the Riemannian distance  $d^\epsilon$ . As a consequence the solution  $W_\epsilon$  tends to  $W$  as  $\epsilon$  goes to 0.

## 7.3 Sub-riemannian fast marching

### 7.3.1 Solution of the Eikonal Equation

Fast-Marching is a fast and accurate technique introduced by Sethian in [156, 157, 158], for solving the stationary eikonal equation when the metric is isotropic (proportional at each point to the identity matrix). It allows to compute an approximate solution of the latter, i.e. the Euclidean distance map from a certain boundary initial condition. Let us go through the method, as originally proposed by Sethian in the Euclidean setting. First, equation (7.1) is discretized with an upwind scheme presented

in formula (8.2) of [156] and in [147].

$$\left[ \begin{array}{l} \max(D_{ijk}^{-x_1} W, -D_{ijk}^{+x_1} W, 0)^2 \\ \max(D_{ijk}^{-x_2} W, -D_{ijk}^{+x_2} W, 0)^2 \\ \max(D_{ijk}^{-x_3} W, -D_{ijk}^{+x_3} W, 0)^2 \end{array} \right]^{1/2} = 1 \quad (7.5)$$

with  $f(x_1, x_2, x_3) = 1$ ,  $D_{ijk}^{+/-}$  denoting forward and backward differences along  $x_1$ ,  $x_2$  or  $x_3$ , directions in  $\mathbb{R}^3$ . Scheme in (7.5) can be solved, as proposed in [147], through iteration. The key innovation proposed by Sethian in [157, 158] is to construct the solution  $W$  using only upwind values, which guarantees the information is propagated *one-way* starting from the boundary, from small values of  $W$  to larger ones. At each step we march downwind and we identify the points around the boundary which minimize the solution  $W$ . This cannot yield a value smaller than that at any of the already computed points. The grid point containing the minimum of  $W$  becomes the new boundary value, and the propagation follows this scheme. To summarize it: first, boundary value points are tagged as *Known*; then, all points that are one grid point away are tagged as *Trial*. Finally, all the others are tagged as *Far*. Then a loop over the stencil is performed, as follows:

- (1) Begin loop: let  $A$  be the *Trial* point with the smallest  $W$  values.
- (2) Add the point  $A$  to *Known*; remove it from *Trial*.
- (3) Tag as *Trial* all the neighbors of  $A$  that are not *Known*. If the neighbor is in *Far*, remove, and add to the set *Trial*.
- (4) Recompute the values of  $W$  at all *Trial* neighbors of  $A$  according to equation (7.5) by solving the quadratic equation (backsolve).
- (5) Return to top of loop.

See figure 7.3.1 for the evolution of the process through the explained iterations. The fast-marching method has been extended in the case of Riemannian metric by Mirebeau,[120], and in [6] was developed in the  $SE(2)$  equipped with a sub-Riemannian metric, with arbitrary external cost. These recent method belong to the Dijkstra's class of algorithms [49], in which the approach for solving the Eikonal equation is slightly different. While the method proposed by Sethian looks for the solution of the continuous problem, Dijkstra's method applies to graphs, where the front propagates by looking for the node reached with the smallest current cost, i.e. the prescribed

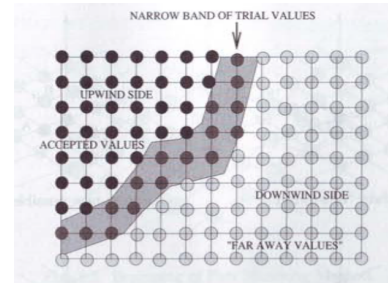


Figure 7.3: Progress of the Fast Marching method along the grid points of the stencil, see [156].

weight of the nodes of the graph. In order to deal with the anisotropic eikonal equation associated to a given Riemannian metric (important for its application to control problems [159] and medical image analysis [8]), Mirebeau in [120] introduced a Fast Marching using lattice basis reduction (LBR, has been introduced in [129]). This means that the considered stencil is sparse and non-negative, in order to adapt to the anisotropic solution we are looking for.

### 7.3.2 Geodesics computations

Once the solution of the Eikonal problem has been recovered, geodesics, length minimizers of the metric, are computed using gradient descent (figure 7.4).

The latter method ensures to move toward the local minimum of a prescribed map (our distance map  $W$ ). This local minimum is reached following the  $-\nabla$  direction of the function  $W$  at a current point. This ensures, looking for example at figure 7.4, that  $W(x_0) > W(x_1) > \dots > W(x_4)$ , meaning that we converge to a desired local minimum. Bekkers et al. in [6] solve the sub-Riemannian Eikonal equation in (7.3) via the Riemannian approximation introduced in 7.4. In order to do so they suitably adapt the method explained in 7.3.1. Then they call  $\gamma(t)$  the solution of the Cauchy problem:

$$\begin{cases} \dot{\gamma}_b(t) = -\nabla_{\mathcal{H}} W(\gamma_b(t)), & t \in [0, T] \\ \gamma_b(0) = \eta_1, \end{cases} \quad (7.6)$$

and prove that  $\gamma(t) = \gamma_b(T - t)$  is the sub-Riemannian geodesic connecting  $e$  and  $\eta_1$ .

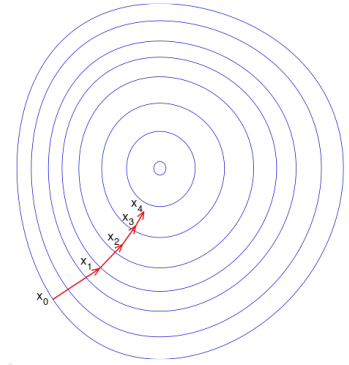


Figure 7.4: Illustration of gradient descent on a series of level sets on a prescribed map.

## 7.4 Poggendorff illusion

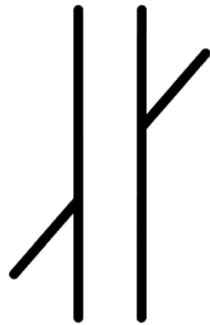


Figure 7.5: The original Poggendorff illusion.

Poggendorff illusion consists in an apparent misalignment of two collinear, oblique, transversals separated by a rectangular surface (shown in Fig. 7.5). It is named after Johann Christian Poggendorff, the editor of the journal *Annalen der Physik*, who discovered it in the figures Johann Karl Friedrich Zöllner submitted when first reporting on what is now known as the Zöllner illusion, in 1860, see [190] and figure 6.3, (e). Referring

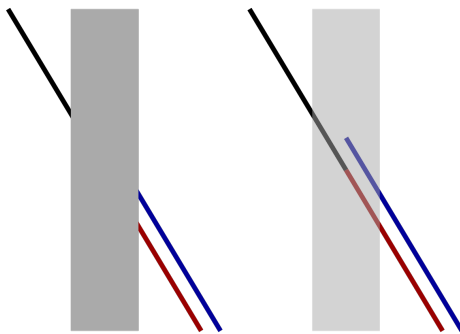


Figure 7.6: Poggendorff illusion in which both completion (blue) and collinear continuation (red) of the left transversal (black) are shown, see Greist et al. see [81].

to figure 7.6, in which a perceptual scheme of the illusion is provided, the perceptual completion of the black line appears to be the blue segment, instead of the red segment, which corresponds to the geometrical continuation of the black line. An interesting overview of the psychological elements contributing to the misperception in Poggendorff illusion has been performed from the 70s by many authors, we recall just few of them [181, 107, 42, 144, 162]. This phenomenon of misalignment occurs in a wide range of figures, see [163, 41]. In their paper Day and Dickinson, [42], identified with psychophysical experiments some of the *components* of the Poggendorff illusions, i.e. the main effects independent one from the other which contribute to the perceptual distortion. The most critical feature is the obtuse angle effect, which was measured psychophysically (see margin note): it consists on the fact that the apparent length of the sides of an obtuse angle is greater than

The experiment used to measure the quantitative contribution of the obtuse angle effect is explained in [42], page 542. The right transversal is substituted by a dot. The illusion is still present, meaning that what accounts for it is the elongation of the central bar produced by the obtuse angle, and not the tendency of the transversal to form a right angle with the parallels. This conclusion have been rejected recently by some experiments performed by the same authors in [43] and summarize in [180].

that of an obtuse angle of equal physical lengths, meaning that is the segment of the parallel that makes an obtuse angle with the outer transversal segment which elongates the central bar, creating the illusory effect [42, 107]. The latter is then produced by a change of the apparent extent in the space between the aligned elements, with consequent change in apparent oblique direction. It follows that the illusion is consistently more perceptually significant in those figures in which one or more obtuse angles occurred [107]. The latter effect can also be called shrinkage of the modal space (the space between the transversal), see [164, 40] and for a similar approach [162]. However, the same authors that claimed for such theory, in later works rejected it through experimental findings, and a uniform interpretation for this phenomenon is still missing. See, for instance, Weintraub [180], 1993, and Day, [43], 1987. Another possible explanation for the phenomenon was the misperception of the orientation of the transversal in the stimulus, the so called regression to right angles tendency presented in [13, 89, 90], in which the misalignment in the Poggendorff illusion is attributed to an apparent angular displacement of the transversals towards a right angle with the parallels, seemed to be insufficient to explain this phenomenon. For example, see figure 7.7, left, it does not account for the abolishment of the effect when only acute angles are shown. However, these studies

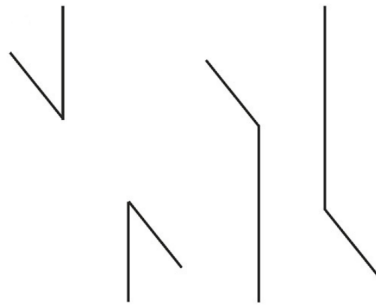


Figure 7.7: From Weintraub and Talasli, see [181, 162], left: the Poggendorff illusion reduced to its acute angular components. Any illusory effect is perceived. Right: the illusion still holds keeping the obtuse components of the Poggendorff stimulus.

were fundamental because they allowed to measure the geometrical components participating to the illusion. As it has already been measured by Weintraub and Krantz in [181], the actual size of the obtuse angle and of the central bar account for the magnitude of the Poggendorff illusion. We should not look for an explanation related to the regression of right angle of the transversal because, as explained in chapter 6, it is a certain number of orientations spiking in a neighbourhood of a spatial point that gives birth to a displacement and a regression to right angle phenomenon (the displacement decreases linearly with the decreasing number of lines which intersect, see the

modified Hering illusion example). In the Poggendorff example only two orientations cross. Another component which seems to play a role, see Weintraub [182] and Ninio [130] is the orientation at which the figure is presented. Even if the illusory effect still holds, it decreases and increases in dependence of the angle used to rotate the standard Poggendorff stimulus. Even if our model still does not account for this last component, because our setting is invariant for rotations and translations, we believe that our explanation is the most near to the real behaviour of the cortex in presence of this stimulus. If the inducers are able to cortical represent the central surface (figure 7.7 right) the illusion is still present. Otherwise (figure 7.7 left) no. Furthermore, as we already said in chapter 6, our approach is in accordance with Bayesian learning theory. Then our findings are in accord with the ones obtained by Howe et al. [92], who were able to fully account for all the possible behaviour of the Poggendorff illusion and other GOIs [91]. The perceptual representation of the central surface induces a misperception of the two segments belonging to the same transversal. This happens because the path joining the two segment (which can be substituted also by two dots) is not the minimum (in length) if we consider the natural metric of the cortex. Then the perceptual curve for such phenomenon projects at some point over the parallel, different from the natural alignment. We will be looking for the perceptual curve as a length minimizer in our metric (7.2).

#### 7.4.1 Polarization of the metric

In the Poggendorff illusion two main effects occur, as the reader may have understood. First the central surface is detected, as we clearly perceive in figure 7.5. This suggests that either the central surface is indentified by its boundaries, or it is of constant color (see fig 7.8) it affects the perception of the image.

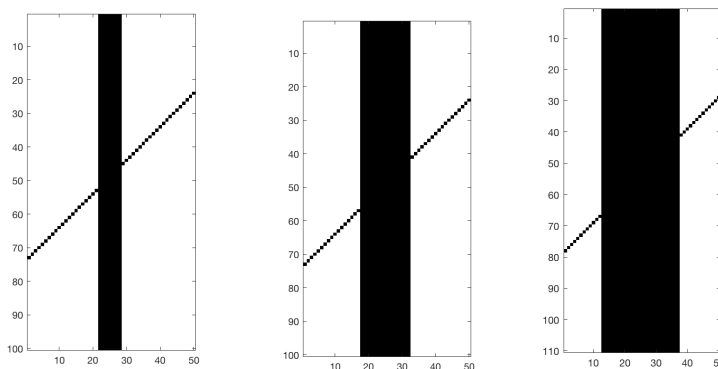


Figure 7.8: Poggendorff stimulus, with modified width of the central bar. From left to right: 7 pixels , 15 pixels, 25 pixels, orientation angle of the transversal  $\pi/4$ .

Then there is a misalignment of the two crossing transversals,

and the illusion arises. In presence of the initial stimulus of the Poggendorff illusion, even gabor filters, which are able to detect contours, give the same non vanishing response either we work with the central surfaces and lines. Then we can discard this constant contribution and focus only on the one provided by Odd Gabor filters. Their contribution selects only the central surface. Indeed

- (1) Odd receptive profiles are able to detect the boundaries of the central surface. Indeed their response is maxima along contours in which polarity plays a role. Polarity means that contours with the same orientation but opposite contrast are referred to opposite angles (see [60]). For this reason we assume that the orientation  $\theta$  takes values in  $[0, 2\pi)$ , while considering odd filters.
- (2) The contribution of odd receptive profiles is null along a straight line. Indeed along a straight line, (see 7.9 left) the only non vanishing contribution is given by the convolution of the initial stimulus with the bank of Even Gabor filters.

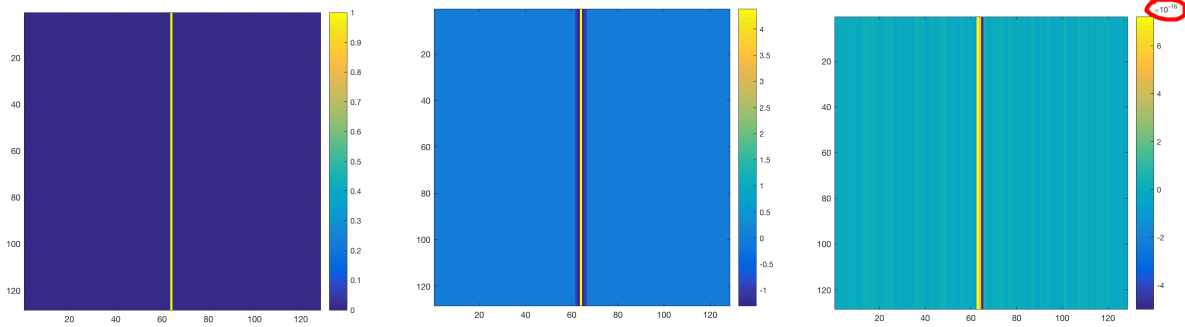


Figure 7.9: Left: a straight line, initial stimulus. Center: the sum along  $\theta$  of the responses to the stimulus of Even Gabor filters. It is not null. Right: same summation along  $\theta$  of the Odd Gabor filters. This last contribution is null along a line.

It follows that the analysis of the three Poggendorff illusions in 7.8 can be reduced to the processing of the images in 7.10, in which we neglect the presence of the entry transversals. The expression of the metric in 7.2 with respect to the Euclidean frame becomes:

$$h^{ij}(x_1, x_2, \theta) = R(x_1, x_2, \theta) \begin{pmatrix} \cos^2 \theta & \sin \theta \cos \theta & 0 \\ \sin \theta \cos \theta & \sin^2 \theta & 0 \\ 0 & 0 & 1 \end{pmatrix}, \quad (7.7)$$

where  $R(x_1, x_2, \theta)$  is the odd filters response opportunely shifted to positive values to be used as weight for the metric:

$$R(x_1, x_2, \theta) = \frac{1 + \text{Im}(O(x_1, x_2, \theta))}{\sqrt{1 + \text{Im}(O(x_1, x_2, \theta))^2}} \quad (7.8)$$

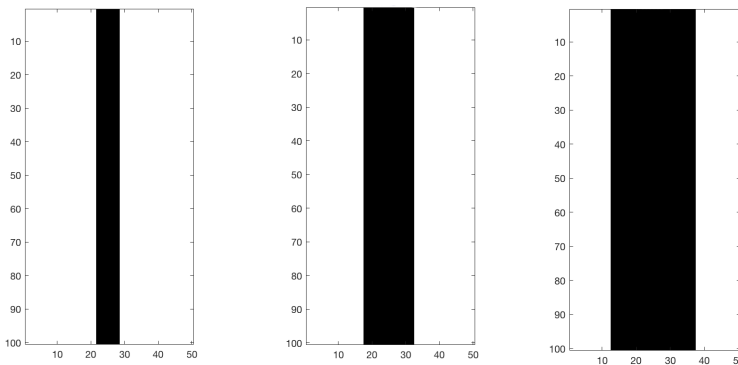
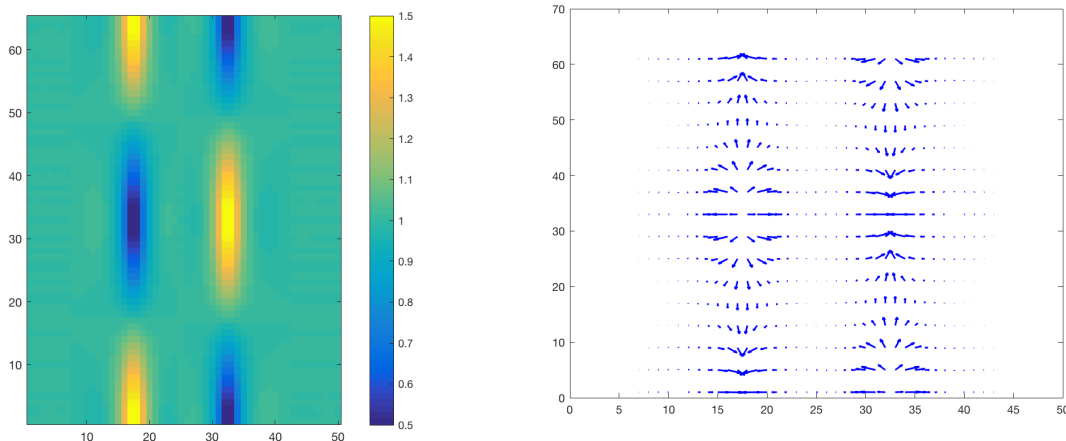


Figure 7.10: Simplified Poggendorff stimulus, with width of the central bar changed. From left to right: 7 pixels, 15 pixels, 25 pixels.

### 7.4.2 The experiment

Let us now go through the implementation process and its parameters. The first part of the processing consists in convolving



the initial image 7.10 with a bank of odd Gabor filters with the following parameters:  $\gamma = 1.5$ ,

$$\theta \in \left\{ -\pi, -\pi + \frac{2\pi}{N}, \dots, \pi - \frac{2\pi}{N}, \pi \right\}$$

( $N = 65$  values),  $\sigma \in \{2, 4\}$  (pixels, for central surfaces width = 15, 25 pixels),  $\sigma = 1$  for central surface width = 7,  $\frac{\sigma}{\lambda} = 2$ . The convolution produces a response, opportunely shifted to positive values:  $R(x_1, x_2, \theta)$ . It corresponds to the polarization of our sub-Riemannian metric and will be used as weight for the connectivity. Figure 7.11 (left) shows a section of the graph of  $R(x_1, x_2, \theta)$ ,  $(x_1, x_2, \theta, R(x_1, x_2, \theta))$ , for  $x_2$  fixed. In figure 7.11 (right) it is visualized  $\nabla R(x_1, x_2, \theta)$ , the gradient of  $R(x_1, x_2, \theta)$ , the cost used in the sub-Riemannian Fast-marching. Up to the Riemannian approximation this gradient directly determines the Christoffel symbols  $\Gamma_{ij}^k$  which define completely the affine Levi-Civita connection arising from the Riemannian approximation of the metric. Here we omitted the dependence on  $\epsilon$  to

Figure 7.11: Left: Representation of a section of  $(x_1, x_2, \theta, R(x_1, x_2, \theta))$ , graph of  $R(x_1, x_2, \theta)$ , for  $x_2$  fixed.  $R(x_1, x_2, \theta)$  is the output positively shifted of odd receptive profiles of simple cells.  $R(x_1, x_2, \theta)$  is constant along  $x_2$ . Right:  $\nabla R(x_1, x_2, \theta)$  is visualized in correspondence of the contours of the central bar, projected onto the  $(x_1, \theta)$  plane. We represent  $x_1$ , and  $\theta$  component of  $\nabla R$ , since the  $y$  component vanishes.

simplify notations. From  $\Gamma_{ij}^k$  it is possible to deduce the equation of the geodesics in  $\mathbb{R}^2 \times S^1$  in the riemannian approximation and letting  $\epsilon$  go to 0, to obtain the sub- Riemannian geodesics. For

$$\begin{aligned}
\Gamma[1, 1, 1] &= -\frac{2(-1+\epsilon^2)(1+\epsilon^2+(-1+\epsilon^2)\cos[2t])\sin[2t]R^{(0,1,0)}[x,y,t]+(-1+10\epsilon^2-\epsilon^4+(-1+\epsilon^2)^2\cos[4t])R^{(1,0,0)}[x,y,t]}{16\epsilon^2R[x,y,t]} \\
\Gamma[1, 2, 1] &= -\frac{(\cos[t]^2+\epsilon^2\sin[t]^2)((\epsilon^2\cos[t]^2+\sin[t]^2)R^{(0,1,0)}[x,y,t]-(-1+\epsilon^2)\cos[t]\sin[t]R^{(1,0,0)}[x,y,t])}{2\epsilon^2R[x,y,t]} \\
\Gamma[1, 2, 2] &= \frac{(\cos[t]^2+\epsilon^2\sin[t]^2)(-(-1+\epsilon^2)\cos[t]\sin[t]R^{(0,1,0)}[x,y,t]+(\cos[t]^2+\epsilon^2\sin[t]^2)R^{(1,0,0)}[x,y,t])}{2\epsilon^2R[x,y,t]} \\
\Gamma[1, 3, 1] &= \frac{1}{2}\left(-\frac{(-1+\epsilon^4)\cos[t]\sin[t]}{\epsilon^2}-\frac{R^{(0,0,1)}[x,y,t]}{R[x,y,t]}\right) \\
\Gamma[1, 3, 2] &= \frac{(-1+\epsilon^2)(1-\epsilon^2+(1+\epsilon^2)\cos[2t])}{4\epsilon^2} \\
\Gamma[1, 3, 3] &= \frac{-(-1+\epsilon^2)\cos[t]\sin[t]R^{(0,1,0)}[x,y,t]+(\cos[t]^2+\epsilon^2\sin[t]^2)R^{(1,0,0)}[x,y,t]}{2R[x,y,t]} \\
\Gamma[2, 1, 1] &= \frac{(\epsilon^2\cos[t]^2+\sin[t]^2)((\epsilon^2\cos[t]^2+\sin[t]^2)R^{(0,1,0)}[x,y,t]-(-1+\epsilon^2)\cos[t]\sin[t]R^{(1,0,0)}[x,y,t])}{2\epsilon^2R[x,y,t]} \\
\Gamma[2, 2, 1] &= \frac{(\epsilon^2\cos[t]^2+\sin[t]^2)((-1+\epsilon^2)\cos[t]\sin[t]R^{(0,1,0)}[x,y,t]-(\cos[t]^2+\epsilon^2\sin[t]^2)R^{(1,0,0)}[x,y,t])}{2\epsilon^2R[x,y,t]} \\
\Gamma[2, 2, 2] &= \frac{(1-10\epsilon^2+\epsilon^4-(-1+\epsilon^2)^2\cos[4t])R^{(0,1,0)}[x,y,t]+2(-1+\epsilon^2)(-1-\epsilon^2+(-1+\epsilon^2)\cos[2t])\sin[2t]R^{(1,0,0)}[x,y,t]}{16\epsilon^2R[x,y,t]} \\
\Gamma[2, 3, 1] &= \frac{(-1+\epsilon^2)(-1+\epsilon^2+(1+\epsilon^2)\cos[2t])}{4\epsilon^2} \\
\Gamma[2, 3, 2] &= \frac{(-1+\epsilon^4)\cos[t]R[x,y,t]\sin[t]-\epsilon^2R^{(0,0,1)}[x,y,t]}{2\epsilon^2R[x,y,t]} \\
\Gamma[2, 3, 3] &= \frac{(\epsilon^2\cos[t]^2+\sin[t]^2)R^{(0,1,0)}[x,y,t]-(-1+\epsilon^2)\cos[t]\sin[t]R^{(1,0,0)}[x,y,t]}{2R[x,y,t]} \\
\Gamma[3, 1, 1] &= \frac{(-1+\epsilon^2)R[x,y,t]\sin[2t]+(\epsilon^2\cos[t]^2+\sin[t]^2)R^{(0,0,1)}[x,y,t]}{2\epsilon^2R[x,y,t]} \\
\Gamma[3, 2, 1] &= -\frac{(-1+\epsilon^2)(2\cos[2t]R[x,y,t]-\sin[2t]R^{(0,0,1)}[x,y,t])}{4\epsilon^2R[x,y,t]} \\
\Gamma[3, 2, 2] &= \frac{-(-1+\epsilon^2)R[x,y,t]\sin[2t]+(\cos[t]^2+\epsilon^2\sin[t]^2)R^{(0,0,1)}[x,y,t]}{2\epsilon^2R[x,y,t]} \\
\Gamma[3, 3, 1] &= -\frac{R^{(1,0,0)}[x,y,t]}{2R[x,y,t]} \\
\Gamma[3, 3, 2] &= -\frac{R^{(0,1,0)}[x,y,t]}{2R[x,y,t]} \\
\Gamma[3, 3, 3] &= -\frac{R^{(0,0,1)}[x,y,t]}{2R[x,y,t]}
\end{aligned}$$

this reason the behaviour of  $\nabla R(x_1, x_2, \theta)$  in figure 7.11 (right) already gives us intuitively an idea of the path followed by the computed geodesics, for example for initial angle  $\theta = 0$  the flow individuated by the gradient shows no deflection, as perceptually expected if inducers are orthogonal to the central bar. A Mathematica (Wolfram Alpha) notebook allows to compute Christoffel symbols given a certain metric. In figure 7.12 we show the symbols for the Riemannian approximation of the metric in formula 7.7. Now that all preliminaries have been clarified, it is possible to choice initial point and final point for the geodesic we want to compute. Still, when we look at an image such as the Poggendorff illusion, we do know that the

Figure 7.12: The Christoffel symbols computed through a Notebook in Mathematica, relative to the metric in formula 7.7. Here  $(x_1, x_2, \theta)$  are encoded as  $(x, y, t)$  and  $R^{(1,0,0)}$  denotes the derivative along the coordinate  $x$  of  $R(x_1, x_2, \theta)$ , i.e. the first component of the gradient. In red it is marked how  $\nabla R(x_1, x_2, \theta)$  affects the Christoffel symbols and as a consequence geodesics equations.

transversal are not perceived as collinear, but we want to be able to draw the perceptual projection for such stimulus, and to identify it. In other words, we want to determine where the left transversal projects over the right parallel (equal to identify the red segment in figure 7.6). Then we will fix the initial seed and give as final tips a discretization of points along the right bar, from the geometrical collinear transversal to the orthogonal projection of the left transversal over the right parallel, see figure 7.13.

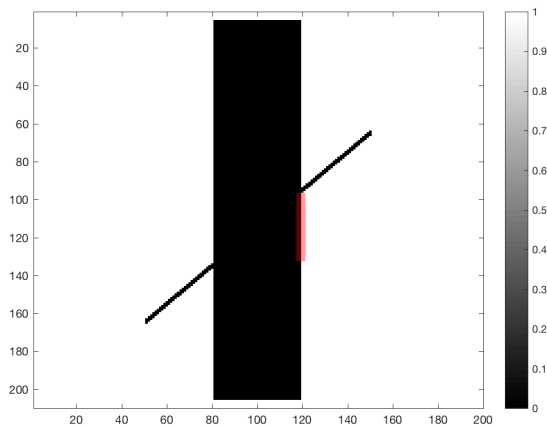


Figure 7.13: Tips for the perceptual completion curve are chosen along the bar in the Red zone.

### 7.4.3 Results

As we already saw in the introduction of this section, manipulating the elements participating to the Poggendorff illusions to understand how to magnify the illusory phenomena has been done in many works, for instance in Day et al. [42], page 545, Burmester in [18], Weintraub and Krantz in [181].

Measurements have been performed, see figure 7.4.3, as follows: the observer was asked, looking at the Poggendorff stimulus, to move the right transversal in order to put it in a perceptual collinear position with the left transversal. This implies that the right transversal is displaced along the right parallel: the measured displacement is called *underestimation* in figure 7.4.3, and it is possible to see how it changes modifying the size of the central surface and the orientation of the transversal. In figure 7.15 and 7.16 some frame of two video representation the change in magnitude of the Poggendorff illusion varying the size of the central surface and the orientation of the transversal cutted by the central surface.

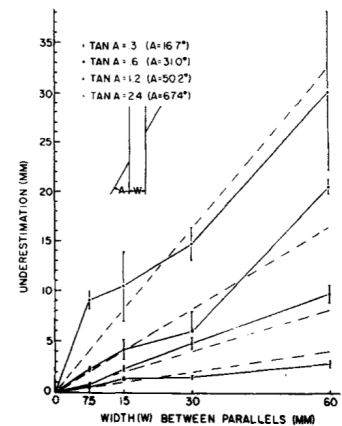


Figure 7.14: From [181]: quantitative measurements of the magnitude of the Poggendorff illusion varying the angle of the entry transversal and the central surface width.

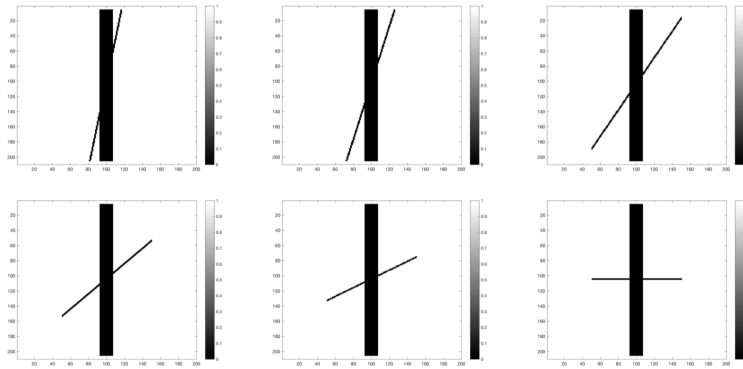


Figure 7.15: These images constitute single frames of a video which shows how the magnitude of the Poggendorff illusion changes varying the entry angle of the transversals. If the consider transversal is perpendicular to the central surface, the illusory effect is abolished.

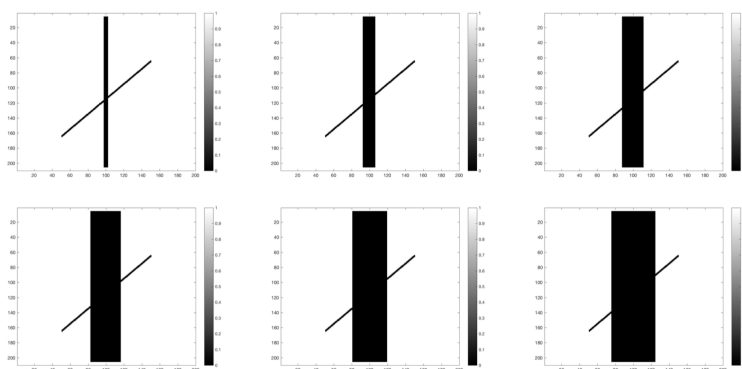


Figure 7.16: These images constitute single frames of a video created by the author which shows how the magnitude of the Poggendorff illusion changes varying the size of the central bar. As shown, increasing this size produces a magnification of the illusory effect, while if we consider a width of the central surface tending to 0, the illusory effect is abolished.

**Processing of the Initial Stimuli** In figure 7.18 we show all the Poggendorff illusions, with also the transversals drawn, that have been considered in order to evaluate and compute the perceptual collinear transversal. We recall that the transversal have been used only to determine the boundary conditions. The width of the central surface had the following values (in pixels): 7, 15, 25. The angles of the entry transversal, i.e. the acute component of the initial stimuli shown in figure 7.18, are:  $\theta = \pi/4, \pi/6, \pi/11, \pi/2$ . The images are  $100 \times 50$  (except for the one with central surface equal to 25 pixels which is  $110 \times 50$ ). Once we compute the response and we properly compute  $R(x_1, x_2, \theta)$  (figure 7.17), we are ready to use it as external cost (polarization of the metric) for the sub- Riemannian Fast- Marching. The metric  $h^{ij}(x_1, x_2, \theta)$  in formula (7.7) will be implemented with the following expression:

$$h^{ij}(x_1, x_2, \theta) = R(x_1, x_2, \theta) \begin{pmatrix} \xi^{-2}(\cos^2 \theta + \varepsilon^2 \sin^2 \theta) & \xi^{-2}(1 - \varepsilon^2) \sin \theta \cos \theta & 0 \\ \xi^{-2}(1 - \varepsilon^2) \sin \theta \cos \theta & \xi^{-2}(\sin^2 \theta + \varepsilon^2 \cos^2 \theta) & 0 \\ 0 & 0 & 1 \end{pmatrix}, \quad (7.9)$$

The parameter  $\xi$  modulates the anisotropy between the two direction,  $\xi \Delta x_1 = \Delta \theta$ , where  $\Delta x_1, \Delta \theta$  are the discretization steps along  $x_1$  and  $\theta$ . It then depends on the entry angle for the transversal and the width of the surface chosen for the experiments: it is directly proportional to the width of the central surface and it varies with a ratio 1/3 if we consider the angle change. Table 7.4.3 shows the values of  $\xi$  for the presented experiments.

$\xi$	Width = 7 pix	Width = 15 pix	Width = 25 pix
$\theta = \pi/4$	0.51	1.09	1.82
$\theta = \pi/6$	0.77	1.64	2.74
$\theta = \pi/11$	1.42	3	5
$\theta = \pi/2$	0.26	0.55	0.92

The parameter  $\varepsilon$  indicates the Riemannian approximation and in our experiments is set equal 0.1. As we said, we only fix the initial point, which will be in all the experiments the crossing point of the left transversal with the parallel, for example for width = 15 and  $\theta = \pi/4$  it is  $\eta_0 = (17, 57, \pi/4)$ , and we let the final points varying along the right parallel as shown in figure 7.13. Then the final points will all share the same  $x_1$  component (i.e. the  $x_1$ - coordinate of the right parallel, 33) and the  $\theta$  component,  $\theta = \pi/4$ , because we know that the perceptual transversal will be parallel to the geometrical collinear one.

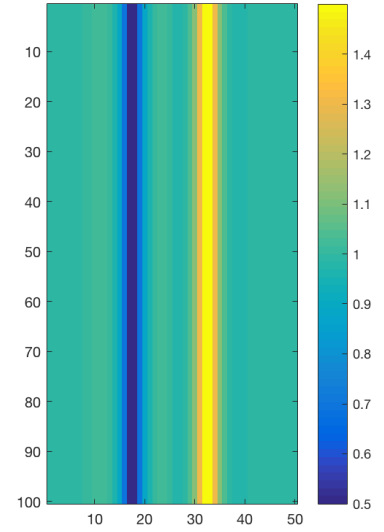


Figure 7.17: Representation of a level set of the cost  $R(x_1, x_2, \theta)$ , output of odd Gabor filter, positively shifted, for  $\theta = 0$ . The maximum of  $R(x_1, x_2, \theta)$  over  $\theta$  is reached over the right bar.

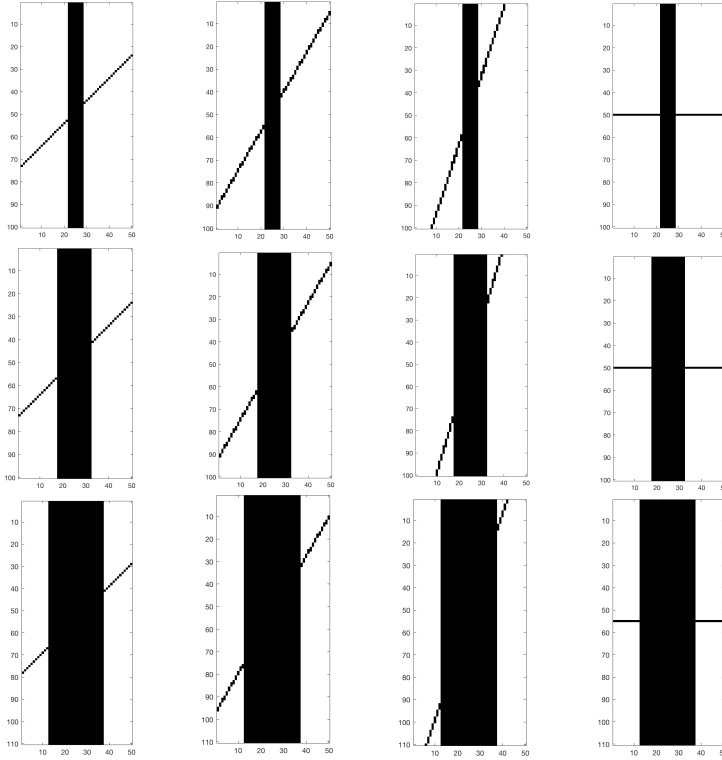


Figure 7.18: Initial stimuli processed in this work. Top: fixed width = 7 pixels, varying the orientation from left to right:  $\theta = \pi/4, \pi/6, \pi/11, \pi/2$ . Central: fixed width = 15 pixels, varying the orientation from left to right:  $\theta = \pi/4, \pi/6, \pi/11, \pi/2$ . fixed width = 25 pixels, varying the orientation from left to right:  $\theta = \pi/4, \pi/6, \pi/11, \pi/2$ .

Once all the parameters and boundary conditions have been set, it is possible to run the sub- Riemannian Fast- Marching, in order to compute the distance map, see figure 7.19, from the initial point, solution of the Eikonal equation (7.3). Geodesics are obtained through gradient descent over the distance map, see section 7.3.2, from the set final points.

**Computed Geodesics** As we said in the previous section, in figure 7.20 we show the computed geodesics for each stimulus in figure 7.18. From each initial point, multiple endpoints (tips) were chosen and the corresponding geodesics have been plotted. In red we put in evidence the 2D projection of the curves, while in cyan we underline the length minimizers. The perceptual geodesic (cyan) is the shortest one. In this way we identify the  $x_2$ - component of the perceptual transversal, and we finally get all the coordinates  $(x_1, x_2, \theta)$  for drawing it. For the representation of the perceptual transversal recovered through the presented method, see figure 7.22. In figure 7.21 we show how the length of the computed geodesics varies along the  $x_2$ - component of the right parallel. The graph in figure 7.21 has on its  $x$ - axis the  $x_2$ - component of the right parallel, while on its  $y$ - axis the correspondent lengths. The dot in cyan identifies the minimum, which corresponds to the curve colored in cyan in figure 7.20. It has been obtained for width = 15 pix-

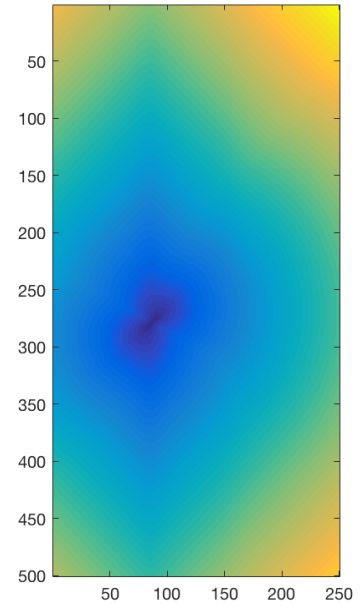


Figure 7.19: Minimum of distance map  $W(\eta)$  from the boundary value condition (initial seed)  $\eta_0 = (17, 57, \pi/4)$  of equation (7.3), along the direction  $\theta$ , computed through SR-Fast-Marching.

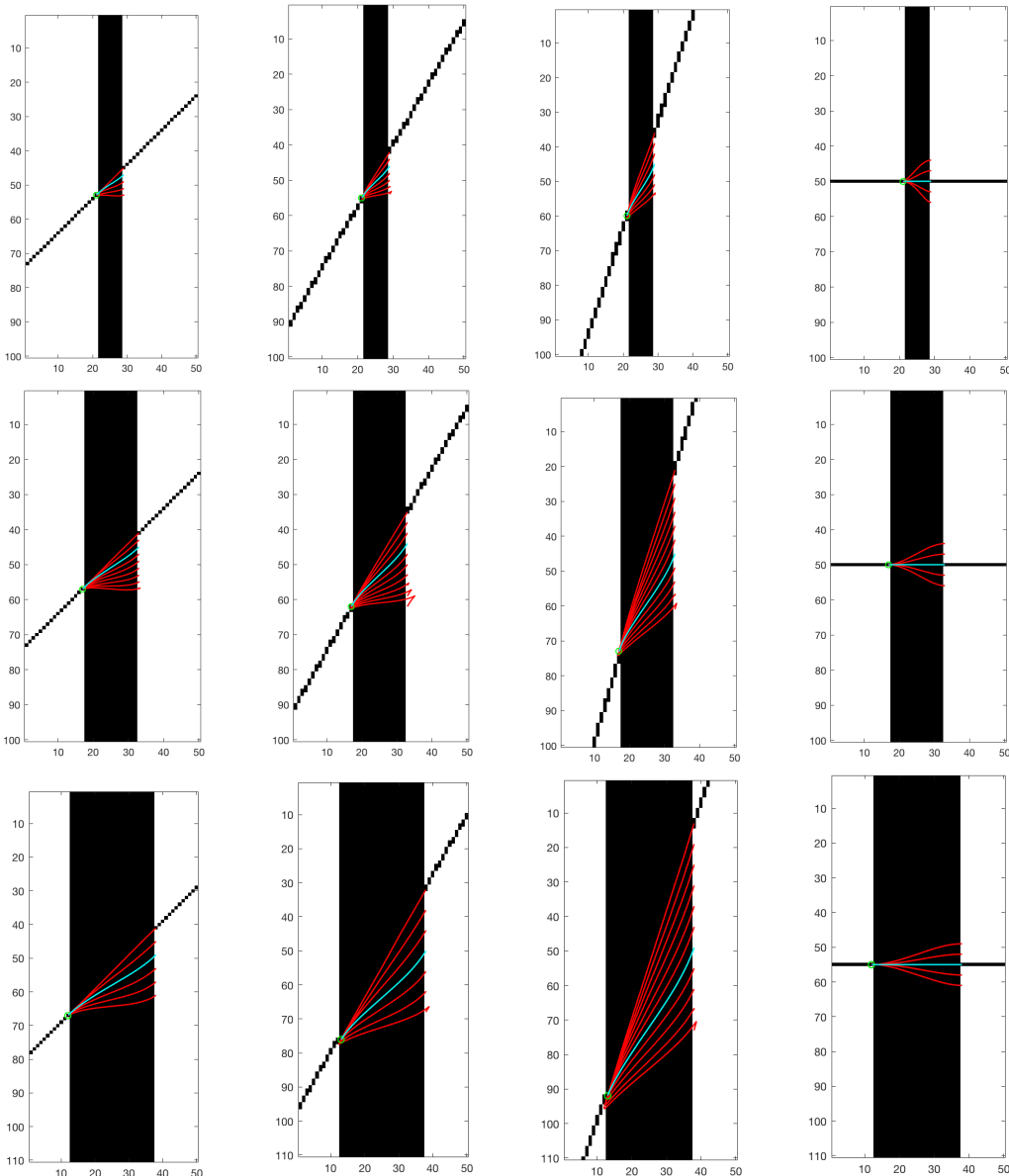


Figure 7.20: Computed geodesic with multiple endpoints (tips). In cyan we color the length minimizer. Fixed width = 7, 15, 25 pixels, varying the orientation from left to right:  $\theta = \pi/4, \pi/6, \pi/11, \pi/2$ .

els and  $\theta = \pi/4$ , but this representation has the same qualitative trend for all presented experiments. Finally in figure 7.23 we show a 3D representation of a couple of geodesics computed for  $\theta = \pi/4$  and the width of the central surface is 15 pixels. Seed = (18, 56,  $\pi/4$ ) and final tips for the geometrical and perceptual collinear are Tip1 = (32, 41,  $\pi/4$ ) and Tip2 = (32, 45,  $\pi/4$ ) respectively. Again, the sub-Riemannian length of the red curve is 2.0480 pixels (the one which connects to actual collinear transversals), and the sub-Riemannian length of the blue curve is 1.8094 (the perceptual collinear transversal). Then as expected, the shortest curve implemented through the considered metric is the perceptual one.

**Remark 7.4.1.** In the Euclidean setting this model would not have worked, since the minimum in the Euclidean metric would

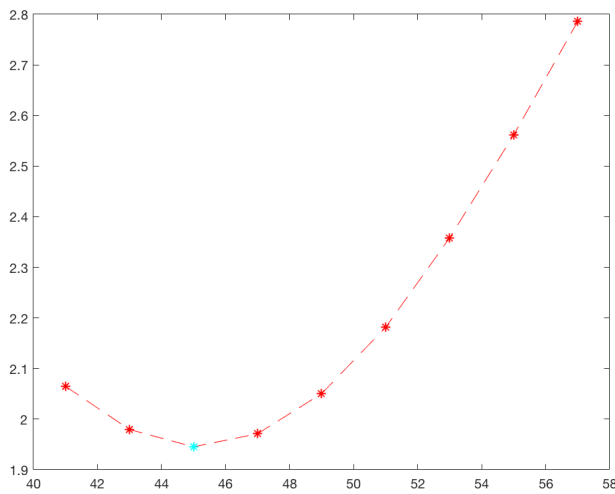


Figure 7.21: Here we show how the length of the computed geodesics varies along the  $x_2$ -component of the right parallel. The graph has on its  $x$ -axis the  $x_2$ -component of the right parallel, while on its  $y$ -axis the correspondent length. The dot in cyan identifies the minimum, which corresponds to the curve colored in cyan in figure 7.20. It has been obtained for width = 15 pixels and  $\theta = \pi/4$ .

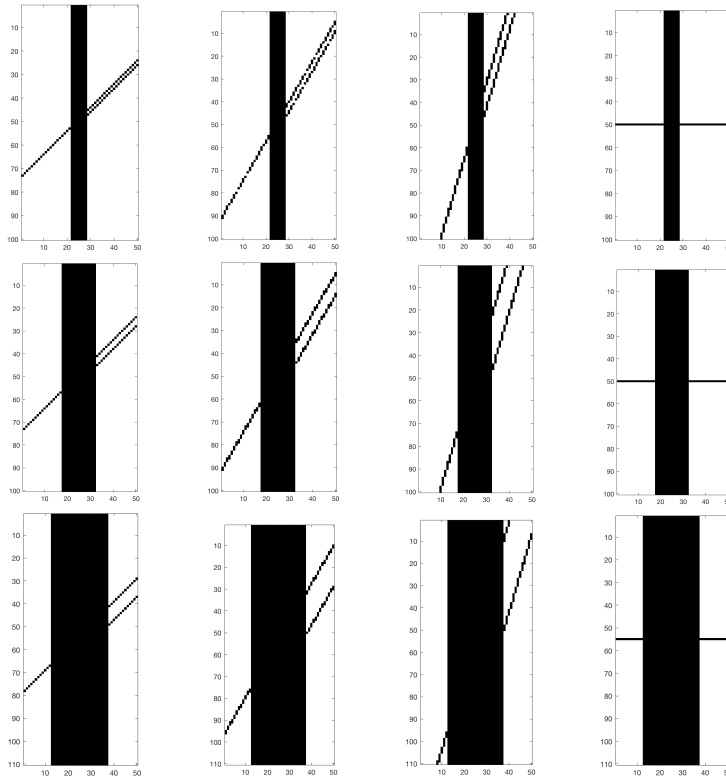


Figure 7.22: Representation of the perceptual transversal: as explained in section 7.4.3, once all geodesics have been computed, we pick up the length minimizer. Its corresponding final point gives us the coordinates of the perceptual transversal. Top: fixed width = 7 pixels, varying the orientation from left to right:  $\theta = \pi/4, \pi/6, \pi/11, \pi/2$ . Central: fixed width = 15 pixels, varying the orientation from left to right:  $\theta = \pi/4, \pi/6, \pi/11, \pi/2$ . fixed width = 25 pixels, varying the orientation from left to right:  $\theta = \pi/4, \pi/6, \pi/11, \pi/2$ .

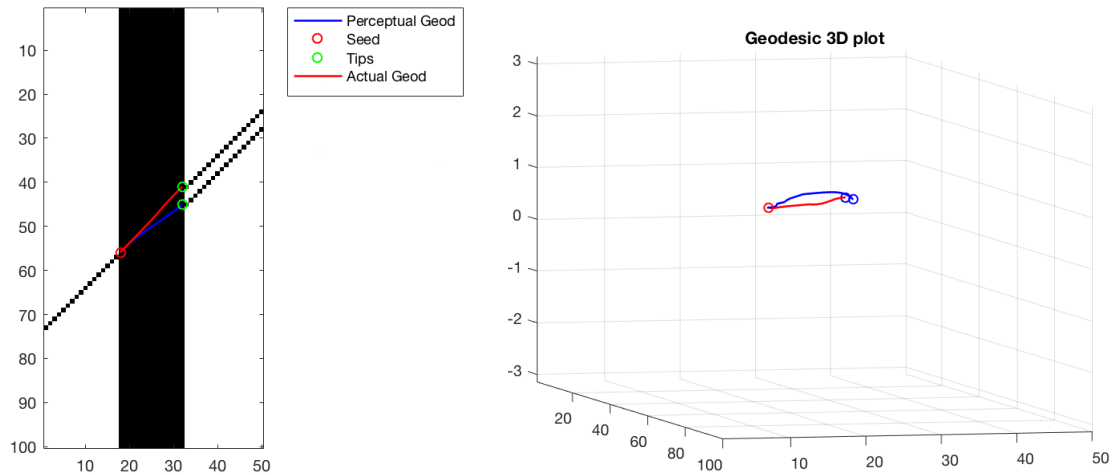


Figure 7.23: Left: 2D projection of the computed geodesics. The perceptual curve is blue, the actual completion of the left side transversal is the red curve. Right: 3D plot of the computed geodesics.

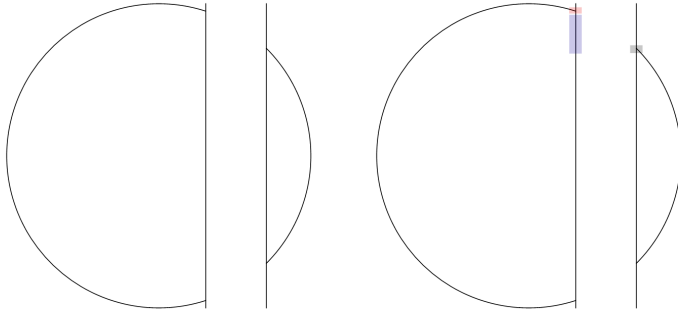
have been the horizontal line, starting from the left crossing point between the transversal and the surface and projecting on the right side of the central bar. The sub-Riemannian metric we have introduced depends on the orientation of the transversal line. Hence if this is not horizontal, also the minimum is not the horizontal line, it is the curve marked in cyan (figure 7.20). This explains that this model captures the phenomenon and that the intrinsic geometry of the cortex responds to the sub-Riemannian model introduced in this thesis.

**Summary** In this paragraph a table reporting the collected data concerning the sub-Riemannian lengths of the computed curves are presented for width of the central surface equal to 15 pixels, angles of the transversal varied in the range presented before. It refers to the change of length if we consider the perceptual curve and the one connecting the geometric collinear transversals.

Type of curve	Width = 15 pixels
Perceptual curve $\theta = \pi/4$	1.945
Actual curve $\theta = \pi/4$	2.065
Perceptual curve $\theta = \pi/6$	1.64
Actual curve $\theta = \pi/6$	1.88
Perceptual curve $\theta = \pi/11$	1.32
Actual curve $\theta = \pi/11$	1.78
Perceptual curve $\theta = \pi/2$	2.92

## 7.5 Round Poggendorff

In this section a variant of the original Poggendorff illusion presented in figure 7.5 is presented. The modified illusion, which will be called Round Poggendorff, is shown in figure 7.24. The



presence of the central surface induces a misperception of the circle, as if the two cutted parts of the circumference (one on the left of the surface and the other on the right) would not belong to the same circumference anymore. In other words, referring to the right figure in Fig. 7.24, the gray part instead of projecting from the perceptual point of view over the co-circular segment in red, it projects at some point at a certain orientation in the region highlighted in blue.

Figure 7.24: Left: Round (or Circular) Poggendorff illusion, see Talasli et al. see [162], fig 1B. Right: using the color notation in figure 7.6, we stress the fact that the gray segment doesn't project onto its co-circular correspondent segment (the red one). It projects at some point that our method wants to identify into the region marked in blue.

### 7.5.1 The experiment

Here the parameters which modulate the metric are  $\xi = 2.5$  and  $\varepsilon = 0.1$ . The seed fixed is  $(x_0, y_0, \theta_0) = (1/\sqrt{2}, 1/\sqrt{2}, -\pi/4)$  and then in order to compute the corrected perceptual completion curve we provide again a final set to the sub-Riemannian Fast-Marching. Possible final orientations detected space between  $[0, -\pi/10]$ , where  $\theta = 0$  is the angle corresponding to the orthogonal projection over the left bar and  $\theta = -\pi/10$  is the boundary condition of the circle at crossing point with the left bar. In an analogous way we took a discretization between possible values of the  $y$  coordinate and we run the Fast-marching, which is able to identify the minimal length curve given a certain seed and multiple tips (final points). Once again, the reason why we chose to perform such experiments is that we didn't not which was the right angle and  $y$  coordinate for the ending point of the perceptual curve. The SR length of minimizing geodesic is 1.32668. The endpoint for min geodesic is 0.31, 0.88, -0.27.

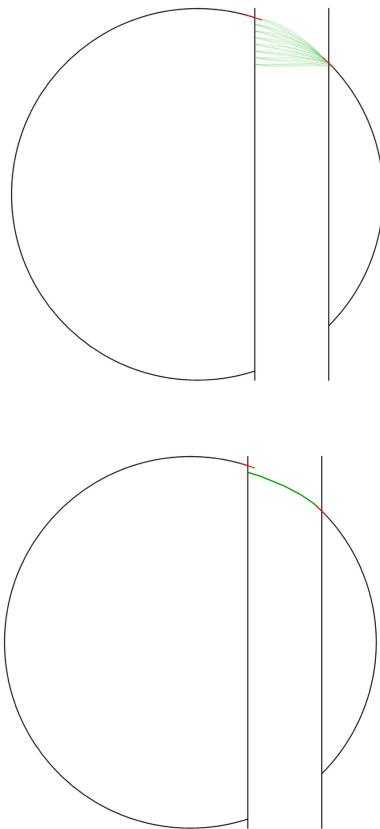


Figure 7.25: Top: Round (or Circular) Poggendorff illusion, from Talasli et al. see [162], fig 1B. Down: using the color notation in figure 7.6, we stress the fact that the gray segment doesn't project onto its co-circular correspondent segment (the red one). It projects at some point that our method wants to identify into the region marked in blue.

## 7.6 Discussion

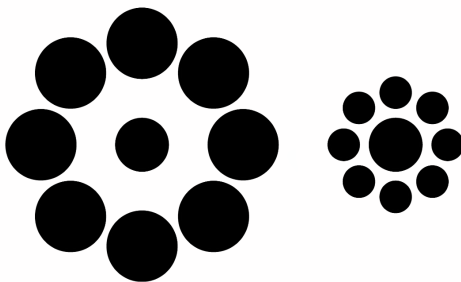
In this chapter we provide a neuro-mathematical model for the perceptual curves arising in phenomena such as the Poggendorff illusion. In this way, the perceptual collinear transversal, which was until now identified by means of psychophysical experiments, is determined through a neuro-geometrical method. In fact, those perceptual curves are found as sub-Riemannian length minimizers of a certain metric modulated by the output of simple cells of V1. This means that the reason why such phenomena arise needs to be found into a polarization of the connectivity performed by our low-level visual process. The presented study is able to fit the changes in the perceived magnitude of the illusion observed by many authors, see [181, 42], once the parameters for the computations are set. Further developments will be in the direction of fitting quantitative data already present in literature, as well as trying to take into account the rotation of the image (see [182]) as a contribution in the perceived magnitude of the illusion. Finally, we believe this method can be extended to other geometrical optical illusions (see figure 6.3) and it will provide important insights in identifying and representing the perceived curves arising in our cortex

while looking at these phenomena.



## 8 Scale/size Geometrical Optical Illusions

THE AIM of this chapter is to extend the model for geometrical optical illusions introduced in chapter 6 to scale- size illusions, those phenomena in which the interaction between objects of different size induce a misperception of the width of a target. If we look at images such as the ones presented in figures 8.1 and 8.2, known as Ebbinghaus and Delboeuf illusions respectively, the presence of circular inducers (figure 8.1) and of an annulus (figure 8.2) varies the perceived sizes of the central targets. These phenomena have been named for their discoverers, the German psychologist Hermann Ebbinghaus (1850–1909), and the Belgian philosopher and mathematician Joseph Remi Leopold Delboeuf (1831 – 1896), [47]. The Ebbinghaus phenomenon has been popularized in the English- speaking world by Edward B. Titchener in a 1901 textbook of experimental psychology, and this is the reason why it is also called Titchener illusion [143]. The main idea here is to identify a connectivity metric



from which it will be possible to compute the displacement and the corresponding perceived misperception. We will consider an isotropic functional connectivity depending on the detected scale and on the distance between the objects composing the stimulus. We will see how this phenomenon is implemented and provide with numerical simulation the perceived deforma-

Figure 8.1: Ebbinghaus (or Titchener) illusion: two circles of identical size are placed near to each other, and one is surrounded by large circles while the other is surrounded by small circles. In the left part of the stimulus, inducers are larger in size than the central circle, inducing a decreasing size-perception of the latter. In the same way when inducers are smaller in size than the target size, the size-perception of the latter increases.

tion. Our computations will be in agreement with judgemental studies of these phenomena [116], as well as the observation of how illusions change with the distance between target and inducers, [143]. These results will be contained in [65].

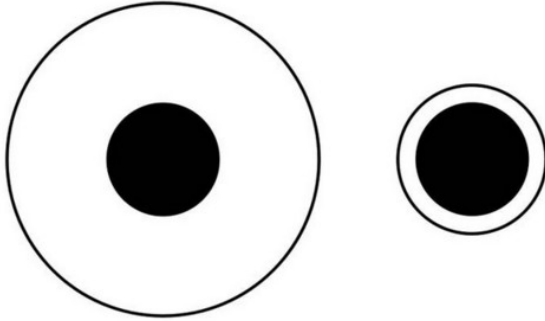


Figure 8.2: Delbouef illusion: the presence of an annulus around the target (black circle) induces a misperception of the size of the latter. If the annulus is big, the target tends to shrink or not displace at all (left). As long as we decrease its width, the target is perceived as expanding.

## 8.1 Scale and size of an object

The intuition of this work is to adapt the previous model of infinitesimal strain theory, chapter 6, section 6.3.1, to different stimuli, such as the ones involving the feature of *scale*, see figures 8.1, 8.2. Scale and size of an object are related concepts: if we consider receptive profiles modelled as Gabor filters, see equation (4.1), the scale  $\sigma$  encodes the distance from the boundary (see formula 4.1). For the extension of the cortical based model presented in chapter 4 to this feature see Sarti, Citti and Petitot in [154, 138]. *Size* is the spatial dimension of an object and is the maximum output of the scale. We compute it through a non-maximal suppression of the other values of scale within an object. The Ebbinghaus and Delboeuf illusions (figures 8.1, 8.2) are phenomena in which the context induces a misperception of the size of the central target, [108]. This means that the early visual process identifies the size of the objects composing an image and we evaluate the interaction between them. For example in figure 8.1 the circles are the perceptual units and we measure their interaction. In order to apply the model introduced in section 6.3.1 we need to modify the metric used for orientation- type illusions. Here we will consider the isotropic functional connectivity related to the detected scale: the activity equation that we will build will decrease with the distance between the objects of the image.

## 8.2 The model

In this section we develop and explain all the passages fundamental to understand the model we built for scale type illusory phenomena. Once the connectivity is described, it will be used as new strain metric tensor in order to allow us to repeat the modeling presented in section 6.3.1 and to recover the displacement vector fields induced by the size perception.

### 8.2.1 Distance selection in V1

It is well known that primary visual cortices are able to detect the distance of a point from the boundaries of the image. From a neurogeometric perspective, it means that we move from the space of rotations to the one of rotation and dilations, see [154] and [138]. Through the usual convolution process of an image with Gabor filters, described in chapter 4, formula (4.3), we are able to detect the response of the hypercolumns of simple cells varying the orientation feature  $\theta$  and the scale  $\sigma$  (section 4.2.2). The intra- cortical mechanism selects the maxima over

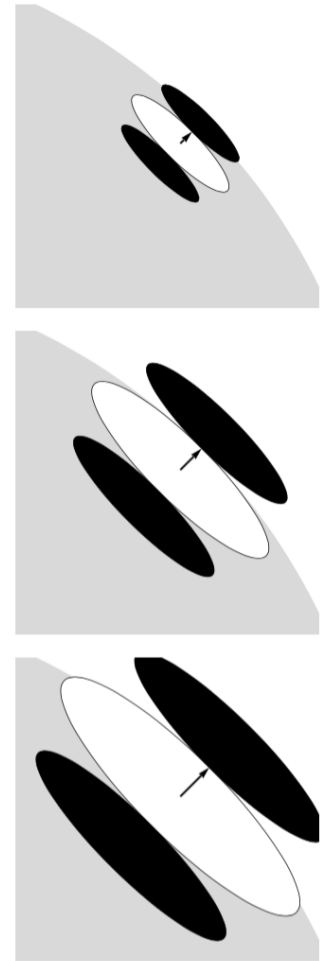


Figure 8.3: From Sanguinetti, [149]. The best scale  $\sigma$  for the gray boundary considered is represented in the middle image, in which the receptive profile is properly aligned, with a correct distance from the boundary.

the orientation and scale hypercolumns, providing the selection of two maximal outputs for both features:  $\bar{\theta}$  and  $\bar{\sigma}$ . In figure 8.4 (right) the selection of  $\bar{\sigma}$  performed through the convolution of the bank of Gabor filters with an initial stimulus (figure 8.4, left) is shown. Here we will discard the orientation selection and we focus on the scale detection. For each point the color identifies the distance  $\bar{\sigma}$  from the nearest boundary, selected over the hypercolumns containing all the possible distances  $\sigma$ .

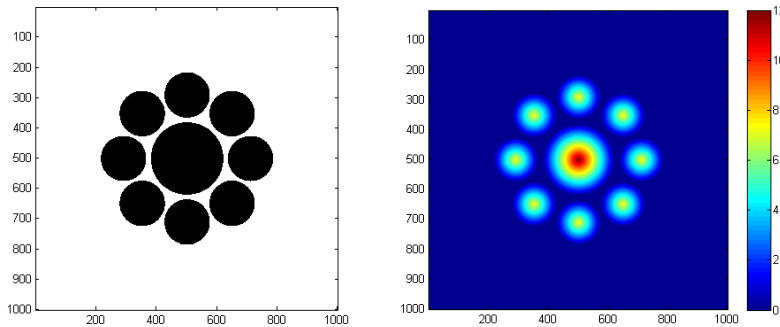


Figure 8.4: Left: the initial stimulus processed. Right: the maximum response  $\bar{\sigma}$  fixing  $\theta$ . For each point the color identifies the distance  $\bar{\sigma}$  from the nearest boundary, selected over the hypercolumns containing all the possible distances  $\sigma$ .

### 8.2.2 Non-maximal suppression

Once the  $\bar{\sigma}(x_1, x_2)$  has been constructed through the selectivity mechanism within the hypercolumnar structure, the aim is to compute the size of each perceptual unit, which is the maximum of  $\bar{\sigma}(x_1, x_2)$  for each considered object. We did it using an advection equation, which allowed us to propagate the maxima of each circle over the whole region. This permits to associate a single size value, called  $\rho(x_1, x_2)$  to each perceptual unit composing the image. Let us look for example at figure 8.5. Starting from the left map representing  $\bar{\sigma}(x_1, x_2)$ , we propagated the maximum information within each circle using an advection equation, (8.2.2) (i.e. motion of a conserved scalar field,  $\nabla \bar{\sigma}$  as it is advected by a known velocity vector field, in this case unitary). We also select the points  $(\bar{x}_1, \bar{x}_2)$  where the maximum is attained.

$$\frac{\partial \bar{\sigma}(x_1, x_2)}{\partial t} = -\nabla \cdot \nabla \bar{\sigma}$$

### 8.2.3 Connectivity expression for scale type illusion

Here we introduce the isotropic connectivity accounting for the interaction of points in scale illusions. Gabor filters are obtained through translation and dilation, hence with an action of a commutative group. It follows that for all  $(x_1, x_2, \sigma)$ , with  $\sigma$  constant, the metric is isotropic and the mechanism explained

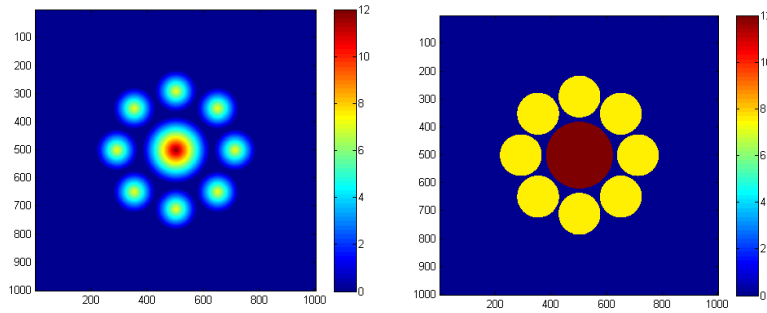


Figure 8.5: Left: representation of  $\bar{\sigma}(x_1, x_2)$ . Right: propagation of the information within each circle using an advection equation. This allows us to recover for each perceptual unit the corresponding value of size,  $\rho(x_1, x_2)$ .

in section 6.3.1 permits to build an isotropic connectivity metric. Once the stimulus has been acquired and the distance has been detected by simple cells of V1/V2 (figure 8.4), the size is evaluated (see figure 8.5). We consider the interaction between the scale of the perceptual units composing the stimulus. Let us consider for example the well-known Ebbinghaus illusion, see 8.1. The *target* circles (the central ones in figure 8.1) and their *inducers* are the perceptual objects. This example of illusion consists in perceiving the target circle as smaller (left) if the surrounding circles are larger, while the target is perceived as larger if the surrounding circles are smaller. The *perceived size of the target*, which is the perceptual component we want to evaluate in this study varies if the size of the inducers varies [116, 143] and if the distance between the inducers and the target increases or decreases [143]. The perceived size of the central target decreases if the distance among target and inducers increases. Albeit this last observation lead scientists to assimilate Ebbinghaus and Delboeuf illusion [79], we will show how the size of the annulus, and not only a matter of distance between the target and the circumference, will play a central role also in the Delboeuf illusion, see figure 8.2. The activity equa-

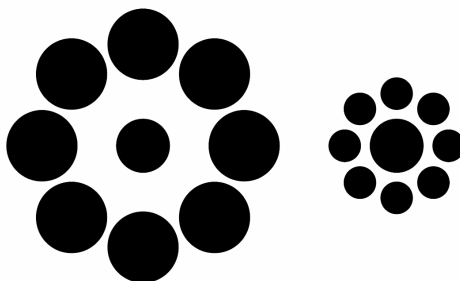


Figure 8.6: Ebbinghaus illusion: the size of the black inducers generates a misperception of the size of the central circle (orange). In the left part of the stimulus, black inducers are larger in size than the central orange circle, inducing a decreasing size-perception of the latter. In the same way when black inducers are smaller in size than the target size, the size-perception of the latter increases.

tion will be expressed as the product between a connectivity

kernel, which decreases with the distance between the considered points, and the computed sizes of the objects. function of the selected sizes of the objects.

$$\rho(x) = \int_{\mathbb{R}^2} \exp^{-c|x-x'|} (\rho(x') - \rho_0) dx' \quad (8.1)$$

where  $x = (x_1, x_2) \in \mathbb{R}^2$  denotes the coordinates of maximal scale of the central target,  $|x - x'|$  indicates the previously described Euclidean retinical distance in  $\mathbb{R}^2$ ,  $\rho_0$  is a global normalization term denoting the *effective size*. The integral can be reduced to the points  $(\bar{x}_1, \bar{x}_2)$  where the scale coincide with the size. From now on we will assume this simplification. Here the kernel is an exponential, but it can be modelled as a function decreasing with the distance. The term  $\rho_0$  is a mean value for

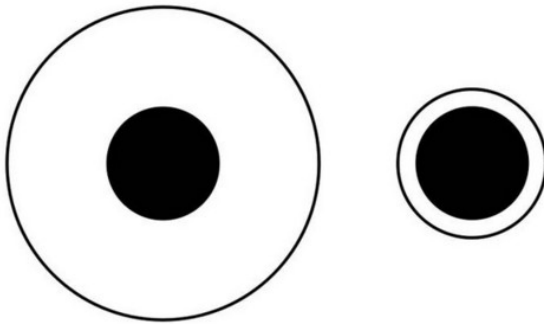


Figure 8.7: Delbouef illusion: the presence of a circumference around the target (black circle) induces a misperception of the size of the latter. If the circumference is situated at a consistent distance from the target, the target tends to shrink or not displace at all (left).

the activity and represents the effective size of the central target. Once the isotropic functional connectivity has been built, it is used as metric for the strain process explain in chapter 6, which allows us to recover the displacement vector field and to reconstruct the percept. However, it is still not clear where the final percept is built in our cortex.

### 8.3 Implementation and Results

In this section we present the implementation of the presented model and we discuss the test performed concerning the Ebbinghaus illusion (figure 8.1) and the Delbouef illusion (figure 8.2). Equation 8.1 becomes in its discretized form:

$$\rho(x) = \sum_{i=1}^N \exp^{-|x-x'|} (\rho(x') - \rho_0) \quad (8.2)$$

where  $N$  is the number of inducers, i.e. points  $(\bar{x}_1, \bar{x}_2)$  where the scale is maxima and coincide with the size.  $c = 1$ , the distance  $|x - x'|$  is expressed in pixels,  $\rho(x')$  is the size of the inducer at point  $x' = (x'_1, x'_2)$ . We always consider points of the image in which the maximum of the scale is attained.

### 8.3.1 Ebbinghaus illusion

We present the computed results through our method relative to the Ebbinghaus illusion. As is it shown, in paragraphs 8.3.1, 8.3.1, 8.3.1 we varied the number of inducers,  $N = 2, 4, 6$ , we kept the distance fixed  $|x - x'| = 6$  pixels,  $\rho_0 = 14.6$  pixels, and we varied the size of the inducers, which is constant for each stimulus,  $\rho(x') = \rho_0 - 8, \rho_0 - 4, \rho_0, \rho_0 + 4, \rho_0 + 8$  pixels respectively, from top to bottom of figure 8.8, 8.9, 8.10. For each row of the cited figures we present: left, the initial stimulus. In the central image it is presented the computed displacement through the infinitesimal strain theory approach introduced in chapter 6, section 6.3.3. Finally, the right image contains the perceived central target: we consider the initial stimulus and we apply vector fields  $\bar{u}(x_1, x_2)$  computed through our method. The red circle is the target reference of the initial stimulus, drawn in order to allow a comparison between the proximal stimulus (displaced image) and the distal one, [105, 77] (see chapter 2).

## Two inducers

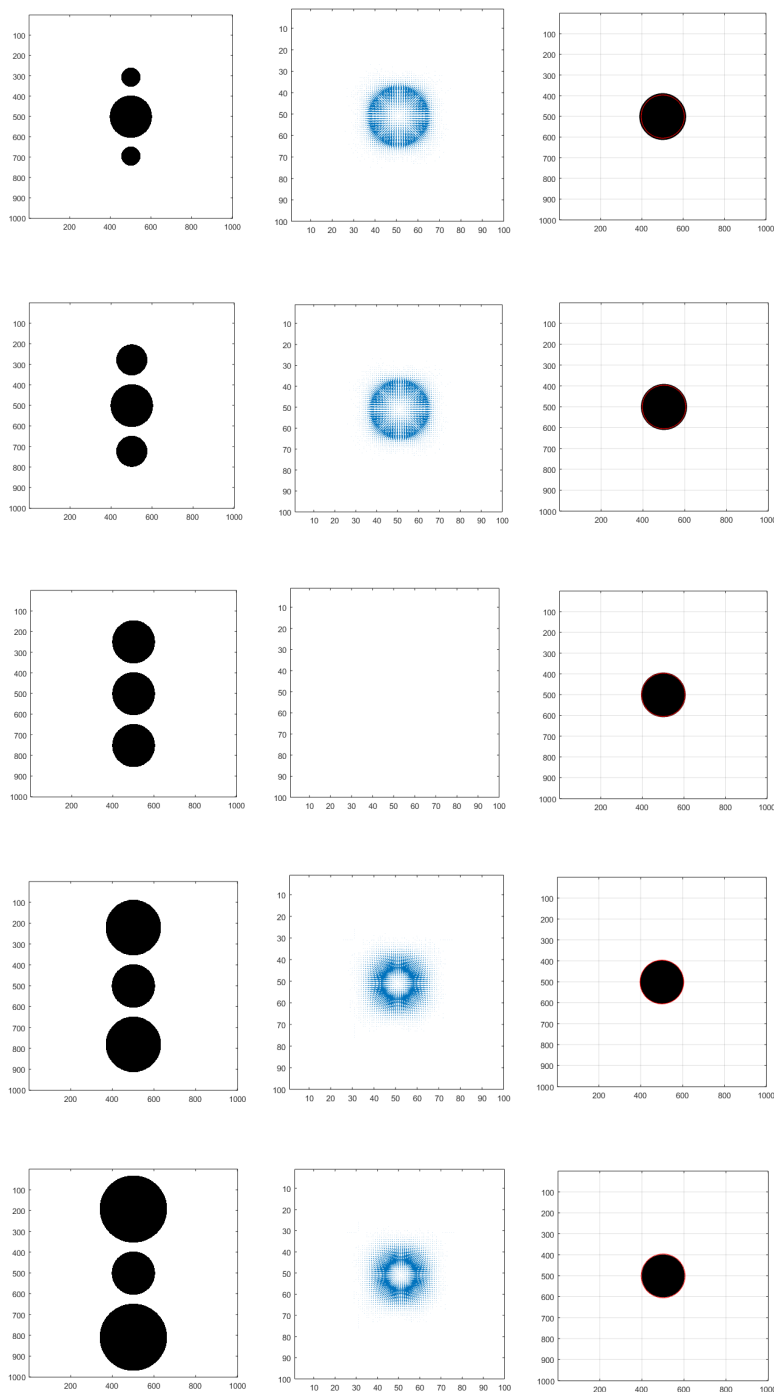


Figure 8.8: Computed displacement  $\vec{u}(x_1, x_2)$  for the Ebbinghaus illusion with two inducers. Rows: each row contains on the left the initial stimulus, on the center the computed displacement vector fields  $\vec{u}(x_1, x_2)$ , on the right the application of  $\vec{u}(x_1, x_2)$  to the initial stimulus. This last operation permits to visualize the proximal stimulus, i.e. the perceived deformation of the central target. Columns: the width of the inducers is increased from the top to the bottom. Fixing the distance between target and inducers, if the latter are small, the target expands, while increasing the dimension of the inducers implies a shrinking of the central target. The perceived deformation can be appreciated because each image in the third column contains also a reference circle (red), representing the size of the initial target.

Four inducers

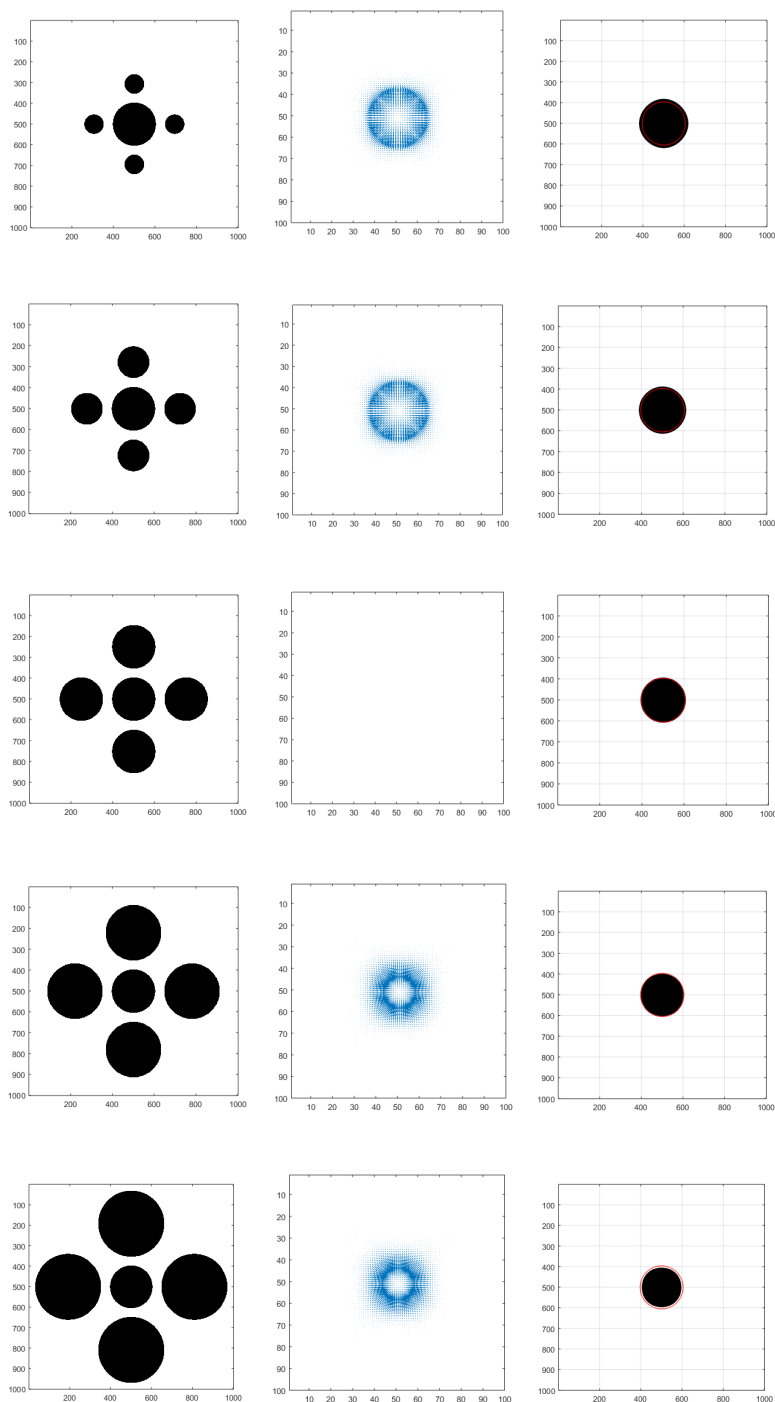


Figure 8.9: Computed displacement  $\vec{u}(x_1, x_2)$  for the Ebbinghaus illusion with four inducers. Rows: each row contains on the left the initial stimulus, on the center the computed displacement vector fields  $\vec{u}(x_1, x_2)$ , on the right the application of  $\vec{u}(x_1, x_2)$  to the initial stimulus. This last operation permits to visualize the proximal stimulus, i.e. the perceived deformation of the central target. Columns: the width of the inducers is increased from the top to the bottom. Fixing the distance between target and inducers, if the latter are small, the target expands, while increasing the dimension of the inducers implies a shrinking of the central target. The perceived deformation can be appreciated because each image in the third column contains also a reference circle (red), representing the size of the initial target.

## Six inducers

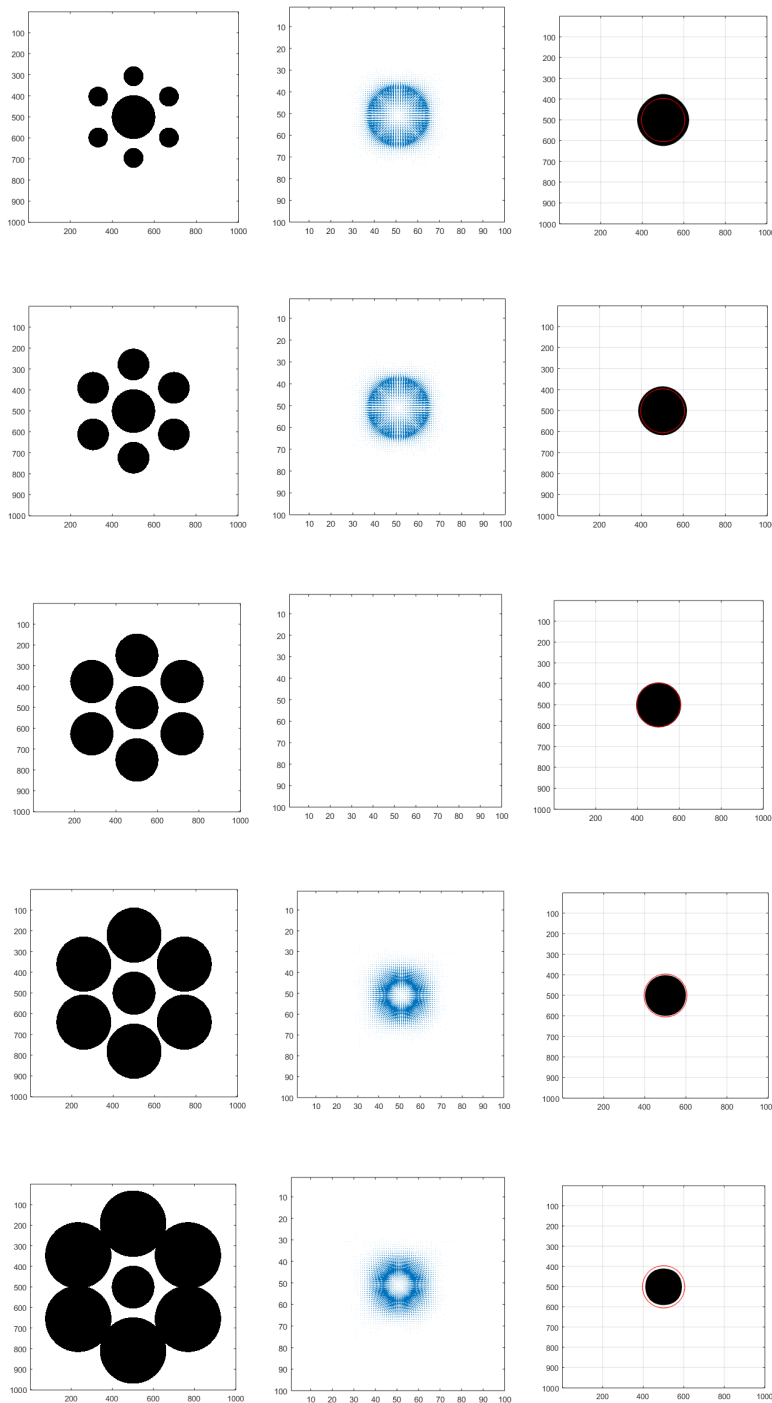


Figure 8.10: Computed displacement  $\bar{u}(x_1, x_2)$  for the Ebbinghaus illusion with six inducers. Rows: each row contains on the left the initial stimulus, on the center the computed displacement vector fields  $\bar{u}(x_1, x_2)$ , on the right the application of  $\bar{u}(x_1, x_2)$  to the initial stimulus. This last operation permits to visualize the proximal stimulus, i.e. the perceived deformation of the central target. Columns: the width of the inducers is increased from the top to the bottom. Fixing the distance between target and inducers, if the latter are small, the target expands, while increasing the dimension of the inducers implies a shrinking of the central target. The perceived deformation can be appreciated because each image in the third column contains also a reference circle (red), representing the size of the initial target.

## Modified distance between target and inducers

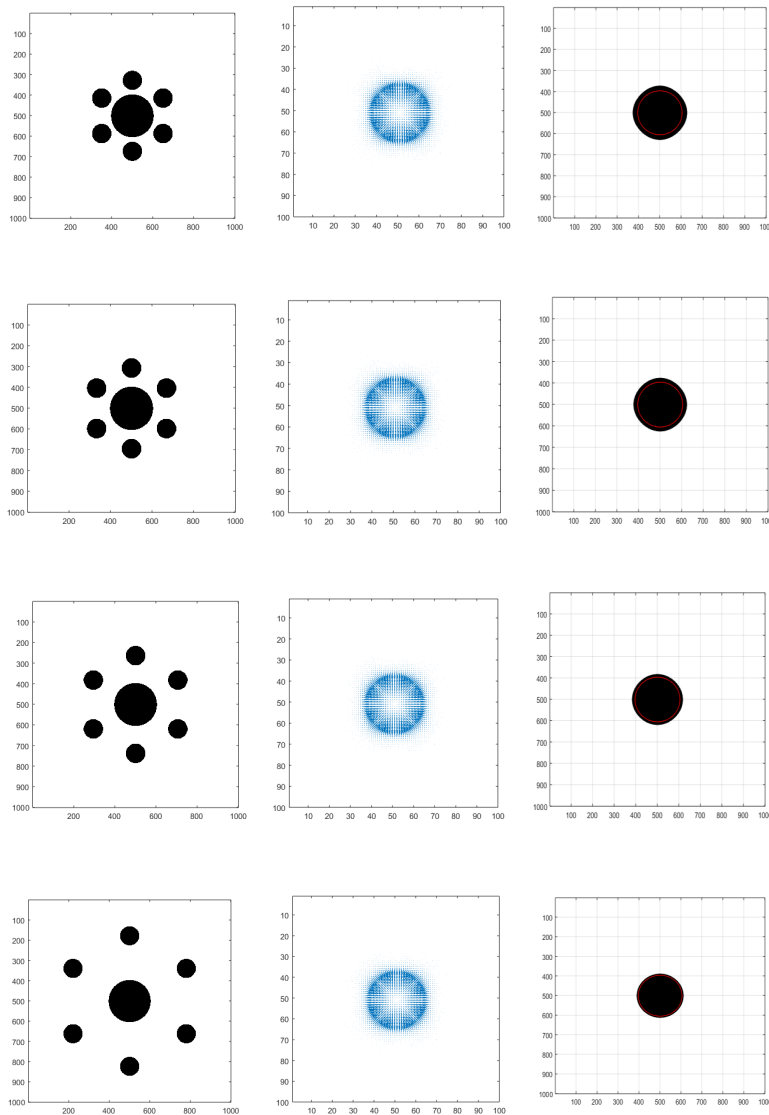
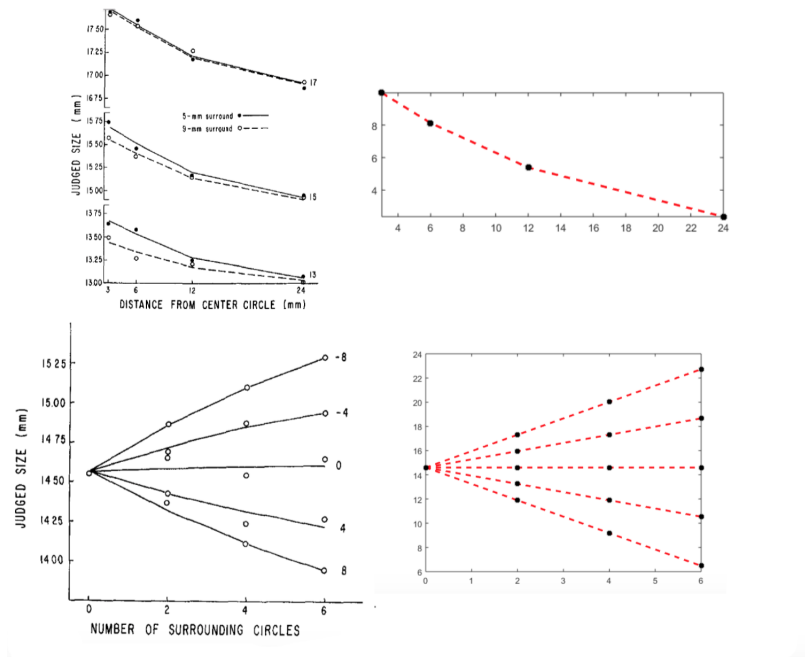


Figure 8.11: Computed displacement  $\bar{u}(x_1, x_2)$  for the Ebbinghaus illusion with six inducers. Rows: each row contains on the left the initial stimulus, on the center the computed displacement vector fields  $\bar{u}(x_1, x_2)$ , on the right the application of  $\bar{u}(x_1, x_2)$  to the initial stimulus. This last operation permits to visualize the proximal stimulus, i.e. the perceived deformation of the central target. Columns: the width of the inducers is increased from the top to the bottom. Fixing the distance between target and inducers, if the latter are small, the target expands, while increasing the dimension of the inducers implies a shrinking of the central target. The perceived deformation can be appreciated because each image in the third column contains also a reference circle (red), representing the size of the initial target.

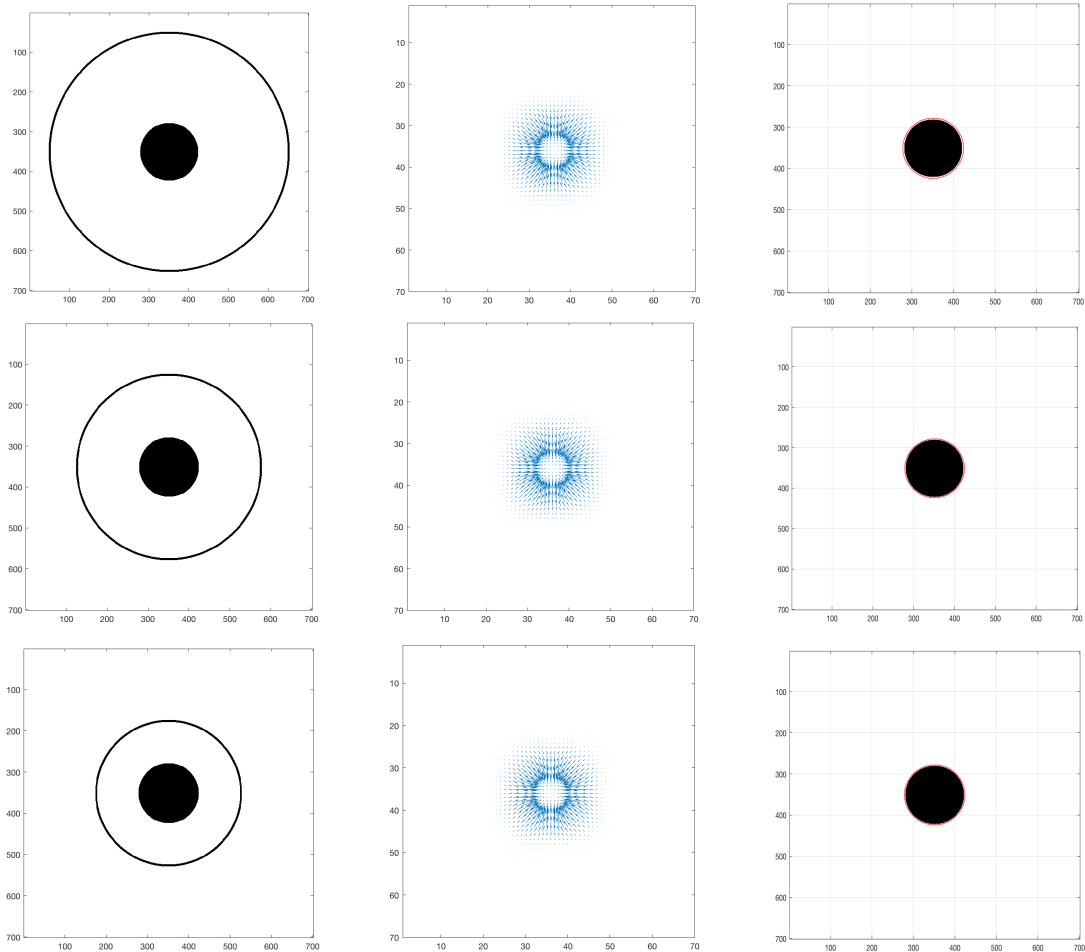
### Comparison with quantitative results

Our previous observations about how the magnitude of the Ebbinghaus illusion varies in dependence of the distance between the target and the context (inducers) and in relation with the size of the inducers has been proven in our previous experiments. Here we compare our results with the ones obtained



through a quantitative analysis by Massaro and Anderson [116]. In figure 8.12 the left column shows the experimental results, while the right one combines our computations (red graphs) shown in the previous paragraphs. It is easy to see how they correctly match. Furthermore, to reproduce these results, we started from the same size values used in [116] for target, inducers and distance between them. The top left graph in figure 8.12 shows how the perceived size of the central target decays as a function of the distance and in dependence of its size. In the top right part we shown the same analysis, but for  $\rho_0 = 15$ . It corresponds to the central curve in figure 8.12 top left. The bottom part of the figure contains an analysis of how the perception of the central target changes in dependence of the number of inducers and their size. In general, increasing the number of inducers intensifies either the perceived shrinking or enlargement of the central target. The numbers on the right of each curve (figure bottom left 8.12) indicates the difference between the effective size of the inducers and the target, meaning that if we put smaller circles around the central one the enlargement of the latter increases linearly with the diminishing size of the context inducers, while we obtain the opposite effect putting

Figure 8.12: Top left: here Massaro and Anderson ([116]) shown how the perceived size of the central target diminishes while decreasing the distance between the inducers and the target in the Ebbinghaus illusion. This variation is studied also in relationship with the effective size of the central target (from top curve to bottom one). Top right: we reproduce the same analysis shown in the top left image, but only for the target with effective size  $\rho_0 = 15$ . Bottom left: the same authors in ([116]) shown how the perceived size of the central target varies in relationship with the size and the numbers of inducers. The little numbers on the right of each curve indicate the difference between the actual size of the inducers and the target, meaning that if we put smaller circles around the central one the enlargement of the latter increases linearly with the diminishing size of the context inducers, while we obtain the opposite effect putting bigger circles around the target. Bottom right: the latter phenomena are exactly reproduced through our model.



bigger circles around the target. These phenomena are reproduced through our model as shown in figure 8.12 right.

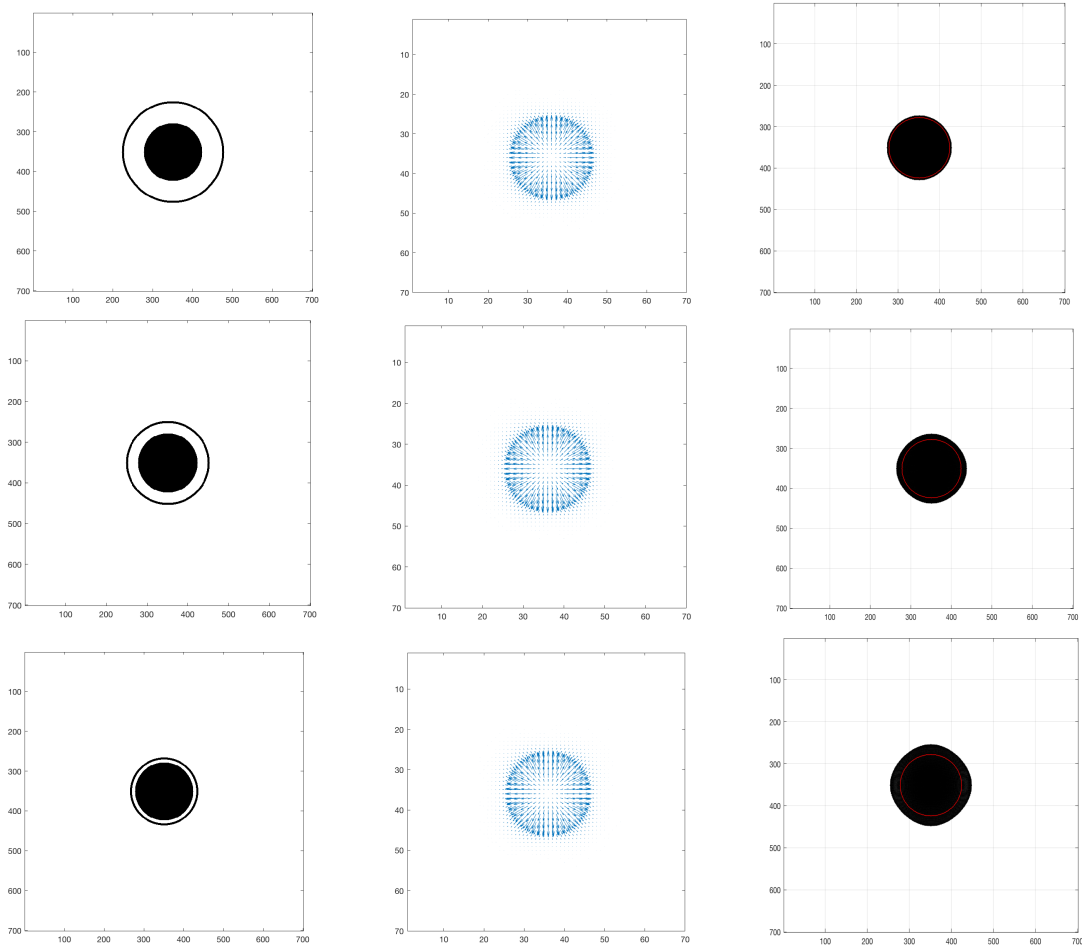
### 8.3.2 Delboeuf illusion

One of the greatest problem analyzed for the Delboeuf illusion (figure 8.2) which mislead many research were the identification of the features playing a role in this phenomenon. Attempts were made for developing an equivalent approach able to explain both phenomena, see for example [79]. One clear fact was the role played by the distance between the inducer (the circumference) and the target ([143]), but this is not sufficient to explain the phenomenon. In our model we show that the size of the annulus plays a central role in the Delboeuf illusion, see figure 8.2. In we consider again formula (8.2):

$$\rho(x) = \exp^{-|x-x'|}(\rho(x') - \rho_0)$$

where  $N$  of formula (8.2) is equal to 1, because the consider inducer is the annulus,  $c = 1$ , the distance  $|x - x'|$  is expressed in pixels and is the distance between the center of the target  $x$

Figure 8.13: Computed displacement  $\bar{u}(x_1, x_2)$  for the Delboeuf illusion. Each row contains on the left the initial stimulus, on the center the computed displacement vector fields  $\bar{u}(x_1, x_2)$ , on the right the application of  $\bar{u}(x_1, x_2)$  to the initial stimulus. This last operation permits to visualize the proximal stimulus, i.e. the perceived deformation of the central target. Columns: the width of the annulus is increased from the top to the bottom. The perceived deformation can be appreciated because each image in the third column contains also a reference circle (red), representing the size of the initial target.

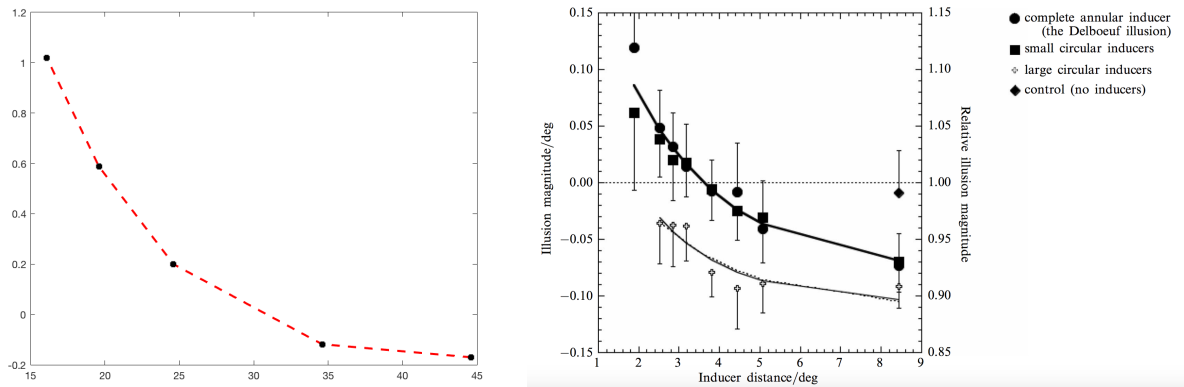


and a the center of the annulus  $x'$ ,  $\rho(x')$  is the size of the annulus and  $\rho_0$  refers again to the effective size. Then  $(\rho(x') - \rho_0)$  expresses the difference between the considered sizes. In figures 8.13 and 8.14 we show the simulation performed with the presented model. On the left column the initial stimulus is presented: we let the size of the annulus  $\rho(x')$  decreasing. In the central column it is presented the computed displacement through the infinitesimal strain theory approach introduced in chapter 6, section 6.3.3. Finally, the right image contains the perceived central target: we consider the initial stimulus and we apply vector fields  $\bar{u}(x_1, x_2)$  computed through our method. The red circle is the target reference of the initial stimulus, drawn in order to allow a comparison between the proximal stimulus (displaced image) and the distal one, [105, 77] (see chapter 2).

#### Discussion of the results

The distance between the center of the annulus and the center of the target  $|x' - x|$  decreases in column left of figures 8.14, 8.14

Figure 8.14: Computed displacement  $\bar{u}(x_1, x_2)$  for the Delbouef illusion. Each row contains on the left the initial stimulus, on the center the computed displacement vector fields  $\bar{u}(x_1, x_2)$ , on the right the application of  $\bar{u}(x_1, x_2)$  to the initial stimulus. This last operation permits to visualize the proximal stimulus, i.e. the perceived deformation of the central target. Columns: the width of the annulus is increased from the top to the bottom. The perceived deformation can be appreciated because each image in the third column contains also a reference circle (red), representing the size of the initial target.



and represents a quantity strictly related with the size of the annulus  $\rho(x')$ . Infact, increasing  $\rho_1$  means we increase the distance between the target and the circumference. Even though they are related, considering just the distance does not fully account for the perceived phenomenon. When the annulus is big, as in the top left image of figure 8.13, we perceive a shrinking (see page 454 of [79]), while if the annulus size is decreased, we observe an enlargement of the central target. This variation is explained by an evaluation of the difference in size between the target and the annulus, as we did for the Ebbinghaus illusion. Figure 8.15 left shows how the perceived displacement decreases as a function of the distance in our computations. In the x-axis we put the distance  $|x' - x|$  and in the y-axis the computed displacement. In the same figure (right) we proposed the results of an experiments conducted in [143]: the black dots refers to the Delboeuf illusion and show how experimentally our results are confirmed.  $\rho_0$  still denotes the effective size of the target. The reconstructed percepts for the Delboeuf illusions shown in the left column images of figures 8.14, 8.14 are presented in the right column. The described shrinking and expanding effect can be appreciated comparing the perceived stimulus (black) with the red circle, which indicates the original target size.

Figure 8.15: Left: the graph shows how the perceived displacement decreases as a function of the distance in our simulations. In the x-axis we put the distance  $|x' - x|$  and in the y-axis the computed displacement. Right: analysis of the decay of the illusion magnitude as a function of the distance between the target and the inducers, from [143]. The circles refers to the Delboeuf illusion. Our results are in agreement with the ones shown in this experiment.



## 9 Conclusion and Perspectives

In this last chapter we detail the different contributions contained within this thesis and we point out possible extension that can be considered in the future.

### 9.1 Contributions

In this thesis we have provided neuromathematical models able to explain and account for many phenomena, starting from amodal completion going through a big set of Geometrical Optical illusions. We underlined the importance of these studies both from an image processing point of view, for developing perceptual based algorithm, and from the neurophysiological perspective of understanding how the visual cortex behaves in presence of such phenomena. This could provide important insights concerning the ventral stream process. Let us go through the original contribution of this thesis. In chapter 5 we provided a perceptual based algorithm for modeling amodal completion and we extend it in order to perform image restoration (inpainting) and contours enhancement. Furthermore a result of existence of solutions for the considered PDEs is shown, as well as a sketch of the proof of convergence of the presented algorithm. This contribution has been published in [30]. In chapter 6 we introduced a neuromathematical model for Geometrical Optical illusions, which allows to recover the perceptual displacement we perceive in presence of such phenomena. This contribution can be found in [68, 69]. The previous model is then extended in chapter 7 in which the deformed curves are recovered as geodesics of the considered metric, modulated by the action of simple cells in V1/V2. The work will be contained in [66, 67]. Finally in chapter 8 size illusions are considered, using the scale feature. We refer for the latter to [65].

### 9.2 Research Perspectives

We aim to enumerate possible research perspectives which will help in contributing to a unified theory for such phenomena,

enlightening our understanding of how the cortex behaves.

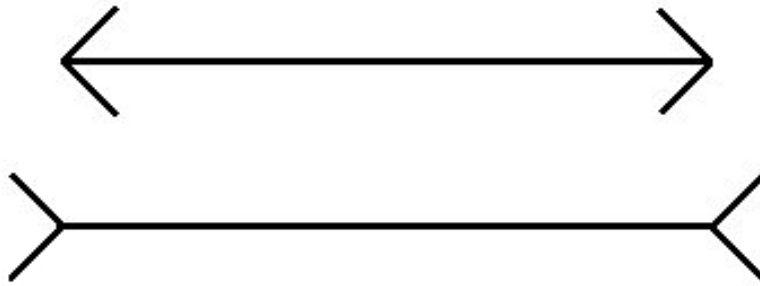


Figure 9.1: The Muller-Lyer illusion: the perceived length of the two central bar is misled by the angles formed by the lateral inducers: if they are acute, the bar is perceived as shorter (top) while if they are obtuse, the bar seems to be larger.

One of the research perspective will be to provide an extension of the model to other features, in order to study other illusions, such for example the Muller-Lyer illusion, matching it with the experimental studies presented in [179, 178, 141]. The Muller-Lyer illusion, figure 9.1 is a complex phenomenon subject of many studies. The perceived length of the two central bar is misled by the angles formed by the lateral inducers: if they are acute, the bar is perceived as shorter (top) while if they are obtuse, the bar seems to be larger. The interesting part of this phenomenon is that recent studies [179, 178, 141] shown how this illusion takes place at higher stages of the visual process.

It will be important to perform further tests using the approach presented in chapter 7 involving the illusions considered in chapter 6, such as the Hering, Wundt and Zollner illusions. In this way a comparison with the findings obtained through the infinitesimal strain approach will be possible.

There is a lack of quantitative studies measuring the perceived magnitude of this illusions. Most of the psychological studies involving these illusions start from modified stimuli (see for example [162, 41, 181]) in order to provide a phenomenological and perceptual explanation for them. However, some of those findings were contradicted by the same authors years later [180, 43]. At a very general level what we actually see from a qualitative point of view [181] is well known and is in agreement with our findings. Still there is a lack of quantitative data which would allow a better validation of all the theories proposed until now. It would be important to design a simple but effective experiment to measure the magnitude of illusions (not only the Poggendorff or Muller Lyer). With the recent increasing development of neuroimaging techniques, one very interesting application will be to identify where these phenomena actually take place.





## Bibliography

- [1] Alessandra Angelucci, Jonathan B Levitt, Emma JS Walton, Jean-Michel Hupe, Jean Bullier, and Jennifer S Lund. Circuits for local and global signal integration in primary visual cortex. *The Journal of Neuroscience*, 22(19):8633–8646, 2002.
- [2] Akiyuki Anzai, Xinmiao Peng, and David C Van Essen. Neurons in monkey visual area v2 encode combinations of orientations. *Nature neuroscience*, 10(10):1313–1321, 2007.
- [3] Jonas August and Steven W Zucker. The curve indicator random field: Curve organization via edge correlation. In *Perceptual organization for artificial vision systems*, pages 265–288. Springer, 2000.
- [4] Martino Bardi and Italo Capuzzo-Dolcetta. *Optimal control and viscosity solutions of Hamilton-Jacobi-Bellman equations*. Springer Science & Business Media, 2008.
- [5] Erik Bekkers, Remco Duits, Tos Berendschot, and Bart ter Haar Romeny. A multi-orientation analysis approach to retinal vessel tracking. *Journal of Mathematical Imaging and Vision*, 49(3):583–610, 2014.
- [6] Erik J Bekkers, Remco Duits, Alexey Mashtakov, and Gonzalo R Sanguinetti. A pde approach to data-driven sub-riemannian geodesics in se (2). *SIAM Journal on Imaging Sciences*, 8(4):2740–2770, 2015.
- [7] G. Ben-Yosef and O Ben-Shahar. A tangent bundle theory for visual curve completion. *IEEE Trans. Pattern Anal. Mach. Intell.*, 34:1263–1280, 2012.
- [8] Fethallah Benmansour and Laurent D Cohen. Tubular structure segmentation based on minimal path method and anisotropic enhancement. *International Journal of Computer Vision*, 92(2):192–210, 2011.
- [9] Marcelo Bertalmio, Guillermo Sapiro, Vincent Caselles, and Coloma Ballester. Image inpainting. In *Proceedings of the 27th annual conference on Computer graphics and interactive techniques*, pages 417–424. ACM Press/Addison-Wesley Publishing Co., 2000.
- [10] Marcelo Bertalmio, Vicent Caselles, Simon Masnou, and Guillermo Sapiro. Inpainting. In *Computer Vision*, pages 401–416. Springer, 2014.
- [11] Thomas Bieske. Comparison principle for parabolic equations in the heisenberg group. *Electronic Journal of Differential Equations*, 2005(95):1–11, 2005.
- [12] Josef Bigun. *Optimal orientation detection of linear symmetry*. Linköping University Electronic Press, 1987.

- [13] Colin Blakemore, Roger HS Carpenter, and Mark A Georgeson. Lateral inhibition between orientation detectors in the human visual system. *Nature*, 228(5266):37–39, 1970.
- [14] Ugo Boscain, Roman A Chertovskih, Jean-Paul Gauthier, and AO Remizov. Hypoelliptic diffusion and human vision: a semidiscrete new twist. *SIAM Journal on Imaging Sciences*, 7(2):669–695, 2014.
- [15] Ugo Boscain, Roman Chertovskih, Jean-Paul Gauthier, Dario Prandi, and Alexey Remizov. Highly corrupted image inpainting through hypoelliptic diffusion. *arXiv preprint arXiv:1502.07331*, 2015.
- [16] William H Bosking, Ying Zhang, Brett Schofield, and David Fitzpatrick. Orientation selectivity and the arrangement of horizontal connections in tree shrew striate cortex. *The Journal of neuroscience*, 17(6):2112–2127, 1997.
- [17] Thomas Brox, Joachim Weickert, Bernhard Burgeth, and Pavel Mrázek. Nonlinear structure tensors. *Image and Vision Computing*, 24(1):41–55, 2006.
- [18] Ernst Burmester. *Beitrag zur experimentellen Bestimmung geometrisch-optischer Täuschungen...*, volume 12. L. Voss, 1896.
- [19] TJ Bussey and LM Saksida. Memory, perception, and the ventral visual-perirhinal-hippocampal stream: Thinking outside of the boxes. *Hippocampus*, 17(9):898–908, 2007.
- [20] Claudy Cancelier, Bruno Franchi, and Elena Serra. Agmon metric for sum-of-squares operators. *Journal d'Analyse Mathématique*, 83(1):89–107, 2001.
- [21] Luca Capogna and Giovanna Citti. Generalized mean curvature flow in carnot groups. *Communications in Partial Differential Equations*, 34(8):937–956, 2009.
- [22] Luca Capogna, Donatella Danielli, Scott D Pauls, and Jeremy Tyson. *An introduction to the Heisenberg group and the sub-Riemannian isoperimetric problem*, volume 259. Springer Science & Business Media, 2007.
- [23] Luca Capogna, Giovanna Citti, and Maria Manfredini. Regularity of non-characteristic minimal graphs in the heisenberg group  $h^1$ . *arXiv preprint arXiv:0804.3406*, 2008.
- [24] Luca Capogna, Giovanna Citti, and Maria Manfredini. Regularity of mean curvature flow of graphs on lie groups free up to step 2. *Nonlinear Analysis: Theory, Methods & Applications*, 126:437–450, 2015.
- [25] Yun Gang Chen, Yoshikazu Giga, Shun'ichi Goto, et al. Uniqueness and existence of viscosity solutions of generalized mean curvature flow equations. *J. Differential Geom*, 33(3):749–786, 1991.
- [26] Jih-Hsin Cheng, Jenn-Fang Hwang, Andrea Malchiodi, and Paul Yang. Minimal surfaces in pseudohermitian geometry. *Annali della Scuola Normale Superiore di Pisa-Classe di Scienze*, 4(1):129–177, 2005.
- [27] Jih-Hsin Cheng, Jenn-Fang Hwang, and Paul Yang. Regularity of  $c_1$  smooth surfaces with prescribed  $p$ -mean curvature in the heisenberg group. *Mathematische Annalen*, 344(1):1, 2009.

- [28] Giovanna Citti and Alessandro Sarti. A cortical based model of perceptual completion in the roto-translation space. *Journal of Mathematical Imaging and Vision*, 24(3):307–326, 2006.
- [29] Giovanna Citti, Maria Manfredini, and Alessandro Sarti. Finite difference approximation of the mumford and shah functional in a contact manifold of the heisenberg space. *Communications on Pure and Applied Analysis (CPAA)*, 9(4):905–927, 2010.
- [30] Giovanna Citti, Benedetta Franceschiello, Gonzalo Sanguinetti, and Alessandro Sarti. Sub-riemannian mean curvature flow for image processing. *SIAM Journal on Imaging Sciences*, 9(1):212–237, 2016.
- [31] Andrew M Colman. *A dictionary of psychology*. Oxford University Press, USA, 2015.
- [32] Stanley Coren and Joan S Girgus. *Seeing is deceiving: The psychology of visual illusions*. Lawrence Erlbaum, 1978.
- [33] G-H Cottet and L Germain. Image processing through reaction combined with nonlinear diffusion. *Mathematics of Computation*, pages 659–673, 1993.
- [34] Michael G Crandall and Pierre-Louis Lions. Viscosity solutions of hamilton-jacobi equations. *Transactions of the American Mathematical Society*, 277(1):1–42, 1983.
- [35] Michael G Crandall and Pierre-Louis Lions. Convergent difference schemes for nonlinear parabolic equations and mean curvature motion. *Numerische Mathematik*, 75(1):17–41, 1996.
- [36] Michael G Crandall, Lawrence C Evans, and P-L Lions. Some properties of viscosity solutions of hamilton-jacobi equations. *Transactions of the American Mathematical Society*, 282(2):487–502, 1984.
- [37] Michael G Crandall, Hitoshi Ishii, and Pierre-Louis Lions. User’s guide to viscosity solutions of second order partial differential equations. *Bulletin of the American Mathematical Society*, 27(1):1–67, 1992.
- [38] Donatella Danielli, Nicola Garofalo, and Duy-Minh Nhieu. Sub-riemannian calculus on hypersurfaces in carnot groups. *Advances in Mathematics*, 215(1):292–378, 2007.
- [39] John G Daugman. Uncertainty relation for resolution in space, spatial frequency, and orientation optimized by two-dimensional visual cortical filters. *JOSA A*, 2(7):1160–1169, 1985.
- [40] RH Day. Zanuttini’s “surface shrinkage” explanation of the poggendorff misalignment effect. *Attention, Perception, & Psychophysics*, 21(3):280–280, 1977.
- [41] RH Day and RG Dickinson. The poggendorff illusion: Apparent misalignment which is not attributable to apparent orientation of the transversals. *The Quarterly journal of experimental psychology*, 27(4):551–557, 1975.
- [42] RH Day and RG Dickinson. The components of the poggendorff illusion. *British Journal of Psychology*, 67(4):537–552, 1976.

- [43] RH Day, WJ Jolly, and FM Duffy. No evidence for apparent extent between parallels as the basis of the poggendorff effect. *Attention, Perception, & Psychophysics*, 42(6):561–568, 1987.
- [44] Gregory C DeAngelis, Izumi Ohzawa, and Ralph D Freeman. Receptive-field dynamics in the central visual pathways. *Trends in neurosciences*, 18(10):451–458, 1995.
- [45] Klaus Deckelnick. Error bounds for a difference scheme approximating viscosity solutions of mean curvature flow. *Interfaces and Free Boundaries*, 2(2):117–142, 2000.
- [46] Klaus Deckelnick and Gerhard Dziuk. Convergence of numerical schemes for the approximation of level set solutions to mean curvature flow. *SERIES ON ADVANCES IN MATHEMATICS FOR APPLIED SCIENCES*, 59:77–94, 2001.
- [47] Franz Joseph Delboeuf. Note sur certaines illusions d’optique: Essai d’une théorie psychophysique de la maniere dont l’oeil apprécie les distances et les angles. *Bulletins de l’Académie Royale des Sciences, Lettres et Beaux-arts de Belgique*, 19:195–216, 1865.
- [48] Agnes Desolneux, Lionel Moisan, and Jean-Michel Morel. Computational gestalts and perception thresholds. *Journal of Physiology-Paris*, 97(2):311–324, 2003.
- [49] Edsger W Dijkstra. A note on two problems in connexion with graphs. *Numerische mathematik*, 1(1):269–271, 1959.
- [50] Nicolas Dirr, Federica Dragoni, and Max Von Renesse. Evolution by mean curvature flow in sub-riemannian geometries. *Communications on Pure and Applied Mathematics*, 9(2):307–326, 2010.
- [51] Federica Dragoni. *Carnot-Carathéodory metrics and viscosity solutions*. PhD thesis, Scuola Normale Superiore, Pisa, Italy, 2006.
- [52] Federica Dragoni. Metric hopf-lax formula with semicontinuous data. *Discrete and Continuous Dynamical Systems*, 17(4):713, 2007.
- [53] Remco Duits and Erik Franken. Left-invariant parabolic evolutions on se (2) and contour enhancement via invertible orientation scores part i: Linear left-invariant diffusion equations on se (2). *Quarterly of Applied Mathematics*, pages 255–292, 2010.
- [54] Remco Duits and Erik Franken. Left-invariant parabolic evolutions on se (2) and contour enhancement via invertible orientation scores part ii: Nonlinear left-invariant diffusions on invertible orientation scores. *Quarterly of applied mathematics*, pages 293–331, 2010.
- [55] Remco Duits, Maurice Duits, Markus van Almsick, and Bart ter Haar Romeny. Invertible orientation scores as an application of generalized wavelet theory. *Pattern Recognition and Image Analysis*, 17(1):42–75, 2007.
- [56] Remco Duits, Michael Felsberg, Gösta Granlund, and Bart ter Haar Romeny. Image analysis and reconstruction using a wavelet transform constructed from a reducible representation of the euclidean motion group. *International Journal of Computer Vision*, 72(1):79–102, 2007.
- [57] David M Eagleman. Visual illusions and neurobiology. *Nature Reviews Neuroscience*, 2(12):920–926, 2001.

- [58] Werner Ehm and Jiří Wackermann. Modeling geometric–optical illusions: A variational approach. *Journal of Mathematical Psychology*, 56(6):404–416, 2012.
- [59] Lawrence C Evans, Joel Spruck, et al. Motion of level sets by mean curvature i. *J. Diff. Geom.*, 33(3):635–681, 1991.
- [60] Marta Favali, Giovanna Citti, and Alessandro Sarti. Local and global gestalt laws: A neurally based spectral approach. *Neural computation*, In publication 2016.
- [61] Michael Felsberg. Adaptive filtering using channel representations. In *Mathematical Methods for Signal and Image Analysis and Representation*, pages 31–48. Springer, 2012.
- [62] Cornelia Fermüller and Henrik Malm. Uncertainty in visual processes predicts geometrical optical illusions. *Vision research*, 44(7):727–749, 2004.
- [63] Fausto Ferrari, Qing Liu, and Juan J Manfredi. On the horizontal mean curvature flow for axisymmetric surfaces in the heisenberg group. *Communications in Contemporary Mathematics*, 16(03):1350027, 2014.
- [64] Wolfgang Förstner and Eberhard Gülch. A fast operator for detection and precise location of distinct points, corners and centres of circular features. In *Proc. ISPRS intercommission conference on fast processing of photogrammetric data*, pages 281–305, 1987.
- [65] B. Franceschiello, G. Citti, and A. Sarti. A neuromathematical model for ebbinghaus and delboeuf illusions. *In preparation*, 2017.
- [66] B. Franceschiello, A. Mashtakov, G. Citti, and A. Sarti. Modelling of the pogendorff illusion via sub-riemannian geodesics in the roto-translation group. *1st International Workshop on Brain-Inspired Computer Vision (WBICV2017)*, 2017.
- [67] B. Franceschiello, A. Mashtakov, G. Citti, and A. Sarti. Modelling of geometrical optical illusions via sub-riemannian geodesics in the roto-translation group. *In preparation*, 2017.
- [68] B. Franceschiello, A. Sarti, and G. Citti. Mathematical models of visual perception for the analysis of geometrical optical illusions. *Proceedings of NeuroMath conference, Springer INdAM Series*, 2017.
- [69] B. Franceschiello, A. Sarti, and G. Citti. A neuro-mathematical model for geometrical optical illusions. *Journal of Mathematical Imaging and Vision*, 2017.
- [70] Bruno Franchi, Raul Serapioni, and F Serra Cassano. Regular hypersurfaces, intrinsic perimeter and implicit function theorem in carnot groups. *Communications in analysis and geometry*, 11(5):909–944, 2003.
- [71] Erik Franken and Remco Duits. Crossing-preserving coherence-enhancing diffusion on invertible orientation scores. *International Journal of Computer Vision*, 85(3):253, 2009.
- [72] Erik Franken, Markus van Almsick, Peter Rongen, Luc Florack, and Bart ter Haar Romeny. An efficient method for tensor voting using steerable filters. In *European Conference on Computer Vision*, pages 228–240. Springer, 2006.
- [73] William T Freeman, Edward H Adelson, et al. The design and use of steerable filters. *IEEE Transactions on Pattern analysis and machine intelligence*, 13(9):891–906, 1991.

- [74] Matteo Galli and Manuel Ritoré. Area-stationary and stable surfaces of class  $c_1$  in the sub-riemannian heisenberg group  $h_1$ . *Advances in Mathematics*, 285:737–765, 2015.
- [75] Michael S Gazzaniga, RB Ivry, and GR Mangun. *Cognitive neuroscience*, new york: W. w, 2002.
- [76] Wilson S Geisler and Daniel Kersten. Illusions, perception and bayes. *Nature neuroscience*, 5(6):508–510, 2002.
- [77] James J Gibson. The concept of the stimulus in psychology. *American Psychologist*, 15(11): 694, 1960.
- [78] Charles D Gilbert, Aniruddha Das, Minami Ito, Mitesh Kapadia, and Gerald Westheimer. Spatial integration and cortical dynamics. *Proceedings of the National Academy of Sciences*, 93(2):615–622, 1996.
- [79] Joan S Girgus, Stanley Coren, and Myra Agdern. The interrelationship between the ebbinghaus and delboeuf illusions. *Journal of Experimental Psychology*, 95(2):453, 1972.
- [80] Richard L Gregory. *Eye and brain: The psychology of seeing*. Princeton university press, 2015.
- [81] Suzanne Greist-Bousquet and Harvey R Schiffman. The poggendorff illusion: an illusion of linear extent? *Perception*, 10(2):155–164, 1981.
- [82] Mikhael Gromov. Carnot-carathéodory spaces seen from within. In *Sub-Riemannian geometry*, pages 79–323. Springer, 1996.
- [83] Heinrich Ewald Hering. *Beiträge zur physiologie*. 1-5. Leipzig, W. Engelmann, 1861.
- [84] Robert K Hladky, Scott D Pauls, et al. Constant mean curvature surfaces in sub-riemannian geometry. *Journal of Differential Geometry*, 79(1):111–139, 2008.
- [85] William C Hoffman. Visual illusions of angle as an application of lie transformation groups. *Siam Review*, 13(2):169–184, 1971.
- [86] William C Hoffman. The visual cortex is a contact bundle. *Applied Mathematics and Computation*, 32(2-3):137–167, 1989.
- [87] Lars Hörmander. Hypoelliptic second order differential equations. *Acta Mathematica*, 119 (1):147–171, 1967.
- [88] Lars Hörmander. *Linear partial differential operators*, volume 116. Springer, 2013.
- [89] WHN Hotopf and CHRISTINE OLLEREARNSHAW. The regression to right angles tendency and the poggendorff illusion. ii. *British Journal of Psychology*, 63(3):369–379, 1972.
- [90] WHN Hotopf, Christine Ollerearnshaw, and Susannah Brown. The regression to right angles tendency and the poggendorff illusion. iii. *British Journal of Psychology*, 65(2):213–231, 1974.
- [91] Catherine Q Howe and Dale Purves. Natural-scene geometry predicts the perception of angles and line orientation. *Proceedings of the National Academy of Sciences of the United States of America*, 102(4):1228–1233, 2005.

- [92] Catherine Q Howe, Zhiyong Yang, and Dale Purves. The poggendorff illusion explained by natural scene geometry. *Proceedings of the National Academy of Sciences of the United States of America*, 102(21):7707–7712, 2005.
- [93] David H Hubel and Torsten N Wiesel. Receptive fields, binocular interaction and functional architecture in the cat’s visual cortex. *The Journal of physiology*, 160(1):106–154, 1962.
- [94] David H Hubel and Torsten N Wiesel. Ferrier lecture: Functional architecture of macaque monkey visual cortex. *Proceedings of the Royal Society of London B: Biological Sciences*, 198 (1130):1–59, 1977.
- [95] David H Hubel, Janice Wensveen, and Bruce Wick. *Eye, brain, and vision*. Scientific American Library New York, 1995.
- [96] Hitoshi Ishii. Viscosity solutions of nonlinear second-order partial differential equations in hilbert spaces. *Communications in partial differential equations*, 18(3-4):601–650, 1993.
- [97] David Jerison et al. The poincaré inequality for vector fields satisfying hörmander’s condition. *Duke Math. J*, 53(2):503–523, 1986.
- [98] Judson P Jones and Larry A Palmer. An evaluation of the two-dimensional gabor filter model of simple receptive fields in cat striate cortex. *Journal of neurophysiology*, 58(6): 1233–1258, 1987.
- [99] Jürgen Jost. *Riemannian geometry and geometric analysis*. Springer Science & Business Media, 2008.
- [100] Gaetano Kanizsa. *Grammatica del vedere: saggi su percezione e gestalt*. Il mulino, 1980.
- [101] H Kennedy, KAC Martin, GA Orban, and D Whitteridge. Receptive field properties of neurones in visual area 1 and visual area 2 in the baboon. *Neuroscience*, 14(2):405–415, 1985.
- [102] David C Knill and Whitman Richards. *Perception as Bayesian inference*. Cambridge University Press, 1996.
- [103] Jan J Koenderink and AJ Van Doorn. Receptive field families. *Biological cybernetics*, 63(4): 291–297, 1990.
- [104] Jan J Koenderink and Andrea J van Doorn. Representation of local geometry in the visual system. *Biological cybernetics*, 55(6):367–375, 1987.
- [105] Kurt Koffka. *Principles of Gestalt psychology*, volume 44. Routledge, 2013.
- [106] Wolfgang Köhler. *Gestalt psychology: An introduction to new concepts in modern psychology*. WW Norton & Company, 1970.
- [107] David H Krantz and Daniel J Weintraub. Factors affecting perceived orientation of the poggendorff transversal. *Attention, Perception, & Psychophysics*, 14(3):511–517, 1973.
- [108] Theodor M Künnapas. Influence of frame size on apparent length of a line. *Journal of Experimental Psychology*, 50(3):168, 1955.

- [109] Tai Sing Lee. Image representation using 2d gabor wavelets. *IEEE Transactions on pattern analysis and machine intelligence*, 18(10):959–971, 1996.
- [110] Jonathan B Levitt, Daniel C Kiper, and J Anthony Movshon. Receptive fields and functional architecture of macaque v2. *Journal of Neurophysiology*, 71(6):2517–2542, 1994.
- [111] Lu Liu, Liang She, Ming Chen, Tianyi Liu, Haidong D Lu, Yang Dan, and Mu-ming Poo. Spatial structure of neuronal receptive field in awake monkey secondary visual cortex (v2). *Proceedings of the National Academy of Sciences*, 113(7):1913–1918, 2016.
- [112] Jacob Lubliner. *Plasticity theory*. Courier Corporation, 2008.
- [113] Jerrold E Marsden and Thomas JR Hughes. *Mathematical foundations of elasticity*. Courier Corporation, 1994.
- [114] Alexey Mashtakov, Andrei Ardentov, and Yuri Sachkov. Parallel algorithm and software for image inpainting via sub-riemannian minimizers on the group of rototranslations. *Numer. Math. Theory Methods Appl.*, 6:95–115, 2013.
- [115] Simon Masnou and J-M Morel. Level lines based disocclusion. In *Image Processing, 1998. ICIP 98. Proceedings. 1998 International Conference on*, pages 259–263. IEEE, 1998.
- [116] Dominic W Massaro and Norman H Anderson. Judgmental model of the ebbinghaus illusion. *Journal of experimental psychology*, 89(1):147, 1971.
- [117] Gérard Medioni, Chi-Keung Tang, and Mi-Suen Lee. Tensor voting: Theory and applications. In *Proceedings of RFLA*, volume 2000, 2000.
- [118] Maurice Merleau-Ponty. *Phenomenology of perception*. Motilal Banarsidass Publishe, 1996.
- [119] Barry Merriman, James Kenyard Bence, and Stanley Osher. *Diffusion generated motion by mean curvature*. Department of Mathematics, University of California, Los Angeles, 1992.
- [120] Jean-Marie Mirebeau. Anisotropic fast-marching on cartesian grids using lattice basis reduction. *SIAM Journal on Numerical Analysis*, 52(4):1573–1599, 2014.
- [121] Richard Montgomery. *A Tour of Subriemannian Geometries, Their Geodesics and Applications*. Mathematical Surveys and Monographs, 2002.
- [122] Roberto Monti. Some properties of carnot-carathéodory balls in the heisenberg group. *Atti della Accademia Nazionale dei Lincei. Classe di Scienze Fisiche, Matematiche e Naturali. Rendiconti Lincei. Matematica e Applicazioni*, 11(3):155–167, 2000.
- [123] Roberto Monti and Francesco Serra Cassano. Surface measures in carnot-carathéodory spaces. *Calculus of Variations and Partial Differential Equations*, 13(3):339–376, 2001.
- [124] Philippos Mordohai and Gérard Medioni. Tensor voting: a perceptual organization approach to computer vision and machine learning. *Synthesis Lectures on Image, Video, and Multimedia Processing*, 2(1):1–136, 2006.
- [125] David Mumford. Elastica and computer vision. In *Algebraic geometry and its applications*, pages 491–506. Springer, 1994.

- [126] Micah M Murray and Christoph S Herrmann. Illusory contours: a window onto the neurophysiology of constructing perception. *Trends in cognitive sciences*, 17(9):471–481, 2013.
- [127] Micah M Murray, Glenn R Wylie, Beth A Higgins, Daniel C Javitt, Charles E Schroeder, and John J Foxe. The spatiotemporal dynamics of illusory contour processing: combined high-density electrical mapping, source analysis, and functional magnetic resonance imaging. *The Journal of Neuroscience*, 22(12):5055–5073, 2002.
- [128] Alexander Nagel, Elias M Stein, and Stephen Wainger. Balls and metrics defined by vector fields i: Basic properties. *Acta Mathematica*, 155(1):103–147, 1985.
- [129] Phong Q Nguyen and Damien Stehlé. Low-dimensional lattice basis reduction revisited. In *International Algorithmic Number Theory Symposium*, pages 338–357. Springer, 2004.
- [130] Jacques Ninio. Geometrical illusions are not always where you think they are: a review of some classical and less classical illusions, and ways to describe them. *Frontiers in human neuroscience*, 8:856, 2014.
- [131] Mark Nitzberg and Takahiro Shiota. Nonlinear image filtering with edge and corner enhancement. *IEEE transactions on pattern analysis and machine intelligence*, 14(8):826–833, 1992.
- [132] Mark Nitzberg, David Mumford, and Takahiro Shiota. *Filtering, segmentation and depth*. Springer-Verlag, 1993.
- [133] N.N. Ural'ceva O. A. Ladyženskaja, V.A. Solonnikow. Linear and quasi-linear equations of parabolic type. *American Mathematical Soc.*, 23, 1988.
- [134] Johann Joseph Oppel. Über geometrisch-optische tauschungen. *Jahresbericht des physikalischen Vereins zu Frankfurt am Main*, 1855.
- [135] Stanley Osher and James A Sethian. Fronts propagating with curvature-dependent speed: algorithms based on hamilton-jacobi formulations. *Journal of computational physics*, 79(1):12–49, 1988.
- [136] Scott D Pauls. H-minimal graphs of low regularity in the heisenberg group. *arXiv preprint math/0505287*, 2005.
- [137] Pietro Perona. Deformable kernels for early vision. *IEEE Transactions on pattern analysis and machine intelligence*, 17(5):488–499, 1995.
- [138] Jean Petitot. *Neurogéométrie de la vision*. Editions Ecole Polytechnique, 2008.
- [139] Jean Petitot and Yannick Tondut. Vers une neurogéométrie. fibrations corticales, structures de contact et contours subjectifs modaux. *Mathématiques informatique et sciences humaines*, 145:5–102, 1999.
- [140] Fangtu T Qiu and Rüdiger Von Der Heydt. Figure and ground in the visual cortex: V2 combines stereoscopic cues with gestalt rules. *Neuron*, 47(1):155–166, 2005.
- [141] Jiang Qiu, Hong Li, Qinglin Zhang, Qiang Liu, and Fenghua Zhang. The müller-lyer illusion seen by the brain: An event-related brain potentials study. *Biological psychology*, 77(2):150–158, 2008.

- [142] Manuel Ritoré and César Rosales. Area-stationary surfaces in the heisenberg group  $h_1$ . *Advances in Mathematics*, 219(2):633–671, 2008.
- [143] Brian Roberts, Mike G Harris, and Tim A Yates. The roles of inducer size and distance in the ebbinghaus illusion (titchener circles). *Perception*, 34(7):847–856, 2005.
- [144] James Outram Robinson. *The psychology of visual illusion*. Courier Corporation, 2013.
- [145] Bart M Haar Romeny. *Front-end vision and multi-scale image analysis: multi-scale computer vision theory and applications, written in mathematica*, volume 27. Springer Science & Business Media, 2008.
- [146] Linda Preiss Rothschild and Elias M Stein. Hypoelliptic differential operators and nilpotent groups. *Acta Mathematica*, 137(1):247–320, 1976.
- [147] Elisabeth Rouy and Agnès Tourin. A viscosity solutions approach to shape-from-shading. *SIAM Journal on Numerical Analysis*, 29(3):867–884, 1992.
- [148] Yuri Sachkov. Cut locus and optimal synthesis in the sub-riemannian problem on the group of motions of a plane. *ESAIM C. Opt. Calc. Var.*, 17:293–321, 2011.
- [149] Gonzalo Sanguinetti. Invariant models of vision between phenomenology, image statistics and neurosciences. *PhD thesis, Montevideo, University of Bologna*, 2011.
- [150] Gonzalo Sanguinetti, Giovanna Citti, and Alessandro Sarti. Implementation of a model for perceptual completion in  $r \times s$ . In *International Conference on Computer Vision and Computer Graphics*, pages 188–201. Springer, 2008.
- [151] Gonzalo Sanguinetti, Giovanna Citti, and Alessandro Sarti. A model of natural image edge co-occurrence in the rototranslation group. *Journal of vision*, 10(14):37–37, 2010.
- [152] Gonzalo Sanguinetti, Erik Bekkers, Remco Duits, Michiel HJ Janssen, Alexey Mashtakov, and Jean-Marie Mirebeau. Sub-riemannian fast marching in  $se(2)$ . In *Iberoamerican Congress on Pattern Recognition*, pages 366–374. Springer, 2015.
- [153] Alessandro Sarti and Giovanna Citti. The constitution of visual perceptual units in the functional architecture of  $v_1$ . *Journal of computational neuroscience*, 38(2):285–300, 2015.
- [154] Alessandro Sarti, Giovanna Citti, and Jean Petitot. The symplectic structure of the primary visual cortex. *Biological Cybernetics*, 98(1):33–48, 2008.
- [155] Alessandro Sarti, Giovanna Citti, and Jean Petitot. Functional geometry of the horizontal connectivity in the primary visual cortex. *Journal of Physiology-Paris*, 103(1):37–45, 2009.
- [156] J. A. Sethian. *Level Set Methods and Fast Marching Methods*. Cambridge University Press, second edition edition, 1999.
- [157] James A Sethian. A fast marching level set method for monotonically advancing fronts. *Proceedings of the National Academy of Sciences*, 93(4):1591–1595, 1996.
- [158] James A Sethian. Theory, algorithms, and applications of level set methods for propagating interfaces. *Acta numerica*, 5:309–395, 1996.

- [159] James A Sethian and Alexander Vladimirsky. Ordered upwind methods for static hamilton–jacobi equations: Theory and algorithms. *SIAM Journal on Numerical Analysis*, 41(1):325–363, 2003.
- [160] David A Smith. A descriptive model for perception of optical illusions. *Journal of Mathematical Psychology*, 17(1):64–85, 1978.
- [161] Chen Song, D Samuel Schwarzkopf, Antoine Lutti, Baojuan Li, Ryota Kanai, and Geraint Rees. Effective connectivity within human primary visual cortex predicts interindividual diversity in illusory perception. *The Journal of Neuroscience*, 33(48):18781–18791, 2013.
- [162] Umur Talasli and Asli Bahar Inan. Applying emmert’s law to the pogendorff illusion. *Frontiers in human neuroscience*, 9, 2015.
- [163] Samuel Tolansky. *Optical illusions*. Pergamon Press;[distributed in the Western Hemisphere by Macmillan, New York], 1964.
- [164] Lillian Tong and Daniel J Weintraub. Contour displacements and tracking errors: Probing’twixt pogendorff parallels. *Attention, Perception, & Psychophysics*, 15(2):258–268, 1974.
- [165] Roger B Tootell, Eugene Switkes, Martin S Silverman, and Susan L Hamilton. Functional anatomy of macaque striate cortex. ii. retinotopic organization. *Journal of neuroscience*, 8(5):1531–1568, 1988.
- [166] Loring W Tu. *An introduction to manifolds*. Springer Science & Business Media, 2010.
- [167] Veeravalli Seshadri Varadarajan. *Lie groups, Lie algebras, and their representations*, volume 102. Springer Science & Business Media, 2013.
- [168] R Von Der Heydt, E Peterhans, and G Baurgartner. Illusory contours and cortical neuron responses. *Science*, 224, 1984.
- [169] Rüdiger von der Heydt, Hong Zhou, and Howard S Friedman. Representation of stereoscopic edges in monkey visual cortex. *Vision research*, 40(15):1955–1967, 2000.
- [170] Hermann von Helmholtz and James Powell Cocke Southall. *Treatise on physiological optics*, volume 3. Courier Corporation, 2005.
- [171] Nicholas Wade. *The art and science of visual illusions*. Routledge Kegan & Paul, 1982.
- [172] Johan Wagemans, James H Elder, Michael Kubovy, Stephen E Palmer, Mary A Peterson, Manish Singh, and Rüdiger von der Heydt. A century of gestalt psychology in visual perception: I. perceptual grouping and figure–ground organization. *Psychological bulletin*, 138(6):1172, 2012.
- [173] Evan Harris Walker. A mathematical theory of optical illusions and figural aftereffects. *Perception & Psychophysics*, 13(3):467–486, 1973.
- [174] Changyou Wang. Viscosity convex functions on carnot groups. *Proceedings of the American Mathematical Society*, pages 1247–1253, 2005.
- [175] Frank W Warner. *Foundations of differentiable manifolds and Lie groups*, volume 94. Springer Science & Business Media, 2013.

- [176] Joachim Weickert. *Anisotropic diffusion in image processing*, volume 1. Teubner Stuttgart, 1998.
- [177] Joachim Weickert. Coherence-enhancing diffusion filtering. *International journal of computer vision*, 31(2-3):111–127, 1999.
- [178] R Weidner, F Boers, K Mathiak, J Dammers, and GR Fink. The temporal dynamics of the müller-lyer illusion. *Cerebral Cortex*, 20(7):1586–1595, 2009.
- [179] Ralph Weidner and Gereon R Fink. The neural mechanisms underlying the müller-lyer illusion and its interaction with visuospatial judgments. *Cerebral Cortex*, 17(4):878–884, 2006.
- [180] Daniel J Weintraub. The logic of misperceived distance (or location) theories of the poggenдорff illusion. *Attention, Perception, & Psychophysics*, 53(2):231–238, 1993.
- [181] Daniel J Weintraub and David H Krantz. The poggenдорff illusion: Amputations, rotations, and other perturbations. *Attention, Perception, & Psychophysics*, 10(4):257–264, 1971.
- [182] Daniel J Weintraub, David H Krantz, and Thomas P Olson. The poggenдорff illusion: consider all the angles. *Journal of Experimental Psychology: Human Perception and Performance*, 6(4):718, 1980.
- [183] Yair Weiss, Eero P Simoncelli, and Edward H Adelson. Motion illusions as optimal percepts. *Nature neuroscience*, 5(6):598–604, 2002.
- [184] Max Wertheimer. *Laws of organization in perceptual forms*. 1938.
- [185] Gerald Westheimer. Illusions in the spatial sense of the eye: Geometrical–optical illusions and the neural representation of space. *Vision research*, 48(20):2128–2142, 2008.
- [186] D Wilkins. *A course in riemannian geometry*. Trinity College, Dublin, 2005.
- [187] Wilhelm Max Wundt. *Die geometrisch-optischen Täuschungen*, volume 24. BG Teubner, 1898.
- [188] Richard A Young. The gaussian derivative model for spatial vision: I. retinal mechanisms. *Spatial vision*, 2(4):273–293, 1987.
- [189] Mitsuru HONMA Yun Gang CHEN Yoshikazu GIGA, Toshio HITAKA. Numerical analysis for motion of a surface by its mean curvature. *Hokkaido University*, 836:147–151, 1993.
- [190] Friedrich Zöllner. Ueber eine neue art von pseudoskopie und ihre beziehungen zu den von plateau und oppel beschriebenen bewegungsphänomenen. *Annalen der Physik*, 186(7): 500–523, 1860.